

Copyright
by
David Martin Rosewater
2020

The Dissertation Committee for David Martin Rosewater
certifies that this is the approved version of the following dissertation:

**Battery Energy Storage Control: Modeling,
Uncertainty, and Applications**

Committee:

Surya Santoso, Supervisor

Ross Baldick

Hao Zhu

Qin (Alex) Huang

Grani Hanasusanto

Raymond Byrne

**Battery Energy Storage Control: Modeling,
Uncertainty, and Applications**

by

David Martin Rosewater

DISSERTATION

Presented to the Faculty of the Graduate School of
The University of Texas at Austin
in Partial Fulfillment
of the Requirements
for the Degree of

DOCTOR OF PHILOSOPHY

THE UNIVERSITY OF TEXAS AT AUSTIN

May 2020

Dedicated to my loving partner Kit and to our acrobat.

Acknowledgments

This research was funded by the U.S. DOE OE, Energy Storage Program. I would like to thank Dr. Imre Gyuk for supporting research to improve control systems for grid energy storage technologies. I would like to thank my manager, Dr. Babu Chalamala, for his unwavering support of my academic ambitions.

I would like to thank Dr. Ross Baldick for his patience in helping me learn optimization, Dr. Raymond Byrne, for his continued mentorship at Sandia, and the rest of my committee for their support and guidance.

Lastly, I wish to thank my advisor, Dr. Surya Santoso, for giving me a chance in the program and for his continued guidance and support throughout the last four years. I am extremely grateful for his skill in mentoring, for his ability to teach the skills needed for technical publication, and for his time and attention.

This dissertation describes objective technical results and analysis. Any subjective views or opinions that might be expressed in the paper do not necessarily represent the views of the U.S. Department of Energy or the United States Government.

Battery Energy Storage Control: Modeling, Uncertainty, and Applications

SAND2020-4029 T

David Martin Rosewater, Ph.D.
The University of Texas at Austin, 2020

Supervisor: Surya Santoso

Battery energy storage systems (BESS) can restore flexibility to power systems that grow increasingly constrained from proliferation of variable renewable power and retirement of fossil-fuel based generation. BESS are often controlled through an energy management system (EMS), which may not have access to detailed, physical models developed by battery manufacturers. The research outlined in this dissertation makes substantive contributions to quantify, reduce, and ultimately account for the effects of battery system modeling uncertainty on energy management and control. Battery models for optimal control are reviewed in detail and metrics for their accuracy and uncertainty are derived. Optimal parameter identification and adaptive modeling methods are developed to reduce model uncertainty as much as possible. As some uncertainty always remains, a method for risk-averse model predictive control for BESS is developed to account for uncertainty and hedge control decisions to reduce optimistic shortfall. Lastly, the potential for controller performance improvement to bolster the value of BESS on the grid is demonstrated. Together,

more accurate, adaptive models working in conjunction with risk-adverse control algorithms dismantle the impacts of model uncertainty on energy storage grid integration. These contributions represent an advance to the state-of-the-art in the engineering methods for addressing modeling uncertainty in BESS control.

Table of Contents

Acknowledgments	v
Abstract	vi
List of Tables	xiii
List of Figures	xv
Chapter 1. Introduction	1
1.1 Background and Motivation	1
1.2 Objectives	4
1.3 Original Research Contributions and Dissertation Outline . .	7
Chapter 2. Battery Energy Storage Models for Optimal Control	17
2.1 Introduction	19
2.2 Problem Statement	24
2.3 State-of-Charge Models	26
2.3.1 Energy Reservoir Models	31
2.3.1.1 ERM Application	36
2.3.2 Charge Reservoir Model (CRM)	40
2.3.2.1 CRM Application	49
2.3.3 Concentration Based Models	52
2.3.3.1 SPM Application	60
2.4 Temperature Models	63
2.4.1 Heat Generation, Consumption, and Transfer	70
2.4.2 Enclosure Thermal Model	75
2.4.3 Temperature Model Types	77
2.4.3.1 Temperature Model Application	82

2.5	Degradation Models	86
2.5.1	Empirical Degradation Models	93
2.5.1.1	Degradation as Regularization	96
2.5.2	Physical Degradation Models	101
2.5.3	Degradation Model Application	105
2.6	Discussion	109
2.6.1	Gap Identification	111
2.7	Summary	114
Chapter 3. Application of a Uniform Testing Protocol for Energy Storage Systems		117
3.1	Introduction	118
3.2	Methodology	120
3.2.1	Procedure Adaptation	120
3.2.2	Test Procedures	121
3.2.3	Performance Calculation	121
3.3	Experimental Setup	125
3.3.1	Equipment Under Test	125
3.3.2	Control and Instrumentation	125
3.4	Results	126
3.4.1	Stored Energy Performance	126
3.4.2	Response Time and Ramp Rate Performance	127
3.4.3	Reference Signal Tracking Test Performance	128
3.5	Discussion	132
3.6	Summary	133
Chapter 4. Battery Energy Storage State-of-Charge Forecasting: Models, Optimization, and Accuracy		134
4.1	Introduction	135
4.2	State of Charge Estimation	137
4.3	SoC Forecast Models	139
4.3.1	Energy Reservoir Model (ERM)	140
4.3.2	Charge Reservoir Model (CRM)	142

4.4	Choosing Model Parameters	145
4.4.1	Choosing Parameters from Specifications	146
4.4.2	Choosing Parameters from Testing	148
4.4.3	Operational Data	148
4.5	Model Implementation and Comparison	149
4.5.1	SoC Estimation	150
4.5.2	Parameter Selection	151
4.5.3	Model Accuracy Framework	156
4.5.4	Model Comparison	158
4.6	Summary	162
Chapter 5. Adaptive Modeling Process for a Battery Energy Management System		164
5.1	Introduction	165
5.2	Battery Model	167
5.3	EMS Model Learning Process	168
5.3.1	Data Requirements	168
5.3.2	Parameter Estimation	171
5.3.3	Accuracy Testing	173
5.3.4	Model Update	174
5.4	Results	176
5.4.1	Model Learning	176
5.5	Summary	178
Chapter 6. Risk-Averse Model Predictive Control Design for Battery Energy Storage Systems		181
6.1	Introduction	182
6.2	Energy Reservoir Model	186
6.3	Charge Reservoir Model	188
6.4	Extended CRM for Simulation	190
6.5	Bounding the Global Minimum	193
6.6	Reducing Control Sensitivity to Uncertainty	197
6.7	Results	201

6.7.1	Open-Loop Control	203
6.7.2	Closed-Loop control	204
6.7.3	Risk-Averse Closed-Loop Control	206
6.8	Summary	207
Chapter 7. Optimal Field Voltage and Energy Storage Control for Stabilizing Synchronous Generators on Flexible AC Transmission Systems		208
7.1	Introduction	209
7.2	System Modeling	211
7.2.1	SMIB Model Equations	212
7.2.2	State Space Model	215
7.3	Optimal Controller Design	216
7.3.1	The LQR Optimal Controller	216
7.3.2	Reduced Order Observer Design	217
7.4	Simulation Results	218
7.4.1	The Open-Loop System Response	219
7.4.2	The Closed-Loop System Response	219
7.4.3	The Effect of Weighting Factors in the Performance Index	222
7.5	Summary	224
Chapter 8. A Voltage Smoothing Algorithm using Energy Storage PQ Control in PV-integrated Power Grid		225
8.1	Introduction	226
8.2	Voltage Smoothing Techniques by ES Power Injection Control	227
8.2.1	Technique I: Active power ramp rate control by monitoring PV inverter power output	227
8.2.2	Technique II: Proposed algorithm of PQ power injection control by monitoring voltage	228
8.3	System Model for Verifications	231
8.4	Summary	235

Chapter 9. Optimal Control of a Battery Energy Storage System with a Charge-Temperature-Health Model	236
9.1 Introduction	237
9.2 Problem Statement	238
9.3 BESS Model	240
9.3.1 Charge Model	242
9.3.2 Temperature Model	242
9.3.3 Health Model	245
9.4 Results	246
9.5 Summary	252
Bibliography	253
Vita	287

List of Tables

2.1	Summary of Case Study Assumptions	26
2.2	Summary of SoC Models I	29
2.3	Summary of SoC Models II	30
2.4	Conversion Between Equivalent Efficiency Representations . .	32
2.5	Energy Reservoir Model Parameters	38
2.6	Battery System Charge Reservoir Model Parameters	53
2.7	Battery System Single Particle Model (SPM) Parameters I . .	64
2.8	Battery System Single Particle Model (SPM) Parameters II . .	65
2.9	Equilibrium Potential Redlich-Kister Expansion Parameters, re- produced from [1]	65
2.10	Summary of Temperature Models	69
2.11	Thermodynamic properties of common battery cooling fluids* [2]	74
2.12	Fluid flow geometry constants for a cylinder in cross-flow [2] .	74
2.13	Example Battery System Temperature Model Parameters . . .	84
2.14	Summary of Degradation Models I	91
2.15	Summary of Degradation Models II	92
2.16	Example battery system degradation model parameters	107
3.1	Test Procedures	122
3.2	Stored Energy Test Results	128
3.3	Response Time and Ramp Rate Test Results	128
3.4	Reference Signal Tracking Test Results	131
4.1	SoC Estimation Model Parameters	151
4.2	Summary of Energy Reservoir Model Parameters	152
4.3	Summary of Charge Reservoir Model Parameters	153
4.4	Smoothing Battery Dynamic Model Parameters	154
4.5	State-of-Charge Forecasting Error Metrics	160

5.1	Charge Reservoir Model Initial Parameters	169
5.2	Charge Reservoir Model Final Parameters	179
6.1	Summary of Case Study Assumptions	183
6.2	Energy Reservoir Model Parameters	187
6.3	Charge Reservoir Model Parameters	191
6.4	Additional Extended CRM Parameters	193
6.5	Convex Relaxation and Approximation Parameters	198
6.6	Summary of Results from Simulated Control Scenarios	202
7.1	Open-loop settling time performace	219
7.2	Closed-loop settling time performace	222
7.3	Settling time performance with reduced ESS control action	223
8.1	Summary of Verification Results	234
9.1	Simulations Results	247
9.2	Battery Energy Storage System Model Parameters I	248
9.3	Battery Energy Storage System Model Parameters II	249

List of Figures

1.1	Graphical illustration of the objectives of this dissertation. . .	8
2.1	Typical energy management system control diagram.	20
2.2	Illustration of the trade-off between model accuracy and complexity (computational complexity equates to CPU time, and model accuracy has also been referred to as “predictability” [3])	22
2.3	Time-of-use price schedule (top), and customer electrical load (bottom) [4]	26
2.4	Thought experiment demonstrating how the electrochemical definition of the SoC of a battery loses physical meaning when applied to strings [5]	27
2.5	Energy Based Kinetic Battery Model [6]	35
2.6	Feasible region for ac power described by the kinetic battery model	36
2.7	Results calculated with the ERM: (a) Net load with BESS power control, (b) Battery power, (c) battery SoC (bottom)	41
2.8	Equivalent Circuit Models	43
2.9	Charge Based Kinetic Battery Model [7,8]	45
2.10	Open-Circuit-Voltage Models	46
2.11	Results calculated with the CRM: (a) net load with BESS power control, (b) battery power, (c) battery SoC, (d) battery current, and (e) battery voltage	54
2.12	Single particle model (SPM)	55
2.13	Equilibrium potentials (open-circuit-voltages) of lithium-cobalt-oxide (LiCO ₂) cathode (top) and MesoCarbon MicroBeads (MCMB) anode (bottom) [1]	59
2.14	pseudo two-dimensional model (P2D)	59
2.15	Concentration reservoir analogy of the SPM with five discrete volumes per particle	60
2.16	Results calculated with the SPM (a) net load with BESS power control , (b) battery power, (c) battery SoC, (d) battery current, (e) battery voltage, (f) cathode concentration fraction, (g) anode concentration fraction	66

2.17	Notional examples of temperature dependent current limits . .	68
2.18	Computed full cell ΔS from individual electrode ΔS for three types of lithium-ion batteries, replotted with data from [9] . .	71
2.19	Thermal transmittance for a 18650 battery cell in cross flow as a function of air speed [2]	74
2.20	Cell thermal model w/ a lumped-volume, resistive-heating, and conduction-cooling	78
2.21	Enclosure model with lumped-air-volume and HVAC efficiency cooling	79
2.22	Cell thermal model w/ internal and surface-volumes, resistive and overpotential heating, and conduction/radiation cooling .	80
2.23	Cell model with multiple-internal-volumes, resistive/overpotential/entropy-heating, and conduction/radiation/convection-cooling	81
2.24	Enclosure model with, lumped-air-volume, heat-exchanger temperature, HVAC efficiency and fan speed based cooling	82
2.25	Results from control incorporating temperature model: (a) net load with BESS power control, (b) battery power, (c) battery SoC, (d) enclosure ac power, and (e) battery, enclosure, and environmental temperatures	85
2.26	Notional example of a manufacturer supplied degradation curve (curve value = \mathfrak{D})	90
2.27	Results from control incorporating a degradation model: (a) net load with BESS power control, (b) battery power, (c) battery SoC, (d) enclosure ac power, and (e) battery, enclosure, and environmental temperatures	108
3.1	Stored Energy Test Data	127
3.2	Response Time and Ramp Rate Test Data (Normalized and Filtered)	129
3.3	Frequency Regulation Duty-Cycle Test Data	130
3.4	State-of-Charge During Duty-Cycle Test	130
4.1	First Order Dynamic Battery Model	138
4.2	Energy Reservoir Model	140
4.3	Dynamic Battery Model	143
4.4	Charge Reservoir Model	143
4.5	Flowchart for Choosing Model Parameters	147

4.6	KF SoC Estimation verses BMS SoC Data Recorded	152
4.7	Inverter ac Power per dc Power (left), Inverter Efficiency per dc Power (right)	155
4.8	Smoothing Battery Power Operation (top), State-of-Charge Forecasts (bottom) for a Sample Day	159
4.9	State-of-Charge Forecasting RMS Error for: Smoothing battery with ERM (top), Smoothing battery with CRM (middle top), Shifting battery with ERM (middle bottom), Shifting battery with CRM (bottom)	161
5.1	First order equivalent circuit model with distinct charge/discharge resistances	168
5.2	Flow chart of the EMS model learning process	170
5.3	One-and-one validation training and testing sets	174
5.4	Updates to the capacity parameter for Battery 1 (top), Battery 2 (bottom). One standard deviation of the previous ten values is shown by upper and lower bounds.	177
5.5	Updates to the battery model's open-circuit-voltage function	177
5.6	EMS model % Error on Baseline Test Data	178
6.1	Time-of-use price schedule (top) [10], and electrical load (bottom) [4]	183
6.2	Open-circuit voltage constraint satisfying (6.3.1e)	190
6.3	Convex Relaxation of Ohms Power Law (6.3.1c), split between positive and negative current	195
6.4	Notional examples of risk-neutral and risk-averse control bill savings probability density functions	200
6.5	Relative benefits of risk-averse control based on model accuracy/precision, given an asymmetric risk application	201
6.6	Optimal SoC schedules calculated and achieved in open-loop control from ERM (top), and CRM (bottom)	205
6.7	Optimal customer net-load results for the ERM in open-loop	205
6.8	Optimal customer net-load results for the CRM in open-loop	205
6.9	Closed-Loop Control Results for ERM and CRM	206

6.10	Control performance sensitivity of the risk-neutral and risk-averse CRM based model predictive controllers (compare to the ideal in Fig. 6.4). Probability refers to the likelihood that the capacity is less than the signified value. When total bills resulting from different capacity values are very close (within 25¢), their probabilities are added, and the total bill is averaged.	207
7.1	The model of a single electric machine connected to a infinite bus with PSS and ESS.	211
7.2	Block diagram representing the system shown in Fig 7.1.	214
7.3	Observer performance.	220
7.4	The response of states at each frequency of interest.	221
7.5	Optimal controls.	221
7.6	Energy storage response	223
7.7	The resulting states when r_2 varies. ($r_2 = \infty$ represents no ESS control action)	224
8.1	Control algorithm of voltage smoothing by limiting active power ramp rate in Technique I.	228
8.2	Power injection control point for ES in (a) Technique I; and (b) Technique II.	229
8.3	Proposed control algorithm of ES PQ power injection by monitoring local PV bus voltage in Technique II.	229
8.4	System model used for verification.	232
8.5	(a) Line to neutral voltage at the load bus (bus 4 phase A); (b) Tap number at load tap changer: (top) case without any voltage smoothing control; (middle) using Technique I; (bottom) using Technique II	233
8.6	(a) Injection of active and reactive power from ES; (b) Battery SOC: (top) Technique I; (bottom) Technique II	234
9.1	Time-of-use price schedule (top), and customer electrical load (bottom) [4]	240
9.2	Representitive-cell model with internal temperature	243
9.3	Optimal net-load (top), charge/discharge (middle), and SoC (bottom) schedules for different operational life expectations	250
9.4	Example AC power, fan power (top), cell, enclosure, and heat-exchanger temperature (bottom) results for 10-year operational life expectation	251

Chapter 1

Introduction

This chapter outlines the research carried out in this dissertation to understand, reduce, and control modeling uncertainty in battery energy management systems. It begins in Section 1.1. with an overview of the services that battery energy storage provides on the grid, and how energy management systems are critical to maximizing these services. The motivation to develop improved solutions and the specific research objectives are explicitly stated in Section 1.2. The original research contributions along with the resulting publications are summarized in Section 1.3.

1.1 Background and Motivation

As power systems around the world integrate renewable energy resources to reduce harmful air pollution and carbon emissions, a significant amount of energy storage will be necessary in maintaining grid reliability and low energy prices throughout the transition [11]. Fundamentally, large swings between energy scarcity and oversupply are the natural result of a grid composed of variable generation and load. These swings are partly addressed through smart grid controllers that make wind and solar resources more controllable and demand response programs that makes load more controllable. Battery energy storage, which can serve as both generation and load, restores flexibility to power systems that grow increasingly constrained from prolifera-

tion of variable renewable power and retirement of fossil-fuel based generation. Storage provides flexibility through a variety of grid services, each of which counteracts variations in the availability (scarcity or oversupply) of energy by absorbing energy when it is available or inexpensive, then supplying energy when it would otherwise be inaccessible or costly. Changes in the availability of energy, at specific locations in the grid, often result in changes in the value of energy to specific economic agents (including energy storage operators). For services where changes in locational value are foreseeable, agents can anticipate and react to the availability of energy based on forecasts of the supply and demand of grid services. Grid services that meet these criteria include energy price arbitrage, peak load management, peak supply management (in cases where supply would otherwise be curtailed), and renewable generation firming. When a storage operator is supplying one or more of these services, they can integrate forecasts into proactive control decisions to improve effectiveness. Grid services that do not meet these criteria, as they are not based on predictable changes in the locational value of energy, include uninterruptible power supply, frequency regulation, voltage support, spinning reserve, and inter-area oscillation damping. For these services, proactive control is either infeasible (cannot forecast) or trivial (a forecast would not change the operator's decisions).

The potential benefits of energy storage are highly sensitive to the service life and the installation cost per effective power and energy capacities [11,12]. Battery energy storage controllers are critical to the energy transition because they maximize a device's effective power and energy while increasing service life. The energy storage controller, often a sub-process within an Energy Management System (EMS), makes these decisions recursively, through

a mathematical algorithm, while observing system states to reach a desired condition. A variety of algorithms are available for making optimal decisions based on forecasts of grid service demand. These algorithms are tailored to the mathematical form of the energy storage system model and the optimization objective. Linear models and objectives can be solved efficiently with a linear programming (LP) algorithm while models with temporal-path-dependence may require dynamic programming (DP) or model predictive control (MPC) to solve. Once the optimal decision has been found and implemented by the controller, time advances and the forecast is updated with new information.

For energy storage controllers, there are two primary sources of uncertainty. First, changes in the value of grid services can be difficult to predict and the underlying load, meteorological, and price forecast models can be imprecise. Deterministic control is especially vulnerable to forecast uncertainty as decisions are made based on predicted events that may never occur. Second, the energy storage system model may be inaccurate. Mismatches between the model employed and the real system can jeopardize the robustness of the controller as decisions are made based on dynamics that the real equipment may not be capable of. Further, because of degradation over calendar and cycle life, electrochemical storage system dynamics can change over time, compounding model mismatch. Robust control can, at least partially, compensate for both of these sources of uncertainty by minimizing the suboptimality of decisions according to the controller's risk tolerance. If a controller is wholly risk adverse, decisions are made based on the worst case scenario within the distribution of possible outcomes, while greater risk tolerance can be handled with value-at-risk objectives. However, more accurate service forecasts, and more accurate energy storage system models, lead to decisions that will be closer to the true

optimal decisions only available from a priori knowledge or hindsight. Given that value forecasting models have already been the subject of extensive study, the research presented here focuses on the aspects of optimal control unique to battery storage, namely the models used to represent battery energy storage system (BESS) dynamics.

1.2 Objectives

The overall objective of this dissertation is to advance the state-of-the-art in battery energy storage control by quantifying and reducing the effects of uncertainty from battery models on grid integration and operation of BESS. This research is expected to improve the ability and reliability of BESSs to supply grid services.

The specific research objectives are stated below:

Objective 1: Perform a Review of the Mathematical Models used for Optimal Control of Electrochemical Energy Storage Systems

Within the BESS model itself, there are two linked sources of uncertainty: unrepresented dynamics and performance variability [13,14]. The battery model most widely used in power system research is also the simplest. Energy reservoir type models represent a battery's energy capacity in kWh. This simplification means that many of the dynamic, non-linear relationships between voltage, current, temperature, and chemical concentrations in batteries are unrepresented. An overly simplistic controller model can generate significant uncertainty in the energy that is available for charge or discharge. An observer, watching the battery's performance over time, would see an apparent variability in the energy capacity of the battery. However, performance

variability is a result of an imperfect model. By using a more precise model, a BESS controller can reduce observed variability and achieve higher and more consistent performance. Selecting the best model for a given application can take unnecessary, extensive research which many companies do not have the resources to perform. Battery modeling is complex and quickly changing, and there have been no comprehensive or critical reviews to help engineers navigate the subject.

This objective presents the state-of-the-art in controller design based on models that mathematically represent the physical dynamics and constraints of batteries. As unrepresented dynamics can lead to suboptimal control, a review of these models will help engineers navigate the range of available design choices and helps researchers by identifying gaps in the field. When choosing a BESS model, implicit assumptions are made about which physical dynamics are important to the controller's operation and which can be ignored. The aim of this objective is to review the forms and functions of BESS models with critical attention to their advantages, disadvantages, and characteristics.

Objective 2: Develop Algorithms for Reducing Uncertainty in Controller Battery Models

Once an appropriate battery controller model has been selected, picking model parameters can be a daunting task. Battery manufacturers often consider certain parameters to be proprietary and so do not provide such information to the engineers designing controllers. Experimental procedures have been developed to estimate parameters, though these procedures can involve expensive laboratory equipment and/or a significant amount of time to perform. Ideally, the controller would pick its own model parameters based on operational data, though the algorithms available for this task are nascent at

best [15].

This objective is to develop methods to minimize the uncertainty of BESS controller models. This is accomplished through the development of experimental procedures, optimal parameter estimation algorithms, and adaptive models.

Objective 3: Develop Methods for Risk-Averse and Robust Optimal Control of BESS

With the BESS control model uncertainty reduced as much as is feasible, controllers can potentially account for the remaining uncertainty in their control decisions through risk-averse and/or robust control. These methods, commonly applied in finance and operations research, enable a controller to hedge its decisions to prevent the worse-case scenario (robust control) or to make large losses less likely (risk-averse control). This kind of control works whenever the benefits of an energy storage service has asymmetric risk. Asymmetric risk in the context of battery control is whenever the downside of overestimating performance outweighs the potential upside of underestimating performance. For example: in peak load management, a battery is used to reduce the peak electrical load as much as possible. If a controller overestimates battery capacity, the battery may run out of energy prematurely and fail to reduce the peak at all. Algorithms for risk averse control in BESS are rarely used and underdeveloped.

This objective is to develop and demonstrate a methodology to design advanced BESS controllers that are able to account for model uncertainty and hedge decisions against asymmetric risk. This is accomplished by shaping the model's uncertainty to consistently and reliably underestimate performance according to a quantitative risk tolerance parameter.

Objective 4: Demonstrate the Potential for Controller Performance Improvement to Maximize the Benefits of BESS in Power Systems

When calculating the cost of battery systems per kW, kWh, or operational life, the control system is generally not considered to be an important factor. However, effective control systems are critical to the integration of BESS on the grid and can act as a performance and life multiplier. A controller cannot literally make a 1 MW battery inverter supply 2 MW but controller improvements can use the 1 MW battery to reduce a customer's peak electrical load as if it were a larger battery. Research that demonstrates how controller improvements directly translate to improvements in the services provided by batteries will help to clarify this blind-spot in the field.

This objective is to demonstrate how controller improvements can use the same hardware to greater effect, thereby reducing costs, increasing revenue, and generally maximizing whatever benefits are being derived from the BESS.

1.3 Original Research Contributions and Dissertation Outline

The research and analysis conducted in this dissertation, as illustrated in Fig. 1.1, broadly improves battery system controllers by managing controller model uncertainty in three ways: 1) by improving the methods for appropriate model selection, 2) by reducing the uncertainty of the selected model as much as possible, and 3) by explicitly representing the remaining quantified model uncertainty. Model selection is performed by finding the simplest model that represents the necessary physical dynamics, to an appropriate degree of both physical salience and model order. Physical dynamics broadly include charge, temperature, and degradation modeling domains, while specific technologies

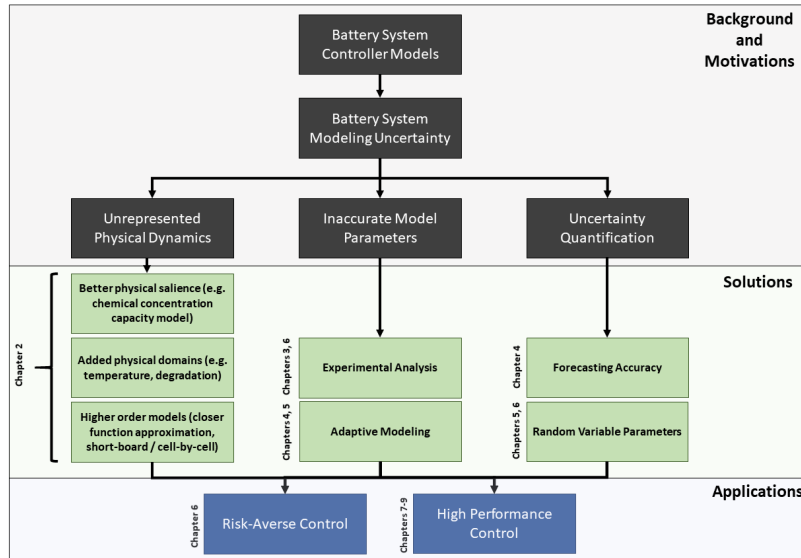


Figure 1.1: Graphical illustration of the objectives of this dissertation.

may also include pressure, volume, or other domains. Physical salience refers to the degree to which the domain model matches the underlying physical mechanism, the most prominent example of which is the distinction between energy, charge, and chemical concentration based state-of-charge models. Lastly, the model order refers to how many parameters are used to approximate a given function (e.g. open-circuit-voltage) or the number of cells explicitly modeled in the controller.

Once a model is selected, its uncertainty is reduced as much as possible through experimental analysis and adaptive modeling. By performing a range of tests on a given device and optimizing a model from the collected data, the model uncertainty can be minimized. Additionally, after a system is operational, data can be collected and used to keep uncertainty low as battery performance changes over time and use. Both methods can be used to calculate and explicitly represent model uncertainty within the controller itself.

Uncertainty is quantified by both state forecast error and by parameterizing models with random variables.

These methods are applied to improve the performance of BESS control systems and to perform risk-averse control. Advanced, high performance BESS controllers are shown to reduce the required size of, or increase the accrued benefits from, BESS in a range of power system applications. Risk-averse control is able to hedge control decisions against asymmetric downside loss in critical applications. Together, high performance risk averse control has the potential to maximize the impact of BESS to integrate renewable power and maintain the reliability, resilience, and efficiency of the electric grid.

The remainder of this section identifies the original research contributions made while achieving the objectives of this dissertation. Major contributions are those that significantly advance the state-of-the-art while minor contributions simply fill in gaps in understanding and only impact the state-of-the-art in aggregate. The section also provides a list of all the publications resulting from this research and outlines the organization of this dissertation.

Contributions to Objective 1

The contribution made while achieving Objective 1 is to perform a comprehensive review of the mathematical models used for optimal control of battery energy storage devices. The goal of this work is to understand the forms and functions of BESS models with critical attention to their advantages, disadvantages, and characteristics. This research helps navigate the complex trade-offs involved in designing a BESS controller. Chapter 2 describes the state-of-the-art in battery system modeling for optimal control (*major*), compares each model's relative strengths and weaknesses (*minor*), and identifies several gaps (*minor*).

The work described in [13] demonstrates the importance of model selection for optimal control by providing several example controller designs. Simpler models may overestimate or underestimate the capabilities of the battery system. Adding physical dynamics can improve accuracy at the expense of model complexity and computation time.

- D. Rosewater, D. Copp, T. Nguyen, R. Byrne, and S. Santoso, “Battery Energy Storage Models for Optimal Control” *IEEE Access*, December 2019. Article DOI: 10.1109/access.2019.2957698, Code DOI: 10.24433/CO.6925148.v1

Contributions to Objective 2

The contribution made while achieving Objective 2 is to reduce the uncertainty of the selected controller models using experimental analysis and operational data. Chapter 3 describes the application of a uniform testing protocol to a battery energy storage system. The Protocol for Uniformly Measuring and Expressing the Performance of Energy Storage [16] enables fair benchmarking and comparison of different storage technologies. The work described in [17], applies the protocol to a 1-megawatt rated energy storage system to collect application experience and data that will help standards development organizations to adapt and adopt the protocol with confidence and clarity (*minor*). The work additionally develops new energy storage performance metrics that provide more information to the device owner (*minor*). Improvements in testing methodologies is one way of reducing model parameter uncertainty.

Chapter 4 develops a method of calculating optimal parameter values for a state-of-charge model using operational data along with methods of quan-

tifying model accuracy. State-of-charge (SoC) forecasting models are widely used in smart grid battery energy storage control design and optimization. The work described in [15] presents three advances to the area of BESS SoC forecasting. First, the work introduces two example models, the energy reservoir model (ERM) and the charge reservoir model (CRM), that are configured for calculation of optimal parameters (*minor*). Second, the work develops a method for optimal ERM and CRM parameter selection using operational data to minimize RMS forecast error (*major*). Third, the work proposes a framework for SoC forecast model accuracy assessment based on three metrics: mean RMS error, 90% high error threshold, and 90% low error threshold (*minor*). The mean RMS error is a single intuitive metric for direct accuracy comparison, whereas the high and low thresholds represent the charge/discharge schedule error margins achievable when using the model. These models and methods were then implemented on two example lead-acid battery systems, and the results were compared to conventional parameter selection methods using the proposed model accuracy framework.

Chapter 5 describes a method for in situ parameter, and parameter uncertainty, estimation. The work described in [14] develops a process for using operational data to steadily improve the accuracy of an EMS model and calculate the modeling uncertainty for use in risk-averse control (*minor*). The process starts with an initial parameter set, which can be based on manufacturer ratings or rough order of magnitude guesses. This parameter set is significantly smaller than alternative methods. It then takes operational data and filters out days that do not meet certain requirements for salience and quality. Qualifying data are then used to estimate candidate model parameters, whose accuracy is then tested on the most recent qualifying day not

used for the estimate. This process improves EMS modeling accuracy, reducing modeling error, as qualifying data are supplied over time and use. By applying this process, the EMS maintains an up-to-date and accurate model to work with in optimizing charge and discharge. The work demonstrates the effectiveness of the adaptive modeling process using real world data (*minor*).

- D. Rosewater, P. Scott and S. Santoso, “Application of a uniform testing protocol for energy storage systems,” in *Proc. 2017 IEEE Power & Energy Society General Meeting*, Chicago, IL, 2017, pp. 1-5. DOI: 10.1109/PESGM.2017.8274603
- D. Rosewater, S. Ferreira, D. Schoenwald, J. Hawkins, and S. Santoso, “Battery Energy Storage State-of-Charge Forecasting: Models, Optimization, and Accuracy,” *IEEE Trans. Smart Grid*, vol. 10, no. 3, pp. 2453-2462, May 2019. DOI: 10.1109/TSG.2018.2798165
- D. Rosewater, B. Schenkman, and S. Santoso, “Adaptive Modeling Process for a Battery Energy Management System” in *Proc. Symposium on Power Electronics, Electrical Drives, Automation and Motion*, Sorrento, Italy, June 2020, to be published.

Contributions to Objective 3

The contribution made while achieving Objective 3 is to incorporate an understanding of uncertainty into the controller itself to shape its decisions to be more robust. Chapter 6 describes a risk averse model predictive controller design for battery energy storage systems. The work described in [18] develops and demonstrates an advanced methodology for designing BESS controllers under time of use (ToU) price arbitrage and peak demand charge management

applications. A state-of-the-art ERM is used as the baseline for control performance comparison. The proposed CRM based model predictive controller outperforms the ERM based controller by achieving a lower total electric bill when pseudo-empirically applied in an example scenario (*major*). Because peak load management has asymmetric risk for overestimating available energy, the uncertainty of the CRM is shaped to consistently underestimate capacity. This risk-averse CRM yields better controller performance than the ERM and is more robust to variations in BESS performance than the CRM (*major*). This methodology for designing BESS controllers can be applied in a broad range of energy storage applications, wherever the risk profile of a scheduled service is asymmetric.

- D. Rosewater, R. Baldick, and S. Santoso, “Risk-Averse model predictive control design for battery energy storage systems” *IEEE Trans. Smart Grid*, September 2019. DOI: 10.1109/TSG.2019.2946130

Contributions to Objective 4

The contribution made while achieving Objective 4 is a broad demonstration of the potential for advanced controllers to improve the performance and value of battery energy storage systems. Chapter 7 designs a controller for stabilizing a synchronous generator using both the field voltage and real power injection by a battery energy storage system (*minor*). The power system stabilizer, described in [19], is enhanced with both low frequency transmission and energy storage. The optimal steady-state optimal feedback control is designed as a linear quadratic regulator, including a needed reduced order observer, to improve stability. Chapter 8 describes an advanced control algorithm for smoothing out the fluctuations in distribution system voltage (*minor*). The

work described in [20] designs a method for selecting real and reactive power from energy storage devices connected to the distribution system to smooth ac voltage. Rather than smoothing PV power, smoothing voltage directly is able to counteract the voltage impacts of PV, whether or not the energy storage is co-located with the PV. Chapter 9 develops an optimal battery controller using SoC, temperature, and degradation models (*minor*). Because battery degradation is highly dependent on both charge and temperature, a controller that accounts for all three physical domains is able to make better control decisions. The work described in [21] demonstrates how a model predictive controller can be tuned to optimally reduce a customer's electrical bill, while constrained to a 5, 10, 15, or 20 year planned operational life.

- D. Rosewater, Q. Nguyen and S. Santoso, "Optimal Field Voltage and Energy Storage Control for Stabilizing Synchronous Generators on Flexible AC Transmission Systems," in *Proc 2018 IEEE/PES Transmission and Distribution Conference and Exposition (T&D)*, Denver, CO, 2018, pp. 1-9. doi: 10.1109/TDC.2018.8440436
- P. Siratarnsophon, K. W. Lao, D. Rosewater and S. Santoso, "A Voltage Smoothing Algorithm using Energy Storage PQ Control in PV-integrated Power Grid," in *IEEE Transactions on Power Delivery*. doi: 10.1109/TPWRD.2019.2892611
- D. Rosewater, A. Headley, F. Mier, and S. Santoso, "Optimal Control of a Battery Energy Storage System with a Charge-Temperature-Health Model" in *Proc. 2019 IEEE Power & Energy Society General Meeting*, August 2019

In summary, this dissertation yields the following key technical contributions:

- Provides a review of the battery system model selection options for optimal controllers
 - (*major*) Provides an complete review of the range of battery energy storage models used in optimal control design (Chapter 2).
 - (*minor*) Compares each model's relative strengths and weaknesses (Chapter 2).
 - (*minor*) Identifies gaps in the state-of-the-art of battery modeling that can serve as opportunities for future research (Chapter 2).
- Develops new methods for uncertainty minimization using experimental and operational data
 - (*major*) Develops a new method for selecting optimal parameter values based on operational data presented (Chapter 4).
 - (*minor*) Applies a uniform test protocol to a grid scale energy storage system to reduce performance uncertainty (Chapter 3).
 - (*minor*) Develops new energy storage performance metrics that provide more information to the device owner (Chapter 3).
 - (*minor*) Reformulates two SoC forecasting models to be conducive to parameter optimization (Chapter 4).
 - (*minor*) Develops a new framework for quantifying model accuracy (Chapter 4).
 - (*minor*) Develops a process for the EMS to calculate and improve the accuracy of its control model using the operational data produced by the battery system (Chapter 5).

- (*minor*) Demonstrates the effectiveness of the adaptive modeling process using real world data (Chapter 5).
- Develops a high performance, risk-averse control system for battery energy storage devices
 - (*major*) Enables the application of a more accurate, but non-convex, battery system model by calculating upper and lower bounds on the globally optimal control solution (Chapter 6).
 - (*major*) Modifies battery controller model to consistently underestimate capacity by a statistically selected margin, thereby hedging its control decisions against normal variations in battery system performance (Chapter 6).
- Demonstrates the effectiveness of controller improvements for maximizing the value of grid energy storage assets
 - (*minor*) Designs and demonstrates an advanced controller that is able to optimally stabilize a synchronous generator, over a range of frequencies, using both field voltage and a co-located energy storage system (Chapter 7).
 - (*minor*) Designs and demonstrates an advanced controller to smooth grid voltage using energy storage in distribution systems with high penetration PV (Chapter 8).
 - (*minor*) Designs and demonstrates an advanced control system to optimally reduce a customer's electrical bill using a BESS, subject to a minimum operational life constraint (Chapter 9).

Chapter 2

Battery Energy Storage Models for Optimal Control

¹ As batteries become more prevalent in grid energy storage applications, the controllers that decide when to charge and discharge become critical to maximizing their utilization. Controller design for these applications is based on models that mathematically represent the physical dynamics and constraints of batteries. Unrepresented dynamics in these models can lead to suboptimal control. Our goal is to examine the state-of-the-art with respect to the models used in optimal control of battery energy storage systems (BESSs). This review helps engineers navigate the range of available design choices and helps researchers by identifying gaps in the state-of-the-art.

BESS models can be classified by physical domain: state-of-charge (SoC), temperature, and degradation. SoC models can be further classified by the units they use to define capacity: electrical energy, electrical charge, and chemical concentration. Most energy based SoC models are linear, with vari-

¹D. Rosewater, D. Copp, T. Nguyen, R. Byrne, and S. Santoso, “Battery Energy Storage Models for Optimal Control” *IEEE Access*, December 2019. Article DOI: 10.1109/access.2019.2957698, Code DOI: 10.24433/CO.6925148.v1

The dissertator was the principle investigator for this research including collecting and organizing literature sources, programming example applications, writing/editing the article itself, and responding to peer review comments. Co-authors helped plan the scope of the article, located additional sources in their areas of specialty, and conducted multiple rounds of technical review.

ations in ways of representing efficiency and the limits on power. The charge based SoC models include many variations of equivalent circuits for predicting battery string voltage. SoC models based on chemical concentrations use material properties and physical parameters in the cell design to predict battery voltage and charge capacity. Temperature is modeled through a combination of heat generation and heat transfer. Heat is generated through changes in entropy, overpotential losses, and resistive heating. Heat is transferred through conduction, radiation, and convection. Variations in thermal models are based on which generation and transfer mechanisms are represented and the number and physical significance of finite elements in the model. Modeling battery degradation can be done empirically or based on underlying physical mechanisms. Empirical stress factor models isolate the impacts of time, current, SoC, temperature, and depth-of-discharge (DoD) on battery state-of-health (SoH). Through a few simplifying assumptions, these stress factors can be represented using regularization norms. Physical degradation models can further be classified into models of side-reactions and those of material fatigue.

This chapter demonstrates the importance of model selection to optimal control by providing several example controller designs. Simpler models may overestimate or underestimate the capabilities of the battery system. Adding details can improve accuracy at the expense of model complexity, and computation time. Our analysis identifies six gaps: deficiency of real-world data in control literature, lack of understanding in how to balance modeling detail with the number of representative cells, underdeveloped model uncertainty based risk-averse and robust control of BESS, underdevelopment of nonlinear energy based SoC models, lack of hysteresis in voltage models used for control, lack of entropy heating and cooling in thermal modeling, and deficiency

of knowledge in what combination of empirical degradation stress factors is most accurate. These gaps are opportunities for future research.

Contributions of this chapter were identified as follows: (*major*) provided an complete review of the range of battery energy storage models used in optimal control design, (*minor*) compared each model's relative strengths and weaknesses, and (*minor*) identified gaps in the state-of-the-art that can serve as opportunities for future research.

2.1 Introduction

BESS can play an integral role in resilient and efficient power systems because of their ability to provide a range of energy services [12]. One of the fundamental problems in BESS integration within the electric power grid is designing control systems to maximize the value of energy services provided [22]. BESS models used in control systems formally represent assumptions about the physics underlying the conversion and storage of electrical energy. The BESS model is a critical element of effective control and operation of BESS that, ultimately, enables more resilient and efficient power systems.

The control objective for a BESS often involves minimizing an objective function (e.g., cost to the operator) subject to the constraints of the system. The controller must decide settings for both real and reactive power (decision variables), within limits on power, energy, state-of-charge (SoC), voltage, current, temperature, and state-of-health (constraints). Unlike in electric vehicles or consumer electronics (where the controller is an element of the battery management system (BMS) [23]), the BESS controller is an element of the energy management system (EMS), which is responsible for issuing control decisions for all devices within its purview (e.g., a home, building, microgrid, etc.). The

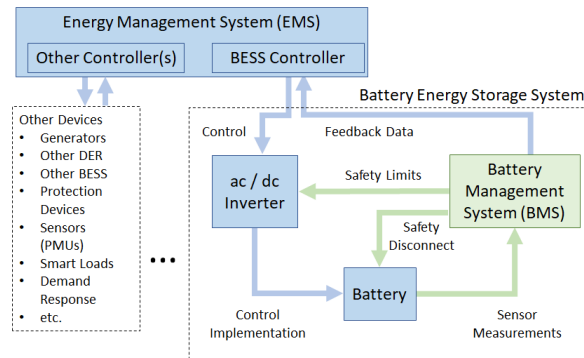


Figure 2.1: Typical energy management system control diagram.

BMS and EMS can share hardware and have overlapping responsibilities, as shown in Fig. 2.1, and often do not share a BESS model. Models used in BMSs are often developed by the battery manufacturers themselves and hence can contain detailed information about underlying chemical process not available to an EMS controller. Further, for applications that require accuracy at very high sample rates, such as power system stability, the inverter can have its own battery model for dynamic optimal control. This chapter focuses on optimal BESS control design within the EMS and so falls between the established fields of optimal control and battery modeling.

The methods for designing optimal controllers for energy storage systems have already been reviewed in [22]. Example methods as applied to BESS include model predictive control (MPC) [24–27], and linear quadratic regulator (LQR) control [19, 28]. While there are large differences between the methods for designing controllers, at the core of any approach is a model of the battery system. In this chapter, we will largely ignore what method is used to design the controller, instead focusing on the commonalities and differences between the models.

BESS models mathematically represent the physical dynamics and constraints of real systems. When choosing a BESS model, implicit assumptions are made about which physical dynamics are important to the controller's operation and which can be ignored. If a model ignores a state variable (e.g., temperature) that ends up as a constraining factor in the physical system, the control will be suboptimal. Similarly, if a model inaccurately represents a system state variable (e.g., battery state-of-charge), the controller will have to constantly correct for the modeling error and again will be suboptimal. However, consideration of which state variables to include and what physical dynamics to represent must inevitably be balanced with the complexity of the model and the computational burden of the controller [3, 29, 30]. The chart in Fig. 2.2 conceptually illustrates the trade-off between model accuracy and complexity. The model categories to the left on the chart are simple enough for control design and do not require detailed knowledge of battery cell construction and chemistry. At some level of model complexity there is a tipping point where the improvements in accuracy are too costly, in terms of computation or level of information required, to be useful in control design. Further, as there are thousands of individual cells in a BESS, there is logically some point at which it is better to represent more cells at the same level of detail rather than increasing the level of detail. These points are different depending on application and technology.

The goal of this chapter is to review the forms and functions of BESS models with critical attention to their advantages, disadvantages, and characteristics. This work will help readers navigate the complex trade-offs involved in designing a BESS controller. To explicitly define the scope of this review, we start with a general optimal control problem and then add detail relevant

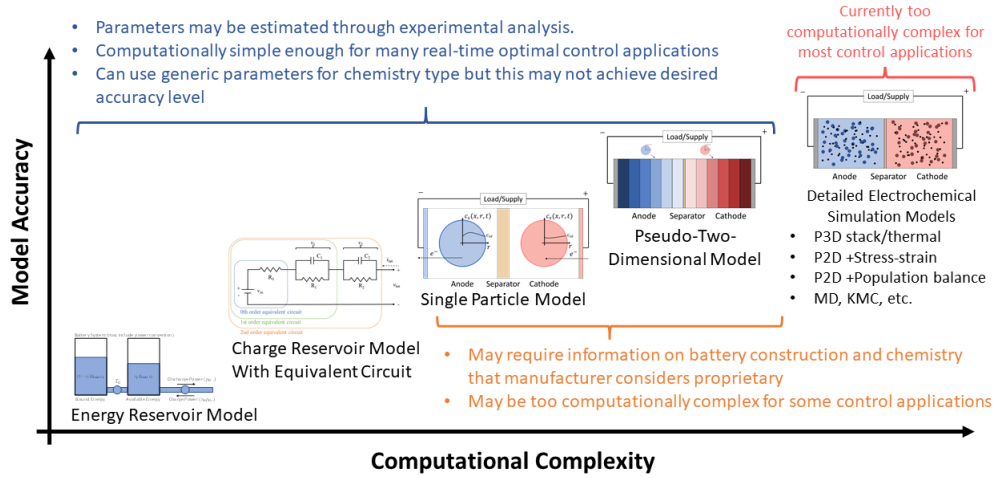


Figure 2.2: Illustration of the trade-off between model accuracy and complexity (computational complexity equates to CPU time, and model accuracy has also been referred to as “predictability” [3])

to BESS in order to classify different aspects of battery models. A general optimal control problem is formulated in:

$$\begin{aligned}
 \min_{\mathbf{x} \in \mathbb{R}^m} \quad & f(\mathbf{x}) \\
 \text{subject to:} \quad & g(\mathbf{x}) = [\mathbf{0}] \\
 & h(\mathbf{x}) \leq [\mathbf{0}]
 \end{aligned} \tag{2.1.1}$$

where \mathbf{x} is a vector of decision variables, m is the total number of decision variables (roughly equal to number of BESS model variables \times the number of time steps in the optimization time horizon), $f : \mathbb{R}^m \rightarrow \mathbb{R}$ is the objective function, $g : \mathbb{R}^m \rightarrow \mathbb{R}^r$ is a vector of equality constraints, and $h : \mathbb{R}^m \rightarrow \mathbb{R}^w$ is a vector of inequality constraints. In general, for BESS applications, the objective function to be minimized can be split into two terms: an objective associated with battery operation and degradation (f_b) and an objective associated with

the service being provided (f_s). Further, the sets of constraints can be split into constraints dealing with the service (e.g., peak load constraint) and constraints based on the equipment (e.g., maximum battery voltage). This split is formalized in the multi-objective optimization problem in:

$$\begin{aligned}
& \min_{\mathbf{x} \in \mathbb{R}^m} && f_s(\mathbf{x}) + f_b(\mathbf{x}) && (2.1.2) \\
\text{subject to:} &&& g_s(\mathbf{x}) = [\mathbf{0}] \\
&&& g_b(\mathbf{x}) = [\mathbf{0}] \\
&&& h_s(\mathbf{x}) \leq [\mathbf{0}] \\
&&& h_b(\mathbf{x}) \leq [\mathbf{0}]
\end{aligned}$$

The purpose of splitting the problem up is to isolate the components of the battery model (f_b , g_b , and h_b), as distinct from those of the service model (f_s , g_s , and h_s).

This chapter conducts a review of the battery model components of the problem in (2.1.2). Specifically, the objective functions $f_b(\mathbf{x})$ and constraints $g_b(\mathbf{x})$, and $h_b(\mathbf{x})$ associated with optimal control of BESS. The inequality constraints $h_b(\mathbf{x}) \leq 0$ ensure safe operation and battery longevity (e.g., preventing over-temperature $T \leq T_{\max}$, where T is the battery temperature, and T_{\max} is the maximum temperature). The equality constraints generally represent a battery's physical dynamics and the mathematical relationships between variables (e.g., $p_{\text{dc}} = v_{\text{bat}} i_{\text{bat}}$, where p_{dc} is the dc power, v_{bat} is the battery voltage, and i_{bat} is the battery current). The expression $f_b(\mathbf{x})$ represents the BESS's contribution to the objective function based on the control action (e.g., where the objective is to minimize costs, $f_b(\mathbf{x})$ may be $C_{\text{EoL}} \dot{\rho}$, where C_{EoL} is the end-of-life cost and $\dot{\rho}$ is the rate of change in state-of-health (SoH)). Our goal is to

present the advantages and disadvantages of various models to inform design and further research on optimal control of BESS.

This chapter is organized as follows. Section 2.2 establishes an example scenario used in each model domain section to demonstrate its application. Section 2.3 introduces the various models for state-of-charge, Section 2.4 discusses temperature models, and Section 2.5 discusses battery degradation models. Each of these sections first introduces the model’s functions, state variables and physical dynamics, and then includes a representative controller design. Section VI discusses broad trends and observations on the state-of-the-art including identified gaps, and Section VII provides a summary and conclusions.

2.2 Problem Statement

In this chapter we introduce models for different battery system dynamics. To illustrate the impact of different classes of models on control system performance, a representative controller is formulated for each modeling domain. This section establishes our example scenario in the form of a problem statement. A summary of scenario assumptions can be found in Table 2.1.

We consider a commercial electrical customer billed for both time-of-use (ToU) energy and peak-demand charges. This customer decides to purchase and install a battery to reduce their electricity bill. The customer’s energy contract charges 9 ¢/kWh during off-peak hours, 11 ¢/kWh during partial-peak hours, and 15 ¢ during peak hours according to the schedule in Fig. 2.3 (top) [10]. The utility then charges a \$50/kW service fee according to the peak net load measured during the billing period. This price is consistent with demand charges in specific localities in California and New York [31]. The load

data used for this problem, as shown in Fig. 2.3 (bottom), are adapted from the EPRI test circuit ‘Ckt5’ loadshape, normalized to a 1.0 MW peak [4]. We will assume that the load and price are known a priori. Without the battery, the total bill would be calculated according to:

$$f_s = \Delta t \mathbf{w}^\top \mathbf{l} + \max(\mathbf{l}) \nu \quad (2.2.1)$$

where $\mathbf{l} \in \mathbb{R}^n$ is the load (kW) over time, $\mathbf{w} \in \mathbb{R}^n$ is the ToU energy price (\$/kWh) over time, ν is the service fee in \$/kW for peak net load measured during the billing period, and \bullet^\top denotes a vector’s transpose. We use a time-step $\Delta t = 15$ minutes (0.25 hours), and $n = 96$ (1 day). For this problem we assume that the net-load is always greater than zero. The total baseline electrical bill for this day is \$52,080 (\$50,000 demand, \$2,080 energy). With the addition of a BESS that can supply (-), or absorb (+), power \mathbf{p} , the customer’s total bill can be modified to:

$$f_s(\mathbf{p}) = \Delta t \mathbf{w}^\top (\mathbf{l} + \mathbf{p}) + \max(\mathbf{l} + \mathbf{p}) \nu \quad (2.2.2)$$

where \mathbf{p} is the battery system power that element wise subtracts from \mathbf{l} when the battery system is discharging. The problem formulation can be expressed as: design an optimal battery dispatch control scheme that minimizes the customer’s total bill subject to the constraints of the battery and the customer’s system. The dispatch is open-loop, and we do not consider modeling uncertainty in this control scheme. Hence, we do not consider the mismatch between the controller model and a real system. Research into the effects of modeling uncertainty on BESS controller performance is presented in Chapter 6.

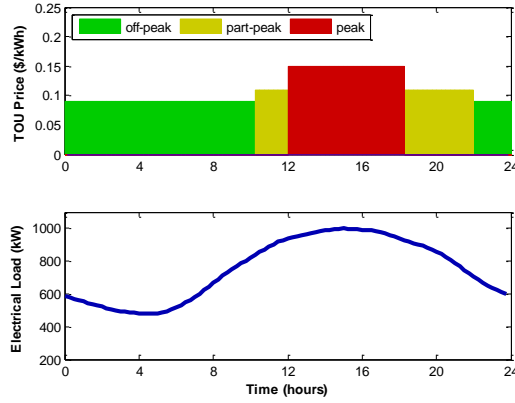


Figure 2.3: Time-of-use price schedule (top), and customer electrical load (bottom) [4]

Table 2.1: Summary of Case Study Assumptions

Ownership	Commercial Electrical Customer
Load Profile	From the EPRI test circuit ‘Ckt5’ loadshape summer, scaled to a 1.0 MW peak [4].
ToU Tariff	9 ¢/kWh off-peak, 11 ¢/kWh partial-peak hours (9:00 to 21:00), 15 ¢/kWh peak (12:00 to 18:00) [10]
Demand Tariff	$\nu = \$50/\text{kW}$ based on peak net load [31].
Billing	Daily, 15 minute time steps.

2.3 State-of-Charge Models

Electrochemically, a battery cell’s SoC is related to the concentration of the limiting active species in the relevant reaction at the associated electrode [5]. This physical association however, breaks down when the electrochemical definition of SoC is applied to strings as the thought experiment in Fig. 2.4 illustrates. The SoC of two cells in series can’t simply be averaged without abstracting its definition. When referring to BESS, it is more common to use

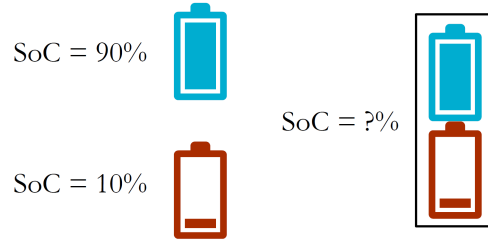


Figure 2.4: Thought experiment demonstrating how the electrochemical definition of the SoC of a battery loses physical meaning when applied to strings [5]

an empirical definition of SoC, represented in:

$$\text{State of Charge} \triangleq \frac{\text{Available Capacity}}{\text{Nominal Capacity}} \quad (2.3.1)$$

which is the ratio of available to nominal capacity. Normalizing SoC to the range $[0,1]$ or $[0\%,100\%]$ is an intuitive simplification, especially as nominal capacity can change over time, but it is not mathematically necessary to do so. In this context, capacity can be measured in energy with units of kilowatt-hours (kWh), charge with units of ampere-hours (Ah) or in concentration with units of moles-per-liter (mol/L). Constraints on SoC are shown in:

$$\varsigma_{\min} \leq \varsigma \leq \varsigma_{\max} \quad (2.3.2)$$

where ς is the SoC, ς_{\max} is the maximum SoC, and ς_{\min} is the minimum SoC. These box constraints are often enforced by a controller to ensure safety and design life, but many alternative methods for incorporating degradation into optimal control are discussed in Section 2.5. Note that a BMS can also prevent overcharge/overdischarge by constraining SoC, but these bounds are generally set at or outside the normal operational range the controller uses.

Modeling SoC helps the controller know when in the future it is likely to encounter these limits and to make control decisions accordingly. In optimal control, SoC models inform the controller how control decisions affect future SoC and enable the controller to adjust decisions to optimize an objective. Therefore, errors in SoC models can lead to poor control performance or even infeasible solutions.

The various models for SoC can be classified by the units with which they define nominal and available capacity according to (2.3.1). Models that define capacity in units of energy (kWh) can be classified as energy reservoir models (ERMs), those which define it in units of charge (Ah) can be classified as charge reservoir models (CRMs), and those which define it in units of concentration (mol/L) can be classified as concentration-based models. ERMs, discussed in Section 2.3.1, do not include dc voltage or current, so they generally have fewer variables and constraints. This simplification can lead to unrepresented physical dynamics that can, under some circumstances, have negative effects. CRMs, discussed in Section 2.3.2, include expressions to represent current-voltage (I-V) dynamics which can improve accuracy at the expense of increased model complexity. Concentration based models, discussed in Section 2.3.3, include many parameters associated with the specific electrochemical reaction and cell design that can predict battery dynamics. Each has its appropriate applications in control design as well as difficulties and drawbacks. Table 2.2 shows a summary of these trade-offs as discussed in detail in the following subsections.

Table 2.2: Summary of SoC Models I

Model Type	Parameters	Advantages	Disadvantages	References
ERM: no efficiency losses or self-discharge	$Q_{\text{cap}}, \varsigma_{\text{max}}, \varsigma_{\text{min}}, p_{\text{max}}, p_{\text{min}}, S_{\text{max}}, \text{p.f.}_{\text{min}}$	convex constraints, lowest computational burden	assumes extremely narrow operational conditions	[27, 32–37]
ERM: with linear efficiency losses, self-discharge, and kinetic-model constraints	$Q_{\text{cap}}, \eta_e, p_{\text{sd}}, \varsigma_{\text{max}}, \varsigma_{\text{min}}, p_{\text{max}}, p_{\text{min}}, m_1, b_1, m_2, b_2, S_{\text{max}}, \text{p.f.}_{\text{min}}$	convex constraints, simple to parameterize	inaccurate when operated over a range of voltage, current, or SoC	Without kinetic-model: [26, 38–49]. With kinetic-model: [6, 50]
ERM: nonlinear	$Q_{\text{cap}}(\varsigma, T), \eta_e(\varsigma, T), p_{\text{sd}}(\varsigma, T), \varsigma_{\text{max}}, \varsigma_{\text{min}}, p_{\text{max}}, p_{\text{min}}, m_1, b_1, m_2, b_2, S_{\text{max}}, \text{p.f.}_{\text{min}}$	potential for higher accuracy depending on accuracy of nonlinear functions	nonlinear models increase complexity and computational burden	[51–53]
CRM: no dynamic voltages	$p_{\text{dc}}(p)^*, C_{\text{cap}}, \eta_c, i_{\text{sd}}, v_{\text{oc}}(\varsigma)^*, R_0, \varsigma_{\text{max}}, \varsigma_{\text{min}}, p_{\text{max}}, p_{\text{min}}, i_{\text{max}}, i_{\text{min}}, v_{\text{max}}, v_{\text{min}}, S_{\text{max}}, \text{p.f.}_{\text{min}}$	high accuracy for low sample rate, long duration model forecast	nonlinear models increase complexity and computational burden	[54–60]

Table 2.3: Summary of SoC Models II

Model Type	Parameters	Advantages	Disadvantages	References
CRM: with dynamic voltages	$p_{dc}(p)^*$, C_{cap} , η_c , i_{sd} , $v_{oc}(\varsigma)^*$, R_0 , R_1 , C_1 , R_2 , C_2 , ς_{max} , ς_{min} , p_{max} , p_{min} , i_{max} , i_{min} , v_{max} , v_{min} , S_{max} , p.f. _{min}	good accuracy for high sample rate, long duration model forecasts	high complexity and computational burden	[24, 25, 61–65]
SPM	$p_{dc}(p)^*$, $\Phi_p(x_{s,p,surf})^*$, $\Phi_n(x_{s,n,surf})^*$, ς_{max} , ς_{min} , p_{max} , p_{min} , i_{max} , i_{min} , v_{max} , v_{min} , S_{max} , p.f. _{min}	good accuracy for high sample rate, long duration model forecasts, enables physical degradation models	difficult to parameterize, much more computationally complex than the CRM.	[1, 59, 66–68]
P2D	$p_{dc}(p)^*$, C_{cap} , η_c , i_{sd} , $v_{oc}(\varsigma)^*$, R_0 , R_1 , C_1 , R_2 , C_2 , ς_{max} , ς_{min} , p_{max} , p_{min} , i_{max} , i_{min} , v_{max} , v_{min} , S_{max} , p.f. _{min}	similar to SPM but more accurate at high currents.	highest complexity and computational burden, may need simplifying assumptions for use in control	[29, 66, 69, 70]

* Functions such as $p_{dc}(p)$ and $v_{oc}(\varsigma)$ each have many variations. The accuracy of these functions has a significant impact on the overall model's accuracy and should be chosen to closely approximate the state variable.

2.3.1 Energy Reservoir Models

ERMs are a class of SoC model that define capacity in units of energy (kWh). An example ERM for SoC is shown in:

$$Q_{\text{cap}} \frac{\partial \varsigma}{\partial t} = \eta_e p^+ + p^- \quad (2.3.3)$$

where ς is the SoC, p^+ and p^- are the charge and discharge ac power respectively, Q_{cap} is the energy capacity, η_e is the round trip energy efficiency, and $\partial \varsigma / \partial t$ represents the rate of change of SoC.

To conveniently represent the round trip efficiency while avoiding non-linearity and non-convexity, charge power and discharge power are formulated as independent variables in (2.3.3). While this means that simultaneous charge and discharge would not violate the explicit constraints, the objective function is often structured such that there is no advantage to candidate solutions that do so. Hence, as long as energy prices are positive, and efficiency is in the range $[0,1]$, the optimal solution to a control problem with this SoC constraint will always satisfy complementary slackness between charge and discharge power. When objective does not have these properties, an additional non-linear/non-convex constraint can be added to prevent solutions with simultaneous charge and discharge ($p^+ p^- = 0$).

Rather than a constant, as shown in (2.3.3), the energy efficiency of a BESS can be a time-varying, nonlinear function of battery SoC, voltage, current, temperature, and state-of-health (SoH). Assuming a constant energy efficiency can, by extension, be an implicit assumption these states are also constant. Some of these assumptions are valid for a range of applications. SoH, for instance, changes very slowly with respect to a control horizon. Other

Table 2.4: Conversion Between Equivalent Efficiency Representations

$$\textbf{Type 1} \quad Q_{\text{cap}}^{(1)} \frac{\partial \kappa}{\partial t} = \eta_{\text{cha}}^{(1)} p^+ + p^- + p_{\text{sd}}^{(1)}$$

$$\textbf{Type 2} \quad Q_{\text{cap}}^{(2)} \frac{\partial \kappa}{\partial t} = \eta_{\text{cha}}^{(2)} p^+ + \frac{1}{\eta_{\text{dis}}^{(2)}} p^- + p_{\text{sd}}^{(2)}$$

$$\textbf{Type 3} \quad Q_{\text{cap}}^{(3)} \frac{\partial \kappa}{\partial t} = p^+ + \frac{1}{\eta_{\text{dis}}^{(3)}} p^- + p_{\text{sd}}^{(3)}$$

	To Type 1	To Type 2	To Type 3
From Type 1	$Q_{\text{cap}}^{(1)}$ $\eta_{\text{dis}}^{(1)}$ $p_{\text{sd}}^{(1)}$	$Q_{\text{cap}}^{(2)} = \frac{Q_{\text{cap}}^{(1)}}{\sqrt{\eta_{\text{cha}}^{(1)}}}$ $\eta_{\text{cha}}^{(2)} = \sqrt{\eta_{\text{cha}}^{(1)}}$ $\eta_{\text{dis}}^{(2)} = \sqrt{\eta_{\text{cha}}^{(1)}}$ $p_{\text{sd}}^{(2)} = \frac{p_{\text{sd}}^{(1)}}{\sqrt{\eta_{\text{cha}}^{(1)}}}$	$Q_{\text{cap}}^{(3)} = \frac{Q_{\text{cap}}^{(1)}}{\eta_{\text{cha}}^{(1)}}$ $\eta_{\text{dis}}^{(3)} = \eta_{\text{cha}}^{(1)}$ $p_{\text{sd}}^{(3)} = \frac{p_{\text{sd}}^{(1)}}{\eta_{\text{cha}}^{(1)}}$
From Type 2	$Q_{\text{cap}}^{(1)} = Q_{\text{cap}}^{(2)} \eta_{\text{dis}}^{(2)}$ $\eta_{\text{cha}}^{(1)} = \eta_{\text{cha}}^{(2)} \eta_{\text{dis}}^{(2)}$ $p_{\text{sd}}^{(1)} = p_{\text{sd}}^{(2)} \eta_{\text{dis}}^{(2)}$	$Q_{\text{cap}}^{(2)} \quad \eta_{\text{cha}}^{(2)}$ $\eta_{\text{dis}}^{(2)} \quad p_{\text{sd}}^{(2)}$	$Q_{\text{cap}}^{(3)} = \frac{Q_{\text{cap}}^{(2)}}{\eta_{\text{cha}}^{(2)}}$ $\eta_{\text{dis}}^{(3)} = \eta_{\text{cha}}^{(2)} \eta_{\text{dis}}^{(2)}$ $p_{\text{sd}}^{(3)} = \frac{p_{\text{sd}}^{(2)}}{\eta_{\text{cha}}^{(2)}}$
From Type 3	$Q_{\text{cap}}^{(1)} = Q_{\text{cap}}^{(3)} \eta_{\text{dis}}^{(3)}$ $\eta_{\text{cha}}^{(1)} = \eta_{\text{dis}}^{(3)}$ $p_{\text{sd}}^{(1)} = p_{\text{sd}}^{(3)} \eta_{\text{dis}}^{(3)}$	$Q_{\text{cap}}^{(2)} = Q_{\text{cap}}^{(3)} \sqrt{\eta_{\text{dis}}^{(3)}}$ $\eta_{\text{cha}}^{(2)} = \sqrt{\eta_{\text{dis}}^{(3)}}$ $\eta_{\text{dis}}^{(2)} = \sqrt{\eta_{\text{dis}}^{(3)}}$ $p_{\text{sd}}^{(2)} = p_{\text{sd}}^{(3)} \sqrt{\eta_{\text{dis}}^{(3)}}$	$Q_{\text{cap}}^{(3)}$ $\eta_{\text{dis}}^{(3)}$ $p_{\text{sd}}^{(3)}$

This conversion table applies equally to the ERM and CRM. For the CRM, replace variables p^+ and p^- with i_{bat}^+ and i_{bat}^- and parameters Q_{cap} and p_{sd} with C_{cap} and i_{sd} respectively.

assumptions, however, are only valid for a narrow operational range. How wide the operational range can be, while the ERM remains a sufficiently accurate approximation, depends on how flat the energy efficiency curve is with respect to each variable. For example, changing battery voltage can change BESS efficiency but some battery types have a wide range of SoC where the open-circuit-voltage is nearly constant. ERMs are more accurate over a wider range of SoC for these types of batteries than for a battery whose open-circuit-voltage changes quickly with respect to SoC. ERMs use a simple representation of SoC that is based on many assumptions, so it may or may not be appropriate for a given application.

Some previous work using ERM ignore efficiency losses entirely [27, 32, 34–36]. However, due to the error it incurs, this is ill-advised for controllers that schedule SoC over any significant time horizon. Much work includes both charge and discharge efficiencies [26, 37–39, 41–46]. Self-discharge power can also be included in an ERM [26, 39, 41, 45–48] as shown in:

$$Q_{\text{cap}} \frac{\partial \zeta}{\partial t} = \eta_e p^+ + p^- + p_{\text{sd}} \quad (2.3.4)$$

where p_{sd} is the self-discharge power.

We refer to (2.3.4) as a Type 1 model, in that it only includes charge efficiency. Models that include both charge and discharge efficiencies are referred to as Type 2 models, while those that only include discharge efficiency are referred to as Type 3 models. These model types are able to produce equivalent relationships between power and the rate of change in SoC over time. Table 2.4 shows the conversion calculations needed to move from one type to another while maintaining this equivalence. We use a Type 1 model in this chapter (with $\eta_{\text{cha}} = \eta_e$ the round trip energy-efficiency) because it has

the intuitive property that the SoC multiplied by the capacity directly reflects how much energy is expected to be available from the battery on discharge.

While most ERM use ac power, a few use dc power [71] by including many of the constraints in the CRM. The manufacturer dc kWh rating for batteries is calculated based on either the Ah rating multiplied by the nominal battery voltage or the energy extracted during a constant current discharge test. Hence, this approach is still subject to the inaccuracy of other ERM, over a wide operational range, if voltage is far from the nominal voltage assumed or the constant current rate used during testing.

Though it is not commonly done, all three parameters can be functions of the SoC or temperature or both ($Q_{\text{cap}}(\varsigma, T)$, $\eta_e(\varsigma, T)$, and $p_{\text{sd}}(\varsigma, T)$) [51–53]. The most common version of this is SoC dependent losses $p_{\text{sd}}(\varsigma) = m_{\text{sd}}\varsigma + b_{\text{sd}}$ where m_{sd} is the proportional power loss and b_{sd} is the power loss at $\varsigma = 0$ [37, 40]. Adding nonlinearity to these functions has the potential to increase predictive accuracy over a wider operational range of SoC and warrants further investigation [51].

To represent the relationship between SoC and the power limits (p_{max} and p_{min}) a two reservoir ERM, also called the kinetic battery model, is sometimes used [6, 50]. The kinetic battery model splits the reservoir into available energy and bound energy as shown in Fig. 2.5 and in:

$$(1 - c_f)Q_{\text{cap}}\frac{\partial\varsigma_1}{\partial t} = \Gamma_e(\varsigma_2 - \varsigma_1) \quad (2.3.5a)$$

$$c_f Q_{\text{cap}}\frac{\partial\varsigma_2}{\partial t} = \eta_e p^+ + p^- + \Gamma_e(\varsigma_1 - \varsigma_2) \quad (2.3.5b)$$

where c_f is the fraction of total capacity in the available reservoir, and Γ_e is a time constant that governs the rate of energy transfer between the two reservoirs. The physical intuition of this model is that the higher the discharge

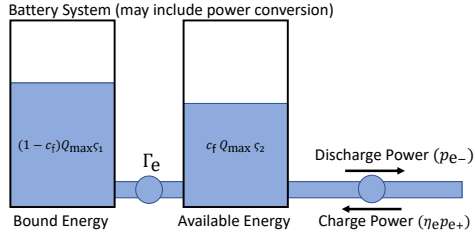


Figure 2.5: Energy Based Kinetic Battery Model [6]

rate the more quickly the available energy is depleted, and the low-level limit of the tank is reached. The kinetic battery model type ERM is equivalent to the linear inequality constraints on power in:

$$p_{\min} \leq p \leq p_{\max} \quad (2.3.6a)$$

$$m_1 \varsigma + b_1 \leq p \leq m_2 \varsigma + b_2 \quad (2.3.6b)$$

where p_{\min} is the discharge power limit, p_{\max} is the charge power limit, m_1 and b_1 are the slope and intercept of the linear power limit on discharge, respectively, and m_2 and b_2 are the slope and intercept of the linear power limit on charge, respectively. These constraints are encountered at high discharge rate more quickly according to the slope m_1 and intercept b_1 . These constraints then reduce maximum power linearly as SoC approaches its minimum, the same as if the maximum power is constrained by the difference between tank levels in the kinetic battery model. The limits defined in (2.3.6) are shown in Fig. 2.6

Injection and absorption of reactive power can be an important capability for BESS in many applications [12]. While reactive power does not directly affect SoC, it can indirectly affect SoC by constraining real power. Constraints

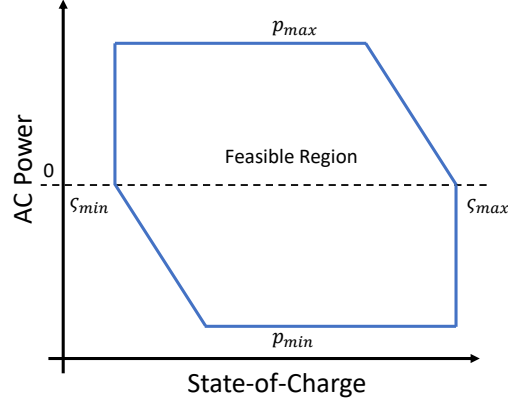


Figure 2.6: Feasible region for ac power described by the kinetic battery model on apparent power and power factor are presented in [42]:

$$p = p^+ + p^- \quad (2.3.7a)$$

$$p^2 + q^2 \leq S_{\max}^2 \quad (2.3.7b)$$

$$\left| \frac{p}{\sqrt{p^2 + q^2}} \right| \geq \text{p.f.}_{\min} \quad (2.3.7c)$$

where q is the reactive power (var), S_{\max} is the apparent power limit, and p.f._{\min} is the minimum power factor. While there are no direct incentives for reactive power, there might be penalties on poor power factors. Therefore in many cases, constraint 2.3.7 must be enforced.

2.3.1.1 ERM Application

In this section we solve the problem outlined in Section 2.2 with an optimal controller designed using an ERM. The ERM is used here to demonstrate its application, however, it is not the most appropriate model for this problem because of its inaccuracy over a wide range of voltage in this scenario.

In cases where the performance of the ERM model is less than desirable, it is sometimes employed because of the computational simplicity. The example scenario listed here serves to demonstrate how the ERM can be applied to solve a simple problem, and one can extrapolate it to how it could be used to solve a more complicated problem. Example parameters for the ERM are listed in Table 2.5.

We can express the constraint described in (2.3.4) between each SoC using the vector equation (2.3.8).

$$Q_{\text{cap}}\mathbf{D}\boldsymbol{\varsigma} = \eta_e\mathbf{p}^+ + \mathbf{p}^- + p_{\text{sd}}[\mathbf{1}] \quad (2.3.8)$$

where $\boldsymbol{\varsigma} \in \mathbb{R}^{n+1}$ is the SoC at each time step, $\mathbf{p}^+ \in \mathbb{R}_+^n$ and $\mathbf{p}^- \in \mathbb{R}_-^n$ are the ac charge and discharge power during each time step, and the matrix \mathbf{D} is defined below.

$$\mathbf{D} = \frac{1}{\Delta t} \begin{bmatrix} -1 & 1 & 0 & \cdot & \cdot & 0 \\ 0 & -1 & 1 & 0 & \cdot & \cdot \\ & & \cdot & \cdot & & \\ & & & \cdot & \cdot & \\ 0 & & & 0 & -1 & 1 \end{bmatrix}_{n \times (n+1)} \quad (2.3.9)$$

The SoC constraint in (2.3.8) can be included with the kinetic battery

Table 2.5: Energy Reservoir Model Parameters

Name	Symbol	Value
Energy Capacity	Q_{cap}	600 kWh
Energy Efficiency	η_e	65%
Self-Discharge Power	p_{sd}	-7 kW
Maximum Discharge Power	p_{max}	500 kW
Maximum Charge Power	p_{min}	-500 kW
Maximum SoC	ς_{max}	95%
Initial SoC	ς_0	60%
Minimum SoC	ς_{min}	20%
Kinetic model discharge slope	m_1	$p_{\text{min}} / 10\%$ *
Kinetic model discharge intercept	b_1	$-\varsigma_{\text{min}} \times m_1$ *
Kinetic model charge slope	m_2	$-p_{\text{max}} / 5\%$ *
Kinetic model charge intercept	b_2	$-\varsigma_{\text{max}} \times m_2$ *

Note: these model parameters are meant to represent a typical battery system and do not necessarily reflect any specific equipment.

* These slope and intercept values are written in terms of the power and SoC limits above. The value $-p_{\text{max}} / 10\%$ indicates that the charge limit will be imposed over an SoC band of 10%, while $-\varsigma_{\text{min}} \times m_1$ calculates a y-intercept that makes the power limit = 0 at $\varsigma = \varsigma_{\text{min}}$.

model constraints in (2.3.6) yielding the problem formulation in:

$$\min_{\mathbf{x}_{\text{ERM}} \in \mathbb{R}^{3n+2}} \Delta t \mathbf{w}^\top (\mathbf{1} + \mathbf{p}^+ + \mathbf{p}^-) + \nu \tau \quad (2.3.10a)$$

subject to:

$$Q_{\text{cap}} \mathbf{D} \boldsymbol{\varsigma} = \eta_e \mathbf{p}^+ + \mathbf{p}^- + p_{\text{sd}}[\mathbf{1}] \quad (2.3.10b)$$

$$\boldsymbol{\varsigma}_{[1]} = \varsigma_0 \quad (2.3.10c)$$

$$\boldsymbol{\varsigma}_{[1]} = \boldsymbol{\varsigma}_{[n]} \quad (2.3.10d)$$

$$p_{\min}[\mathbf{1}] \leq \mathbf{p}^+ + \mathbf{p}^- \leq p_{\max}[\mathbf{1}] \quad (2.3.10e)$$

$$\varsigma_{\min}[\mathbf{1}] \leq \boldsymbol{\varsigma} \leq \varsigma_{\max}[\mathbf{1}] \quad (2.3.10f)$$

$$m_1 \boldsymbol{\varsigma} + b_1[\mathbf{1}] \leq \mathbf{p}^+ + \mathbf{p}^- \leq m_2 \boldsymbol{\varsigma} + b_2[\mathbf{1}] \quad (2.3.10g)$$

$$\mathbf{1} + \mathbf{p}^+ + \mathbf{p}^- \leq \tau[\mathbf{1}] \quad (2.3.10h)$$

where $\mathbf{x}_{\text{ERM}} = \{\mathbf{p}^+, \mathbf{p}^-, \boldsymbol{\varsigma}, \tau\} \in \mathbb{R}^{3n+2}$, and $\tau \in \mathbb{R}$ is a dummy variable that represents the peak net load. The constraint (2.3.10c) ensures that control decisions are made based on the current estimated SoC. The constraint (2.3.10d) represents the intuitive assumption that the BESS will continue to operate after the end of the current control horizon and that the next period will be similar to this one. In this application, (2.3.10d) is used to make simulation results easier to interpret and compare. The objective has been modified to use the dummy variable τ to represent peak load in the objective and add a constraint that it be greater than the net load at every time (2.3.10h).

In the code accompanying this chapter the minimum heat generation regularization term, described in Section 2.5.1.1 ($\Pi \|\mathbf{p}^+ + \mathbf{p}^-\|_2^2$, with a very small weight $\Pi = 1e-5$), is applied to the objective in this and each application script. This has the effect of avoiding spikes or abrupt changes in power, while not significantly impacting the minimum value achieved.

Information on numerical algorithms for solving general linear and non-linear optimization problems can be found in [72, 73]. We solve this using the Pyomo optimization modeling language [74, 75] and the Ipopt interior point optimization problem solver [76]. The solution is shown in Fig. 2.7. Note that even though the maximum discharge power is 500 kW, the battery is only able to reduce the peak net load by approximately 85 kW because of limitations on energy. The effect of the kinetic battery model can be observed around hour 10, when the battery finishes charging then pauses for one time step only to then charge at a low level to maintain 94.8% SoC. This artifact of the model is because the maximum charge rate at 95% SoC is 0 kW which is insufficient to counter self-discharge power. The ERM expects to be able to reduce the peak to 914.7 kW and it is clear from the calculated net load the schedule allocates charging to the periods of low electricity price.

The control solution reduces the total electrical bill from \$52,080 (\$50,000 demand, \$2,080 energy) to \$47,837 (\$45,737 demand, \$2101 energy). The net effect is a \$4,243, or 8.15%, reduction in the electrical bill. Note that while the demand charge is reduced significantly, the energy bill increases due to efficiency losses in the BESS.

2.3.2 Charge Reservoir Model (CRM)

CRMs are a class of BESS models that define capacity in units of charge (Ah). An example CRM is shown in:

$$C_{\text{cap}} \frac{\partial \zeta}{\partial t} = \eta_c i_{\text{bat}}^+ + i_{\text{bat}}^- \quad (2.3.11)$$

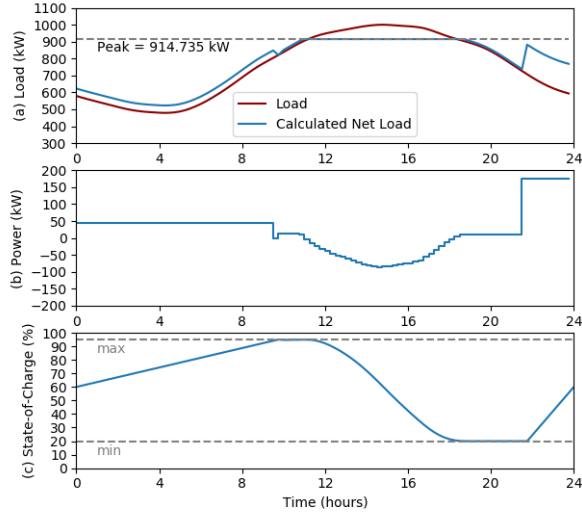


Figure 2.7: Results calculated with the ERM: (a) Net load with BESS power control, (b) Battery power, (c) battery SoC (bottom)

where i_{bat}^+ and i_{bat}^- are the charge and discharge current respectively, ς is the battery SoC, C_{cap} is the charge capacity, η_c is the coulombic efficiency, and $\partial\varsigma/\partial t$ represents the rate of change of SoC. Like with the ERM, to conveniently represent efficiency while avoiding non-linearity and non-convexity, charge current and discharge current are formulated as independent variables in (2.3.11). Simultaneous charge and discharge is avoided in the same way, by structuring the objective function such that there is no advantage to those candidate solutions.

Peukert's equation relates the charge capacity to the discharge rate in amps [77, 78]:

$$C_{\text{cap}} = (i_{\text{bat}}^-)^{k_{\text{peu}}} t_{\text{discharge}} \quad (2.3.12)$$

where k_{peu} is the Peukert exponent, and t_{peu} discharge time before the battery

reaches its low voltage limit. Peukert's equation is sometimes used in control design [79]. However, it makes several simplifying assumptions that do not make sense for optimal control applications. The parameters of Peukert's equation assume a constant-current discharge, where 0% SoC corresponds to battery reaching its minimum voltage under load. This model implies a battery equivalent circuit, which is better to represent explicitly, and a static operating condition (constant-current discharge) which is one of the decision variables in our problem formulation.

While some previous work ignore efficiency losses [54–58], this may not be accurate for controllers that predict SoC over an extended time horizon for the same reason as discussed in Section 2.3.1. Self-discharge current can be included in a CRM [55, 65, 80] as in:

$$C_{\text{cap}} \frac{\partial \zeta}{\partial t} = \eta_c i_{\text{bat}}^+ + i_{\text{bat}}^- + i_{\text{sd}} \quad (2.3.13)$$

where i_{sd} is the self-discharge current. While less common for CRM, efficiency in this model can be represented equivalently with Type 2 and Type 3 models as shown in Table 2.4.

Several additional constraints are needed to govern internal relationships between voltage, current, dc power, and ac power. The foundation of these is an equivalent circuit model [62, 63, 81, 82]. The most common battery equivalent circuit models are shown in Fig. 2.8 and described in:

$$i_{\text{bat}} = i_{\text{bat}}^+ + i_{\text{bat}}^- \quad (2.3.14a)$$

$$\frac{\partial v_1}{\partial t} = \frac{-1}{R_1 C_1} v_1 + \frac{1}{C_1} i_{\text{bat}} \quad (2.3.14b)$$

$$\frac{\partial v_2}{\partial t} = \frac{-1}{R_2 C_2} v_2 + \frac{1}{C_2} i_{\text{bat}} \quad (2.3.14c)$$

$$v_{\text{oc}} + R_0 i_{\text{bat}} + v_1 + v_2 = v_{\text{bat}} \quad (2.3.14d)$$

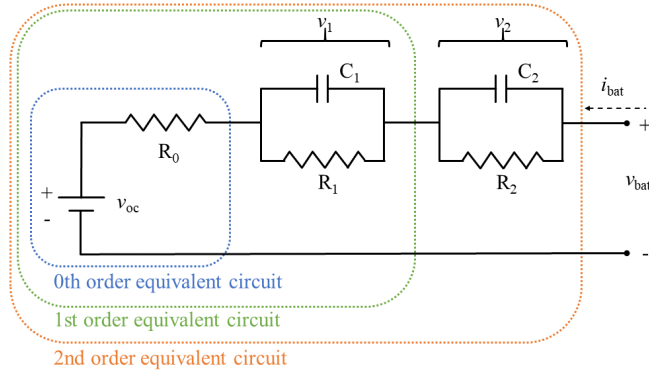


Figure 2.8: Equivalent Circuit Models

where R_0 , R_1 , C_1 , R_2 , and C_2 are equivalent circuit resistor and capacitor parameters. The 0th order equivalent circuit is accurate for steady state analysis as it accounts for battery ohmic resistance R_0 but not any time-domain dynamic response. The 1st and 2nd order models are increasingly accurate for analyses requiring short time steps (roughly faster than 10 minutes between samples or (1/600)Hz) [61]. The R-C parallel elements of the circuit can represent different chemical reaction dynamics within battery cells: R_1 & C_1 can represent ion-diffusion (Warburg impedance) whereas R_2 & C_2 can represent anode-cathode capacitance or constant phase element [81]. Note that the time constant of the diffusion element ($\tau_1 = R_1 C_1$) is generally much larger than the time constant of the capacitance element ($\tau_2 = R_2 C_2$). The equivalent circuit's impedance parameters can be calculated using least squares system identification [83]. These parameters can be functions of current, SoC, SoH, temperature, or any combination thereof [65].

There are many variations of these equivalent circuits. Adding a resistor across the voltage source is equivalent to making i_{sd} a linear function of v_{oc} . Adding a resistor across the battery terminals is equivalent to making i_{sd} a

linear function of v_{bat} . Several other configurations are discussed in [61], but it is unclear how these additions affect the accuracy of the model.

Though it is rare to do so in a controller, battery voltage hysteresis can be incorporated into the equivalent circuit model [5] as shown in:

$$\frac{\partial v_{\text{hys}}}{\partial t} = \gamma_{\text{hys}} \text{sgn}(i_{\text{bat}}) (M(\varsigma, i_{\text{bat}}) - v_{\text{hys}}) \quad (2.3.15)$$

where v_{hys} is the dynamic voltage hysteresis, γ_{hys} is a decay rate tuning constant, and $M : \mathbb{R}^2 \mapsto \mathbb{R}$ is a function that returns the maximum voltage hysteresis. Specifically, $M(\varsigma, i_{\text{bat}})$ is an empirical approximation based on experimental data that is positive for charge and negative for discharge. Alternatively, the hysteresis can be modeled using an additional charge reservoir as in [7, 8]. This approach splits the total charge capacity into two states: bound charge, and available charge as shown in Fig. 2.9 and in:

$$(1 - c_f) C_{\text{cap}} \frac{\partial \varsigma_1}{\partial t} = \Gamma_c (\varsigma_2 - \varsigma_1) \quad (2.3.16a)$$

$$c_f C_{\text{cap}} \frac{\partial \varsigma_2}{\partial t} = \eta_c i_{\text{bat}}^+ + i_{\text{bat}}^- + \Gamma_c (\varsigma_1 - \varsigma_2) \quad (2.3.16b)$$

where c_f is the fraction of total capacity in the available reservoir, and Γ_c is a time constant that governs the rate of charge transfer between the two reservoirs. The open-circuit-voltage is then based on the available charge level only. This effectively represents energy recovery effect and is structurally similar to the discrete version of the single particle model to be discussed in Section 2.3.3.

Open-circuit-voltage v_{oc} , also referred to as electromotive potential or force, is the terminal voltage of the battery when measured ‘at-rest’ and is a function of the SoC, SoH and temperature of the cell. Several example

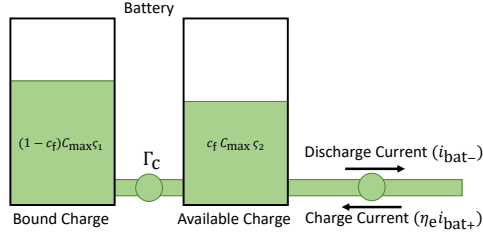


Figure 2.9: Charge Based Kinetic Battery Model [7, 8]

functions for v_{oc} are given in:

$$v_{oc} = v_m \varsigma + v_0 \quad (2.3.17a)$$

$$v_{oc} = k_T (T - T_{ref}) (m \varsigma + v_0) \quad (2.3.17b)$$

$$v_{oc} = a \varsigma^2 + b \varsigma + c \quad (2.3.17c)$$

$$v_{oc} = \alpha \varsigma^3 + \beta \varsigma^2 + \gamma \varsigma + \delta \quad (2.3.17d)$$

$$v_{oc} = b_k - m_k \frac{(1 - \varsigma)}{\varsigma} + c_k e^{d_k \varsigma} \quad (2.3.17e)$$

$$v_{oc} = \alpha(\varsigma) \varsigma^3 + \beta(\varsigma) \varsigma^2 + \gamma(\varsigma) \varsigma + \delta(\varsigma) \quad (2.3.17f)$$

where v_m and v_0 are the slope and intercept of a linear v_{oc} model, respectively, k_T is a linear temperature adjustment, T and T_{ref} are the battery temperature and reference battery temperature, respectively, a , b , and c are the coefficients for a quadratic polynomial fit, α , β , γ , and δ are the coefficients for a cubic polynomial fit, b_k , m_k , c_k , and d_k are the coefficients for a negative reciprocal and exponential function fit, and $\alpha(\varsigma)$, $\beta(\varsigma)$, $\gamma(\varsigma)$, and $\delta(\varsigma)$ are piecewise functions that collectively comprise a cubic spline. The simplest function for v_{oc} is a linear approximation (2.3.17a) which can be accurate within a narrow range of SoC [24, 49, 63, 84]. A temperature adjustment can also be applied (2.3.17b) to improve accuracy [63, 80]. Polynomial approximations are also used, (2.3.17c) or (2.3.17d), but these are sometimes non-convex and so can

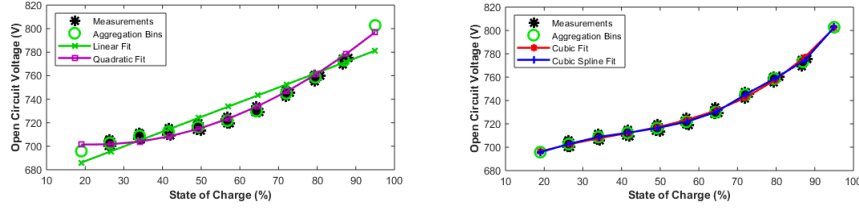


Figure 2.10: Open-Circuit-Voltage Models

be more computationally intensive to work with. Another approach is to model v_{oc} as a combination of a negative reciprocal and exponential functions (2.3.17e) [85,86]. This model works better for lithium-cobalt batteries or other chemistries with exponential curves near 100% and 0% SoC but that are relatively flat and straight in a wide range around 50% SoC. Note that (2.3.17e) has an asymptote at $\varsigma = 0$, and hence the model must constrain SoC to some positive threshold to work well. Piecewise cubic splines (2.3.17f) are the most accurate [61], but these can be very difficult functions to work with in optimization. Example open-circuit-voltage data along with different fit types are shown in Fig. 2.10. Battery voltage hysteresis can alternatively be represented within the open-circuit-voltage function by modeling v_{oc} differently on charge and discharge [85].

Battery power is modeled through Ohm's power law:

$$p_{dc} = i_{bat} v_{bat} \quad (2.3.18)$$

where p_{dc} is the dc power.

The conversion efficiency from ac to dc power, or vice versa, is sometimes ignored. When it is modeled, conversion efficiency is commonly modeled as a constant [42]. One way of modeling inverter efficiency as a constant is

shown in:

$$p_{\text{dc}} = \phi_e p^+ + \frac{1}{\phi_e} p^- \quad (2.3.19)$$

where $\phi_e \in [0, 1]$ is the conversion efficiency constant. Alternatively, a linear fit or quadratic fit can be used [87]:

$$p_{\text{dc}} = \phi_m p + \phi_b \quad (2.3.20)$$

$$p_{\text{dc}} = \phi_0 p^2 + \phi_1 p + \phi_2 \quad (2.3.21)$$

where ϕ_m and ϕ_b are the slope and intercept of a linear efficiency function, respectively, and ϕ_0 , ϕ_1 , and ϕ_2 are the coefficients of a quadratic efficiency function. Inverter efficiency can be a nonlinear function of ac voltage, dc voltage, and temperature [88].

While CRMs normally include box constraints on SoC and real/reactive power, additional box constraints on current and battery voltage are shown in:

$$i_{\min} \leq i_{\text{bat}} \leq i_{\max} \quad (2.3.22a)$$

$$v_{\min} \leq v_{\text{bat}} \leq v_{\max} \quad (2.3.22b)$$

Unlike the ERM, it is not necessary to add SoC dependent power constraints as the voltage constraints handle these limits implicitly.

An important factor to consider is that battery cells within a string may have significantly different parameters resulting from normal manufacturing variation. When using a CRM in a controller design, there are at least three methods for accounting for distributions in parameters and states within a BESS [81, 89]. What follows is a discussion of these methods and their relative advantages for optimal control.

“Big cell” method: This method is based on a simplification that models a battery pack as one large battery cell. In this approach, the battery voltage is the individual cell voltage multiplied by the number of cells in series, the capacity is the total capacity and so on. Intercell balancing is generally handled within the self-discharge current parameter. This method is most accurate when a string is made up of very well-matched cells, which are manufactured to have a very narrow distribution of performance. For poorly matched cells, or for cells that have degraded and hence have widened in their performance distribution, this approach is optimistic in its approximation of string capacity on both charge and discharge.

“Short board effect” method: This method uses models of the extreme cells in a string to better represent limiting factors. The maximum SoC cell and minimum SoC cell are tracked independently, each with their own decision variables and limits. The total string voltage is then the sum of the highest SoC cell voltage, the lowest SoC cell voltage, and the voltage of a “big cell” representing all remaining cells. This approach more accurately models when the string will encounter cell voltage or SoC limits. There is some increase in the computational complexity as there must be additional decision variable for voltage, dynamic voltage, and SoC as well as their associated constraint sets.

“One-by-one calculation” method: This method explicitly represents all cells in a battery pack. In cases where cells have a wide variance in capacity and coulombic efficiency, it is possible that the highest SoC cell and/or lowest SoC cell will switch cells within the control horizon. This method will be able to predict and optimize operation whichever cell is the limiting factor for a given cycle. Explicitly modeling every cell within a string also enables

the direct representation of cell balancing circuits within the controller, as in [89, 90]. This also enables the representation of unequal current splitting in parallel cells or strings. With hundreds or even thousands of cells in a grid scale BESS, this approach can easily become computationally infeasible to apply in practice.

As CRMs account for changes in battery dynamics over the range of voltage and current, they are more accurate than ERMs in applications where the SoC and charge/discharge currents vary significantly. However, given the increase in complexity, they are much more difficult to use in the design of optimal controllers. Hence, CRMs are best used in applications relying on long duration, if sparse, charge/discharge schedules (e.g., day-ahead hourly energy arbitrage). In such applications the high rate battery dynamics in (2.3.14) can often be ignored.

2.3.2.1 CRM Application

In this section we solve the problem outlined in Section 2.2 with an optimal controller designed around a CRM. Example parameters for a CRM are listed in Table 2.6.

The ‘CRM: no dynamic voltages’ from Table 2.2 is the most appropriate model for this problem because of the long forecast horizon, low (15 minute) time resolution, and because we are only controlling one battery system. We also use the “big battery” approach to modeling the dc battery string. Implementing the CRM into a usable format requires reformulating the differential equation for SoC defined in (2.3.11) into the vector of equality constraints as

shown in:

$$C_{\text{cap}}\mathbf{D}\boldsymbol{\varsigma} = \eta_c \mathbf{i}_{\text{bat}}^+ + \mathbf{i}_{\text{bat}}^- \quad (2.3.23)$$

where $\boldsymbol{\varsigma} \in \mathbb{R}^{n+1}$ is the vector of SoC at each time step, $\mathbf{i}_{\text{bat}}^+ \in \mathbb{R}_+^n$ and $\mathbf{i}_{\text{bat}}^- \in \mathbb{R}_-^n$ are the vectors of charge and discharge dc current respectively, and \mathbf{D} is a matrix defined above in (2.3.9). Like with the ERM, charge current and discharge current are formulated as separate decision variables. While this does not make the optimization problem convex, it does improve the convergence time of the solver (over the problem formulation with a single current decision variable per time step) without affecting the solution. The resulting problem

formulation is shown in:

$$\min_{\mathbf{x}_{\text{CRM}} \in \mathbb{R}^{6n+2}} \Delta t \mathbf{w}^\top (\mathbf{1} + \mathbf{p}) + \nu \tau \quad (2.3.24a)$$

subject to:

$$\mathbf{p}_{\text{dc}} = \phi_0 \mathbf{p}^2 + \phi_1 \mathbf{p} + \phi_2 \quad (2.3.24b)$$

$$\mathbf{p}_{\text{dc}} = (\mathbf{i}_{\text{bat}}^+ + \mathbf{i}_{\text{bat}}^-) \mathbf{v}_{\text{bat}} \quad (2.3.24c)$$

$$\mathbf{v}_{\text{bat}} = \mathbf{v}_{\text{oc}[1:n]} + R_0 (\mathbf{i}_{\text{bat}}^+ + \mathbf{i}_{\text{bat}}^-) \quad (2.3.24d)$$

$$\mathbf{v}_{\text{oc}} = \alpha \boldsymbol{\varsigma}^3 + \beta \boldsymbol{\varsigma}^2 + \gamma \boldsymbol{\varsigma} + \delta \quad (2.3.24e)$$

$$C_{\text{cap}} \mathbf{D} \boldsymbol{\varsigma} = \eta_c \mathbf{i}_{\text{bat}}^+ + \mathbf{i}_{\text{bat}}^- \quad (2.3.24f)$$

$$\boldsymbol{\varsigma}[1] = \varsigma_0 \quad (2.3.24g)$$

$$\boldsymbol{\varsigma}[1] = \boldsymbol{\varsigma}[n] \quad (2.3.24h)$$

$$p_{\min}[\mathbf{1}] \leq \mathbf{p} \leq p_{\max}[\mathbf{1}] \quad (2.3.24i)$$

$$\varsigma_{\min}[\mathbf{1}] \leq \boldsymbol{\varsigma} \leq \varsigma_{\max}[\mathbf{1}] \quad (2.3.24j)$$

$$v_{\min}[\mathbf{1}] \leq \mathbf{v}_{\text{bat}} \leq v_{\max}[\mathbf{1}] \quad (2.3.24k)$$

$$i_{\min}[\mathbf{1}] \leq \mathbf{i}_{\text{bat}}^- \leq [\mathbf{0}] \quad (2.3.24l)$$

$$[\mathbf{0}] \leq \mathbf{i}_{\text{bat}}^+ \leq i_{\max}[\mathbf{1}] \quad (2.3.24m)$$

$$\mathbf{1} + \mathbf{p} \leq \tau[\mathbf{1}] \quad (2.3.24n)$$

where $\mathbf{x}_{\text{CRM}} = \{\mathbf{p}, \mathbf{p}_{\text{dc}}, \mathbf{i}_{\text{bat}}, \mathbf{v}_{\text{bat}}, \mathbf{v}_{\text{oc}}, \boldsymbol{\varsigma}, \tau\} \in \mathbb{R}^{6n+2}$, $\mathbf{p}_{\text{dc}} \in \mathbb{R}^n$ is the dc electrical power provided to the battery, $\mathbf{v}_{\text{bat}} \in \mathbb{R}^n$ is the battery terminal voltage, $\mathbf{v}_{\text{oc}} \in \mathbb{R}^{n+1}$ is the battery open-circuit-voltage, and τ is the dummy variable for peak power. The CRM includes constraints on inverter conversion efficiency (2.3.24b), Ohm's law relating dc power, voltage and current (2.3.24c), the battery equivalent circuit model (2.3.24d), and the open-circuit-voltage curve (2.3.24e). The constraint (2.3.24g) ensures that control decisions are made based on the current estimated SoC. The constraint (2.3.24h) represents the

intuitive assumption that the BESS will continue to operate after the end of the current control horizon and that the next period will be similar to this one. In this application, (2.3.24h) is used to make simulation results easier to interpret and compare. Again, while simultaneous charge and discharge does not violate explicit constants, the structure of the objective ensures that solutions will comply with complementary slackness between charge and discharge current.

The resulting customer's net load and optimal control schedule for the BESS are shown in Fig. 2.11 (a) and (b) respectively. The simulated battery current and voltage are shown in Fig. 2.11 (c) and (e) respectively. The CRM based controller expects to be able to reduce the peak load by approximately 83 kW. The peak battery voltage reached 780 V and the dc current reached -120 A on discharge. The control solution reduces the total electrical bill from \$52,080 (\$50,000 demand, \$2,080 energy) to \$47,948 (\$45,871 demand, \$2077 energy). The net effect is a \$4,132, or 7.93%, reduction in the electrical bill.

If we assume that the example ERM and CRM represent the same physical BESS, then we can investigate which one is a better controller. We can observe that the ERM expects to be able to reduce the peak load, and the total bill, more than the CRM. If the ERM is the more accurate model, then the CRM will underutilize the batteries. However, if the CRM is more accurate, as we expect it to be, then the control solution from the ERM controller may be infeasible. This would result in suboptimal control performance and optimistic shortfall as will be discussed in Chapter 6.

2.3.3 Concentration Based Models

Concentration based models measure capacity in units of the concentration (mol/L) of the active materials of the electrodes. These models can

Table 2.6: Battery System Charge Reservoir Model Parameters

Name	Symbol	Value		
Charge Capacity	C_{cap}	800 Ah		
Coulombic Efficiency	η_c	94.6%		
Self-Discharge Current	i_{sd}	0.50 A		
Inverter Efficiency Coefficient	ϕ_0	-2.0503e-04		
Inverter Efficiency Coefficient	ϕ_1	0.99531		
Inverter Efficiency Coefficient	ϕ_2	-6.1631		
Battery Internal Resistance	R_0	71.6 m Ω		
Maximum Discharge Power	p_{min}	-500 kW		
Maximum Charge Power	p_{max}	500 kW		
Maximum SoC	\mathbf{s}_{max}	95%		
Initial SoC	\mathbf{s}_0	60%		
Minimum SoC	\mathbf{s}_{min}	20%		
Minimum Battery Voltage	v_{min}	680 V		
Maximum Battery Voltage	v_{max}	820 V		
Maximum Current Discharge	i_{min}	-1000 A		
Maximum Current Charge	i_{max}	1000 A		
Cubic Poly- nomial Fit	α	β	γ	δ
$0.2 \leq \varsigma \leq 0.95$	320.377	-368.742	201.004	669.282

Note: these model parameters are meant to represent a representative battery system and do not necessarily reflect any specific equipment.

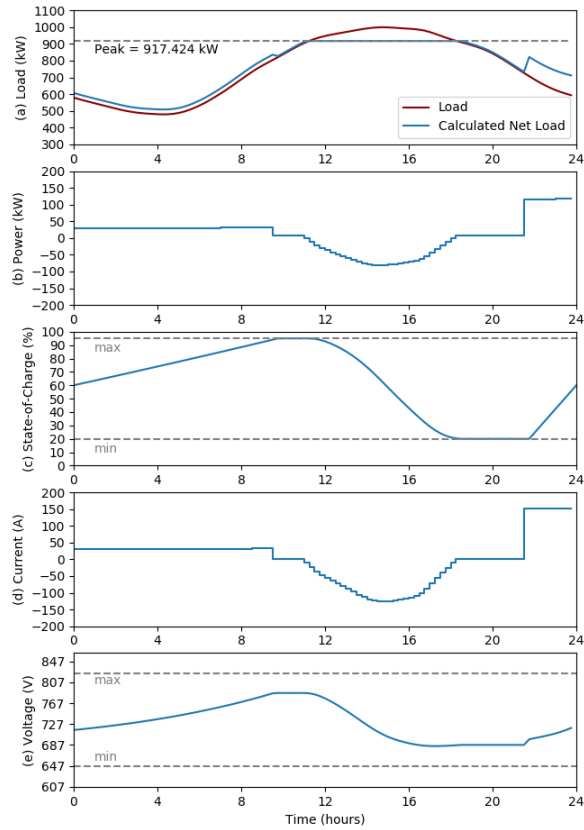


Figure 2.11: Results calculated with the CRM: (a) net load with BESS power control, (b) battery power, (c) battery SoC, (d) battery current, and (e) battery voltage

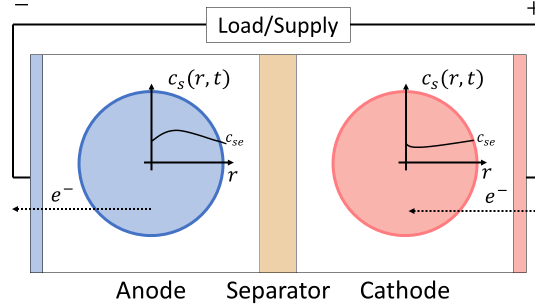


Figure 2.12: Single particle model (SPM)

be further classified into single particle model (SPM), pseudo-two-dimensional model (P2D), and many others [3]. In this section we briefly cover SPM and P2D models as these are the concentration models most widely used in controllers. Note that concentration models may require parameters based on cell construction and chemistry that manufacturers consider proprietary and would not be available to the controller. However, there are methods available to estimate some or all of these parameters empirically [67, 70].

SPMs represent each electrode as a single particle [66, 91–93] which is useful for modeling the effects of transport phenomena but loses some accuracy at high current, or wherever variations across the electrodes are significant [30, 94]. Figure 2.12 shows an simple generic SPM. The differential equation for mass balance in an intercalation particle is governed by Fick’s law in a spherical coordinate system [95, 96]:

$$\frac{\partial c_{s,j}}{\partial t} = \frac{D_{s,j}}{r_j^2} \frac{\partial}{\partial r_j} \left(r_j^2 \frac{\partial c_{s,j}}{\partial r_j} \right) \quad (2.3.25)$$

where $c_{s,j}$ is the concentration of electrode j as a function of both time t and particle radius r_j , $D_{s,j}$ is the solid phase diffusion coefficient, and the subscript $j \in \{p, n\}$ represents the positive/negative electrode. The SoC is a

function of the average normalized concentration (stoichiometry) in each electrode (2.3.26). To calculate SoC, we first define $x_{s,j,100\%}$ and $x_{s,j,0\%}$ as the stoichiometry at which electrode j is at its maximum and minimum respectively. Using these definitions, SoC is the state of the anode's stoichiometry between $x_{s,n,100\%}$ and $x_{s,n,0\%}$ (or equivalently, 1 - the state of the cathode's stoichiometry between $x_{s,p,100\%}$ and $x_{s,p,0\%}$) [5] as expressed in:

$$x_{s,j,\text{ave}} = \frac{1}{\bar{r}_j c_{s,j,\text{max}}} \int_0^{\bar{r}_j} c_{s,j} dr \quad (2.3.26)$$

$$\zeta = \frac{x_{s,n,\text{ave}} - x_{s,n,0\%}}{x_{s,n,100\%} - x_{s,n,0\%}} \quad (2.3.27)$$

$$= 1 - \frac{x_{s,p,\text{ave}} - x_{s,p,0\%}}{x_{s,p,100\%} - x_{s,p,0\%}} \quad (2.3.28)$$

where ζ is the SoC of the cell, $c_{s,j,\text{max}}$ is the maximum concentrations of electrode j , and \bar{r}_j is the radius of the representative particle.

Battery voltage in the SPM is based on the open circuit voltage, the chemical overpotential, and the electrical resistance, while the SoC is based on average concentration throughout the particle, open-circuit-voltage is based only on its surface concentration [5]. These relationships are shown in:

$$v_{oc} = \Phi_p(x_{s,p,\text{surf}}) - \Phi_n(x_{s,n,\text{surf}}) \quad (2.3.29)$$

$$x_{s,p,\text{surf}} = \frac{c_{s,p}|_{r=\bar{r}_p}}{c_{s,p,\text{max}}} \quad (2.3.30)$$

$$x_{s,n,\text{surf}} = \frac{c_{s,n}|_{r=\bar{r}_n}}{c_{s,n,\text{max}}} \quad (2.3.31)$$

where $\Phi_p : [0, 1] \mapsto \mathbb{R}$ and $\Phi_n : [0, 1] \mapsto \mathbb{R}$ are the positive and negative electrode potentials as functions of their normalized surface concentrations ($x_{s,p,\text{surf}}$ and $x_{s,n,\text{surf}}$ respectively). Like with open circuit voltage in the CRM, Φ_p and Φ_n can be approximated using polynomial or exponential functions.

Authors in [1, 5] use a Redlich-Kister expansion as a general best fit function for Φ_p and Φ_n :

$$\Phi_j = v_{bat}^0 + \frac{RT}{F} \ln \left(\frac{1 - x_{s,j,\text{surf}}}{x_{s,j,\text{surf}}} \right) + \left\{ \sum_{k=0}^N \frac{A_k}{F} \left((2x_{s,j,\text{surf}} - 1)^{k+1} - \frac{2x_{s,j,\text{surf}}^k (1 - x_{s,j,\text{surf}})}{(2x_{s,j,\text{surf}} - 1)^{1-k}} \right) \right\} \quad (2.3.32)$$

where Φ_j is the potential at electrode j , $x_{s,j,\text{surf}}$ is the normalized surface concentration at electrode j , R is the ideal gas constant (8.314 J mol/K), T is the battery temperature in Kelvin², F is Faraday's constant 96,487 coulombs/mol, k is the summation index number, and N , v_{bat}^0 and A_k are the fitting parameters. Figure 2.13 shows example anode and cathode equilibrium potential functions. When fully charged, the active material concentration is at its maximum in the anode and at its minimum in the cathode. This means there is potential for ion movement from anode to cathode and electron movement from cathode to anode (a.k.a. discharge).

Chemical overpotential can be calculated according to the Butler-Volmer equation [5, 97, 98]:

$$J_j = \frac{i_{\text{bat}}}{a_s AL} = k_j c_{s,j,\text{max}} c_e^{1-\alpha_c} (1 - x_{s,j,\text{surf}})^{1-\alpha_c} x_{s,j,\text{surf}}^{\alpha_c} \times \left\{ \exp \left(\frac{(1 - \alpha_c)F}{RT} \eta_j \right) - \exp \left(-\frac{\alpha_c F}{RT} \eta_j \right) \right\} \quad (2.3.33)$$

$$k_j = k_{j,\text{ref}} \exp \left[\frac{E_{k,j}}{R} \left(\frac{1}{T} - \frac{1}{T_{\text{ref}}} \right) \right] \quad (2.3.34)$$

where η_j is the reaction overpotential, J_j is the current density on the particle's surface, a_s is the specific interfacial surface area (volumetric fraction of the

²Note that battery temperature can be assumed to be constant, or this can be coupled with one of the thermal models discussed in Section 2.4

active material $\times 3 / \bar{r}_j$), A is the current collector area, L is the electrode thickness, k_j is the Arrhenius rate of the electrochemical reaction, $E_{k,j}$ is the activation energy of the Arrhenius relationship, c_e is the concentration of the electrolyte, and α_c is the charge-transfer coefficient. This equation can be solved for η_j in terms of i_{bat} making it possible to compute the Jacobian metrics with respect to the parameters as was demonstrated in [98].

Electrical resistance is a combination of resistances in the electrolyte, the current collectors, the tabs, and the terminals. These can all be modeled using an single constant resistor R_{cell} , but it is also common to apply a temperature correction factor, current correction factor, or both [98]. With the open-circuit-voltage, the chemical overpotential, and the electrical resistance calculated, the SPM battery voltage is shown in:

$$v_{\text{bat}} = \Phi_p - \Phi_n + \eta_p - \eta_n + R_{\text{cell}}i_{\text{bat}} \quad (2.3.35)$$

To make this model more accurate at high currents, we can extend it to an additional spatial dimension along the length from the anode current collector, through the separator, to the cathode current collector, as illustrated in Fig. 2.13. With one dimension along the cell's thickness and the pseudo dimension describing a concentration gradient within spherical particles, this is called a pseudo-two-dimensional (P2D) model [5, 99, 100]. Whereas with the SPM, c_e , $x_{s,j,\text{surf}}$, η_j , and therefore the J_j are essentially averaged over each electrode, the P2D represents these quantities as functions of the dimension from one current-collector to the other [101]. Full order P2D built with the partial differential equations are too computationally complex for most real-time control applications [69]. However, discretized or reformulated P2D models can be applied successfully in control applications [29, 69, 70].

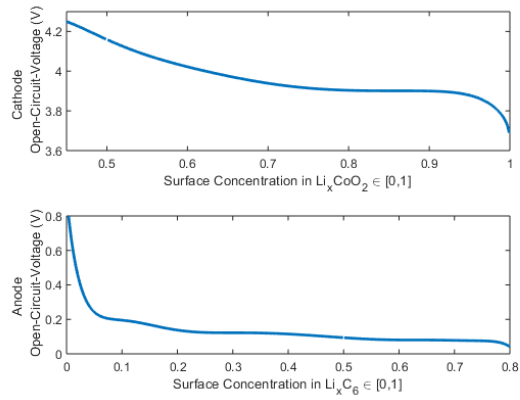


Figure 2.13: Equilibrium potentials (open-circuit-voltages) of lithium-cobalt-oxide (LiCoO_2) cathode (top) and MesoCarbon MicroBeads (MCMB) anode (bottom) [1]

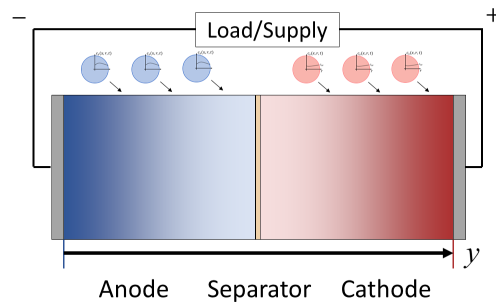


Figure 2.14: pseudo two-dimensional model (P2D)

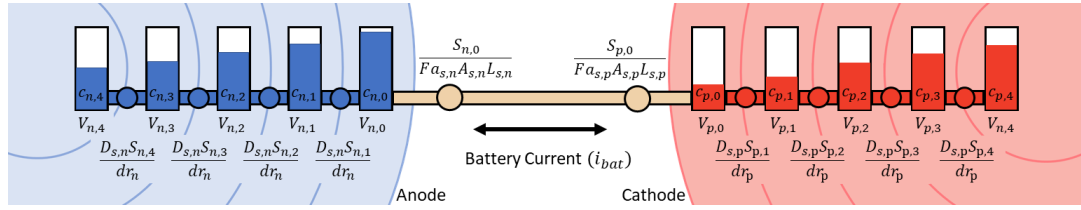


Figure 2.15: Concentration reservoir analogy of the SPM with five discrete volumes per particle

2.3.3.1 SPM Application

In this section we solve the problem outlined in Section 2.2 with an optimal controller designed around a SPM. Example parameters for the SPM are listed in Table 2.7 with Redlich-Kister expansion parameters for the anode and cathode voltages listed in Table 2.9. The SPM is used here to demonstrate its application; however, it is not the most appropriate model for this problem because of its high complexity relative to the time resolution and scale required. This model would be more appropriate for higher sample rate applications where voltage dynamics are more salient. Further, the model parameters used here are derived from literature sources on cell-level design. With calculated capacity of roughly 1.9 Ah per cell, 445 parallel cells were simulated to achieve a comparable capacity to the CRM (800 Ah). This means that the “Big Cell” modeling assumption extrapolates the performance of a single cell to $445 \times 196 = 87,220$ cells. One advantage of the SPM is that it enables investigation of how changes to cell level design parameters might affect simulated system level performance.

Within each particle we model five discrete volumes to approximate the radial dimension of the model. The core volume is spherical with radius dr_j which is surrounded by four shell volumes each with a thickness of dr_j . Fig.

2.15 illustrates how electrical current is transformed to current density which is transformed in turn to changes in the chemical concentrations within the modeled volumes. Fick's second law describes a concentration gradient in the representative particle that can be approximated using discrete volumes, each being shells around a spherical core. Each of these shells has a chemical concentration capacity proportional to its volume and the maximum concentration. The surface between each volume has a chemical resistance proportional to the surface area and inversely proportional to the diffusion coefficient. The current density at each particle's surface is proportional to the battery current (i_{bat}). The resulting optimization problem is formulated in:

$$\min_{\mathbf{x}_{\text{SPM}} \in \mathbb{R}^{18n+13}} \Delta t \mathbf{w}^\top (\mathbf{1} + \mathbf{p}) + \nu \tau \quad (2.3.36a)$$

subject to:

$$\mathbf{p}_{\text{dc}} = \phi_0 \mathbf{p}^2 + \phi_1 \mathbf{p} + \phi_2 \quad (2.3.36b)$$

$$\mathbf{p}_{\text{dc}} = \mathbf{i}_{\text{bat}} \mathbf{v}_{\text{bat}} \quad (2.3.36c)$$

$$\mathbf{v}_{\text{bat}} = \Phi_{p[1:n]} - \Phi_{n[1:n]} + \boldsymbol{\eta}_p - \boldsymbol{\eta}_n + R_0 \mathbf{i}_{\text{bat}} \quad (2.3.36d)$$

$$\Phi_j = v_{\text{bat}}^0 + \frac{RT}{F} \ln \left(\frac{c_{j,\text{max}} - \mathbf{c}_{j,0}}{\mathbf{c}_{j,0}} \right) + \sum_{k=0}^N \frac{A_k}{F} \left[\left(\frac{2\mathbf{c}_{j,0}}{c_{j,\text{max}}} - 1 \right)^{k+1} - \frac{2\mathbf{c}_{j,0} k (c_{j,\text{max}} - \mathbf{c}_{s,j,0})}{c_{j,\text{max}} (2\frac{\mathbf{c}_{j,0}}{c_{j,\text{max}}} - 1)^{1-k}} \right] \quad (2.3.36e)$$

$$\frac{\mathbf{i}_{\text{bat}}}{a_{s,j} A_{s,j} L_{s,j}} = k_{s,j} c_{j,\text{max}} c_e^{0.5} (-\mathbf{c}_{j,0[1:n]})^{0.5} \mathbf{c}_{j,0[1:n]}^{0.5} \times \left\{ \exp \left(\frac{0.5 F}{RT} \boldsymbol{\eta}_j \right) - \exp \left(-\frac{0.5 F}{RT} \boldsymbol{\eta}_j \right) \right\} \quad (2.3.36f)$$

$$V_{j,0} \mathbf{D} \mathbf{c}_{j,0} = \frac{S_{j,0} \mathbf{i}_{\text{bat}}}{F a_{s,j} A_{s,j} L_{s,j}} - \frac{D_{s,j} S_{j,1} (\mathbf{c}_{j,1[1:n]} - \mathbf{c}_{j,0[1:n]})}{dr} \quad (2.3.36g)$$

$$\begin{aligned} \frac{dr V_{j,1}}{D_{s,j}} \mathbf{D} \mathbf{c}_{j,1} &= S_{j,1}(\mathbf{c}_{j,0[1:n]} - \mathbf{c}_{j,1[1:n]}) + \\ &S_{j,2}(\mathbf{c}_{j,2[1:n]} - \mathbf{c}_{j,1[1:n]}) \end{aligned} \quad (2.3.36h)$$

$$\frac{dr V_{j,2}}{D_{s,j}} \mathbf{D} \mathbf{c}_{j,2} = S_{j,2}(\mathbf{c}_{j,1[1:n]} - \mathbf{c}_{j,2[1:n]}) + \quad (2.3.36i)$$

$$S_{j,3}(\mathbf{c}_{j,3[1:n]} - \mathbf{c}_{j,2[1:n]}) \quad (2.3.36j)$$

$$\frac{dr V_{j,3}}{D_{s,j}} \mathbf{D} \mathbf{c}_{j,3} = S_{j,3}(\mathbf{c}_{j,2[1:n]} - \mathbf{c}_{j,3[1:n]}) + \quad (2.3.36k)$$

$$S_{j,4}(\mathbf{c}_{j,4[1:n]} - \mathbf{c}_{j,3[1:n]}) \quad (2.3.36l)$$

$$\frac{dr V_{j,4}}{D_{s,j}} \mathbf{D} \mathbf{c}_{j,4} = S_{j,4}(\mathbf{c}_{j,3[1:n]} - \mathbf{c}_{j,4[1:n]}) \quad (2.3.36m)$$

$$\mathbf{c}_{j,\{0:4\},[1]} = \mathbf{c}_{j,\text{init}}[\mathbf{1}] \quad (2.3.36n)$$

$$\mathbf{c}_{j,\{0:4\},[n]} = \mathbf{c}_{j,\text{init}}[\mathbf{1}] \quad (2.3.36o)$$

$$p_{\min}[\mathbf{1}] \leq \mathbf{p} \leq p_{\max}[\mathbf{1}] \quad (2.3.36p)$$

$$v_{\min}[\mathbf{1}] \leq \mathbf{v}_{\text{bat}} \leq v_{\max}[\mathbf{1}] \quad (2.3.36q)$$

$$i_{\min}[\mathbf{1}] \leq \mathbf{i}_{\text{bat}} \leq i_{\max}[\mathbf{1}] \quad (2.3.36r)$$

$$[\mathbf{0}] \leq \mathbf{c}_{j,\{0:4\}} \leq c_{j,\max}[\mathbf{1}] \quad (2.3.36s)$$

$$\mathbf{l} + \mathbf{p} \leq \tau[\mathbf{1}] \quad (2.3.36t)$$

where $\mathbf{x}_{\text{SPM}} = \{\mathbf{p}, \mathbf{p}_{dc}, \mathbf{i}_{\text{bat}}, \mathbf{v}_{\text{bat}}, \mathbf{\Phi}_p, \mathbf{\Phi}_n, \boldsymbol{\eta}_p, \boldsymbol{\eta}_n, \mathbf{c}_{p,\{0:4\}}, \mathbf{c}_{n,\{0:4\}}, \tau\} \in \mathbb{R}^{18n+13}$, $\mathbf{\Phi}_p \in \mathbb{R}^{n+1}$ and $\mathbf{\Phi}_n \in \mathbb{R}^{n+1}$ are the open-circuit-voltages of the cathode and anode respectively, $\boldsymbol{\eta}_p \in \mathbb{R}^n$ and $\boldsymbol{\eta}_n \in \mathbb{R}^n$ are the overpotential voltages of the cathode and anode respectively, and $\mathbf{c}_{p,\{0:4\}} \in \mathbb{R}^{5 \times (n+1)}$ and $\mathbf{c}_{n,\{0:4\}} \in \mathbb{R}^{5 \times (n+1)}$ are the molar concentrations of active material in the five discretized volumes of the cathode and anode respectively.

Under this control design customer's net load and optimal control schedule for the BESS are shown in Fig. 2.16 (a) and (b) respectively. The simulated battery current and voltage are shown in Fig. 2.16 (c) and (e) re-

spectively. The SPM based controller expects to be able to reduce the peak load by approximately 86 kW. The peak battery voltage reached 800 V and the dc current reached -125 A on discharge. Note that the dc voltage is based on the anode and cathode voltage functions which are in turn based on anode and cathode concentration fractions. As these functions are different from what the CRM uses, the results are not directly comparable. As shown in Fig. 2.16 (f) and (g), the cathode concentration fraction ranges from 0.50 at peak SoC to 0.87 at minimum SoC while the anode concentration ranges from 0.76 at peak SoC to 0.2 at minimum SoC. At low current densities there is almost no difference between core and surface particle concentrations. The control solution reduces the total electrical bill from \$52,080 (\$50,000 demand, \$2,080 energy) to \$47,754 (\$45,682 demand, \$2072 energy). The net effect is a \$4,325, or 8.31%, reduction in the electrical bill.

The SPM is structurally similar to the CRM, as illustrated in the comparison of Fig. 2.9 and Fig. 2.15. However, the SPM accounts for overpotential voltages in a different way from the equivalent circuit models in the CRM. These differences are not salient at the low sample rate in the example application and hence the models appear to have very similar results.

2.4 Temperature Models

Temperature is a critical factor to consider when controlling BESS. Cell temperature can affect many of the parameters for the SoC and SoH models discussed in Sections 2.3 and 2.5. The highest cell temperature can be the limiting factor for control action in hot environments or under high power conditions. Constraining temperature prevents over-temperature and, in a few cases, under-temperature conditions which can shorten battery life or cause

Table 2.7: Battery System Single Particle Model (SPM) Parameters I

Name	Symbol	Units	Anode	Cathode
Diffusion coefficient ^a	$D_{s,j}$	m ² /s	3.9e-14	1.0e-14
Particle Radius ^a	\bar{r}_j	m	12.5e-6	8.5e-6
Electrode thickness ^a	$L_{s,j}$	m	7.35e-6	7.0e-6
Electrode area per cell ^a	$A_{s,j}$	m ²	1.1167	0.7824
Volume fraction ^b	$\varepsilon_{s,j}$	m ³ /m ³	0.49	0.59
Specific interfacial surface area ^{a,b}	$a_{s,j}$	m ² /m ³	1.176e5	2.0824e5
Reaction rate constant ^b	$k_{s,j}$	$\frac{A/m^2}{\sqrt{\text{mol}/m^3}}$	8.351e-3	6.374e-3
Charge-transfer coefficient ^{a,b}	α_c		0.5	0.5
Maximum concentration ^{a,b}	$c_{j,\text{max}}$	mol/m ³	3.1833e4	5.1410e4
Initial concentration (60 %SoC)	$c_{j,\text{init}}$	mol/m ³	1.5917e4	3.4445e4
100% SoC concentration	$c_{j,100\%}$	mol/m ³	2.5466e4	2.3135e4
95% SoC concentration	$c_{j,95\%}$	mol/m ³	2.4273e4	2.4548e4
20% SoC concentration	$c_{j,20\%}$	mol/m ³	0.6366e4	4.1128e4
0% SoC concentration	$c_{j,0\%}$	mol/m ³	0	5.1410e4
Volume 0 (surface)	$V_{j,0}$	m ³	3.9924e-15	1.2553e-15
Volume 1	$V_{j,1}$	m ³	2.42164e-15	7.6144e-16
Volume 2	$V_{j,2}$	m ³	1.2435e-15	3.9101e-16
Volume 3	$V_{j,3}$	m ³	4.5815e-16	1.4406e-16
Volume 4 (core)	$V_{j,4}$	m ³	6.5450e-17	2.0580e-17
Surface Area 0 (surface)	$S_{j,0}$	m ²	1.9635e-9	9.0792e-10
Surface Area 1	$S_{j,1}$	m ²	1.2566e-9	5.8107e-10
Surface Area 2	$S_{j,2}$	m ²	7.0686e-10	3.2685e-10
Surface Area 3	$S_{j,3}$	m ²	3.1416e-10	1.4527e-10
Surface Area 4 (core)	$S_{j,4}$	m ²	7.8540e-11	3.6317e-11

^a - Ref. [98]

^b - Ref. [95]

^c - Calculated using method described in Ref. [5]

* Note that the actual configuration would vary by system design (e.g. 5 systems, each with 30 strings, each string with 3 cells in parallel would have 450 cells in parallel)

Table 2.8: Battery System Single Particle Model (SPM) Parameters II

Name	Symbol	Units	Value
Number of cells in parallel			445
Total calculated capacity ^c	C_{cap}		802.36 Ah
Electrolyte concentration ^a	c_e	mol/m ³	1000
Ideal gas constant	R	J mol/K	8.314
Faraday constant	F	C/mol	96,487

^a - Ref. [98]

^b - Ref. [95]

^c - Calculated using method described in Ref. [5]

* Note that the actual configuration would vary by system design (e.g. 5 systems, each with 30 strings, each string with 3 cells in parallel would have 450 cells in parallel)

Table 2.9: Equilibrium Potential Redlich-Kister Expansion Parameters, reproduced from [1]

Parameter	MCMB (anode)	LiCoO ₂ (cathode)
N	10	7
v_{bat}^0	-1.7203	-29.614
A_0	-0.35799×10^6	0.64832×10^7
A_1	-0.35008×10^6	-0.65173×10^7
A_2	-0.35247×10^6	0.65664×10^7
A_3	-0.35692×10^6	-0.65787×10^7
A_4	-0.38633×10^6	0.63021×10^7
A_5	-0.35908×10^6	-0.50465×10^7
A_6	-0.28794×10^6	0.27113×10^7
A_7	-0.14979×10^6	-0.69045×10^6
A_8	-0.39912×10^6	
A_9	-0.96172×10^6	
A_{10}	-0.63262×10^6	

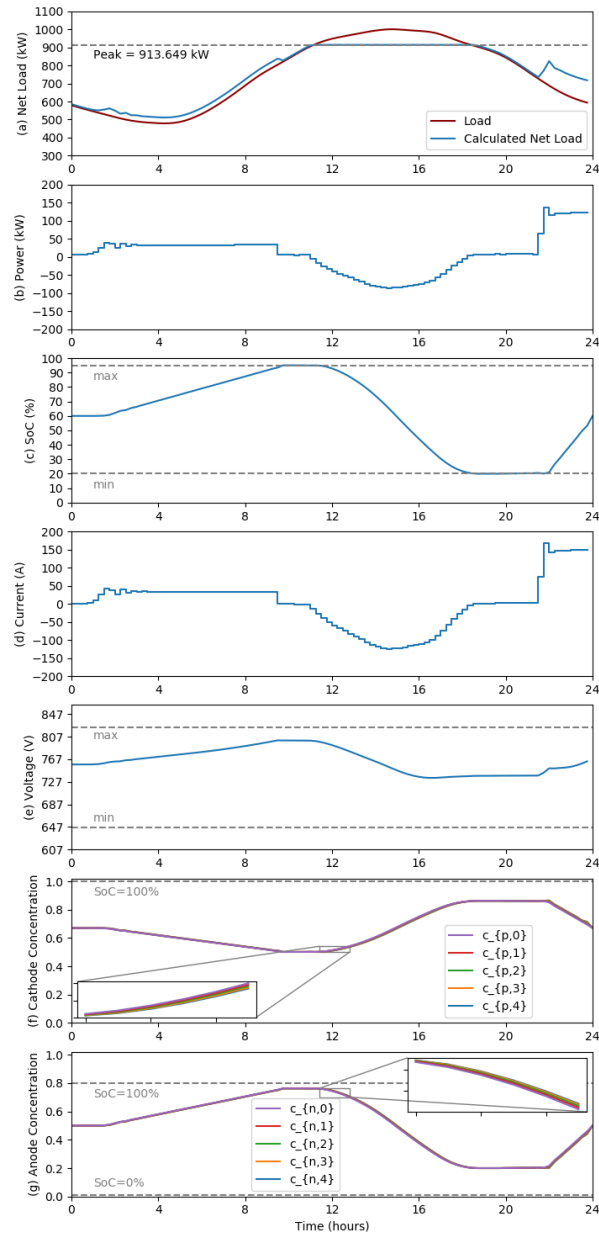


Figure 2.16: Results calculated with the SPM (a) net load with BESS power control, (b) battery power, (c) battery SoC, (d) battery current, (e) battery voltage, (f) cathode concentration fraction, (g) anode concentration fraction

hazards such as thermal run-away. The following constraint enforces limits on temperature:

$$T_{\min} \leq T \leq T_{\max} \quad (2.4.1)$$

where T is the battery temperature, T_{\min} is the minimum battery temperature, and T_{\max} is the maximum battery temperature.

Battery specification sheets will often define a lower maximum charge rate at higher temperatures [102]. This requirement would specify a conditional dynamic charge limit based on if the battery temperature exceeds a given threshold, an example of which is shown in:

$$i_{\min} \leq i_{\text{bat}} \leq i_{\max} \quad (2.4.2a)$$

$$i_{\text{bat}} \leq i'_{\max} \quad (2.4.2b)$$

$$i'_{\max} = \begin{cases} i_{\max} & \text{if } T \leq T_{\text{thr}} \\ i_{\max}/2 & \text{if } T_{\text{thr}} < T \leq T_{\max} \\ 0 & \text{if } T > T_{\max} \end{cases} \quad (2.4.2c)$$

where i'_{\max} is a dynamic charge current limit, T_{thr} is the temperature threshold. This type of constraint is non-convex and difficult to work with in optimal control design. Alternatively, these restrictions can be implemented with affine constraints on current as in:

$$m_1 T + b_1 \leq i_{\text{bat}} \leq m_2 T + b_2 \quad (2.4.3a)$$

$$m_3 T + b_3 \leq i_{\text{bat}} \leq m_4 T + b_4 \quad (2.4.3b)$$

where m_{1-4} and b_{1-4} are the slopes and intercepts of the temperature dependent current constraints. Fig. 2.17 shows how the constraints in (2.4.2) and

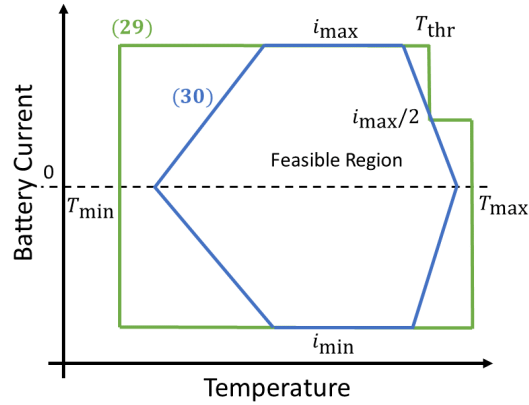


Figure 2.17: Notional examples of temperature dependent current limits

(2.4.3) enclose different feasible regions. This kind of limit can be imposed on dc power instead of current [103].

Battery temperature models are based on how much heat is generated in the cell, and how much heat is lost to the environment. As controllers must balance accuracy with model complexity, we cannot use the high order finite-element-models used in simulation based design, like in [104]. Instead controller models choose a few critical temperatures to represent. Section 2.4.1 explains the physical mechanisms underlying heat generation and transfer for batteries. Section 2.4.3 then introduces several specific modeling approaches that can incorporate temperature into optimal control decisions. Table 2.10 shows a summary of the benefits and tradeoffs of the different temperature models as they apply to optimal controller design.

Table 2.10: Summary of Temperature Models

Model Type	Parameters*	Advantages	Disadvantages	References
Cell Lumped-volume resistive-heating conduction-cooling	C_T, R_0, U	lowest computational complexity, convex	lowest predictive accuracy	[105–107]
Cell Internal / surface-volumes resistive / overpotential-heating conduction / radiation-cooling	$C_T, C'_T, R_0, U, \sigma_{em}$	low computational complexity, convex reformulation, improved accuracy at high temperature gradients	low to moderate predictive accuracy	[64, 108, 109]
Cell Multiple-internal-volumes resistive / overpotential / entropy-heating conduction / radiation / convection-cooling	$C_{T\{1:K\}}, \Delta S(\varsigma)^{**}, R_0, U(\mu_\infty)^{***}, \sigma_{em}$	high predictive accuracy, entropy term improves accuracy at low currents	moderate to high complexity and computational burden	[21, 29, 98, 108, 110, 111]
Enclosure Lumped-air-volume HVAC efficiency cooling	C_{EN}, U_{EN}, N_{cell}	low computational complexity, convex	low to moderate predictive accuracy	[108](includes heater temperature)
Enclosure Lumped-air-volume w/ heat-exchanger HVAC efficiency / Fan speed cooling		somewhat higher predictive accuracy	enables fan speed control, higher complexity, non-convex	[21]

*All inputs, outputs, state variables and parameters presented here are in addition to those presented for the CRM, with dynamic voltages model from Section 2.3

**The function $\Delta S(\varsigma)$ can vary significantly with ς and depends on the specific battery chemistry. However, it is commonly ignored ($\Delta S = 0$) or assumed to be constant ($\frac{\partial \Delta S}{\partial T} = 0$).

***The heat transmittance U is a function of the thermodynamic properties of the environment and the velocity of fluid flow over the conductive surface. Under a constant flow rate, U can be assumed to be constant.

2.4.1 Heat Generation, Consumption, and Transfer

The temperature of the battery is a function of the rate of heat generated by the battery during operation (J_{in}) and the rate of heat lost to the environment (J_{out}). Heat is generated or consumed by an electrochemical cell in three ways: change in entropy, overpotential losses, and resistive heating. Changes in entropy from the electrochemical reactions reversibly generate and consume heat within cells. This process is referred to as reversible heat generation because the heat generated during charge or discharge is consumed during the reverse reaction. Charging a battery can be endothermic (e.g., some types of lithium batteries in specific ranges of SoC), or exothermic (e.g., lead-acid batteries) [29, 77, 98, 110–112]. When losses are considered, we reintroduce the equivalent circuit models outlined in Section 2.3.2. Overpotential losses result from the kinetic and mass transport aspects of the chemical recreation which are modeled by the resistor-capacitor ladder in the 2nd order equivalent circuit. The voltage drop across these elements are v_1 and v_2 respectively. Alternatively, if the SPM or P2D model is used for a SoC model, the overpotential voltages η_p and η_n can be used in place of v_1 and v_2 . Resistive or joule heating losses result from the power dissipated to the battery's internal resistance. Combining these three sources of internal heat generation yields :

$$J_{\text{in}} = i_{\text{bat}} T \frac{\Delta S(\zeta)}{n_{\text{mol}} F} + (v_1 + v_2) i_{\text{bat}} + R_0 (i_{\text{bat}})^2 \quad (2.4.4)$$

where J_{in} is the rate of heat generation (W), i_{bat} is the battery current (A), T is battery temperature (K), ΔS is the change in entropy ($\Delta S = n_{\text{mol}} F (\partial v_{\text{oc}} / \partial T)$), n_{mol} is the number of electrons per reaction, F is the Faraday constant ($-1/96,485$ Coulombs per electron), v_1 and v_2 are the dynamic

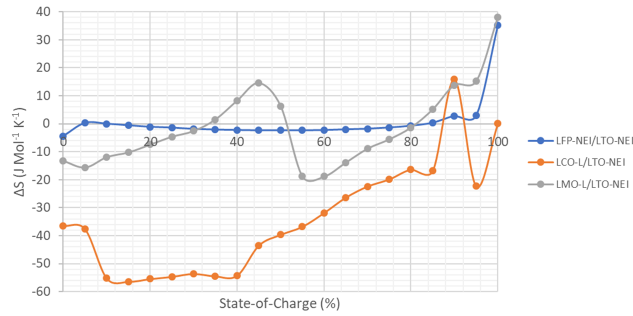


Figure 2.18: Computed full cell ΔS from individual electrode ΔS for three types of lithium-ion batteries, replotted with data from [9]

battery voltages from the equivalent circuit (V), R_0 is the battery internal resistance (Ω), and v_{oc} is the open-circuit-voltage (V). The total change in entropy in a battery can change drastically as a function of SoC which can be difficult to model for the purposes of control design. The change in entropy over the domain of SoC was calculated from precise measurements of $\partial v_{oc}/\partial T$ for a selection of lithium-ion battery types as shown in Fig. 2.18 [9]. From these data we can contrast the low entropic heat generated on discharge from lithium-iron-phosphate (LFP) batteries to the relatively high entropic heat from lithium-cobalt-oxide (LCO), especially in the range of 10% to 40% SoC. Lithium-manganese-oxide (LMO) batteries in further contrast change from generating heat (negative ΔS) to consuming heat (positive ΔS) when passing 50% SoC on discharge. Depending on the battery chemistry, and the range of operational SoC, the $\Delta S(\zeta)$ function may be neglected entirely, or approximated by a constant, a linear function, a quadratic function, or cubic function, or even a cubic spline [68, 113]. Accurate yet simple models for changes in entropy that controllers can use to predict temperature are an underdeveloped area that warrants additional research.

Most of the heat generated in a cell, especially in high power applications, comes from the resistive heating term. Because of this, some choose to ignore overpotential losses and the thermochemistry entirely [105]. Just as with the equivalent circuit, the heat generation can be calculated with different sets of parameters depending on if the battery is charging or discharging. However, the accuracy improvement may not warrant the increased computational complexity.

Heat can be transferred between the battery and the environment through conduction, radiation, and convection. Heat conduction is proportional to the temperature difference while heat radiation is proportional to the temperature of the surface raised to the 4th power according to Stefan-Boltzmann's law [114]. The combined heat loss function is shown in:

$$J_{\text{out}} = U(T_{\text{env}} - T) + \epsilon\sigma_{\text{em}}(T_{\text{env}}^4 - T^4) \quad (2.4.5)$$

where J_{out} is the rate of heat loss (W), U is the battery's thermal transmittance with its environment (W/K), T_{env} is the environmental temperature (K), ϵ is the Stefan-Boltzmann constant ($5.6 \times 10^{-8} \text{ Wm}^{-2} \text{ K}^{-4}$), σ_{em} is the emission ratio with respect to the ideal (0.95 is common for plastics in a variety of battery designs [114]).

In an unregulated environment T_{env} can be forecasted based on local weather data. In a temperature controlled environment, it can sometimes be assumed that T_{env} is a constant. The heat transfer from radiation is normally much smaller than the heat conduction meaning that it can be ignored in many systems. A simplifying assumption is that the airflow rate is constant, thereby yielding a constant U . However, in some cases variable speed fans can be integrated into the optimal control design. Under variable airflow conditions

the rate of heat transfer is described by Nusselt number (Nu) which itself is a function of Reynolds number (Re) and Prandtl number (Pr). One example of this relationship, from [2], is shown in:

$$\text{Re} = \frac{\rho u_{\infty} l_{\text{mm}}}{\mu} \quad (2.4.6a)$$

$$\text{Nu} = C_1 \text{Re}^{\theta} \text{Pr}^{\frac{1}{3}} \quad (2.4.6b)$$

$$U = \frac{\text{Nu} k_{\text{tc}}}{l_{\text{mm}}} \quad (2.4.6c)$$

where ρ is the fluid's density, u_{∞} is the unobstructed velocity of the fluid, l_{mm} is the characteristic length, μ is the dynamic viscosity, C_1 and θ are empirically derived model parameters, and k_{tc} is the thermal conductivity of the fluid.

Table 2.11 shows the thermodynamic constants associated with air and water under standard temperature and pressure. As water has a much higher density and thermal conductivity, some BESS designs include water cooling systems [115]. For a cylinder in cross-flow, the characteristic length l_{mm} equals the diameter (18.63 mm for an 18650-type cell). The parameters C_1 and θ , shown in Table 2.12, are properties of the geometry of the fluid flow over the battery surface and change with the Reynolds number. Together, these material properties yield the functional relationship between air speed thermal transmittance shown in Fig. 2.19.

The complex relationships described in (2.4.6) impact control design in several ways. First, heat transfer rate increases with increasing fluid velocity u_{∞} . However, there are diminishing returns meaning that the marginal improvement in heat transfer decreases with increased fluid velocity. Hence there is likely to be an optimal, non-zero flow rate that effectively transfers heat while not consuming too much power to move air. A fan controller can be implemented to optimize battery temperature along with charge/discharge [21].

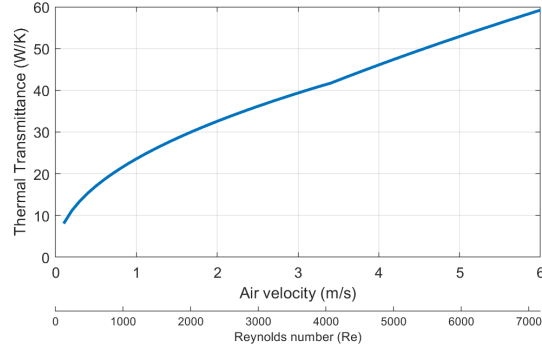


Figure 2.19: Thermal transmittance for a 18650 battery cell in cross flow as a function of air speed [2]

Table 2.11: Thermodynamic properties of common battery cooling fluids* [2]

Fluid	ρ (kg/m ³)	μ (N·s/m ²)	k_{tc} (W/m·K)	Pr
Air	1.1614	$1.846e^{-5}$	0.0263	0.707
Water	997.0	$8.55e^{-4}$	0.613	0.857

*all values reported assume atmospheric pressure and 300 Kelvin

Table 2.12: Fluid flow geometry constants for a cylinder in cross-flow [2]

Re	C_1	θ
0.4-4	0.989	0.330
4-40	0.911	0.385
40-4000	0.683	0.466
4000-40,000	0.193	0.618
40,000-400,000	0.027	0.805

2.4.2 Enclosure Thermal Model

The simplest enclosure thermal model is implicit in the assumption of constant environmental temperature. This is valid if the BESS is small and installed in a temperature-controlled space. Temperature forecasts can be used in environments where temperature is weather dependent. As there is generally thermal separation between the weather dependent environment and the environment that the batteries are operating in, we can model these temperatures separately.

For a given BESS and environment, the heat transfer rate between the enclosure and the environment U_{EN} can be empirically calculated with heating ventilation and air conditioning (HVAC) systems off, and over their range of control. We may also consider the effect of solar heating which is proportional to irradiance. The HVAC power draw can also be calculated under these conditions, and the resulting functions can be included in the BESS model. Further, an HVAC system can transfer a greater amount of heat from the enclosure to the environment, or vice versa, than it requires in electrical energy. The efficiency of a room air conditioner is measured in the energy efficiency ratio (EER), which is the ratio of Btu per hour cooling to power input (W). The EER ranges from roughly 10-20 for high efficiency units [116] which, given that 1 Btu per hour = 0.293 watts, correlates to a energy efficiency (η_{HVAC}) of 300-700%. A modified version of the heat dissipation equation for a BESS enclosure is shown in:

$$J_{\text{EN,out}} = U_{\text{EN}}(T_{\text{env}} - T_{\text{EN}}) + \epsilon\sigma_{\text{em}}(T_{\text{env}}^4 - T_{\text{EN}}^4) + \epsilon\sigma_{\text{em}}p_{\text{irr}} - \eta_{\text{HVAC}}p_{\text{HVAC}} \quad (2.4.7)$$

where U_{EN} is the thermal transmittance between the enclosure and the envi-

ronment, T_{EN} is the enclosure temperature, p_{irr} is solar irradiance, p_{HVAC} is the ac power load of the HVAC unit, and η_{HVAC} is the HVAC's energy efficiency. This approach assumes constant airflow and temperature in the HVAC's heat exchanger. By modeling the heat exchanger temperature and fan, we can improve the controller's accuracy predicting temperature management costs. The expanded enclosure thermal model is shown in:

$$J_{\text{EN,out}} = U_{\text{EN}}(T_{\text{env}} - T_{\text{EN}}) + \epsilon\sigma_{\text{em}}(T_{\text{env}}^4 - T_{\text{EN}}^4) + \epsilon\sigma_{\text{em}}p_{\text{irr}} + U_{\text{EX}}(u_{\infty})(T_{\text{EX}} - T_{\text{EN}}) \quad (2.4.8a)$$

$$C_{\text{EX}} \frac{\partial T_{\text{EX}}}{\partial t} = U_{\text{EX}}(u_{\infty})(T_{\text{EN}} - T_{\text{EX}}) - \eta_{\text{HVAC}}p_{\text{HVAC}} \quad (2.4.8b)$$

$$u_{\infty} = \eta_{\text{fan}}p_{\text{fan}} \quad (2.4.8c)$$

where $U_{\text{EX}}(u_{\infty})$ is the thermal transmittance between the HVAC heat exchanger and the air, which is a function of the airflow u_{∞} , T_{EX} is the heat exchanger temperature, C_{EX} is the heat exchanger's heat capacity, p_{fan} is the fan power, and η_{fan} is the fan's efficiency ($\text{m s}^{-1} \text{ kW}^{-1}$).

Many HVAC systems are controlled using thermostats, which activate heating or cooling modes when outside a set temperature range. The simplest thermostat implementation is shown in:

$$p_{\text{HVAC}} = \begin{cases} p_{\text{cool}} & T_{\text{EN}} > T_{\text{high}} \\ 0 & T_{\text{low}} \leq T_{\text{EN}} \leq T_{\text{high}} \\ p_{\text{heat}} & T_{\text{EN}} < T_{\text{low}} \end{cases} \quad (2.4.9a)$$

where p_{cool} is the power of the HVAC when in cooling mode, p_{heat} is the heating power of the HVAC when in heating mode, and T_{high} and T_{low} are the high and low environment temperature limits respectively. To limit the on/off cycling frequency, the mode will often stay latched for a set duration, or until the desired temperature is reached. However, this operational mode is recursive,

meaning its state dynamics have path-dependence and must be modeled sequentially through time. This property makes recursive control modes difficult to incorporate into a computationally efficient optimal controller design. If it is feasible in the design of the HVAC system, HVAC power (p_{HVAC}) and/or fan power (p_{fan}) can be decision variables available to the controller. This modeling approach enables optimal HVAC control scheduling, including pre-cooling batteries [21] or pre-heating batteries [108] to prepare for usage later in the control horizon.

2.4.3 Temperature Model Types

In this section we develop several increasingly complex, battery-cell thermal models to illustrate the different options for thermal model design. To build these models we pull together the physical mechanisms discussed in Sections 2.4.1 and 2.4.2 into systems of constraints. The simplest, and most widely used, model is to only represent a single temperature (often the hottest cell), considering only resistive heating and conduction-based cooling. An example of this type of model is shown in Fig. 2.20 and in:

$$C_T \frac{\partial T}{\partial t} = R_0 (i_{\text{bat}})^2 + U(T_{\text{env}} - T) \quad (2.4.10)$$

where C_T is the heat capacity of the lumped-volume. In this lumped-volume model the measurable surface temperature is assumed to be the temperature throughout the cell [105, 106]. Note that while we have depicted the cell geometry as cylindrical, this approach works equally well for pouch or prismatic cells. Note that when only the hottest cell is represented, imposing a low temperature constraint is unnecessary and potentially misleading. Instead, the low temperature limit is enforced either by battery selection at the design

stage (i.e. picking a battery chemistry that is suitable for its environment) or by designing a HVAC system with a thermostat that regulates environmental temperature.

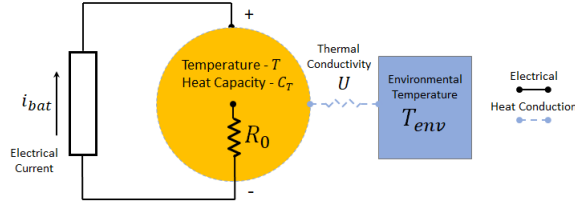


Figure 2.20: Cell thermal model w/ a lumped-volume, resistive-heating, and conduction-cooling

Where the BESS includes an enclosure with a controllable HVAC system, the model can include an additional state variable for the enclosure temperature [108] as in Fig. 2.21 and in:

$$\begin{aligned}
 C_T \frac{\partial T}{\partial t} &= R_0 (i_{\text{bat}})^2 + U (T_{\text{EN}} - T) \\
 C_{\text{EN}} \frac{\partial T_{\text{EN}}}{\partial t} &= N_{\text{cell}} (U (T - T_{\text{EN}})) + U_{\text{EN}} (T_{\text{env}} - T_{\text{EN}}) \\
 &\quad - \eta_{\text{HVAC}} P_{\text{HVAC}}
 \end{aligned} \tag{2.4.11a}$$

where C_{EN} is the heat capacity of the BESS enclosure, U_{EN} is the thermal transmittance between the enclosure and the environment, and N_{cell} is the number of cells in the enclosure. This model assumes constant or no airflow.

While temperature measurement is performed on the surface of batteries it is a better practice to constrain operation based on limiting the maximum internal temperature [64, 109]. The internal temperature can be estimated based on the surface temperature and the battery's operation. We can also

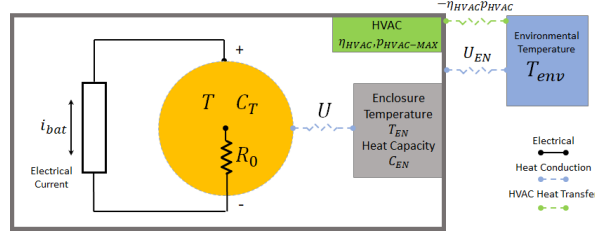


Figure 2.21: Enclosure model with lumped-air-volume and HVAC efficiency cooling

include battery over-potential heating to improve accuracy as shown in:

$$C'_T \frac{\partial T'}{\partial t} = (v_1 + v_2) i_{\text{bat}} + R_0 (i_{\text{bat}})^2 \quad (2.4.12a)$$

$$+ U'(T - T') \quad (2.4.12b)$$

$$C_T \frac{\partial T}{\partial t} = U'(T' - T) + U(T_{\text{env}} - T) \quad (2.4.12c)$$

$$+ \epsilon \sigma_{\text{em}} (T_{\text{env}}^4 - T^4)$$

where C'_T is the heat capacity of the internal mass of the cell, T' is the internal temperature, and U' is the thermal transmittance between the internal mass to the surface. As the model now distinguishes between surface and internal temperature, C_T is now the heat capacity of the surface of the cell, T is the surface temperature, and U is the thermal transmittance between the battery surface and its environment. The resulting model structure is illustrated in Fig. 2.22.

Building on this framework we can add additional internal volumes, entropy based heating, and convection cooling as a function of air velocity as

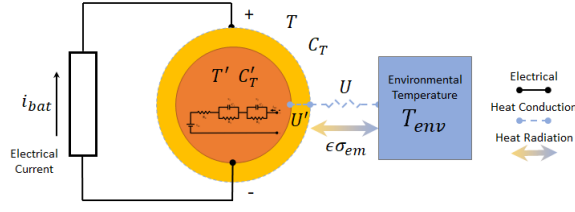


Figure 2.22: Cell thermal model w/ internal and surface-volumes, resistive and overpotential heating, and conduction/radiation cooling

shown in:

$$C_{T1}' \frac{\partial T_1'}{\partial t} = U_1'(T_2' - T_1') + V_1 \left(i_{bat} T_1' \frac{\Delta S(\zeta)}{n_{mol} F} + (v_1 + v_2) i_{bat} + R_0 (i_{bat})^2 \right) \quad (2.4.13a)$$

$$C_{T[2:K]}' \frac{\partial T_{[2:K]}'}{\partial t} = U'_{[2:K]}(T'_{[3:K+1]} - T'_{[2:K]}) + V_{[2:K]} \left(i_{bat} T'_{[2:K]} \frac{\Delta S(\zeta)}{n_{mol} F} + (v_1 + v_2) i_{bat} + R_0 (i_{bat})^2 \right) + U'_{[1:K-1]}(T'_{[1:K-1]} - T'_{[2:K]}) \quad (2.4.13b)$$

$$C_T \frac{\partial T}{\partial t} = U(u_\infty) (T_{env} - T) + U'_K (T'_K - T) + \epsilon\sigma_{em} (T_{env}^4 - T^4) \quad (2.4.13c)$$

where $T_{T[1:K]}'$ are the K internal temperatures, $C_{T[1:K]}'$ are each internal volume's heat capacity, $V'_{[1:K]}$ are the volumetric fractions of each internal volume normalized to the total internal volume, and $U'_{[1:K]}$ are the thermal transmittances between internal volumes. Note that for notation simplicity the surface temperature $T'_{K+1} = T$ in (2.4.13b). The resulting model structure is illustrated in Fig. 2.23.

To take advantage of the convection cooling term, the enclosure model can be further developed to include fan power, air velocity, and the temper-

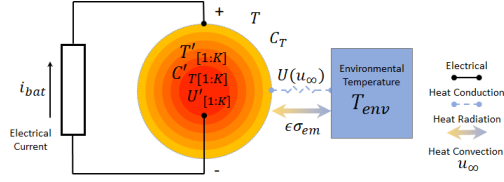


Figure 2.23: Cell model with multiple-internal-volumes, resistive/overpotential/entropy-heating, and conduction/radiation/convection-cooling

ature of the HVAC heat-exchanger. To accomplish this, we replace T_{env} with T_{EX} in (2.4.13c) and add the additional constraints shown in:

$$\begin{aligned}
 C_{EN} \frac{\partial T_{EN}}{\partial t} = & N_{cell} (U(u_\infty) (T - T_{EN}) + \epsilon\sigma_{em} (T^4 - T_{EN}^4)) \\
 & + U_{EN} (T_{env} - T_{EN}) + \epsilon\sigma_{EN} (T_{env}^4 - T_{EN}^4) \\
 & + U_{EX}(u_\infty) (T_{EX} - T_{EN}) \tag{2.4.14a}
 \end{aligned}$$

$$C_{EX} \frac{\partial T_{EX}}{\partial t} = U_{EX}(u_\infty) (T_{EN} - T_{EX}) - \eta_{HVAC} p_{HVAC} \tag{2.4.14b}$$

$$u_\infty = \eta_{fan} p_{fan} \tag{2.4.14c}$$

where T_{EX} is the heat-exchanger temperature, C_{EX} is the heat exchanger heat capacity, $U_{EX}(u_\infty)$ is the air velocity dependent thermal transmittance between the air and heat-exchanger, p_{fan} is the fan power, and η_{fan} is the fan efficiency. The resulting model structure is illustrated in Fig. 2.24.

There are many useful combinations of these models. For example, a controller may want to have a more detailed cell model and a less detailed enclosure model or vice-versa. Alternatively, these models can be customized to a specific cell design or enclosure architecture. The ‘‘Big cell’’ modeling assumption is commonly used but the ‘‘Short-board effect’’ and ‘‘One-by-one calculation’’ can be used in thermal modeling as well. A similar model extension to the enclosure would be to represent a finite number of internal volumes.

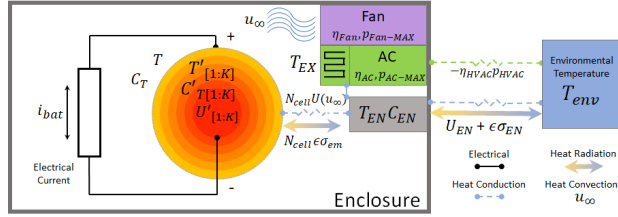


Figure 2.24: Enclosure model with, lumped-air-volume, heat-exchanger temperature, HVAC efficiency and fan speed based cooling

Each cell would reside within a volume and the heat transfer would only depend on that volume's temperature. Each of these options greatly increases model complexity with unknown, perhaps limited, benefits to controller performance.

2.4.3.1 Temperature Model Application

For this application we solve the optimal control problem in Section 2.2 using a thermal model. However, in this section we assess how the control changes if it is in a very hot environment. In some regions, the temperature can commonly reach 43.3 °C (110 °F) during the day. BESS in such an environment are generally installed in enclosures with HVAC systems. Given this environment, we determine an optimal control schedule for both the BESS power and the HVAC system power using the parameters in Table 2.13. The modified objective and constraints, in addition to those for the CRM defined

in Section 2.3.2.1, are shown in:

$$\min_{\mathbf{x}_T \in \mathbb{R}^{9n+5}} \Delta t \mathbf{w}^\top (\mathbf{l} + \mathbf{p} + \mathbf{p}_{\text{HVAC}}) + \nu \tau \quad (2.4.15a)$$

subject to:

⋮ in addition to the constraints in (2.3.24)

$$\mathbf{l} + \mathbf{p} + \mathbf{p}_{\text{HVAC}} \leq \tau \quad (2.4.15b)$$

$$C_T \mathbf{D} \mathbf{T} = R_0 (\mathbf{i}_{\text{bat}})^2 + U(\mathbf{T}_{\text{EN}[1:n]} - \mathbf{T}_{[1:n]}) \quad (2.4.15c)$$

$$C_{\text{EN}} \mathbf{D} \mathbf{T}_{\text{EN}} = K_H (\mathbf{T}_{[1:n]} - \mathbf{T}_{\text{EN}[1:n]}) + U_{\text{EN}} (\mathbf{T}_{\text{env}} - \mathbf{T}_{\text{EN}[1:n]}) \\ - \eta_{\text{HVAC}} \mathbf{p}_{\text{HVAC}} \quad (2.4.15d)$$

$$\mathbf{T}_{[1]} = T_0 \quad (2.4.15e)$$

$$\mathbf{T}_{\text{EN}[1]} = T_0 \quad (2.4.15f)$$

$$\mathbf{T} \leq T_{\text{max}}[\mathbf{1}] \quad (2.4.15g)$$

$$[\mathbf{0}] \leq \mathbf{p}_{\text{HVAC}} \leq p_{\text{HVAC-max}}[\mathbf{1}] \quad (2.4.15h)$$

where $\mathbf{x}_T = \{\mathbf{p}, \mathbf{p}_{\text{dc}}, \mathbf{i}_{\text{bat}}, \mathbf{v}_{\text{bat}}, \mathbf{v}_{\text{oc}}, \mathbf{s}, \mathbf{T}, \mathbf{p}_{\text{HVAC}}, \mathbf{T}_{\text{EN}}, \tau, \} \in \mathbb{R}^{9n+5}$, $\mathbf{T} \in \mathbb{R}^{n+1}$ is the temperature of the hottest cell at each time step, $\mathbf{T}_{\text{EN}} \in \mathbb{R}^{n+1}$ is the enclosure temperature, and $\mathbf{i}_{\text{bat}} \in \mathbb{R}^n$ is the dc current. The environmental temperature is assumed to be sinusoidal, with a period of 24 hours, a peak of 45°C at 3:00 pm, and a magnitude of 2.5°C. The formal expression for the temperature is shown in:

$$\mathbf{T}_{\text{env}} = 2.5 \cos \left(\frac{2\pi \Delta t}{24} k - 15 \right) + 42.5 \quad \forall k \in \{1, 2, \dots, n\} \quad (2.4.16)$$

where $\mathbf{T}_{\text{env}} \in \mathbb{R}^n$ is the environmental temperature at each time step.

The net load achieved over the control horizon from the combined SoC-Thermal model is shown in Fig. 2.25 (a). The optimal control schedule calculated is shown in Fig. 2.25 (b). The HVAC power schedule is shown in Fig.

Table 2.13: Example Battery System Temperature Model Parameters

Name	Symbol	Value
Battery Thermal Transmittance	U	0.2 W/°C
Battery Heat Capacity	C_T	1.495 J/°C
Maximum Temperature	T_{\max}	45 °C
Initial Battery Temperature	T_0	40 °C
Minimum Temperature	T_{\min}	-20 °C
Nominal Temperature	T_{nom}	20 °C
Enclosure Thermal Transmittance	U_{EN}	1 W/°C
Enclosure Heat Capacity	C_{EN}	30 kJ/°C
Initial Enclosure Temperature	$T_{\text{EN}0}$	40 °C
Max HVAC power	$p_{\text{HVAC-max}}$	100 kW
HVAC Efficiency	η_{HVAC}	700%

Note: these model parameters are meant to represent a typical battery system and do not necessarily reflect any specific equipment.

2.25 (d) and the environmental, battery, and enclosure temperature trajectories are shown in Fig. 2.25 (e). The controller can anticipate a period of high temperature and pre-cool the enclosure, and hence the battery, to achieve the desired schedule. Note also that the pre-cooling takes place during the off-peak electricity pricing period. The magnitude and duration of the HVAC cooling is precisely tuned such that the battery’s temperature reaches its limit (45 °C) exactly at the end of the schedule. Note also that the power profile no-longer preferentially charges during off-peak times. This is a result of the quadratic increase in temperature from high rate charging that generates too much heat for the system to transfer to the environment cost-effectively.

The control solution reduces the total electrical bill from \$52,080 (\$50,000 demand, \$2,080 energy) to \$48,001 (\$45,871 demand, \$2,130 energy). Within the energy bill, the energy required to cool the battery accounts for \$51. The

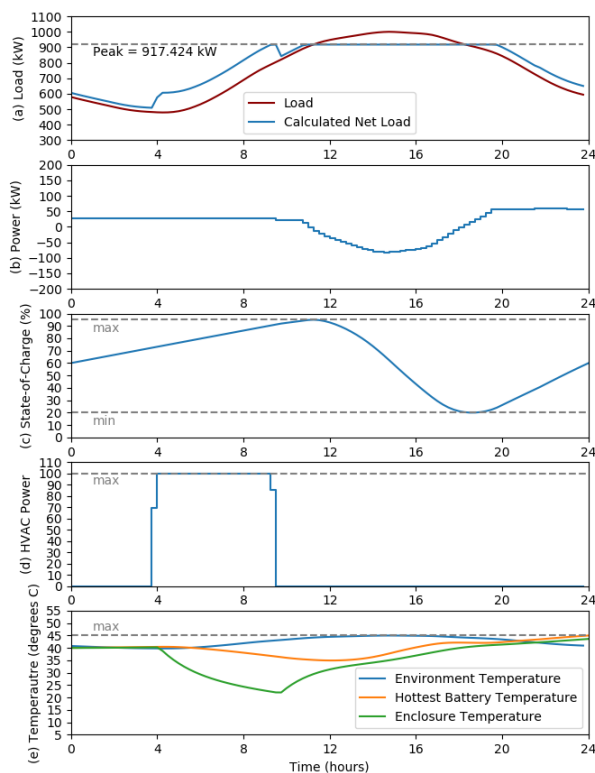


Figure 2.25: Results from control incorporating temperature model: (a) net load with BESS power control, (b) battery power, (c) battery SoC, (d) enclosure ac power, and (e) battery, enclosure, and environmental temperatures

net effect is a \$4,079 (7.83%) reduction from the baseline electrical bill, or a \$53 (0.11%) increase in the electrical bill calculated using only the CRM. The more important comparison is that if we model battery temperature in this environment under the control solution developed using only the CRM, the hottest battery reaches a peak temperature of 55.6 °C. By incorporating a thermal model into the controller, we can plan control actions to maintain defined temperature limits.

2.5 Degradation Models

As batteries age with time and use, their energy storage and supply capabilities degrade until they no-longer meet the requirements of their designed services. When degradation is included in optimal control, it tends to rely on empirical degradation models that abstract many of the physical processes in favor of model simplicity. However, there are several studies that use the SPM or a simplified P2D to incorporate physical degradation models into a controller design [59, 91, 117–120].

This section first establishes definitions for state-of-health (SoH) and how they fit into optimal control. We then introduce and assess empirical stress factor based models for accurate degradation modeling. Linearizing and simplifying the detailed empirical degradation model allows us to calculate several norm-based regularization factors that efficiently incorporate degradation into optimal control objectives. Last, we cover physical degradation models based on intercalation stresses and two different side-reactions in lithium-ion batteries.

We use the terminology beginning-of-life (BoL) to denote the conditions when the battery is new, end-of-life (EoL) to denote the conditions when the battery can no-longer reliably supply energy services, and state-of-life (SoL) to denote the conditions, between BoL and EoL, that the battery is in at a given state. The EoL conditions are often specified by the battery or BESS manufacturer as a part of a warranty. Because of this lack of standardization, SoH can be defined in many ways (e.g., based on changes in capacity [121], resistance, round trip efficiency, etc.). We use a more general definition of SoH

(ϱ), represented in:

$$\varrho = 1 - \left| \frac{y_{\text{BoL}} - y_{\text{SoL}}}{y_{\text{BoL}} - y_{\text{EoL}}} \right| \quad (2.5.1)$$

where ϱ is the SoH of the battery and y is a critical parameter for the battery to reliably supply services. In (2.5.1), SoH is defined as the ratio of a specific parameter's (or combination of parameters) movement from its initial state at BoL to its final state at EoL. In this context, SoH can represent movement in energy capacity (kWh), available energy (kWh), charge capacity (Ah), available active material (e.g. through “loss-of-lithium” in mols), coulombic efficiency (%), or internal resistance (Ω). Available energy is a combination of available charge/discharge power, and energy capacity that is defined very precisely in the electric vertical context [121] but analogs can be imagined for energy storage applications as well. Using this definition, no matter what parameter is used, and whatever the BoL and EoL conditions are specified, ϱ at BoL always equals 1, and ϱ at EoL always equals 0. As we are focused on controller design, this definition does not account for “rejuvenation” cycles wherein lead-acid and some types of flow batteries can recover some loss of SoH.

For the purposes of control design, we can assume that the change in model parameters from degradation over any forward-looking control horizon is extremely small. That is, absolute changes in parameters from degradation happen over the course of months or even years, while controllers operate over hours or days. For this reason, from the perspective of control design, it is unimportant which parameter is used to calculate SoH. The rate of degradation, in contrast, can change quickly and is a critical factor in determining optimal control. Hence, rather than modeling SoH, we model the rate of degradation directly as a calculated variable.

There are at least two ways to incorporate the rate of degradation into optimal control design. The first way is to add incremental battery replacement/refurbishment cost in the objective [44]. The second method is to constrain operation to a maximum degradation rate to ensure a warranty period [42]. The following is a detailed introduction to these two methods.

When batteries reach EoL, they can be replaced with new batteries that restore the system's functionality to BoL conditions. In certain cases, the old batteries can be resold/re-purposed in a new application. The net costs predicted to be incurred at EoL, denoted by C_{EoL} , provide a quantitative estimate of how much the controller should weight battery degradation. The cost incurred through battery degradation is calculated in:

$$f_b = C_{\text{EoL}} \frac{\partial \varrho}{\partial t} = C_{\text{EoL}} \dot{\varrho} \quad (2.5.2)$$

where f_b is the cost of the battery degradation over a full control horizon, C_{EoL} is the net cost at EoL, ϱ is the present SoH, and $\dot{\varrho}$ is the average degradation rate over the control horizon.

As the cost incurred in (2.5.2) is the present value of a predicted future cost, it is possible to apply a discount rate based on an assumed interest rate. The number of compounding periods would then be estimated linearly from the current SoH, the average rate of degradation, and an assumed compound period, as shown in:

$$f_b = (1 + \mathbf{i})^{-\mathbf{n}} C_{\text{EoL}} \dot{\varrho} \quad (2.5.3a)$$

$$\mathbf{n} = \left(\frac{1}{t_{\text{comp}}} \right) \frac{\varrho}{\dot{\varrho}} \quad (2.5.3b)$$

where \mathbf{i} is the interest rate, \mathbf{n} is the number of compounding periods between SoL and EoL, and t_{comp} is the duration of each compounding period. This is

meant to illustrate only one of many methods available for discounting future cost. It is sensible that control design using this method reflects whatever financial structure and assumptions are used for projected EoL costs.

Alternatively, a controller can be designed to maximize value while enforcing a designed or warranted service life. This method does not include an additional cost term in the objective and instead includes an additional constraint on the average rate of degradation, as shown in:

$$\dot{q} \geq -\frac{\varrho}{L_{\text{war}} - L} \quad (2.5.4)$$

where L_{war} is the total warranty life (e.g., 15 years), and L is the current life (years that the BESS has been in service). Critically, the degradation rate should be allowed to temporarily exceed the rate at which the BESS would reach EoL before the warranted service life as this allows for periods of rest to counterbalance period of high utilization. If this method is used, it is important to account for how the controller should transition operation past EoL as (2.5.4) is infeasible if $L \geq L_{\text{war}}$. Note that (2.5.4) can be imposed as a soft constraint, with a slack variable subtracted from the limit and maximized in the objective. This approach can handle infeasibility at the expense of additional decision variables, which can be helpful when more complex degradation models are used.

A useful reformulation of this is for a manufacturer to supply a “warranty life curve” as shown in Fig. 2.26. This curve has a maximum warranty life and a function that describes how the warranty period would be shortened based on BESS operation increasing a supplied degradation metric (e.g., cycles as in [122]). This curve may or may not be accompanied by an equation to calculate the degradation metric as it is often described by just a few points

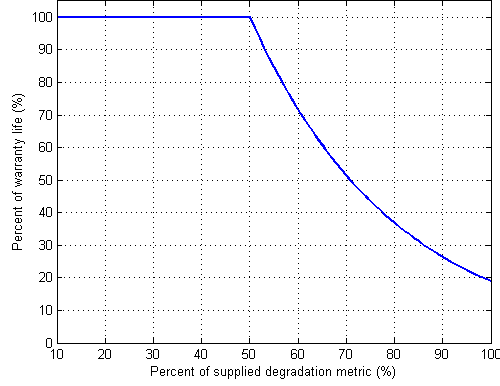


Figure 2.26: Notional example of a manufacturer supplied degradation curve (curve value = \mathfrak{D})

to prevent reverse engineering. The warranty life can be interpreted in the context of control as the reciprocal of the rate of degradation, as in:

$$\dot{q} = -\frac{1}{\mathfrak{D}L_{\text{war}}} \geq -\frac{\varrho}{L_{\text{war}} - L} \quad (2.5.5)$$

where $\mathfrak{D} : \mathbb{R} \mapsto \mathbb{R}$ is the warranty life curve supplied by the battery or BESS manufacturer. This formulation allows a generic warranty life curve to be implemented as a constraint into a BESS controller.

This section outlines various models for calculating the average rate of degradation for use in optimization. We adapt a stress factor model used for life prediction of lithium-ion cells for use in control design. We then illustrate how, through a series of operational assumptions, this stress factor model can be reduced to simple norm-based regularization. Last, we introduce several physical degradation models. Table 2.14 shows a summary of the types of degradation models discussed in the following sections.

Table 2.14: Summary of Degradation Models I

Model Type	Parameters	Advantages	Disadvantages	References
ℓ_1 Power regularization ¹	$C_{\text{EoL}}, L_{\text{cyc}}$	simple convex reformulation, can be applied to ERM	assumptions: static cycle DoD, average SoC, cell temperature, and time horizon	[42,44,123]
ℓ_2 Power regularization ¹	C_{EoL}, K_T	simple convex epigraph reformulation, can be applied to ERM	assumptions: static cycle DoD, average SoC, cell temperature, number of cycles, and time horizon	
ℓ_1 Current regularization ²	$C_{\text{EoL}}, L_{\text{cyc}}$	simple convex reformulation	assumptions: static cycle DoD, average SoC, cell temperature, and time horizon	[59,64,84]
ℓ_2 Current regularization ²	C_{EoL}, K_T	simple convex epigraph reformulation	assumptions: static cycle DoD, average SoC, cell temperature, number of cycles, and time horizon	[124–126]
ℓ_1 SoC regularization ¹	C_{EoL}, K_S	simple convex reformulation	assumptions: static cycle DoD, cell temperature, number of cycles, and time horizon	
ℓ_∞ DoD regularization ¹	$C_{\text{EoL}}, K_{\text{DoD}}$	simple convex reformulation	assumptions: static cell temperature, and time horizon, can only be applied accurately to one cycle at a time.	[127]

¹ Requires at least ERM SoC model from Section 2.3.1² Requires at least CRM SoC model from Section 2.3.2³ Requires CRM SoC model and a temperature model from Sections 2.3 and 2.4⁴ Requires at least SPM SoC model from Section 2.3.3⁵ Requires SPM SoC model and a temperature model from Sections 2.3.3 and 2.4

Table 2.15: Summary of Degradation Models II

Model Type	Parameters	Advantages	Disadvantages	References
Rainflow cycle-counting stress factor model ³	$k_t, k_c, S_{ref}, k_T, T_{ref}, k_{\delta 1}, k_{\delta 2}, k_{\delta 3}$	accurate predictor of SoH, no assumptions about static operating conditions, convex if stress factors are convex	must either discretize SoC, temperature, and current or use a sub-gradient solver before application in optimal control, high computational burden, assumes operational windows for DoD, SoC, and temperature	[21, 65, 127–133]
SEI layer formation model ⁵	$n_{SEI}, k_{SEI}, D_{SEI}, M_{SEI}, \rho_{SEI}, A_{s,n}$	physical salience, accounts for accelerated degradation from increased temperature	difficult to isolate from other physical degradation mechanisms, only applies to lithium based battery chemistries	[59, 117, 134–136]
Lithium-plaiting model ⁴	$\Phi_{sr}, R_{film}, k_{sr}, \alpha_{sr}, C_{l.p.}, L_{l.p.,EoL}$	physical salience, can be avoided entirely by constraining $\eta_{sr} \geq 0$	difficult to isolate from other physical degradation mechanisms, not accurate model for degradation in performance if used on its own, only applies to lithium based battery chemistries	[91, 118]
Intercalation stress model ⁴	$\Omega_n, E_n, v_{poi}, L_{stress,EoL}$	physical salience, applies to many battery chemistries	difficult to isolate from other physical degradation mechanisms, added complexity is proportional to number of particle volumes modeled in the SPM or P2D	[119, 120, 137, 138]

¹ Requires at least ERM SoC model from Section 2.3.1

² Requires at least CRM SoC model from Section 2.3.2

³ Requires CRM SoC model and a temperature model from Sections 2.3 and 2.4

⁴ Requires at least SPM SoC model from Section 2.3.3

⁵ Requires SPM SoC model and a temperature model from Sections 2.3.3 and 2.4

2.5.1 Empirical Degradation Models

Empirical battery degradation models can be classified as either calendar aging or cycle aging, with total degradation being the superposition of the two [139]. Calendar aging models are functions of time, average SoC, and average temperature and impact SoH whether or not the battery is charged or discharged. Cycle aging models are based on cycle SoC, current, cycle depth-of-discharge (DoD), and cycle temperature. Models based on current (or C-rate), such as the models presented in [140] and [141], generally work best for constant current cycling performed in laboratory experiments and have unknown accuracy in application that require variable charge or discharge rates.

It is common to represent degradation based on an exponential decay function of calendar and cycle degradation [128], as shown in:

$$\varrho = e^{-f_d} \quad (2.5.6)$$

where f_d is the aggregate degradation stress factor based on a combination of calendar life stress factors, and cycle life stress factors. We can model the value of the aggregate degradation stress factor as an additional variable in our system representation.

A rainflow cycle counting algorithm originally developed for material degradation [142] is widely used for accurate cycle-life modeling [65, 129, 130]:

$$f_d = S_t S_\zeta S_T + \sum_{i=1}^N w_i S_\delta S_\zeta S_T \quad (2.5.7)$$

where N is the number of cycles in the control horizon, i is a cycle index variable, w_i is a binary variable indicating a full cycle or a partial cycle, and

each stress factor is shown in:

$$S_t = k_t t \quad (2.5.8)$$

$$S_\varsigma = e^{k_\varsigma(\varsigma - \varsigma_{\text{ref}})} \quad (2.5.9)$$

$$S_T = e^{k_T(T - T_{\text{ref}}) \frac{T_{\text{ref}}}{T}} \quad (2.5.10)$$

$$S_\delta = a \delta^4 + b \delta^3 + c \delta^2 + d \delta + e \quad (2.5.11)$$

where t is time, S_t is the time stress factor, ς is SoC, S_ς is the SoC stress factor, T is temperature, S_T is the temperature stress factor, δ is DoD, and S_δ is the DoD stress factor. The parameters T_{ref} , ς_{ref} , k_t , k_ς , k_T , a , b , c , d , and e enable their associated stress factors to be tuned to specific batteries. Degradation models that do not use rainflow cycle counting often make duty-cycle profile assumptions such as in [143, 144].

Here we could extend the short board and cell-by-cell modeling approaches introduced in Section 2.3.2 to the distribution of degradation rates within a battery string or pack. However, from a control perspective, representing the maximum and minimum SoH in a string is less critical than for either SoC or Temperature because particularly low SoH cells can be replaced during regular maintenance, and hence would not limit operation. For this reason, the “big cell” representation of string level degradation is generally the most appropriate for optimal control applications.

As the controller objective is to minimize the change in SoH, we can take the derivative of (2.5.6) to obtain:

$$\dot{q} = - \frac{\partial f_d}{\partial t} e^{-f_d} = -k_t S_\varsigma S_T e^{-f_d} \quad (2.5.12)$$

yielding the form of SoH used in a controller model. Modeling SoH in this way presents a fundamental challenge. The rainflow counting algorithm in (2.5.7)

is recursive in that, under most conditions, we cannot determine the number or time of each cycle within an schedule. When performing a rainflow counting algorithm on a known schedule, the schedule is broken into many smaller pieces that add up to the total degradation. However, this schedule splitting cannot be done a priori and hence is very difficult for optimization algorithms to work with. We discuss three imperfect workarounds and one apparent solution to this problem. First, there are some cases where the time windows for each cycle are predetermined (e.g., daily cycling). This makes the rainflow counting algorithm trivially simple and easy to implement in optimization. However, under some circumstances, the optimal solution, assuming only one cycle, yields two or more cycles. Similarly, the optimal solution assuming two cycles can often yield an optimal schedule that includes just one cycle, or cycles with different boundaries than expected. The second approach is to discretize the control schedule as demonstrated in [122, 131]. By breaking the available range of SoC and current into a number of discrete states it allows the controller to map each state transition onto a piecewise linearized degradation curve. This approach has the benefit of accuracy of the degradation function at the cost of precision of the control solution and computation time. The third workaround is to linearize the degradation rate around assumed static operational conditions, including cycles. Doing this, it can be found that the rate of degradation can be written in the form of a regularization term. This third approach is discussed in the following section. Lastly, an apparent solution is presented by Shi et al, who first prove the convexity of the rainflow counting algorithm and then demonstrate a subgradient algorithm for efficient optimal control [132]. This method works by recognizing that every charge (and discharge) action belongs to either one charge half cycle or two charge half cycles if it is at the time boundary between two cycles. The cost of a

charge action at the boundary can be mapped from the cycle depth of either of its member half cycles. Hence the subgradient algorithm can avoid the calculation of the number of cycles entirely, instead adding the cost associated with the member half cycle to the subgradient of the charge action.

2.5.1.1 Degradation as Regularization

In machine learning, regularization is commonly used to prevent a model from overfitting data. Here we use similar methods to prevent our controller from over-using batteries. In this section we derive several different kinds of regularization terms based on the stress factors described above. While most of the degradation stress factors are nonlinear functions, their first-order Taylor series approximations can be reformulated as the norms of specific decision variables.

The simplest approach to calculating the rate of degradation ($\dot{\rho}$) is to linearize it to an assumed cycle depth-of-discharge, temperature, and average SoC. Under these assumptions, the degradation rate can be written:

$$\dot{\rho} = \frac{|p_e|}{(1 + \frac{1}{\eta_e})L_{cyc}Q_{cap}} \quad (2.5.13)$$

$$\dot{\rho} = \frac{|i_{bat}|}{(1 + \frac{1}{\eta_c})L_{cyc}C_{cap}} \quad (2.5.14)$$

where p is BESS ac real power, i_{bat} is the battery current, η_c is the coulombic efficiency, L_{cyc} is the rated cycle-life to EoL, Q_{cap} is the energy capacity, and C_{cap} is the charge capacity. Under these narrow conditions, degradation is proportional to the absolute value of the battery power as shown in (2.5.13) when using the ERM [42, 44, 123, 145] or to the absolute value of the battery current as shown in (2.5.14) when using the CRM [59, 84]. A modification

to this approach is to establish a power or current threshold above which the linear cost increases as in [47]. Another modification is to multiply the absolute value of power or current by a stress factor based on temperature and charge/discharge rate as in [64, 123]. Note that, when adding (2.5.13) or (2.5.14) up over a discrete control horizon, this form of degradation is equivalent to applying a ℓ_1 norm power regularization, or ℓ_1 norm current regularization, as shown in:

$$f_b(\mathbf{p}) = \Pi_{\text{cyc}} \|\mathbf{p}\|_1 \quad (2.5.15a)$$

$$\Pi_{\text{cyc}} = \frac{\Delta t C_{\text{EoL}}}{(1 + \frac{1}{\eta_e}) L_{\text{cyc}} Q_{\text{cap}}} \quad (2.5.15b)$$

$$f_b(\mathbf{i}_{\text{bat}}) = \Pi_{\text{cyc}} \|\mathbf{i}_{\text{bat}}\|_1 \quad (2.5.16a)$$

$$\Pi_{\text{cyc}} = \frac{\Delta t C_{\text{EoL}}}{(1 + \frac{1}{\eta_c}) L_{\text{cyc}} C_{\text{cap}}} \quad (2.5.16b)$$

The regularization weight Π_{cyc} has units of $\$/kW$ or $\$/A$ depending on which equation it is in because of the units of the relevant decision variable.

At an assumed static temperature, the derivative of degradation rate with respect to temperature is constant (K_T) as shown in (2.5.17). Ignoring the reversible heat generation, overpotential heating, and assuming that battery temperature and environmental temperature are very close, the derivative of temperature in (2.4.10) reduces to simply the resistive heating term, as in:

$$K_T = \frac{\partial^2 \varrho}{\partial T \partial t} = \frac{\partial}{\partial T} \left(-\dot{f}_d e^{-f_d} \right) \Bigg|_{\substack{T=T_0 \\ t=t_0 \\ \delta=\delta_0 \\ \varsigma=\varsigma_0}} \quad (2.5.17)$$

$$\frac{\partial T}{\partial t} = \frac{R_0}{C_T} i_{\text{bat}}^2 \quad (2.5.18)$$

where K_T is the partial derivative of degradation rate with respect to temperature, T is the battery temperature, t is time, R_0 is the battery ohmic resistance, and C_T is the battery's total heat capacity. From (2.5.17) and (2.5.18), we obtain the second derivative of degradation:

$$\ddot{\varrho} = \frac{K_T R_0}{C_T} i_{\text{bat}}^2 \quad (2.5.19)$$

Assuming piecewise constant values for current, integrating (2.5.19) yields an approximation of the average degradation rate:

$$\dot{\varrho} \approx \frac{\Delta t K_T R_0}{C_T} \|\mathbf{i}_{\text{bat}}\|_2^2 \quad (2.5.20)$$

Again note that, when added up over the control horizon, this form of degradation is equivalent to applying a ℓ_2 norm-squared current regularization to the objective function as shown in:

$$f_b(\mathbf{i}_{\text{bat}}) = \Pi_T \|\mathbf{i}_{\text{bat}}\|_2^2 \quad (2.5.21a)$$

$$\Pi_T = \frac{\Delta t^2 C_{\text{EoL}} K_T R_0}{C_T} \quad (2.5.21b)$$

where the regularization weight Π_T in this equation has units of $\$/A^2$. This form of degradation cost has been used in [124–126] to minimize heat generation in hybrid vehicle energy management optimization.

Further, assuming a constant battery voltage ($v_{\text{bat}} = v_0$), (2.5.21) can be reformulated using ac power instead of dc current. Assuming the ac/dc conversion model in (2.3.20), with $\phi_b = 0$, the minimum heat generation regularization is shown in:

$$f_b(\mathbf{p}) = \Pi_T \|\mathbf{p}\|_2^2 \quad (2.5.22a)$$

$$\Pi_T = \frac{\Delta t^2 C_{\text{EoL}} K_T R_0 \phi_m^2}{C_T v_0} \quad (2.5.22b)$$

where the regularization weight Π_T in this equation has units of $\$/kW^2$.

At an assumed static average SoC (ς_{avg}), the the derivative of the degradation rate with respect to average SoC is constant, as shown in:

$$\varsigma_{\text{avg}} = \frac{\|\boldsymbol{\varsigma}\|_1}{n} \quad (2.5.23)$$

$$K_{\varsigma} = \frac{d^2 \varrho}{d\varsigma_{\text{avg}} dt} = \frac{\partial}{\partial \varsigma_{\text{avg}}} \left(-\dot{f}_d e^{-f_d} \right) \Bigg|_{\substack{T=T_0 \\ t=t_0 \\ \delta=\delta_0 \\ \varsigma=\varsigma_0}} \quad (2.5.24)$$

where K_{ς} is the partial derivative of degradation rate with respect to SoC, ς_{avg} is the average SoC, and n is the number of steps in the discrete control horizon. Multiplying both sides by $\partial \varsigma_{\text{avg}}$ and, assuming piecewise constant values for SoC, integrating yields an approximation for the average degradation rate:

$$\dot{\varrho} \approx \frac{K_{\varsigma}}{n} \|\boldsymbol{\varsigma}\|_1 \quad (2.5.25)$$

This form of degradation is equivalent to applying a ℓ_1 norm SoC regularization to the objective function as shown in:

$$f_b(\boldsymbol{\varsigma}) = \Pi_{\varsigma} \|\boldsymbol{\varsigma}\|_1 \quad (2.5.26a)$$

$$\Pi_{\varsigma} = \frac{\Delta t C_{\text{EoL}} K_{\varsigma}}{n} \quad (2.5.26b)$$

where the regularization weight Π_{ς} in this equation has units of $\$/(\%\text{SoC})$.

At an assumed static cycle DoD, the derivative of degradation rate with respect to DoD is constant, as shown in:

$$\delta = \max(\boldsymbol{\varsigma}) - \min(\boldsymbol{\varsigma}) = \|\boldsymbol{\varsigma}\|_{\infty} + \|\mathbf{1} - \boldsymbol{\varsigma}\|_{\infty} - 1 \quad (2.5.27)$$

$$K_{\text{DoD}} = \frac{\partial^2 \varrho}{\partial \delta \partial t} = \frac{\partial}{\partial \delta} \left(-\dot{f}_d e^{-f_d} \right) \Bigg|_{\substack{T=T_0 \\ t=t_0 \\ \delta=\delta_0 \\ \varsigma=\varsigma_0}} \quad (2.5.28)$$

where K_{DoD} is the partial derivative of degradation rate with respect to DoD, and δ is the DoD. Multiplying both sides by $\partial\delta$ and, assuming piecewise constant values for SoC, integrating yields an approximation for the average degradation rate:

$$\dot{\rho} \approx K_{\text{DoD}}\delta = K_{\text{DoD}} (\|\boldsymbol{\varsigma}\|_{\infty} + \|\mathbf{1} - \boldsymbol{\varsigma}\|_{\infty} - 1) \quad (2.5.29)$$

This form of degradation is equivalent to applying an ℓ_{∞} norm ς and $1 - \varsigma$ regularization to the objective function as shown in:

$$f_{\text{b}}(\boldsymbol{\varsigma}) = \Pi_{\text{DoD}} (\|\boldsymbol{\varsigma}\|_{\infty} + \|\mathbf{1} - \boldsymbol{\varsigma}\|_{\infty}) \quad (2.5.30\text{a})$$

$$\Pi_{\text{DoD}} = C_{\text{EoL}} K_{\text{DoD}} \quad (2.5.30\text{b})$$

Note that the -1 can be omitted from ς_{DoD} in this formulation because, as a constant, it would not affect the minimizers of the optimization. This degradation cost has been applied to BESS in a daily energy market arbitrage application [127]. The regularization weight Π_{DoD} in this equation has units of $\$/(\%\text{DoD})$.

Now that the partial derivatives have each been derived, we can combine them to yield a function for total degradation. As the current based cycle-counting and heat-generation degradation functions require fewer assumptions than their ac power based counterparts, we use (2.5.16) and (2.5.21) instead of (2.5.15) and (2.5.22) though either option produces a viable estimate of total degradation. The formulation for linearized total degradation cost is shown in:

$$\begin{aligned} f_{\text{b}}(\mathbf{i}_{\text{bat}}, \boldsymbol{\varsigma}) = & \Pi_{\text{cyc}} \|\mathbf{i}_{\text{bat}}\|_1 + \Pi_{\text{T}} \|\mathbf{i}_{\text{bat}}\|_2^2 + \Pi_{\varsigma} \|\boldsymbol{\varsigma}\|_1 \\ & + \Pi_{\text{DoD}} (\|\boldsymbol{\varsigma}\|_{\infty} + \|\mathbf{1} - \boldsymbol{\varsigma}\|_{\infty}) \end{aligned} \quad (2.5.31)$$

2.5.2 Physical Degradation Models

Physical degradation models have already been reviewed in [95, 146, 147]. These models are built on top of the concentration-based SoC model type discussed in Section 2.3.3. As with empirical models, physical degradation models can emphasize calendar aging [148] or cycle aging [149]. However, a better classification is to distinguish models that focus on chemical side-reactions [136, 148–152] or material fatigue [119, 138]. Rather than duplicating a review of all the models available, the rest of this section analyzes the narrower intersection between physical degradation modeling and optimal control.

In lithium-ion batteries, which are the primary focus of research on degradation mechanisms, the formation of the solid electrolyte interphase (SEI) layer both increases resistance and reduces the available lithium resulting in both power and capacity fade [117]. The current density of the side-reaction that leads to the growth of the SEI layer [59, 134, 135] is shown in:

$$J_{\text{SEI}} = \frac{\exp\left(-\frac{F}{RT}\eta_n\right)}{\frac{1}{n_{\text{SEI}} F k_{\text{SEI}} \exp\left(\frac{n_{\text{SEI}} F}{RT}(\Phi_n - 0.4)\right)} - \frac{\delta_{\text{SEI}}}{n_{\text{SEI}} F D_{\text{SEI}}}} \quad (2.5.32)$$

where J_{SEI} is the SEI side-reaction current density, F is Faraday's constant, R is the ideal gas constant, T is the battery temperature, η_n is the negative electrode overpotential, n_{SEI} is the number of electrons in the SEI side-reaction, k_{SEI} is the chemical rate constant of the SEI side-reaction, Φ_n is the open circuit voltage of the negative electrode, δ_{SEI} is the thickness of the SEI layer, and D_{SEI} is the diffusion coefficient of lithium in the SEI layer.

If power is the critical parameter for operation, then we use the growth in the thickness of the SEI layer to calculate the rate of change in SoH as

shown in:

$$\frac{\partial \delta_{\text{SEI}}}{\partial t} = \frac{J_{\text{SEI}} M_{\text{SEI}}}{n_{\text{SEI}} F \rho_{\text{SEI}}} \quad (2.5.33a)$$

$$\varrho_{\text{SEI}} = 1 - \frac{\delta_{\text{SEI}}}{\delta_{\text{SEI,EoL}}} \quad (2.5.33b)$$

where M_{SEI} is the molar volume of SEI reaction products, and ρ_{SEI} is the density of the SEI layer. It should be noted that there are many other ways of modeling the growth of the SEI layer [136].

If capacity is the critical parameter for operation, then we use the loss-of-lithium to calculate the rate of change in SoH as shown in:

$$\frac{\partial L_{\text{SEI}}}{\partial t} = J_{\text{SEI}} A_{s,n} \quad (2.5.34a)$$

$$\varrho_{\text{SEI}} = 1 - \frac{L_{\text{SEI}}}{L_{\text{SEI,EoL}}} \quad (2.5.34b)$$

where L_{SEI} is the lost lithium content, and $A_{s,n}$ area of the negative electrode.

Another side-reaction to consider is lithium-plating, which can occur under adverse charging conditions or as a result of accidental overcharge [91, 118]. In this case, the rate of change in SoH can be calculated as the magnitude of the side-reaction over-potential if it is negative as shown in:

$$\eta_{\text{sr}} = \phi_{1,n} - \phi_{2,n} - \Phi_{\text{sr}} - F J_{\text{sr}} R_{\text{film}} \quad (2.5.35)$$

$$J_{\text{sr}} = k_{\text{sr}} (x_{s,n,\text{surf}})^{\alpha_{\text{sr}}} \quad (2.5.36)$$

$$\times \left\{ \exp \left(\frac{(1 - \alpha_{\text{sr}}) F}{R T} \eta_{\text{sr}} \right) - \exp \left(- \frac{\alpha_{\text{sr}} F}{R T} \eta_{\text{sr}} \right) \right\} \quad (2.5.37)$$

$$\frac{\partial L_{\text{l.p.}}}{\partial t} = C_{\text{l.p.}} |\min(\eta_{\text{sr}}, 0)| \quad (2.5.38)$$

where η_{sr} is the side-reaction overpotential, $\phi_{1,n}$ is the solid-phase potential, $\phi_{2,n}$ is the solution-phase potential, η_n is the anode overpotential, calculated

using the Butler-Volmer equation (2.3.33), Φ_{sr} is the side reaction reference voltage, which can be conservatively estimated to be zero in this case [91, 118], J_{sr} is the side-reaction current density, R_{film} is the lithium metal film resistance, k_{sr} is the side-reaction rate constant $x_{s,n,\text{surf}}$ is the surface concentration of lithium divided by the maximum concentration, α_{sr} is the side-reaction transfer coefficient, $C_{l.p.}$ is the ratio between negative magnitude of η_{sr} and the quantity of lithium-plaiting, $L_{l.p.}$ is a quantitative measure of the accumulated lithium plaiting, and $L_{l.p.,\text{EoL}}$ is the lithium-plaiting limit at EoL. Authors in [91] simplify this by assuming that R_{film} is zero, meaning that $\eta_{\text{sr}} = \eta_n - \Phi_n$. Alternatively, a controller can be configured to prevent this side-reaction entirely by constraining η_{sr} to be non-negative as shown in:

$$\eta_{\text{sr}} \geq 0 \tag{2.5.39}$$

A controller can be designed to minimize intercalation-induced fatigue [119, 120]. Intercalation-induced fatigue occurs in many battery chemistries, including lithium-ion, and so this mechanism is more general than the side-reactions discussed above. The radial and tangential intercalation stresses in

a spherical partial can be calculated as shown in:

$$\frac{3\sigma_r(r)}{\left(\frac{\Omega_n E_n c_{n,max}}{(1-\nu_{poi})}\right)} = \frac{2}{3} \left(\int_0^1 x_{s,n}(r) r^2 dr - \frac{1}{r^3} \int_0^r x_{s,n}(r) r^2 dr \right) \quad (2.5.40a)$$

$$\frac{3\sigma_t(r)}{\left(\frac{\Omega_n E_n c_{n,max}}{(1-\nu_{poi})}\right)} = 2 \left(\int_0^1 x_{s,n}(r) r^2 dr + \frac{1}{r^3} \int_0^r x_{s,n}(r) r^2 dr - x_{s,n}(r) \right) \quad (2.5.40b)$$

$$\frac{\partial L_{stress}}{\partial t} = \max_{r \in [0, \bar{r}_n]} \{\sigma_r(r), \sigma_t(r)\} \quad (2.5.40c)$$

$$\varrho_{stress} = 1 - \frac{L_{stress}}{L_{stress, EoL}} \quad (2.5.40d)$$

where σ_r is the radial intercalation stress, σ_t is the tangential intercalation stress, $c_{n,max}$ is the maximum concentration of lithium in the negative electrode, Ω_n is the partial molar volume, E_n is Young's modulus, ν_{poi} is Poisson's ratio, $x_{s,n}$ is the normalized concentration in the negative electrode, r is the radial distance, L_{stress} is the accumulated stress, and $L_{stress, EoL}$ is the accumulated stress limit at EoL.

It can be difficult to know how these physical degradation mechanisms combine. Each have been shown to be accurate on their own, meaning that simply adding them would overestimate the rate of degradation. One method is to calculate a weighted combination of degradation factors as shown in:

$$\dot{\varrho} = \frac{\alpha_\varrho \dot{\varrho}_{stress} + \beta_\varrho \dot{\varrho}_{stress} + \gamma_\varrho \dot{\varrho}_{stress}}{\alpha_\varrho + \beta_\varrho + \gamma_\varrho} \quad (2.5.41)$$

where α_ϱ , β_ϱ , and γ_ϱ are unitless weights selected to linearly combine physical degradation mechanisms. However, degradation clearly does not follow simple superposition (e.g. intercalation stress and loss of lithium may have

compounding effects) so this simplistic combination may be inaccurate. We are not aware of any experimental methods for isolating the effects of different physical degradation mechanisms and so selecting weights to combine them may be misleading.

2.5.3 Degradation Model Application

For this application we solve the optimal control problem in Section 2.2 while incorporating the stress-factor degradation model with parameters listed in Table 2.16.

The rainflow, static-cycle model is the most appropriate for this problem given that there is one-cycle that takes the whole day, and a low time resolution so low computational burden. The modified objective and constraints, in addition to those for the CRM and temperature models defined in Sections 2.3.2.1 and 2.4.3.1, are shown in:

$$\min_{\mathbf{x}_H \in \mathbb{R}^{9n+12}} \Delta t \mathbf{w}^\top (\mathbf{1} + \mathbf{p} + \mathbf{p}_{\text{HVAC}}) + \nu \tau + C_{\text{EoL}} \dot{\varrho} \quad (2.5.42a)$$

subject to:

⋮ in addition to the constraints in (2.3.24) and (2.4.15)

$$\dot{\varrho} = -k_t S_\varsigma S_T e^{-\mathbf{f}_d} \quad (2.5.42b)$$

$$\mathbf{f}_d = S_t S_\varsigma S_T + S_\delta S_\varsigma S_T \quad (2.5.42c)$$

$$S_t = k_t n \Delta t \quad (2.5.42d)$$

$$S_\varsigma = e^{k_\varsigma (\frac{\|\mathbf{s}\|_1}{n} - \varsigma_{\text{ref}})} \quad (2.5.42e)$$

$$S_T = e^{k_T (\|\mathbf{T}\|_1 - T_{\text{ref}}) \frac{T_{\text{ref}}}{\|\mathbf{T}\|_1}} \quad (2.5.42f)$$

$$\delta = \max(\boldsymbol{\varsigma}) - \min(\boldsymbol{\varsigma}) \quad (2.5.42g)$$

$$S_\delta = a \delta^4 + b \delta^3 + c \delta^2 + d \delta + e \quad (2.5.42h)$$

where $\mathbf{x}_H = \{\mathbf{p}, \mathbf{p}_{dc}, \mathbf{i}_{bat}, \mathbf{v}_{bat}, \mathbf{v}_{oc}, \mathbf{s}, \tau, \mathbf{p}_{HVAC}, \mathbf{T}, \mathbf{T}_{EN}, \dot{q}, f_d, S_t, S_\zeta, S_T, \delta, S_\delta, \} \in \mathbb{R}^{9n+12}$, $\dot{q} \in \mathbb{R}$ is the rate of degradation, $f_d \in \mathbb{R}$ is the degradation forcing function, $S_t \in \mathbb{R}$ is the time stress-factor, $S_\zeta \in \mathbb{R}$ is the SoC stress-factor, $S_T \in \mathbb{R}$ is the temperature stress-factor, $\delta \in \mathbb{R}$ is the cycle depth-of-discharge (DoD), and $S_\delta \in \mathbb{R}$ is the DoD stress-factor.

The net load achieved using the combined SoC-Thermal-Degradation model is shown in Fig. 2.27 (a). The optimal control schedule calculated over the control horizon is shown in Fig. 2.27 (b). Observe that the period of high HVAC power in Fig. 2.27 (d), compared to the solution using only the SoC-Temperature model, simply shifts to the beginning of the control horizon. The resulting environmental, battery, and enclosure temperature trajectories are shown in Fig. 2.27 (e).

The control solution reduces the total electrical bill from \$52,080 (\$50,000 demand, \$2,080 energy) to \$48,006 (\$45,871 demand, \$2,135 energy). Within the energy bill, the energy required to cool the battery accounts for \$56. The net effect is a \$4074 (7.82%) reduction from the baseline electrical bill, or a \$5 (0.01%) increase in the electrical bill calculated using only the charge and temperature models. The cost of degradation was reduced from \$209, calculated by applying the degradation model to the schedule derived from the SoC-Temperature model application in Section 2.4.3.1, to \$111 from this schedule (a 47% reduction in estimated degradation rate). Further, when compared to the solution calculated using only the SoC model in Section 2.3.2.1, the cost of degradation was reduced from \$897 to \$111 (an 88% reduction). Again, these results are highly conditional based on the specific BESS parameters. This analysis demonstrates that even small changes in control actions can have large impacts on the rate of degradation.

Table 2.16: Example battery system degradation model parameters

Name			Symbol	Value		
Thermal Degradation Constant			k_T	0.0693		
Time Degradation Constant			k_t	1.49e-6		
SoC Degradation Constant			k_c	1.04		
Reference SoC			S_{ref}	50%		
Reference Temperature			T_{ref}	25%		
EoL Cost Assumed			C_{EoL}	-\$800,000		
Regularization weight			Π	1e-5		
Polynomial Fit	<i>a</i>	<i>b</i>	<i>c</i>	<i>d</i>	<i>e</i>	
DoD Stress Factor	5.7905	-6.8292	3.3209	5.3696 e-01	6.1638 e-02	

Note: The parameters in [128] were used as a basis for the representative BESS presented here. The model parameters were modified to for use in Pyomo (in the case of the DoD Stress Factor being a polynomial), and to more clearly demonstrate the effect of degradation on controller action (in the case of k_T and k_c). The DoD Stress Factor has be multiplied by five to represent a battery cell type with 1/5 the cycle life.

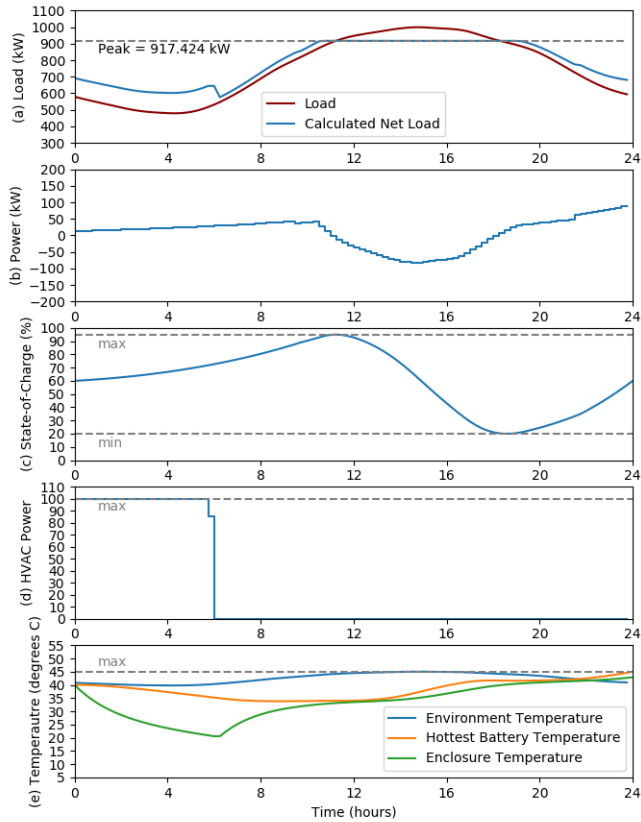


Figure 2.27: Results from control incorporating a degradation model: (a) net load with BESS power control, (b) battery power, (c) battery SoC, (d) enclosure ac power, and (e) battery, enclosure, and environmental temperatures

2.6 Discussion

Section 2.3 introduced several varieties of models for BESS SoC, with the primary classification distinguishing energy based models, charge based models, and concentration-based models. By applying all three to the same problem we can identify several differences in how controllers might work differently when operating with each type. Contrasting Fig. 2.7 and 2.11, we can observe that by accounting for the change in battery voltage, the CRM steadily increases power as SoC increases. The ERM does not model voltage and hence is imprecise in its estimates for how much power is needed to charge or available for discharge. In general, the ERM is best for use in large scale systems where a more detailed model would be impractical (e.g. centralized control of 1000's of individual BESS) or in very short duration problems that are insensitive to changes in voltage. The CRM and SPM are mathematically similar in structure, in that they both require empirical open-circuit-voltage functions and several internal storage elements in the form of either a equivalent circuit model or a partial concentration model. The CRM tends to simplify or combine many of the nuances of SPM type models, such as only using a single open-circuit-voltage function as opposed to one for the cathode and another for the anode. The SPM has the advantage of the ability to incorporate the physical degradation models, while the ERM and CRM must rely on empirical degradation models. To give a sense for the relative complexity of the model types, the minimal ERM has $3n + 2$ decision variables (were n is the number of time-steps), the minimal CRM has $6n + 2$, and the minimal SPM has $18n + 13$. Further, the ERM is convex, while the CRM and SPM have several non-convex constraints.

In Section 2.4 we introduce three cell temperature models and two en-

closure temperature models. The primary difference between the cell models is what heating and cooling mechanisms are considered, with another distinction being how many internal volumes are modeled. The enclosure models generally rely on an assumption of well-mixed air but can be classified based on how precisely they represent the HVAC system. As was demonstrated in the application section, by including the HVAC system in the control design the batteries can be pre-cooled to have maximum temperature margin during peak discharge when significant heat is being generated. Not accounting for temperature in control actions can lead to over-temperature shutdown or curtailment during peak times when the battery is needed most.

Lastly, Section 2.5 introduces several models to incorporate battery degradation into control decisions. Including degradation allows for charge/discharge to be balanced against how much the increase in use also accelerates degradation. A wide range of empirical degradation models is available that can be used on their own or in combinations to consider many different underlying mechanisms. Physical degradation mechanisms are less widely used but offer the potential to reduce the uncertainty of degradation modeling. Also, it can be observed from Fig. 2.27 that modeling the HVAC system and degradation together can have compounding benefits to prolonging battery life. Not accounting for degradation in control design allows batteries to operate in ways that could lead to premature EoL conditions. The following is a discussion of the gaps identified in the current state-of-the-art in models for optimal control of battery energy storage.

2.6.1 Gap Identification

This chapter has focused on providing guidance for how and where to use different types of battery models for optimal control. In this section we take a broader perspective to understand the state-of-the-art more generally and identify opportunities for advancement.

Real-world Data

There is a significant deficit of operational performance data in studies on optimal control of battery energy storage. This results in many of the modeling assumptions that proposed controllers are based on having gone unchallenged. This gap emphasizes the importance of systematic data collection and publication in BESS demonstration projects.

Control of large-scale parallel and series combinations of batteries

The ‘big-cell’ assumption is widely used to reduce the complexity of a large battery system to a manageable level. However, we do not know at what point the uncertainty of cell-to-cell variations outweighs the uncertainty from other modeling assumptions. Using a simpler model, with more representative cells, may yield better performance at a lower complexity than a highly precise battery model that assumes all cells behave the same. This trade-off is poorly understood even though it could greatly impact BESS performance.

Risk-averse and robust control

While there exists a large body of experimental work quantifying the uncertainty of the different model types, this uncertainty is rarely incorporated into the battery controller design. Even many controllers that consider the uncertainty of renewable power, through risk-averse or robust control, fail to

consider the uncertainty of the battery model's, implicitly assuming them to be deterministic systems.

Nonlinear ERM

Nonlinear system dynamics can be integrated into ERM used in controller design to improve model accuracy. The degree to which this improved model accuracy improves optimal control is an under-explored branch of research.

Voltage hysteresis in control

The path dependence of open circuit voltage can be a large contributor to error in SoC models. However, few controller designs consider hysteresis in their equivalent circuit, or solid-electrolyte interface voltage models. As these models are already nonlinear, and the optimal control problems are already non-convex, adding hysteresis should have minimal impact on computation time.

Entropy in thermal modeling

The electrochemical reaction in batteries can be exothermic or endothermic, depending on the specific chemistry and the SoC. While this concept is well understood in battery simulation, it is rare in optimal control. Incorporating the entropy-based heat generation and consumption into controllers could greatly reduce optimistic shortfall in many applications.

Comparative analysis of empirical degradation stress factors

Battery degradation is a complex phenomenon to research. Cycling studies try and isolate the stress factors that accelerate aging, but many of these factors either can't be isolated or have nonlinear effects when combined

with others. For example, charge/discharge current generates heat and leads to higher temperatures. A cycling study cannot fully isolate these variables because they are interlinked. Further, if battery degradation is a nonlinear function of both current and temperature, then a stress factor model that assumes independence will be inaccurate. The current direction of research on degradation models improves accuracy with increasing complexity, but controllers require computational efficiency and hence can make limited use of these improved methods. Research is needed to improve the accuracy of stress factor models that are simple enough to be incorporated into on-board controllers.

The literature intersecting battery energy storage modeling and optimal control is primarily simulation based with very little work that includes experimental analysis or real-world application. This is a natural result of the combination of battery energy storage technologies having tremendous potential to change grid operation, and only recently coming down in cost enough to the point where demonstration projects can proliferate. This means that there is significant academic interest while there are relatively few operational systems. A result of this lack of data is that there is little understanding of the impact of modeling assumptions on the design of controllers. Most of the gaps identified in the state-of-the-art stem from this lack of understanding. The remaining gaps can be summarized as an underdeveloped optimization framework. Stochastic optimization methods have been widely used in operation research to incorporate uncertainty into the optimization problem. This mathematical background has been underutilized in BESS controller design. With more data will come improvements in the understanding of uncertainty which can, in turn, be incorporated into optimal control approaches to achieve

risk averse or robust control.

Broadly speaking, the field on optimal control of BESS is still nascent when compared to the markets and control systems for thermal generation systems. The most commonly used models (ERM) are a simplistic approximation of extremely complicated electrochemical systems. If we are to learn from the historical course of optimization of thermal generation, we can understand that simplistic models are normal at this stage of development. We may expect that these models will become more developed and accurate as time progresses, leading to greater utilization of BESS to supply services on the grid. Additionally, we might also expect that the models used to optimize energy storage within markets will be more abstract than the models used by individual systems to optimize their operation. Navigating the balance between the applications that desire model simplicity and applications that desire model accuracy will require ongoing research, especially given the accelerated pace of battery energy storage technology development.

2.7 Summary

The choice of what model to use is critical in the design of optimal controllers for any physical system. This is especially true for electrochemical energy storage as we have shown the wide range of physical mechanisms that impact batteries during operation. Understanding the assumptions that are implicit in the choice of battery models will help engineers and researchers to improve the design of optimal controllers in BESS serving the electric grid.

This chapter thoroughly reviews battery models used for optimal control of BESS. We identify three broad types of SoC models: energy reservoir models (ERMs), charge reservoir models (CRMs), and concentration-

based models that include both single partial models (SPMs) and pseudo two-dimensional (P2D) models. ERMs are computationally efficient and hence are more appropriate for the optimization of large fleets of BESS. However, ERMs can be inaccurate over wide operational ranges. CRMs, in contrast, are more computationally intensive but have the potential for better accuracy. An under-explored middle ground for these is a nonlinear ERM, that may provide improved accuracy with a modest increase in computational complexity. Concentration based models are significantly more complex than either ERM or CRM and include many parameters that may be considered proprietary by a battery manufacturer. As the concentration-based SPM has a similar mathematical structure to the CRM, it is unclear how much this increase in complexity yields increased predictive accuracy. The SPM has the distinct advantage of enabling the application of physical degradation models that may reduce modeling uncertainty.

When battery temperature can limit BESS control actions, it is important to include a temperature model in the controller. Heat is generated in a battery from joule heating, over potential heating, and thermodynamic entropy. While the impact of entropy can be significant, it is rarely calculated in control systems. Heat is transferred from the battery, or the battery's enclosure, to the environment through conduction, convection, or radiation. Representing these mechanisms in the controller model enables optimal cooling control that can efficiently enforce temperature limits and significantly reduce battery degradation.

Lastly, battery degradation can be critical to consider when making control decisions. Factors such as SoC, temperature, and DoD can stress the materials in batteries and cause degradation over time and use. The empirical

rainflow cycle counting algorithm or physical degradation models for calculating degradation are both highly accurate but difficult to fully incorporate into an optimization problem. With a few simplifying assumptions, the stress factor model can be reduced to take the form of a sum of regularization terms in the objective function. These assumptions partially justify the more widely used formulations for degradation based on number of cycles, heat generation, and DoD. However, by including the nonlinear models in the controller, we observe that small changes in controller schedules can have disproportionate impacts on the rate of degradation. The myriad of trade-offs between model complexity and model accuracy can be difficult to navigate, but these engineering decisions can offer significant benefits in terms of BESS controller performance.

Chapter 3

Application of a Uniform Testing Protocol for Energy Storage Systems

¹ Methods for benchmarking and comparison can either limit or accelerate the adoption of emerging energy storage technologies on the grid. This chapter assesses the efficacy of the methods in the U.S. DOE Protocol for Uniformly Measuring and Expressing the Performance of Energy Storage to remove barriers to the technology’s acceptance. The protocol enables standardized data collection to compare different technologies for energy storage applications fairly. We apply the relevant portions of the protocol to a 1-megawatt lithium-ion battery system to provide a critical assessment of procedures and methods it stipulates. Field experience and data will be invaluable to standards development organizations as they begin to consider these methods for codification.

Contributions of this chapter were identified as follows: (*minor*) application of a uniform test protocol to a grid scale energy storage system to reduce performance uncertainty, (*minor*) development of new, useful en-

¹D. Rosewater, P. Scott and S. Santoso, “Application of a uniform testing protocol for energy storage systems,” in *Proc. 2017 IEEE Power & Energy Society General Meeting*, Chicago, IL, 2017, pp. 1-5. DOI: 10.1109/PESGM.2017.8274603

The dissertator was the principle investigator for this research including collecting experimental data, calculating performance metrics, and writing/editing the article itself. Paul Scott designed and lead the project to build the device under test and Surya Santoso provided guidance and technical review.

ergy storage performance metrics that provide more information to the device owner.

3.1 Introduction

With the increasing role of renewables and aging grid infrastructure, the need to enhance the stability, reliability, and efficiency of the electric grid has become critical. While the value of deploying energy storage systems for this purpose in the grid is widely recognized, so far energy storage integration has been limited [12]. Projections in [153] indicate a growing role for energy storage in the grid signaling a pressing need to understand better how energy storage can provide grid services. Consistent metrics for system performance are useful for comparing different energy storage technologies and for matching each technology to the appropriate set of grid services that it can provide.

Standardized methods are required to obtain comparable and consistent performance metrics from different storage technologies and different testing laboratories. IEEE Std 1679 contains guidance on many of the methods of energy storage testing [154]. The Protocol for Uniformly Measuring and Expressing the Performance of Energy Storage [16] was developed through a collaboration between the national laboratories and industry to continue to build agreement over best practices for testing energy storage technologies. The protocol contains procedures for administering reference performance tests on energy storage systems to derive stored energy, efficiency, responsiveness, standby losses, and self-discharge rate. Additionally, application specific duty-cycle performance tests are provided for a few grid services including frequency regulation. Frequency regulation is a grid service that helps a utility or regional transmission operator manage the moment-to-moment differences be-

tween load and supply in their areas [155]. Each application specific test in the protocol includes a duty-cycle which has been assessed to represent of the demands of that service. The derivation of the frequency regulation duty cycle is explained in depth in [156] and includes the incorporation of a mix of nominal and extreme operation.

We apply the frequency regulation testing procedure of the protocol, including a reference performance test and a duty-cycle performance test, to a 1-megawatt lithium-ion battery system. A preliminary report on this system's performance was made in [157]. In this chapter, we present a detailed investigation of how the protocol was applied to aid standards developers. As with any test procedure, adaptations and accommodations must be made to the procedure to collect the data required to measure performance. Similarly, the system itself must be designed and configured in such a way to enable accurate, time-synchronized data to be collected in a uniform manner. This chapter presents an in-depth discussion on these challenges to inform performance testing standard development. Our data and observations will be useful to standards development organizations seeking to codify methods for energy storage performance testing.

The rest of this chapter is organized as follows: Section 3.2 explains the relevant parts of the protocol and what modifications are done to its procedures to apply them to the equipment under test. Section 3.3 describes the laboratory setup used to perform the experimental regimen including the energy storage test pad (ESTP), the equipment under test (EUT), and the control/instrumentation configuration. Section 3.4 provides the data collected from the EUT during each test and the resulting calculated performance values. Section 3.5 discusses the qualitative and quantitative experience devel-

oped through application of the protocol. Lastly, Section 3.6 summarizes this research and explores what conclusions can be drawn as a result.

3.2 Methodology

This section explains how the test procedures outlined in the protocol along with the equipment under test were adapted and configured to measure energy storage performance uniformly.

3.2.1 Procedure Adaptation

The scope and schedule of our testing were limited by both technical and financial constraints, and so it was not possible to perform the entire protocol as specified. Because of this, the procedure had to be prioritized and adapted to provide highest relevance and portability of the generated performance metrics using the fewest number of tests. Relevance in this context refers to the ability of a metric to predict the performance of the system when it is in operation and portability is the ability of a metric to contrast the salient characteristics of the system with other storage technologies tested at other laboratories. For this EUT, we decided to perform a subset of the protocol's tests for energy capacity and efficiency, additional tests for responsiveness (averaging the resulting metrics), and a shortened duty cycle test for frequency regulation. Tests for energy capacity take hours to complete and so only one could be completed per day whereas tests for responsiveness took only a few seconds to complete and so could be repeated many times with very little marginal cost. The shortened duty-cycle was selected because the control signal is energy-neutral (equal charge and discharge energy) whereas, due to losses, the system requires more energy input than output to maintain

its SOC. The two-hour cycle was short enough to allow the system to stay in a normal SOC range throughout. These adaptations were sufficient to satisfy our constraints while producing relevant and portable metrics for analysis.

3.2.2 Test Procedures

The test procedures in the protocol are designed to measure the characteristics of how a specific device provides its functionality. Tests can be broken into two categories, reference performance tests (RPTs), and duty-cycle tests. RPTs measure the characteristics of a system that affect how well it can store energy (e.g. maximum stored energy) but that do not necessarily map to a specific grid service. The Stored Energy Test is an RPT to measure the maximum energy a system can store and the efficiency of full capacity cycles [16]. The Response Time and Ramp Rate Test is an RPT to characterize the responsiveness of a system to external power commands [16]. Duty-cycle tests measure a system’s emergent ability to provide a specific grid service (e.g. frequency regulation). The Reference Signal Tracking Test measures how closely a system can follow a duty-cycle which is representative of a given grid service [16]. The adapted procedures used here are shown in Table 3.1.

3.2.3 Performance Calculation

Many performance metrics are important when benchmarking an energy storage system. Two of the most fundamental are stored energy and round trip efficiency. Stored energy is defined as the energy which can be supplied by the system at a given rate before it must be recharged [16]. Stored energy is analogous to energy rating from [154]. This calculation is shown in (3.2.1). The stored charge energy, shown in (3.2.2), is then defined as the maximum

Table 3.1: Test Procedures

Step Procedure	
1.0	Stored Energy Test (adapted from [16])
1.1	Charge the EUT to full SOC
1.2	Discharge the EUT to its minimum SOC level at full rated power, measure and record the energy delivered by the EUT
1.3	Charge the system to full SOC, measure and record the energy absorbed by the EUT
1.4	Repeat Steps 1.2 and 1.3 at $\frac{1}{2}$ rated power
2.0	Response Time and Ramp Rate Test (adapted from [16])
2.1	Charge or discharge the EUT to near 50% SOC
2.2	Precondition the EUT into a state of active standby (power set to 0 kW)
2.3	Discharge the EUT at rated discharge power, measure and record the command time-stamp, voltage and current
2.4	Return the system to active standby
2.5	Repeat steps 2.3 and 2.4 at rated charge power
2.6	Repeat steps 2.3 through 2.5 twice
3.0	Reference Signal Tracking Test (adapted from [16])
3.1	Charge the EUT to full SOC
3.2	Discharge the EUT at $\frac{1}{2}$ rated power to 50% SOC
3.3	Apply the time-series of commands for the frequency regulation duty-cycle
3.4	Once the duty-cycle is complete, charge the EUT at $\frac{1}{2}$ rated power to full SOC

energy which can be absorbed by the system before it must be discharged [16]. Round Trip Efficiency (RTE), (3.2.3), is then defined as the ratio of these two energy values [16]. RTE is an analog to energy efficiency as defined in [154].

$$Wh_d = \frac{1}{n} \sum_{i=1}^n Wh_{di} \quad (3.2.1)$$

$$Wh_c = \frac{1}{n} \sum_{i=1}^n Wh_{ci} \quad (3.2.2)$$

$$RTE = \frac{\sum_{i=1}^n Wh_{di}}{\sum_{i=1}^n Wh_{ci}} \quad (3.2.3)$$

Communication latency is defined in the protocol as the time between receiving the power command and starting to change its power output [16]. Ramp rate is defined in the protocol as the settling time divided by rated power (settling time is measured from when the system starts to respond to when it settles within 2% of its rated power) [16]. There are no directly analog metrics available in [154]. As the exact time that the system starts to respond can be difficult to measure we modify this definition of Communication Latency to be the time from sending the command to when system power exceeds 2% of rated power. Similarly, the definition of ramp rate was modified to be the average rate of change in system power between 10% and 90% of the set point [158]. These changes make measurements more robust to noise and hence more consistent.

For a grid service-specific performance, the protocol uses duty-cycle round-trip efficiency, signal tracking squared error, absolute error, energy error, and % time the signal is tracked [16]. Duty-cycle round-trip efficiency is

calculated the same as round trip efficiency, using (3.2.1), (3.2.2), and (3.2.3), except the duty cycle is used as the control signal. Duty cycle tests fall under the general category of functional testing in [154]. In the protocol, the error metrics are not normalized to either the size of the system or the sample rate of the data acquisition making the results difficult to compare to other systems tested by other laboratories. For this reason, this chapter uses the following additional service specific duty-cycle performance metrics: tracking error RMS, tracking error RMS %, and Alt. % of the time signal is tracked. The formulas for these metrics are shown in (3.2.4), (3.2.5), and (3.2.6).

Tracking Error RMS =

$$\sqrt{\frac{\sum (P_{Signal}(k) - P_{ESS}(k))^2}{N}} \quad (3.2.4)$$

Tracking Error RMS % =

$$\frac{\sqrt{\frac{\sum (P_{Signal}(k) - P_{ESS}(k))^2}{N}}}{P_{rated}} \quad (3.2.5)$$

Alt. % of time signal is tracked =

$$\frac{\sum_{k=1}^N \frac{(P_{Signal}(k) - P_{ESS}(k))}{P_{rated}}}{N} < 2\% \quad (3.2.6)$$

where P_{Signal} is the commanded power, P_{ESS} is the instantaneous energy storage power output, N is the number of points in the time record, and P_{rated} is EUT rated discharge power.

3.3 Experimental Setup

Experimental data were collected at the Energy Storage Test Pad (ESTP) located at the Sandia National Laboratories in Albuquerque New Mexico. The ESTP is a laboratory designed for experimentation on large grid-connected energy storage systems. More information on the ESTP and its capabilities can be found in [159].

3.3.1 Equipment Under Test

The TransPower GridSaver was commissioned by the California Energy Commission (CEC) as part of their public interest energy research program. The 1-megawatt rated system is comprised of four 250kW lithium-ion battery strings. The system is built into a semi-trailer for easy transportation. While the equipment is capable of functioning in many applications, it was designed primarily for high-power, short-duration services. Battery SOC data was collected through a battery management system which also provides passive cell balancing. A full description of the system can be found in the final project report to the CEC [160].

3.3.2 Control and Instrumentation

The EUT was primarily controlled through its HMI which allows system operators to send real power commands, view system data including warnings and errors, and change some automated functions, such as voltage and temperature limits. In addition to the HMI, commands and data were available on a controller area network bus. Custom-designed control equipment and software allowed operators to automate some of the EUT's functions. This equipment sent open loop commands to the EUT and was used during the

Response Time and Ramp Rate Test and the Reference Signal Tracking Test which required time synchronized data for commands and system response.

Alternating voltage data were collected from both the 3-phase, Delta, 480V grid power connection bus, as well as the 3-phase, Y; 208V house power used to supply the lights, battery management, battery rack fans, and inverter coolant pump. Alternating current data were collected from each phase of all four of the system's power inverters, each phase of the air conditioner, and each phase of the house power (house power and air conditioner are considered auxiliary loads). All voltage measurements were calibrated to within 0.1% of nominal voltage while all current measurements were calibrated to within 0.5% of full-scale current. For the Stored Energy and Reference Signal Tracking Tests data were collected at 24 kHz and averaged for recording to 1 sample per second (1Hz). For the Response Time and Ramp Rate Time Test data were collected and recorded at 12.5 kHz with a clock accuracy within 50 parts-per-million. Assuming that errors in current, voltage, and time measurements are independent, it can be calculated that power measurement accuracy was within $\pm 0.51\%$ of full scale (5.1 kW) for the results described in Section 3.4.

3.4 Results

3.4.1 Stored Energy Performance

Figure 3.1 shows the data collected from the EUT during the Stored Energy Test. These data were processed according to (3.2.1), (3.2.2), and (3.2.3). The performance metrics calculated for these conditions are shown in Table 3.2. These results are useful to grid operators and energy storage designers alike. Note that the system's maximum power, recorded at 990 kW, was only available near 100% SOC. This limitation on available power means

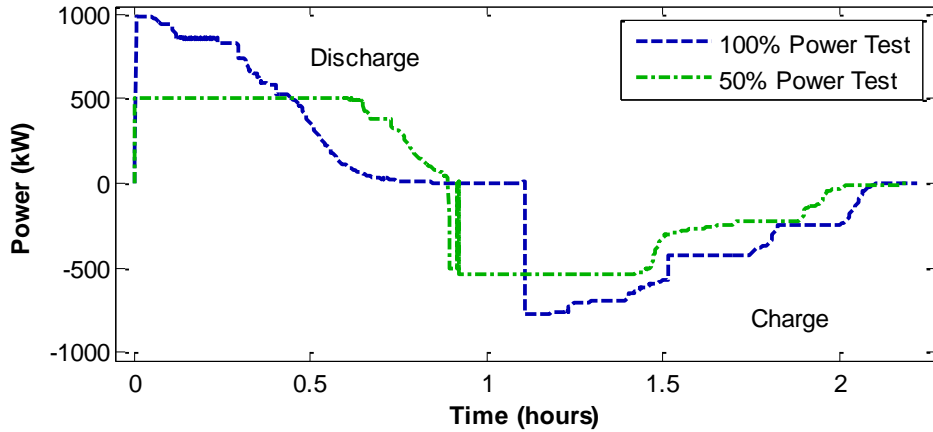


Figure 3.1: Stored Energy Test Data

that when the EUT is operating at a partial state of charge, it will have significant apparent power capacity to provide reactive power to support grid voltage. It can also be observed that a roughly 7% drop in RTE comes from the auxiliary loads, primarily cooling. Therefore a highly efficient cooling system would be a valuable design feature for services that require higher efficiency.

3.4.2 Response Time and Ramp Rate Performance

The data collected during the Response Time and Ramp Rate Test on one battery string in the EUT is shown in Figure 3.2. Charge and discharge tests were performed separately and plotted together. Instantaneous power was calculated from three-phase voltage and current. A 5th order digital Butterworth low-pass filter was applied to clean up the instantaneous power signal for analysis. Charge power and discharge power were normalized separately to 1.0 and -1.0 p.u. respectively. Figure 3.2 shows fully processed response characteristics for 100% charge and discharge power for one of the three tests. In this plot, $t = 0$ represents the time when the EUT receives a command.

Table 3.2: Stored Energy Test Results

Metric	100% Power Performance	50% Power Performance
Max Power Discharge	990 kW	502 kW
Duration Max Discharge	219 seconds	2305 seconds
Stored Energy	383 kWh	409 kWh
Max Power Charge	780 kW	543 kW
Charged Energy	433 kWh	468 kWh
Mean Auxiliary load	13.24 kW	15.04 kW
Round Trip Efficiency*	82.9 %	81.6 %

All values were measured at the grid connection with aggregate accuracy within ± 5.1 kW, *Includes auxiliary load

Table 3.3: Response Time and Ramp Rate Test Results

Metric	Performance
Mean Communication Latency	1.079 s
Mean Ramp Rate	2.12 MW/s

The result of the performance metric calculations are shown in Table 3.3. As the system's ramp time to full power is faster than the communication latency, if this system were to be used in a fast response application it would benefit significantly from a streamlined network infrastructure.

3.4.3 Reference Signal Tracking Test Performance

The data recorded during the Reference Signal Tracking Test is shown in Figure 3.3. The calculated performance metrics are shown in Table 3.4. Additionally, SOC data recorded during the experiment are shown in Figure 3.4. The change in SOC was found to be -11.22% from the beginning to the end of

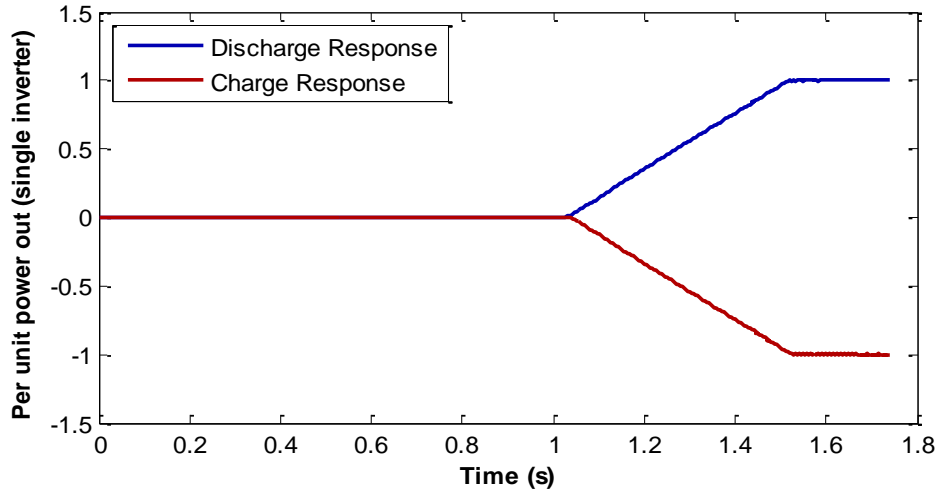


Figure 3.2: Response Time and Ramp Rate Test Data (Normalized and Filtered)

the duty cycle. Note that the battery management system did not record the SOC returning to 100%. The wide difference between the highest cell voltage and the lowest cell caused all four strings highest cell voltages to reach their maximum charge voltage when the systems average SOC was only 70.96%. These performance metrics are relevant for predicting how the system would perform if it were installed in an RTO with a frequency regulation market. An 83.6% duty-cycle RTE, along with the test time of 3.346 hours and the discharge energy 567 kWh, implies that the system would require approximately 27.8 kW on average to maintain the system’s SOC during operation. This SOC maintenance power could also be used to compare the performance of this system with other systems.

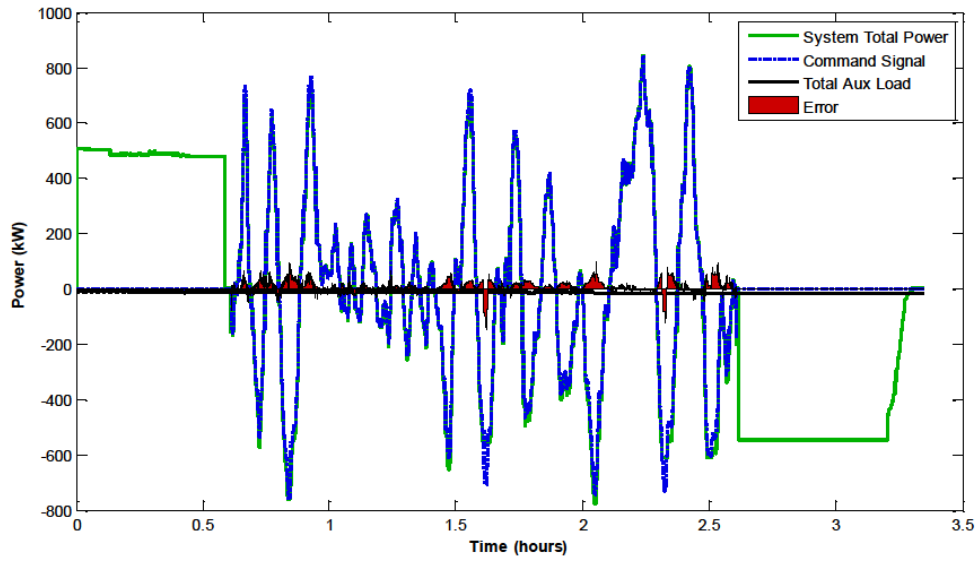


Figure 3.3: Frequency Regulation Duty-Cycle Test Data

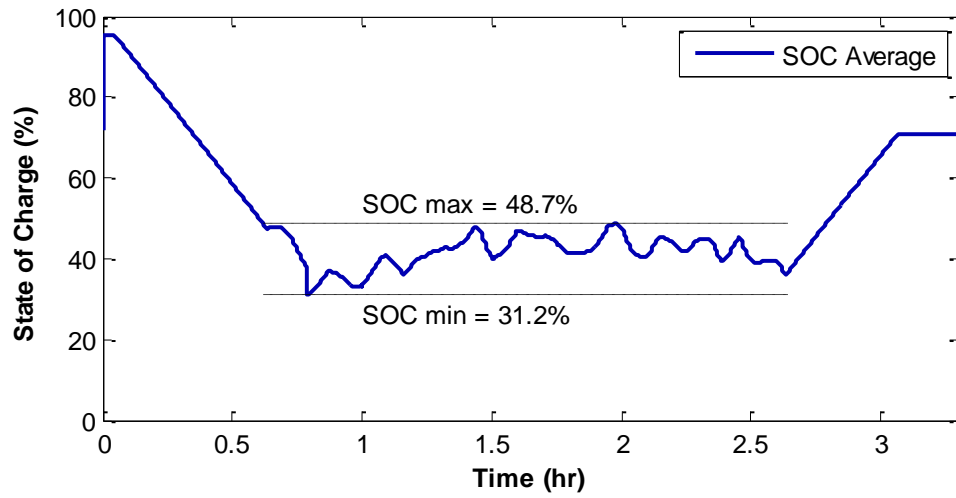


Figure 3.4: State-of-Charge During Duty-Cycle Test

Table 3.4: Reference Signal Tracking Test Results

Metric	Performance
Discharge Energy	567 kWh
Charge Energy	638 kWh
Auxiliary load	12.11 kW
Duty cycle RTE	83.6%
Sum of squared error	3,646,416 kW ²
Sum of absolute error	60,491 kW
Sum of energy error	381,561,167 kWh
% of time signal is tracked	24.5%
*Tracking Error RMS	22.5 kW
*Tracking Error RMS %	2.3 %
*Alt. % of time signal is tracked	73.5%

*Additional metrics not in the protocol

3.5 Discussion

Applying the protocol to a 1-MW energy storage system developed a better understanding of the requirements of the protocol. Three observations are discussed here along with recommendations for improvements to the protocol.

First, the EUT must be designed and configured to respond to an external command signal. The control scheme for energy storage systems varies widely and depend on their intended applications. For example, a system designed for peak shaving could respond to a clock while a system designed for voltage regulation could respond to voltage. As the protocol is written now, it does not fully account for these alternate control mechanisms when testing systems. A full description of how to implement a control signal for each test would increase the versatility of the protocol for wider adoption.

Second, an RPT to measure or verify SOC accuracy would be helpful in accounting for a variety of system designs. A clear picture is needed of the system's available power and energy throughout its operational SOC range to plan and execute test routines successfully. This requirement means that the system needs both an accurate estimation system for SOC and an accurate model for SOC forecasting that can be used to plan tests and predict the system's behavior. This model could be developed through a routine of pre-tests on SOC accuracy.

Last, reported metrics should be normalized to account for a variety of system sizes and test durations. Normalized versions of the sum of squared error and sum of absolute error, including RMS error and RMS% error, are easier to interpret and compare across energy storage technologies. Similarly,

the requirement for the % Time the signal is tracked metric, as it is currently normalized to the instantaneous requested power, is nearly impossible to satisfy at low power levels. Not normalizing causes a misleading result for how closely the system follows the duty cycle which can be corrected for by normalizing to the rated power instead.

3.6 Summary

The Protocol for Uniformly Measuring and Expressing the Performance of Energy Storage enables fair benchmarking and comparison of different storage technologies. We applied the protocol to a 1-megawatt rated energy storage system to collect application experience and data that will help standards development organizations to adapt and adopt the protocol with confidence and clarity. The equipment under test had to be adapted to the protocol's requirements, and the protocol had to be adapted to the system's constraints. This led to the development of three concrete recommendations for improvements to the Protocol concerning: addition of guidance for configuration of the command signal, addition of explicit state-of-charge accuracy test procedures, and three new proposed metrics for reference signal tracking error. As standard developers consider the provisions in the protocol this information will help guide their assessment.

Chapter 4

Battery Energy Storage State-of-Charge Forecasting: Models, Optimization, and Accuracy

¹ Battery energy storage systems (BESS) are a critical technology for integrating high penetration renewable power on an intelligent electrical grid. As limited energy restricts the steady-state operational state-of-charge (SoC) of storage systems, SoC forecasting models are used to determine feasible charge and discharge schedules that supply grid services. Smart grid controllers use SoC forecasts to optimize BESS schedules to make grid operation more efficient and resilient. This chapter presents three advances in BESS state-of-charge forecasting. First, two forecasting models are reformulated to be conducive to parameter optimization. Second, a new method for selecting optimal parameter values based on operational data is presented. Last, a new framework for quantifying model accuracy is developed that enables a comparison between models, systems, and parameter selection methods. The

¹D. Rosewater, S. Ferreira, D. Schoenwald, J. Hawkins, and S. Santoso, "Battery Energy Storage State-of-Charge Forecasting: Models, Optimization, and Accuracy," *IEEE Trans. Smart Grid*, vol. 10, no. 3, pp. 2453-2462, May 2019. DOI: 10.1109/TSG.2018.2798165
The dissertator was the principle investigator for this research including organizing field data, developing the forecasting and model optimization algorithms, programming the data analysis and accuracy metric cancellations, and writing/editing the article itself. J. Hawkins was the project manager for the PNM Prosperity BESS installation studied. All co-authors provided guidance in their areas of specialization and multiple rounds of technical review.

accuracies achieved by both models, on two example battery systems, with each method of parameter selection are then compared in detail. The results of this analysis suggest variation in the suitability of these models for different battery types and applications. The proposed model formulations, optimization methods, and accuracy assessment framework can be used to improve the accuracy of SoC forecasts enabling better control over BESS charge/discharge schedules.

Contributions of this chapter were identified as follows: (*minor*) reformulated two SoC forecasting models to be conducive to parameter optimization, (*major*) developed a new method for selecting optimal parameter values based on operational data is presented, (*minor*) developed a new framework for quantifying model accuracy.

4.1 Introduction

Battery energy storage can help meet renewable portfolio standards in the U.S., or similar goals set by countries around the world [12, 161]. Because of this need, there is significant work being done to research the benefits, drawbacks, and challenges of integrating BESS into the grid using a variety of mathematical models. A fundamental component of all BESS models is a sub-model to estimate and forecast its state-of-charge (SoC). The definition of SoC, represented in (4.1.1), is the ratio of remaining to nominal capacity.

$$\text{State of Charge} \triangleq \frac{\text{Remaining Capacity}}{\text{Nominal Capacity}} \quad (4.1.1)$$

In this context, capacity can be measured in energy (kWh) or in charge (Ah). SoC estimation models are commonly used in consumer electronics and

electric vehicles to provide an onboard reading of present remaining capacity. These allow users to approximate how long their devices will last before needing to be charged or how far their vehicles will drive before needing to reach a charging station. SoC estimation models have been reviewed in detail [162] and are used in this chapter as a reference to compare the accuracy of SoC forecasting models.

SoC forecasting models are commonly used in control design and optimization [32, 34, 39, 46, 54, 55, 57]. Considering that error in SoC forecasts can lead to suboptimal control, forecasting model error has been underexamined in research on energy storage control. This chapter advances the field of BESS SoC forecasting through the reformulation of two distinct models, an optimal parameterization method, and a forecasting accuracy assessment framework.

We introduce two novel formulations of energy storage system SoC forecasting models that are conducive to regression methods for selecting optimal parameters. The energy reservoir model (ERM) measures capacity in units of energy and accounts for round-trip energy efficiency and self-discharge power. The charge reservoir model (CRM) measures capacity in units of charge and accounts for battery coulombic efficiency and self-discharge current. The CRM also uses functions for inverter efficiency, battery voltage, and battery resistance to calculate dc current from ac power. Both forecasting models use linear algebra to decouple the forcing function from the model parameters resulting in simple formulations and an analytic solution to optimal parameter calculation.

The various methods for choosing model forecasting parameters are then introduced, along with a novel method specific to the ERM and CRM for utilization of operational data to select optimal parameters. The objective of

this optimization is to minimize SoC forecasting error. We then demonstrate these methods to choose ERM and CRM parameters for an operational energy storage system. The forecasting error of each model is then analyzed in detail using robust accuracy metrics to understand where each is best applied.

The rest of this chapter is organized as follows: Section 4.2 establishes a method for SoC estimation which is robust to sensor noise. Section 4.3 develops the ERM and CRM forecast models. In Section 4.4, the conventional methods for parameter selection are listed and an optimal parameter selection method is developed using operational data. Section 4.5 then applies these methods to a large scale battery system, then proposes and applies a framework for model accuracy assessment. Lastly, Section 4.6 reviews the conclusions from this work and posits how they will direct future work.

4.2 State of Charge Estimation

In order to develop an accurate SoC forecast model we must first estimate SoC from the operational system. A SoC forecast model takes historical sensor measurements from a battery and produces an estimate of remaining capacity. Model inputs include measurements of battery voltage, current, and, in certain cases, low precision SoC estimates from a battery management system (BMS). A Kalman filter (KF) can be developed to incorporate these measurements and knowledge of the variance of the process and sensor noise to produce a more accurate on-line estimation of SoC. A plant model can be developed for the battery starting with the first order dynamic battery model as shown in Fig. 4.1 [163, 164].

In addition to a dynamic model, a SoC model, such as in [54], is also required. To select parameters for this model we draw on the manufacturer's

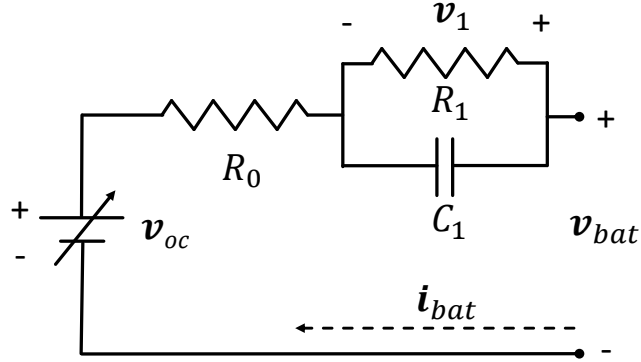


Figure 4.1: First Order Dynamic Battery Model

specification sheet and laboratory testing data. The methods of parameter selection are discussed in greater detail in Section 4.4. From [165] and [162] we can derive a KF to estimate SoC. The following linear system model can be used:

$$\dot{z} = \mathbf{A}z + \mathbf{B}u + \tilde{w} \quad (4.2.1)$$

$$y = \mathbf{C}z + \mathbf{D}u + \tilde{v}$$

$$\tilde{w} \sim \mathcal{N}(0, \mathbf{Q}), \quad \tilde{v} \sim \mathcal{N}(0, \mathbf{R})$$

$$z = \begin{bmatrix} v_1 \\ \varsigma_+ \\ \varsigma_- \end{bmatrix} \quad z_0 = \begin{bmatrix} 0 \\ 0 \\ 0 \end{bmatrix} \quad y = \begin{bmatrix} v_{bat} \\ \varsigma \end{bmatrix} \quad u = \begin{bmatrix} i_d \\ i_c \end{bmatrix}$$

$$\mathbf{A} = \begin{bmatrix} \frac{-1}{R_1 C_1} & 0 & 0 \\ 0 & 0 & 0 \\ 0 & 0 & 0 \end{bmatrix} \quad \mathbf{B} = \begin{bmatrix} \frac{1}{C_1} & \frac{1}{C_1} \\ \frac{1}{C_{cap}} & 0 \\ 0 & \frac{\eta_c}{C_{cap}} \end{bmatrix}$$

$$\mathbf{C} = \begin{bmatrix} 1 & \gamma & \gamma \\ 0 & 1 & 1 \end{bmatrix} \quad \mathbf{D} = \begin{bmatrix} R_0 & R_0 \\ 0 & 0 \end{bmatrix}$$

With this model, the steady state error covariance (Σ) can be calculated

by solving the matrix Riccati equation in (4.2.2),

$$\mathbf{A}\boldsymbol{\Sigma} + \boldsymbol{\Sigma}\mathbf{A}^T + \mathbf{Q}^T - \boldsymbol{\Sigma}\mathbf{C}^T\mathbf{R}^{-1}\mathbf{C}\boldsymbol{\Sigma} = 0, \quad (4.2.2)$$

where $\mathbf{Q} \in \mathbb{S}_+^{3 \times 3}$ reflects the variance of the process noise or model error, and $\mathbf{R} \in \mathbb{S}_{++}^{2 \times 2}$ reflects the variance of the sensor noise in measuring the output y . Using the error covariance matrix, the KF feedback gains can be calculated using (4.2.3).

$$\mathbf{L} = \boldsymbol{\Sigma}\mathbf{C}^T\mathbf{R}^{-1} \quad (4.2.3)$$

Using the results above, the state estimation (\hat{z}) can be calculated recursively in (4.2.4).

$$\dot{\hat{z}} = \mathbf{A}\hat{z} + \mathbf{B}u + \mathbf{L}(y - \mathbf{C}\hat{z} - \mathbf{D}u) \quad (4.2.4)$$

By updating the state estimation recursively based on measurements from the system, the KF will follow the actual system states rather than what the model would project. This means that if this same model were used as a forecasting model, which would not benefit from measurements, there would still be error between the forecast and the actual system states.

4.3 SoC Forecast Models

This section presents two SoC forecasting models: the Energy Reservoir Model (ERM) and Charge Reservoir Model (CRM). As the names suggest, the

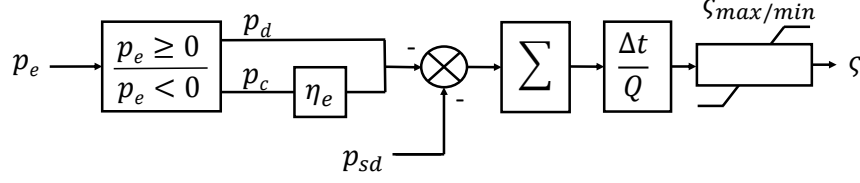


Figure 4.2: Energy Reservoir Model

ERM's capacity is measured in energy (kWh) where the CRM's capacity is measured in charge (Ah).

4.3.1 Energy Reservoir Model (ERM)

The energy reservoir model (ERM) records its available capacity in units of energy (kWh). There are many variations of this model including: models that assume 100% charge efficiency [26, 32, 34, 35], models that do not include self-discharge power [32, 34, 38, 46], and models that have distinct charge and discharge efficiencies [38, 39, 41, 46]. The ERM is governed by (4.3.1 - 4.3.4).

$$\boldsymbol{\varsigma}(n) = \hat{\varsigma}_0 - \frac{\Delta t}{Q_{\text{cap}}} \sum_{k=1}^n (\boldsymbol{p}_d(k) + \eta_e \boldsymbol{p}_c(k) + p_{sd}(1\text{kW})) \quad (4.3.1)$$

$$\boldsymbol{p}_c = \min(\boldsymbol{p}_e, 0) \quad (4.3.2)$$

$$\boldsymbol{p}_d = \max(\boldsymbol{p}_e, 0) \quad (4.3.3)$$

$$\varsigma_{\min} \leq \boldsymbol{\varsigma}(k) \leq \varsigma_{\max} \quad (4.3.4)$$

The mathematical structure of this model is similar to many of those found in the literature and discussed above. Note that p_{sd} is defined to be the

unitless scaling factor for a (1kW) self-discharge power for simplicity of the model reformulation below. The state flow diagram for the ERM is shown in Fig. 4.2. It has an open-loop structure which is linear and computationally efficient. Note that the input \mathbf{p}_e is the real power actuated by the system which may be slightly different from power commands sent to the system by a controller. The recursive formulation of this model, with three separate constraints, is not conducive to efficient optimization. To configure the model as a system of n linear equations (4.3.1-4.3.3) are then reformulated using the following definitions.

Let

$$\mathbf{x} = \frac{-1}{Q_{\text{cap}}} \begin{bmatrix} 1 \\ \eta_e \\ p_{sd} \end{bmatrix} \quad (4.3.5)$$

and

$$\mathbf{P} = \begin{bmatrix} \Delta t \mathbf{p}_d(1) & \Delta t \mathbf{p}_c(1) & \Delta t \\ \Delta t(\mathbf{p}_d(1) + \mathbf{p}_d(2)) & \Delta t(\mathbf{p}_c(1) + \mathbf{p}_c(2)) & 2\Delta t \\ \vdots & \vdots & \vdots \\ \Delta t \sum_{k=1}^n \mathbf{p}_d(k) & \Delta t \sum_{k=1}^n \mathbf{p}_c(k) & n\Delta t \end{bmatrix} \quad (4.3.6)$$

The $n \times 3$ matrix \mathbf{P} is made up of the cumulative sum of the discharging energy (kWh) in the first column, the cumulative sum of the charging energy (kWh) in the second column, and the cumulative sum of a unit energy (kWh) in the third column. The vector \mathbf{x} is then the linear separation of the coefficients of the three model parameters associated with the capacity (Q) the energy efficiency (η_e), and the self-discharge power scaling factor (p_{sd}). Hence (4.3.1-

4.3.3) can be written:

$$\boldsymbol{\varsigma} = \mathbf{P}\mathbf{x} + \hat{\boldsymbol{\varsigma}}_0 \quad (4.3.7)$$

4.3.2 Charge Reservoir Model (CRM)

The charge reservoir model (CRM) records its available capacity in units of charge (Ah). This model is also commonly referred to as the “ampere-hour method” or as “coulomb-counting.” As charge and discharge schedules are provided in units of power (kW), we include a power conversion model. Inverter based power conversion efficiency is modeled as a constant percentage [55], a piecewise constant percentage [166], or as a function of power [56, 57, 167]. The power conversion model used here is a quadratic polynomial fit ϕ where $\mathbf{p}_{bat} = \phi(\mathbf{p}_e)$.

The above efficiency model yields dc power, while the charge based model requires dc current. In batteries, the power and current are related by battery voltage and battery impedance. These properties can be approximated using the dynamic battery model shown in Fig. 4.3. Battery impedance can be independent of SoC [55, 57, 166, 167], or dependent on SoC [56]. The open-circuit voltage of this circuit is governed by (4.3.8). The dc current (i_{bat}) can be derived as a function of ac power as shown in (4.3.9).

$$\mathbf{v}_{oc} = h_v(\boldsymbol{\varsigma}) \quad (4.3.8)$$

$$\mathbf{i}_{bat} = \frac{-\mathbf{v}_{oc} \pm \sqrt{\mathbf{v}_{oc}^2 + 4R_0\mathbf{p}_{bat}}}{2R_0} \quad (4.3.9)$$

Note that two solutions exist for each \mathbf{p}_{bat} , one at high $|\mathbf{i}_{bat}|$ and low terminal voltage, and one at low $|\mathbf{i}_{bat}|$ and high terminal voltage. As the

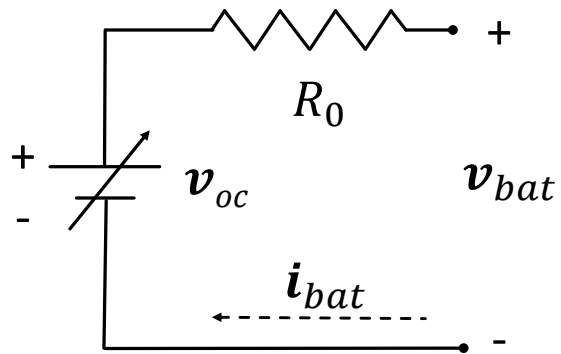


Figure 4.3: Dynamic Battery Model

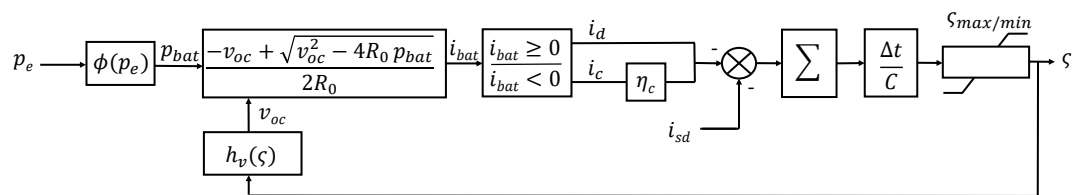


Figure 4.4: Charge Reservoir Model

high $|\mathbf{i}_{bat}|$ solution is out of range for safe battery operation, only the low $|\mathbf{i}_{bat}|$ solution is used. Because of the sign convention, the usable solution is associated with the additive (+) permutation of the equation. The function $h_v(\boldsymbol{\varsigma})$, is highly dependent on the battery chemistry. The function used here is a linear approximation $\mathbf{v}_{oc} = K_1\boldsymbol{\varsigma} + K_2$.

With dc current available from (4.3.9), SoC can be calculated using (4.3.10). Similar models assume 100% coulombic efficiency [54–57], and no self-discharge current [56, 57]. The model presented here includes both coulombic efficiency and self-discharge current as parameters to be selected.

$$\boldsymbol{\varsigma}(n) = \hat{\varsigma}_0 - \frac{\Delta t}{C_{cap}} \sum_{k=1}^n (\mathbf{i}_d(k) + \eta_c \mathbf{i}_c(k) + i_{sd}(1A)) \quad (4.3.10)$$

$$\mathbf{i}_c = \min(\mathbf{i}_{bat}, 0) \quad (4.3.11)$$

$$\mathbf{i}_d = \max(\mathbf{i}_{bat}, 0) \quad (4.3.12)$$

Note that i_{sd} is defined to be the unitless scaling factor for a (1A) self-discharge power for simplicity of the model reformulation below. The state flow diagram for the charge reservoir model is shown in Fig. 4.4. This is a closed-loop model structure with the non-linear function $h_v(\boldsymbol{\varsigma})$ in the feedback. This is computationally less efficient than the ERM because it must be run recursively at a high enough sample rate to account for the feedback dynamics. However, the section between \mathbf{i}_{bat} and $\boldsymbol{\varsigma}$ is nearly identical in structure to the ERM. Similarly to the ERM, (4.3.10-4.3.12) can be reformulated for optimization using the following definitions.

Let

$$\mathbf{y} = \frac{-1}{C_{cap}} \begin{bmatrix} 1 \\ \eta_c \\ i_{sd} \end{bmatrix} \quad (4.3.13)$$

and

$$\mathbf{I} = \begin{bmatrix} \Delta t \mathbf{i}_d(1) & \Delta t \mathbf{i}_c(1) & \Delta t \\ \Delta t(\mathbf{i}_d(1) + \mathbf{i}_d(2)) & \Delta t(\mathbf{i}_c(1) + \mathbf{i}_c(2)) & 2\Delta t \\ \vdots & \vdots & \vdots \\ \Delta t \sum_{k=1}^n \mathbf{i}_d(k) & \Delta t \sum_{k=1}^n \mathbf{i}_c(k) & n\Delta t \end{bmatrix} \quad (4.3.14)$$

The $n \times 3$ matrix \mathbf{I} is made up of the cumulative sum of the discharge (Ah) in the first column, the cumulative sum of the charge (Ah) in the second column, and the cumulative sum of a unit discharge (Ah) in the third column. The matrix \mathbf{y} is then the linear separation of the coefficients of the three decision variables associated with the capacity (C_{cap}) the coulombic efficiency (η_c), and the self-discharge current scaling factor (i_{sd}). Hence (4.3.10) can be written:

$$\boldsymbol{\varsigma} = \mathbf{I}\mathbf{y} + \boldsymbol{\varsigma}_0 \quad (4.3.15)$$

4.4 Choosing Model Parameters

This section provides three methods to choose the parameter values for each model. The energy reservoir model is fully specified by the scalar values of Q_{cap} , η_e , and p_{sd} . The charge reservoir model is fully specified by the scalar values of C_{cap} , η_c , and i_{sd} , along with two functions $\phi(\mathbf{p}_e)$, and $h_v(\boldsymbol{\varsigma})$. The following sections demonstrate how to determine these parameters based on the information available to an analyst. Fig. 4.5 shows the pros and cons for using information available from specifications, testing data, and operational data. Before a system is installed, often the only performance information available comes from the manufacturers' specifications. Section

4.4.1 outlines the difficulties of choosing parameters from this information. Once a system is installed, testing data outlined in Section 4.4.2 can be used to choose parameters that improve model accuracy. After a system has been operational for some time, historical measurements and SoC estimation data can be used as outlined in Section 4.4.3 to optimize forecast accuracy.

4.4.1 Choosing Parameters from Specifications

The simplest way to select parameter values is to use the system's design specifications or ratings. However, the system ratings corresponding to each parameter in the ERM and CRM incorporate assumptions about operation. Because of the link between operation and performance, it is difficult to know how the system will perform before it is operational. Choosing parameters from specifications also implicitly assumes that the manufacturer ratings are true values rather than conservative approximations. It is common practice to rate a system based on how it will be able to perform at the end of the warranty period as a contractual obligation rather than a design value. Less commonly, manufacturers sometimes rate their system's power and energy separately, meaning a 10 kW, 10 kWh system may only be able to provide 10 kW for a few minutes and get 10 kWh from a low rate discharge. A system may also have aspirational ratings based on ideal operational conditions, as is common for inverter efficiencies. Despite these issues, manufacturer ratings are often the only information available and so are commonly used to select parameters.

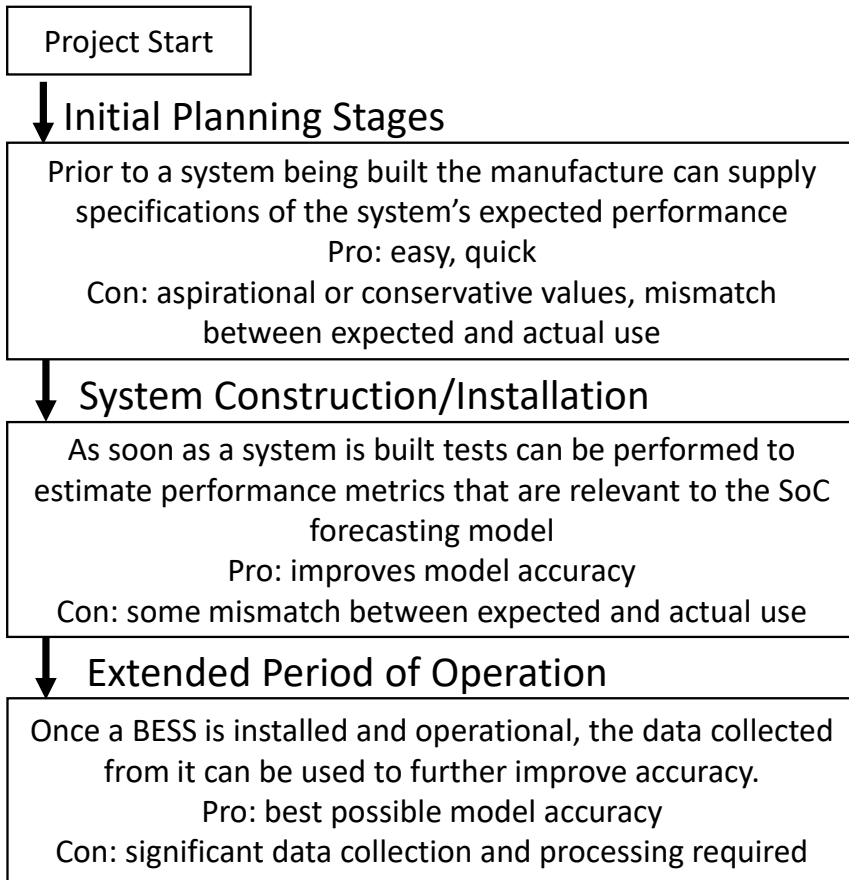


Figure 4.5: Flowchart for Choosing Model Parameters

4.4.2 Choosing Parameters from Testing

Performance metrics derived from testing can be used to select model parameter values and improve forecasting accuracy. Test procedures for benchmarking capacity and round-trip energy efficiency can be found in [16]. The requirements for a test to estimate self-discharge rate can be found in [168]. These protocols also include duty-cycles associated with a variety of applications that can help determine the performance of the system under the operational conditions it may expect when in service. A protocol for calculating a polynomial function for $\phi(\mathbf{p}_e)$ can be found in [87]. For batteries, standard methods and procedures for testing the performance of batteries sufficient to derive the function $h_v(\boldsymbol{\varsigma})$, as well as battery capacity, coulombic efficiency, and self-discharge current can be found in [121].

4.4.3 Operational Data

Once a BESS is installed and operational, the data collected from it can be used to further improve forecasting accuracy. During operation, SoC data is obtained from the KF SoC estimation algorithm presented in Section 4.2. The parameter vector \mathbf{x} in (4.4.1) is chosen to minimize the sum of squared differences (l^2 norm) between $\boldsymbol{\varsigma}$ and $\hat{\boldsymbol{\varsigma}}_{\text{KF}}$.

$$\min_{\mathbf{x} \in \mathbb{R}^3} \|\mathbf{P}\mathbf{x} + \boldsymbol{\varsigma}_0 - \hat{\boldsymbol{\varsigma}}_{\text{KF}}\|_2^2 \quad (4.4.1)$$

The charge reservoir model is optimized in the same way. The parameter vector \mathbf{y} can be optimized to minimize the l^2 norm using (4.4.2).

$$\min_{\mathbf{y} \in \mathbb{R}^3} \|\mathbf{I}\mathbf{y} + \boldsymbol{\varsigma}_0 - \hat{\boldsymbol{\varsigma}}_{\text{KF}}\|_2^2 \quad (4.4.2)$$

The advantage of this formulation is that the objective functions (4.4.1) and (4.4.2) can be solved analytically using the pseudoinverse specified in (4.4.3) [169].

$$\begin{aligned} \mathbf{x}^o &= (\mathbf{P}^T \mathbf{P})^{-1} \mathbf{P}^T (\hat{\boldsymbol{\varsigma}}_{\text{KF}} - \boldsymbol{\varsigma}_0) \\ \mathbf{y}^o &= (\mathbf{I}^T \mathbf{I})^{-1} \mathbf{I}^T (\hat{\boldsymbol{\varsigma}}_{\text{KF}} - \boldsymbol{\varsigma}_0) \end{aligned} \quad (4.4.3)$$

For these problems to have solutions $\mathbf{P}^T \mathbf{P}$ and $\mathbf{I}^T \mathbf{I}$ must be invertible, meaning they must have full rank. This would not hold if either the device were not used ($\mathbf{p}_e = 0$ / $\mathbf{i}_{bat} = 0$) or if the device were only charged or only discharged ($\mathbf{p}_d = 0$ or $\mathbf{p}_c = 0$ / $\mathbf{i}_d = 0$ or $\mathbf{i}_c = 0$)

4.5 Model Implementation and Comparison

These methods are applied to two large scale energy storage installations with carbon enhanced lead-acid batteries. The example installations are two co-located but independent BESS: a photovoltaic power smoothing battery, and peak shifting battery [170]. Time series ac power, dc current, dc voltage, and onboard SoC (from each system's BMS) were collected for 260 days. These days were selected because out of one year surveyed, they were found to have sufficient data integrity for analysis. To reduce the effects of sensor noise, power below 5 kW (and current below 5 A in the case of the CRM for the shifting battery) were set to zero. Measurement noise above this level

was filtered first by the data collection system and then by the data archival system which was configured to only record changes in data trends outside of set parameters. Section 4.5.1 outlines the results of using an SoC estimation model to recover the precision of battery SoC lost to the data archiving server settings. Section 4.5.2 shows how parameters are selected for the example system using the methods described in Section 4.4. Section 4.5.3 proposes a quantitative error based framework to assess forecasting model accuracy. Section 4.5.4 then compares the relative accuracy of each model, on both systems, using conventional and optimal parameter selection methods.

4.5.1 SoC Estimation

This section covers the results of applying the general method described in Section 4.2 to the example system to estimate SoC. The purpose of this step is to recover SoC precision lost to the data archival system. The data archival system maintains zero digits of precision (whole SoC percentages only) and then reduces the number of points needing to be stored by only recording a new point when it changes the linear trend of the data. This data compression means that variable signals like current or power will have significantly higher resolution data than slow changing signals like SoC. The KF model parameters are listed in Table 4.1.

As the smoothing battery's operation is made up of short duration charge or discharge pulses to counteract fluctuations in PV system output, the resulting fluctuations in SoC are small. The data archival system used by the example system filtered these small fluctuations into straight line trends, losing precision that is important to our analysis. The KF is able to recover the small fluctuations in SoC resulting from active PV smoothing. In the

Table 4.1: SoC Estimation Model Parameters

Parameter	Smoothing Battery	Shifting Battery
R_0	143 m Ω	95 m Ω
R_1	0.15 m Ω	0.05 m Ω
C_1	3.4 kF	10.1 kF
C_{cap}	1,000 Ah	3,000 Ah
γ	0.635 V/%SoC	0.635 V/%SoC
η	99%	99%
Q	diag([5 0.1 0.1])	diag([5 0.1 0.1])
R	diag([14 5])	diag([14 5])

following sections the restored SoC signal is used to select parameters and to determine the each model’s accuracy. Figure 4.6 shows the SoC recorded from the BMS, along with the SoC estimated using the KF, on a sample day where the smoothing battery was active. The KF estimate has double precision, zero mean error, and an unknown error distribution. In similar applications of the KF the error distribution has been reported to be within 3% of the true value [162]. The trend for the KF estimated SoC is the same as from the BMS. However, the effects on SoC of the short duration smoothing pulses are now clear in the data.

4.5.2 Parameter Selection

This section describes the process of choosing parameters for the example system. Tables 4.2, 4.3, and 4.4 show a summary of the model parameters selected. An important caveat to these parameters is that they are static throughout the year, even though the underlying performance of the batteries is likely to change some in that time. Adaptive modeling that would account for this change is out of the scope of this work.

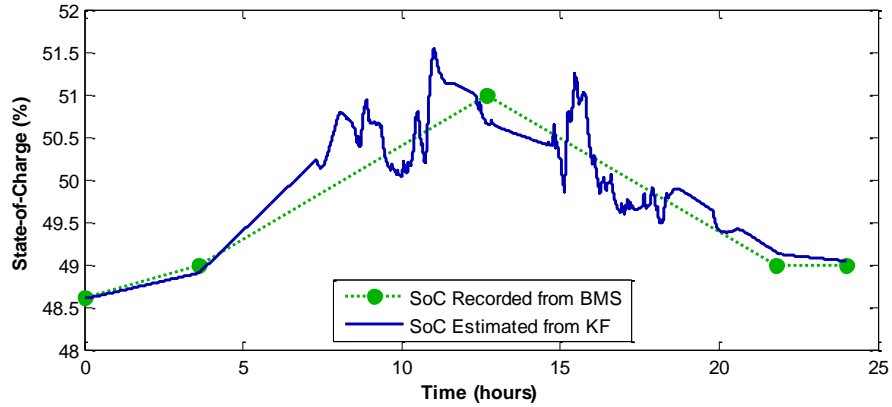


Figure 4.6: KF SoC Estimation versus BMS SoC Data Recorded

Table 4.2: Summary of Energy Reservoir Model Parameters

Battery	Selection Method	Capacity (kWh)	Efficiency (%)	Self-Discharge Rate S.F. (%)
Smooth [43]	S	180	95	0
Smooth	T	761.2	91.86	1.545
Smooth	O	797.56	90.04	0.672
Shift [43]	S	990	70	0
Shift	T	1982	89.30	9.52
Shift	O	2371	91.2	3.38

Specifications (S), Testing (T), Optimal (O), Scaling Factor (S.F)

Table 4.3: Summary of Charge Reservoir Model Parameters

Battery	Selection Method	Capacity (Ah)	Coulombic Efficiency (%)	Self-Discharge Current S.F. (%)
Smooth	S	1000	99	0
Smooth	T	1162	89.6	0
Smooth	O	1123	88.4	2.423
Shift	S	3000	70	0
Shift	T	3354	98.14	2.45
Shift	O	3557	91.87	2.42
Inverter	Selection Method	P_e^2 Coefficient	P_e Coefficient	Offset Coefficient
Smooth	S	0	0.95	0
Smooth	T	0	Discharge / Charge 95.2 / 94.2	0
Smooth	O	4.6296e-5	1.0041	7.9188

Specifications (S), Testing (T), Optimal (O), Scaling Factor (S.F)

For the ERM, the shifting and smoothing battery system specifications are found in [43] which has an expected power operation close to 250 kW resulting in an energy specification of $Q_{\text{cap}} = 180$ kWh. Similarly, values for η_e and p_{sd} are 95% and 0 respectively. To build on the work in [43] we use these same parameter values for our study of forecast accuracy. Specifications for the shifting battery are $Q_{\text{cap}} = 990$ kWh, $\eta_e = 70\%$, and $p_{sd} = 0$ respectively. For the CRM, more information on the batteries in the example systems is required. The power smoothing battery is built from 320, 2 V cells [172], and is rated at 1000 Ah (C_{cap}) and 640 V. The inverter has a rated peak conversion efficiency of 95%. Coulombic efficiency and self-discharge current specifications were not available for our analysis, but for a reasonable approximation we use $\eta_c = 99\%$ and $i_{sd} = 0$ respectively. Similarly, values for the shifting battery

Table 4.4: Smoothing Battery Dynamic Model Parameters

Battery Voltage	Linear Model [171]
ς Coefficient	0.19833 V/%
Offset Coefficient	1.9483 V
Battery Resistance	Resistance
R_0 per cell	3.419e-4 Ω

can also be chosen to be $C_{\text{cap}} = 3000$ Ah, $\eta_c = 70\%$, and $i_{sd} = 0$. Note that sufficient data were not available to parameterize a dynamic battery model for the shifting battery so power conversion was not modeled in the CRM in this example. Instead, dc current is used as the charge/discharge input to the shifting battery CRM.

Several tests were found in the course of battery operation sampled. These tests can be used to calculate parameters for the ERM, and CRM for both batteries. For the ERM, a capacity test, similar to what is described in [16], was performed on the smoothing battery. The test took the system from a maximum SoC of 100% to a minimum 23% and back again to 100%. This test enables the calculation of both energy capacity, $Q_{\text{cap}} = 761.2$ kWh, and energy efficiency $\eta_e = 91.86\%$. A self-discharge test, consistent with the requirements described in [168], was also performed on the smoothing battery. This test, which holds the SoC constant for 24 hours using whatever charge power is needed, enables the calculation of self-discharge power scale factor $p_{sd} = 1.545$. Similar tests were found for the shifting battery which resulted in parameter values of $Q_{\text{cap}} = 1981.5$ kWh, $\eta_e = 89.30\%$, and $p_{sd} = 9.524$.

In order to calculate CRM parameters for the smoothing battery we combine data from literature, the laboratory, and the field. The open-circuit voltage of the battery can be approximated by a linear function $\mathbf{v}_{oc} = h_v(\varsigma) =$

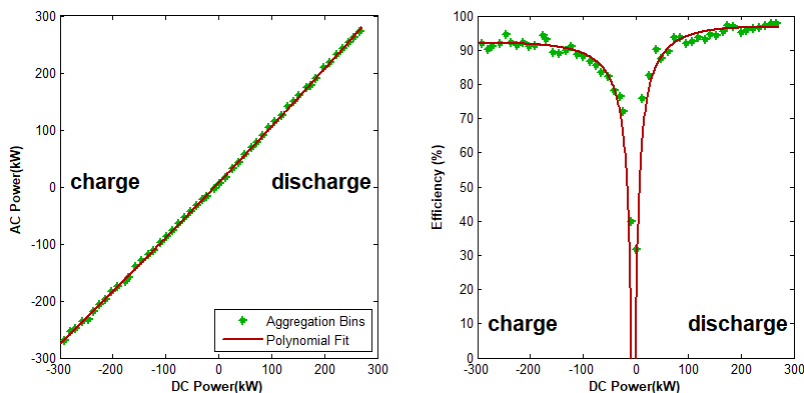


Figure 4.7: Inverter ac Power per dc Power (left), Inverter Efficiency per dc Power (right)

$K_1\varsigma + K_2$ where $K_1 = 0.198V$ and $K_2 = 1.95V$ (calculated from published string voltage as a function of depth of discharge) [171]. Six laboratory capacity tests performed on the battery are analyzed to derive capacity $C_{\text{cap}} = 1,162$ Ah, and coulombic efficiency $\eta_c = 89.6\%$. These cycles were also used to derive the battery impedance R_0 shown in Table 4.4. The power conversion function $\phi(\mathbf{p}_e)$ can be found through regression of field performance data [87]. As batteries spend much of their time near zero power, a direct curve fit would over-weight low power measurements. This problem is corrected by creating an even distribution of aggregation bins along the dc axis wherein the ac power measurements are averaged. The least-squares quadratic fit can be determined for the aggregation bins as shown in Fig. 4.7.

The optimal parameters for both models of both batteries are solved according to Section 4.4.3. The optimal solution over the whole dataset provides a benchmark by which to measure the effectiveness of the other parameter selection methods. The optimal parameters calculated are shown in Tables 4.2 and 4.3.

When building a forecast model for control systems, it is better to randomly assign a subset of the available data as a training set and the rest as a testing set. The model is optimized for the training set, but the accuracy is assessed on the testing set. This split helps ensure that models are not over-fit, and represent larger trends rather than fine detail. We have chosen not to do this in our study as we are not using it for control and because it becomes useful to know what the minimum possible error is for each model. The SoC forecasting error is the result of unmodeled system dynamics, inaccurate parameters, and measurement noise. Measurement noise is likely to be Gaussian and small. The KF applied in Section 4.5.1 reduces the impact of measurement noise, though it is likely that some of its effects remain. By choosing globally optimal parameters, the remaining forecasting error is primarily the result of unmodeled system dynamics which do not have a clear, noise like, distribution that can be easily modeled. Unmodeled system dynamics are likely to have non-Gaussian impacts, have non-zero mean, and both will be functions of the SoC, current, voltage and many other factors. This allows for a more direct comparison of the relative magnitude of unmodeled system dynamics between the ERM and CRM for these example systems.

4.5.3 Model Accuracy Framework

In this section, a methodology is proposed for quantifying the accuracy of SoC forecasting models. First, a forecast horizon is chosen based on the needs of the service being scheduled. A large sample of operational data is then broken into discrete periods each with the length of one horizon. For each period in the sample, a model is supplied the initial estimation of SoC (ζ_0) and that period's reference charge/discharge schedule (\mathbf{p}_e). The model then uses

that schedule to calculate a forecast (ς). The maximum positive error (4.5.1), maximum negative error (4.5.2), and RMS error (4.5.3) are then recorded for all periods in the sample, and a histogram is developed to display the RMS error level occurrence rate graphically.

$$\mu_{\max+} = \max(\varsigma - \hat{\varsigma}_{\text{KF}}) \quad (4.5.1)$$

$$\mu_{\max-} = \min(\varsigma - \hat{\varsigma}_{\text{KF}}) \quad (4.5.2)$$

$$\mu_{\text{rms}} = \sqrt{\frac{1}{n} \sum_{k=1}^n (\varsigma(k) - \hat{\varsigma}_{\text{KF}}(k))^2} \quad (4.5.3)$$

The mean RMS error is an intuitive metric that is robust to outliers. The histogram allows the error distribution to be compared visually between models and systems. The record of maximum positive and negative errors enables the calculation of probabilistic limits on forecast error. We define a 90% high error threshold as the SoC error under which the maximum positive error in a randomly selected forecast will occur 90% of the time. Similarly, we define a 90% low error threshold as the SoC error above which the maximum negative error in a randomly selected forecast will occur 90% of the time. These thresholds can be calculated from a discrete set of forecasts by first sorting the forecasts ($\mu_{\max+}$ and $\mu_{\max-}$ separately) from lowest to highest magnitude errors, and then selecting the error corresponding to the k^{th} forecast, where $k = \text{floor}(90\% \times m)$. Practically, these thresholds define the SoC error margins for a proposed schedule. Mean RMS, 90% high error threshold, and 90% low error threshold form the accuracy framework on which we based comparisons between models and example systems.

4.5.4 Model Comparison

Using the methods described above, we can compare forecasting accuracy of the proposed models and parameter selection methods. As a control system model is not used, each model is supplied the actual charge/discharge schedule (\mathbf{p}_e), rather than the control reference. On an i5 CPU with 1.8 GHz clock speed the computation time required for each model to produce forecasts for this sample were 0.476 seconds and 28.7 seconds for the ERM and CRM respectively. The increased computation time is a result of the open-circuit voltage feedback and non-linear current calculation required in the CRM. The CRM is supplied the battery current charge/discharge schedule for the shifting battery (\mathbf{i}_{bat}) because data were not available to select parameters for its dynamic battery model. Fig. 4.8 shows a selected forecast period for the smoothing battery. Each trajectory is produced by a different parameter selection method. As more information is incorporated into the parameter calculation the SoC forecast more closely follows the KF SoC estimate. By assessing many forecast horizons we can calculate a distribution of error magnitudes as outlined in Section 4.5.3.

Over a large sample of forecasting periods this trend, and its limitations, become clearer. Fig. 4.9 shows the histograms of RMS error for each model and battery calculated from 260 periods, each with a 24-hour forecast horizon. Each histogram identifies the parameter selection method used: specifications (blue), testing (green), and optimization using operational data (red). Table 4.5 then lists the 90% high error threshold, mean RMS error, and 90% low error threshold for the example systems. In each case, incorporating better information, from testing or operational data, reduces the overall distribution of forecasting error. However, the magnitude of this benefit is highly variable.

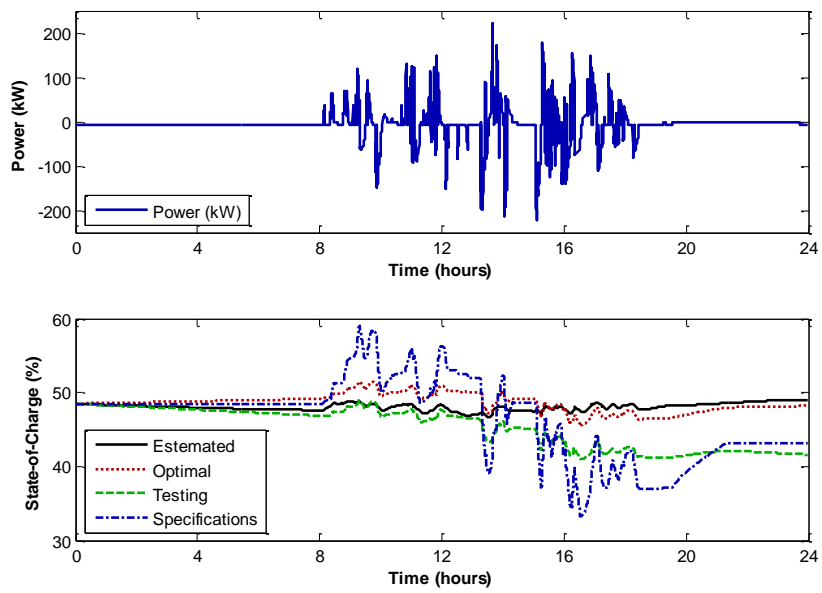


Figure 4.8: Smoothing Battery Power Operation (top), State-of-Charge Forecasts (bottom) for a Sample Day

Table 4.5: State-of-Charge Forecasting Error Metrics

Battery	Model	Selection Method	90% High	Mean RMS	90% Low
Smooth	ERM	S	48.10	8.79	-25.31
Smooth	ERM	T	6.65	4.11	-10.46
Smooth	ERM	O	12.96	2.93	-5.92
Smooth	CRM	S	6.09	4.47	-9.96
Smooth	CRM	T	6.15	3.58	-7.85
Smooth	CRM	O	6.41	3.02	-6.12
Shift	ERM	S	34.23	9.04	-38.83
Shift	ERM	T	17.56	4.15	-18.14
Shift	ERM	O	16.90	3.91	-18.85
Shift	CRM*	S	20.29	4.37	-17.15
Shift	CRM*	T	19.25	3.95	-17.87
Shift	CRM*	O	16.63	3.93	-19.13

Specifications (S), Testing (T), Optimal (O)

* a dynamic battery model was not used for the shifting battery

For the smoothing battery, the ERM is greatly improved by selecting parameters based on testing data and then based on operational data, reducing mean RMS error from 8.79% to 4.11% and then to 2.93%. Whereas for the shifting battery, this parameter selection progression reduces mean RMS error from 9.04% to 4.15% and then to 3.91%. For the CRM, use of testing data does not appreciably improve the shifting battery accuracy, whereas it results in a 1.5 fold improvement for the smoothing battery. Updating the forecasting model as better information becomes available has the potential to, but is not guaranteed to, improve forecasting accuracy.

For this example system the manufacturer specifications yielded more accurate forecasts using the CRM. This is because the CRM parameters are accurate over a wider range of operation and hence the model is less sensitive to a mismatch between expected and actual use. Both model's parameters

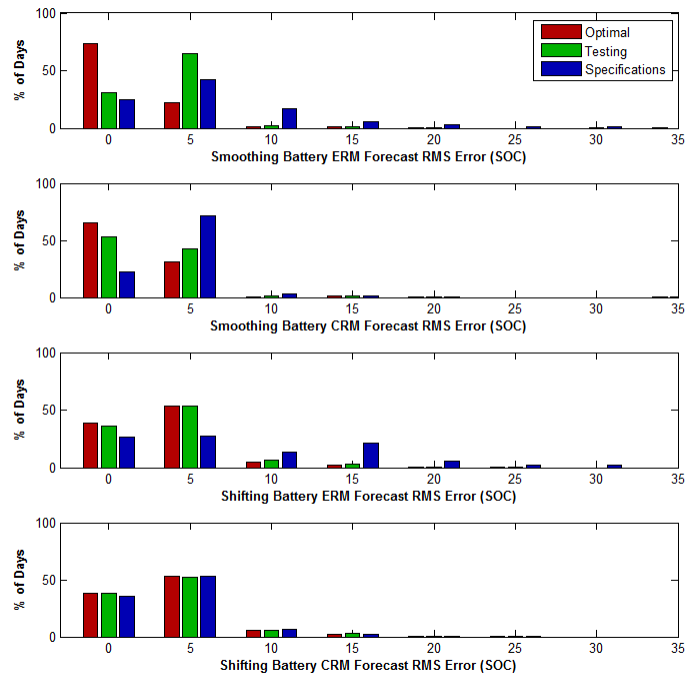


Figure 4.9: State-of-Charge Forecasting RMS Error for: Smoothing battery with ERM (top), Smoothing battery with CRM (middle top), Shifting battery with ERM (middle bottom), Shifting battery with CRM (bottom)

were selected based on the expectation that the system would be operated at high charge and discharge rates. As actual use was, on average, at low charge and discharge rates the model that whose parameters change less with changes in operation produces more accurate forecasts.

When comparing models with optimal parameters on the same battery system we expect that the majority of the error is the result of unmodeled system dynamics. For both battery systems, the optimal mean RMS for the ERM and CRM are roughly identical. This can be interpreted as evidence that the additional dynamics modeled by the CRM are not critical for these systems in their operational environments. While the CRM significantly increases forecast computation time, in this case it does not significantly improve forecast accuracy. Note that, for the shifting battery, a dynamic battery model would introduce additional error from unmodeled dynamics and hence its absence would not account for lower CRM model accuracy. The generalization of this result is that there are battery systems and applications where a simple model is fully sufficient to achieve accurate forecasts. We speculate that this is likely to be true in highly consistent operational environments or where a battery system varies little in voltage, temperature, or charge and discharge rates. This result also suggests that different batteries and different applications may be modeled better by either the ERM or CRM, and that it is critical to understand the forecasting error of the BESS models used in grid integration analysis.

4.6 Summary

This chapter has presented two novel formulations of SoC forecasting models and a method to calculate their optimal parameters. We then

compared the forecasting accuracy of both models, on two example battery systems, using three different methods of parameter selection: manufacturer's specifications, testing data, and selecting optimal parameters based on operational data. While both models were found to be more accurate forecasting the smoothing battery's SoC, the CRM was found to have better accuracy than the ERM when parameters were chosen from the manufacturer's specification sheet. This was the result of the CRM's accuracy being less sensitive than the ERM's accuracy to a mismatch between expected and actual use. However, for these system's in their operational environment, the CRM and ERM were equally impacted by unmodeled system dynamics, meaning they were equally accurate when they each had optimally selected parameters.

A general conclusion of this research is that different battery models will be more accurate than others for specific systems in specific applications. Further, there are specific systems and applications where the SoC forecast accuracy of the open-loop ERM is not significantly improved by the additional dynamics modeled in the CRM. The proposed framework for model accuracy assessment is a useful and widely applicable method to quantify forecasting accuracy. We intend to continue to expand the technical foundation of SoC forecasting models to improve their utility through the development of more accurate models, and methods of model adaptation to improve accuracy over time. Understanding and controlling the effects of battery model uncertainty will be critical to the integration of energy storage into a smart power system.

Chapter 5

Adaptive Modeling Process for a Battery Energy Management System

¹ Battery energy storage systems are often controlled through an energy management system (EMS), which may not have access to detailed models developed by battery manufacturers. The EMS contains a model of the battery system’s performance capabilities that enables it to optimize charge and discharge decisions. In this chapter, we develop a process for the EMS to calculate and improve the accuracy of its control model using the operational data produced by the battery system. This process checks for data salience and quality, identifies candidate parameters, and then calculates their accuracy. The process then updates its model of the battery based on the candidate parameters and their accuracy. We use a charge reservoir model with a first order equivalent circuit to represent the battery and a flexible open-circuit-voltage function. The process is applied to one year of operational data from two lithium-ion batteries in a battery system located in Sterling, MA USA. Results show that the process quickly learns the optimal model parameters and

¹D. Rosewater, B. Schenkman, and S. Santoso, “Adaptive Modeling Process for a Battery Energy Management System” in *Proc. Symposium on Power Electronics, Electrical Drives, Automation and Motion*, Sorrento, Italy, June 2020.

The dissertator was the principle investigator for this research including organizing field data, developing the optimization and adaptation algorithms, programming the data analysis and uncertainty cancellations, and writing/editing the article itself. Co-authors provided guidance in their areas of specialization and technical review.

significantly reduces modeling uncertainty. Applying this process to an EMS can improve control performance and enable risk-averse control by accounting for variations in capacity and efficiency.

Contributions of this chapter were identified as follows: (*minor*) developed a process for the EMS to calculate and improve the accuracy of its control model using the operational data produced by the battery system, and (*minor*) demonstrated the effectiveness of this process using real world data.

5.1 Introduction

The energy management system (EMS) is critical to the operational longevity and profitability of a battery energy storage system (BESS). In many BESS, the battery management system (BMS) is responsible for battery protection and state estimation, while the EMS is responsible for deciding when to charge and discharge. The models used by BMS and EMS can be very different. Much of the detailed chemistry data available to the BMS designers, is not available to the EMS designer. What is available however, can be a deluge of operational data. These data can be used to develop a highly accurate model that an EMS can use to optimize its decisions.

EMS models have been reviewed in detail in [13], and the methods to optimize decisions using these models has been reviewed in [22]. Models can vary from simple to extremely complex. Current practice is either to configure an EMS's battery model using manufacturer specifications or using data from performance testing during commissioning. However, recent work has focused on developing adaptive EMS models that learn from operational data [52, 173–175].

The primary contribution of this chapter is to improve the process for adaptive EMS modeling. We reduce the prior knowledge of the battery that the EMS needs to get started, improve the prediction accuracy over alternatives methods, and to calculate and track modeling uncertainty such that the model can be used for risk-averse or robust state estimation and control.

The adaptive EMS modeling process is started with the battery's open-circuit-voltage at two known states-of-charge (SoC). Using this information and data collected during daily operation, the adaptive process identifies battery capacity and efficiency, the open-circuit-voltage function, and the parameters of a battery equivalent circuit. Additionally, this process calculates and tracks the uncertainty of each of its parameters. The model then updates its parameters at a Bayesian learning rate determined by the candidate model's accuracy tested against a subset of the available data. This process has the benefit of continuing to keep model uncertainty low as battery parameters change with time and use. The resulting EMS model can then be used for state estimation and control. The uncertainty parameters make these process improvements work with a risk-averse controller design such as the one presented in [18].

The remainder of this chapter is organized as follows. Section 5.2 introduces the battery model, Section 5.3 discusses the proposed process to update the EMS model, including the data and methods used to estimate and test model parameters in situ. The results of applying the proposed process to a grid scale lithium-ion battery system are discussed in Section 5.4, and our conclusions are discussed in Section 5.5.

5.2 Battery Model

In this section we define a battery model that can be parameterized on-line and used in state estimation and control. The state equations for the equivalent circuit model presented in Fig. 5.1 are shown below:

$$v = v_{oc} + v_1 + R_c i^+ + R_d i^- \quad (5.2.1)$$

$$\frac{\partial v_1}{\partial t} = -\frac{v_1}{R_1 C_1} + \frac{i^+ + i^-}{C_1} \quad (5.2.2)$$

where v is the battery terminal voltage, v_{oc} is the open-circuit-voltage, v_1 is the dynamic voltage, t is time, R_c and R_d are the charge/discharge resistances, i^+ and i^- are the charge/discharge currents, R_1 is the dynamic resistance, and C_1 is the dynamic capacitance. The open-circuit-voltage function is approximated using a cubic polynomial as shown below:

$$v_{oc} = \alpha \varsigma^3 + \beta \varsigma^2 + \gamma \varsigma + \delta \quad (5.2.3)$$

where ς is the battery SoC, and α , β , γ , and δ are the polynomial coefficients. The SoC is then a function of the charge and discharge current as shown below:

$$\frac{\partial \varsigma}{\partial t} = \frac{\eta_c i^+ + i^-}{C_{cap}} \quad (5.2.4)$$

where C_{cap} is the battery's charge capacity, and η_c is the coulombic efficiency.

The initial parameter set for this model is shown in Table 5.1. While having initial parameters derived through manufacturer specifications may be beneficial to initial performance, our initial set is intentionally inaccurate to demonstrate the learning speed of the process. Only four parameters must be known or assumed prior to the start of the process: ς_{max} , ς_{min} , v_{oc-max} , and v_{oc-min} . This is because the maximum and minimum SoC, and their associated

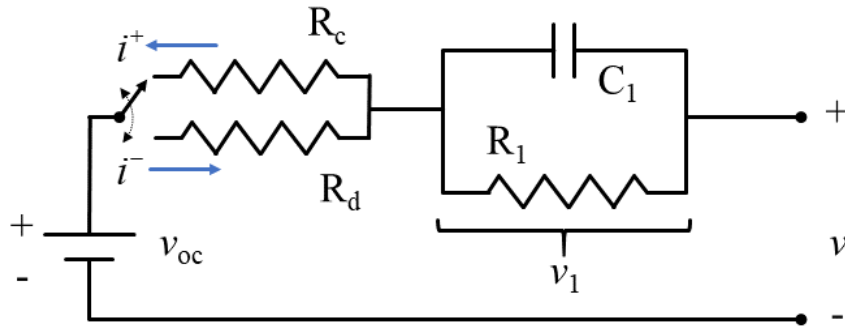


Figure 5.1: First order equivalent circuit model with distinct charge/discharge resistances

open-circuit-voltages, reflect the expected use and lifetime of a given cell design. For example, a manufacturer could sell two physically identical products: a deep-discharge cell with a voltage range of 2.7-4.2 V and an expected life of 800 cycles, and a long-lasting cell with a voltage range of 3.2-4.1 V and an expected life of 10,000 cycles. Because of this convention, defining what maximum and minimum SoC means can be an implicit method of incorporating a cell's degradation into a control system [13].

5.3 EMS Model Learning Process

For the EMS to be able to configure itself it must be able to learn its model parameters using the operational data. A summary of the EMS model learning process is illustrated by the flowchart shown in Fig. 5.2.

5.3.1 Data Requirements

While collecting operational data, a subset of the data are useful for parameter identification while the remainder either does not provide salient

Table 5.1: Charge Reservoir Model Initial Parameters

Name	Symbol	Value
Maximum state-of-charge*	s_{\max}	100.0%
Minimum state-of-charge*	s_{\min}	0.0%
Open-circuit-voltage at* s_{\max}	$v_{\text{oc-max}}$	1,027.6 V
Open-circuit-voltage at* s_{\min}	$v_{\text{oc-min}}$	807.4 V
Charge capacity	C_{cap}	3000 Ah
Coulombic efficiency	η_c	1.0
Charge resistance	R_c	0.1 Ω
Discharge resistance	R_d	0.1 Ω
Dynamic element Capacitance	R_1	0.1 Ω
Dynamic element resistance	C_1	0.1 F
Open-circuit-voltage parameter 0	α	0.0
Open-circuit-voltage parameter 1	β	0.0
Open-circuit-voltage parameter 2	γ	100.0
Open-circuit-voltage parameter 3	δ	900.0

* These are the only parameters that must be accurate from the start. All other initial parameters are purposefully inaccurate guesses, intended to demonstrate the learning speed of the process.

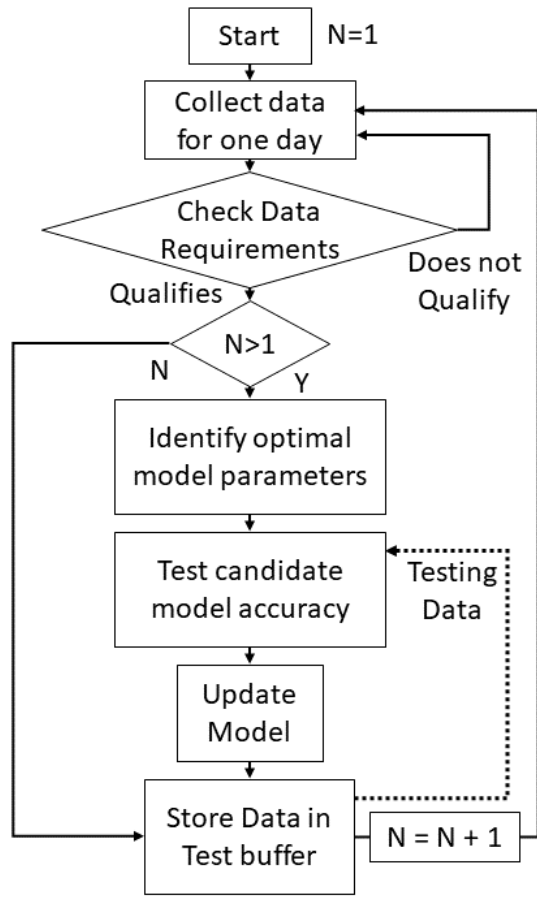


Figure 5.2: Flow chart of the EMS model learning process

information or has ill-conditioned measurements that could corrupt results. For this analysis we assess one day at a time. To qualify for parameter estimation, the data collected from a day must show that the BESS undergoes both charge and discharge, its range of SoC must be greater than 15%, and it must not contain any invalid or out-of-range data (e.g. battery voltage < 100 V). If the day being assessed does not meet these requirements, then the process simply passes it over to assess the next day.

5.3.2 Parameter Estimation

In this section, we introduce the on-line optimal parameter estimation process. Samples of voltage, current, and the SoC reported by the BMS are taken at a variable interval of $\Delta t_{[i]}$ to construct the measurement vectors: battery voltage \mathbf{v} , charge current \mathbf{i}^+ , discharge current \mathbf{i}^- and SoC $\boldsymbol{\varsigma}$. These vectors are then fed into the two-part optimization problem shown below:

Part 1, battery capacity and efficiency:

$$\min_{\mathbf{x}_1 \in \mathbb{R}^{n+3}} \|\boldsymbol{\varsigma} - \hat{\boldsymbol{\varsigma}}\|_2^2 \quad (5.3.1a)$$

subject to :

$$\hat{C}_{\text{cap}} \mathbf{D} \hat{\boldsymbol{\varsigma}} = \hat{\eta}_e \mathbf{i}^+ + \mathbf{i}^- \quad (5.3.1b)$$

where $\mathbf{x}_1 = \{\hat{\boldsymbol{\varsigma}}, \hat{\eta}_e, \hat{C}_{\text{cap}}\} \in \mathbb{R}^{n+3}$ is the set of all decision variables in the estimation of capacity and coulombic efficiency, and n is the number of samples in the data window.

Part 2, battery equivalent circuit parameters:

$$\min_{\mathbf{x}_2 \in \mathbb{R}^{3n+12}} \|\mathbf{v} - \hat{\mathbf{v}}\|_2^2 \quad (5.3.2a)$$

subject to :

$$\hat{\mathbf{v}} = \hat{\mathbf{v}}_{oc[1:n]} + \hat{\mathbf{v}}_{1[1:n]} + \hat{R}_c^+ \mathbf{i}^+ + \hat{R}_d^- \mathbf{i}^- \quad (5.3.2b)$$

$$\mathbf{D} \hat{\mathbf{v}}_1 = -\frac{\hat{\mathbf{v}}_{1[1:n]}}{\hat{R}_1 \hat{C}_1} + \frac{\mathbf{i}^+ + \mathbf{i}^-}{\hat{C}_1} \quad (5.3.2c)$$

$$\hat{\mathbf{v}}_{oc} = \hat{\alpha} \boldsymbol{\varsigma}^3 + \hat{\beta} \boldsymbol{\varsigma}^2 + \hat{\gamma} \boldsymbol{\varsigma} + \hat{\delta} \quad (5.3.2d)$$

$$v_{oc-max} = \hat{\alpha} \varsigma_{max}^3 + \hat{\beta} \varsigma_{max}^2 + \hat{\gamma} \varsigma_{max} + \hat{\delta} \quad (5.3.2e)$$

$$v_{oc-min} = \hat{\alpha} \varsigma_{min}^3 + \hat{\beta} \varsigma_{min}^2 + \hat{\gamma} \varsigma_{min} + \hat{\delta} \quad (5.3.2f)$$

$$3\hat{\alpha} \boldsymbol{\varsigma}_{hold}^2 + 2\hat{\beta} \boldsymbol{\varsigma}_{hold} + \hat{\gamma} \geq 0 \quad (5.3.2g)$$

where $\mathbf{x}_2 = \{\hat{\mathbf{v}}, \hat{\mathbf{v}}_{oc}, \hat{\mathbf{v}}_1, \hat{R}_c, \hat{R}_d, \hat{R}_1, \hat{C}_1, \hat{\alpha}, \hat{\beta}, \hat{\gamma}, \hat{\delta}\} \in \mathbb{R}^{3n+12}$ is the set of all decision variables in the parameter estimation, n is the number of samples in the data window, ς_{max} and ς_{min} are the maximum and minimum SoC, v_{oc-max} and v_{oc-min} are the open-circuit-voltages associated with the maximum and minimum SoC, $\boldsymbol{\varsigma}_{hold}$ is a vector of SoC that covers the range from ς_{max} to ς_{min} (this can be the same vector that is used for the open-circuit-voltage holding values discussed in Section 5.3.4) and the differential matrix \mathbf{D} is shown below:

$$\mathbf{D} = \Delta \begin{bmatrix} -1 & 1 & 0 & \cdot & \cdot & 0 \\ 0 & -1 & 1 & 0 & \cdot & \cdot \\ & & \cdot & \cdot & & \\ 0 & & & 0 & -1 & 1 \end{bmatrix}_{n \times (n+1)} \quad (5.3.3)$$

$$\Delta = \begin{bmatrix} \frac{1}{\Delta t_{[1]}} & 0 & \cdot & \cdot & 0 \\ 0 & \frac{1}{\Delta t_{[2]}} & 0 & \cdot & \cdot \\ & \cdot & \cdot & \cdot & 0 \\ & & 0 & 0 & \frac{1}{\Delta t_{[n]}} \end{bmatrix}_{n \times n} \quad (5.3.4)$$

where $\Delta t_{[i]}$ is the sample period, and $\mathbf{\Delta}$ is a square matrix where the diagonal is made up of the reciprocal of the sample period at each time step. The equivalent circuit is modeled in (5.3.2b) and (5.3.2c), the open-circuit-voltage is estimated in (5.3.2d) with constraints on the maximum and minimum open-circuit-voltages in (5.3.2e) and (5.3.2f), respectively. The constraint in (5.3.2g) ensures that the calculated open-circuit-voltage function is monotonically increasing. These problems are solved using pyomo [74,75], and the interior-point solver ipopt [76]. The critical outcome of this optimization problem is the optimal estimated parameter set $\{\hat{C}_{cap}, \hat{\eta}_c, \hat{R}_c, \hat{R}_d, \hat{R}_1, \hat{C}_1, \hat{\alpha}, \hat{\beta}, \hat{\gamma}, \hat{\delta}\}$. These parameters are used to test the accuracy of the candidate model parameters in cross validation.

5.3.3 Accuracy Testing

To evaluate the predictive accuracy of an SoC forecasting model we partition the available operational data record into separate training and testing sets. Both parameter estimation and accuracy testing for an SoC forecasting model require contiguous operational data. Because we assess one day at a time, partial days may not meet the data requirements. This means we are limited to using one full day for parameter estimation and another full day for accuracy testing. To keep validation data as relevant as possible we use the scheme illustrated in Fig. 5.3.

After collecting operational data for two days that meet the data requirements, we first estimate the model parameters for the second day (\mathbf{x}_1 and \mathbf{x}_2) using (5.3.1) and (5.3.2) respectively. We then simulate day one using the updated model, recording the root-mean-squared (RMS) and percent

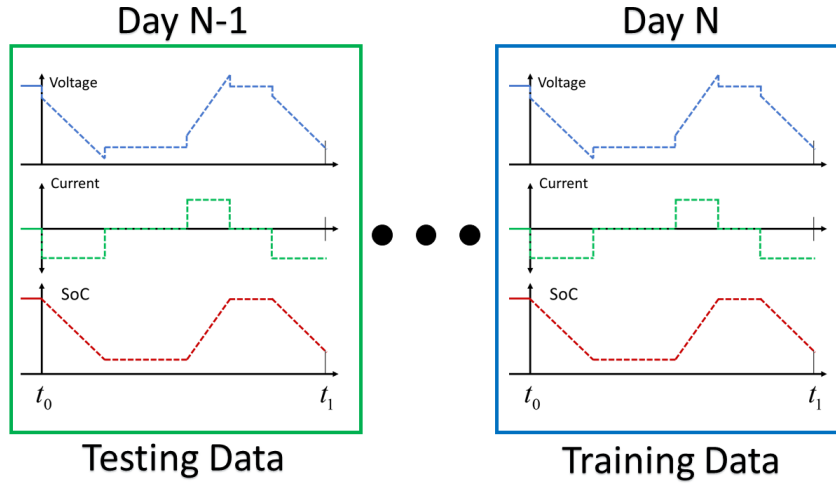


Figure 5.3: One-and-one validation training and testing sets

forecasting error for the battery voltage according to:

$$\varepsilon_{\text{RMS}} = \sqrt{\frac{\sum_{k=1}^n (v_k - \hat{v}_k)^2}{n}} \quad (5.3.5)$$

$$\varepsilon_{\%} = \sum_{k=1}^n \frac{|v_k - \hat{v}_k|}{v_k} \quad (5.3.6)$$

where ε_{RMS} is the RMS forecasting error, and $\varepsilon_{\%}$ is the percent forecasting error.

5.3.4 Model Update

At each new qualifying day, prior model parameters are updated in the diction of the newly estimated parameters and by a magnitude proportional to their accuracy on training data. Accuracy, in this context, is the inverse of percent error as calculated above, and is used as a proxy for the likelihood of the parameter set being correct. The update for the model parameters, not

including the open-circuit-voltage function parameters, is shown below:

$$\Gamma = \min \left\{ \frac{0.05}{\varepsilon_{\%}}, 0.25 \right\} \quad (5.3.7a)$$

$$R_c = (1 - \Gamma)R_c + \Gamma \hat{R}_c \quad (5.3.7b)$$

$$R_d = (1 - \Gamma)R_d + \Gamma \hat{R}_d \quad (5.3.7c)$$

$$R_1 = (1 - \Gamma)R_1 + \Gamma \hat{R}_1 \quad (5.3.7d)$$

$$C_1 = (1 - \Gamma)C_1 + \Gamma \hat{C}_1 \quad (5.3.7e)$$

$$C_{cap} = (1 - \Gamma)C_{cap} + \Gamma \hat{C}_{cap} \quad (5.3.7f)$$

$$\eta_c = (1 - \Gamma)\eta_c + \Gamma \hat{\eta}_c \quad (5.3.7g)$$

where Γ is the learning rate.

The open-circuit-voltage function parameters are updated by first updating a set of holding values for open-circuit-voltage, evenly spaced in the range from ς_{\min} to ς_{\max} . Each point is updated based on the expression below:

$$v_{oc\text{-hold}}(\varsigma) += \frac{\Gamma}{m} \sum_{k=1}^m \mathcal{N}(\varsigma - \varsigma_{\text{hold-}k}) \left(\hat{\alpha}_{\varsigma_{\text{hold-}k}}^3 + \hat{\beta}_{\varsigma_{\text{hold-}k}}^2 + \hat{\gamma}_{\varsigma_{\text{hold-}k}}^3 + \hat{\delta} \right) \quad (5.3.8)$$

where $v_{oc\text{-hold}}(\varsigma)$ is the open-circuit-voltage holding value at ς , $\varsigma_{\text{hold-}k}$ are the states-of-charge at which the open-circuit-voltage holding values are located (iterated by k), $\mathcal{N}(\mu)$ is the probability density of a standard normal distribution at distance from the mean μ . The probability density function is acting as a proxy for the accuracy of the state-of-charge estimate in this update.

Note that parameter values outside of a reasonable range are a sign that the optimization may have found a non-global minimum. The update stage is skipped in these cases and the process waits for the next day of qualifying data.

5.4 Results

The methods discussed above are applied to the operational data of a 2 MW, 3.9 MWh lithium-ion battery system in Sterling, MA USA [176]. The system is split into two sub-batteries which we term batteries 1 and 2 respectively. One year of data were assessed starting on July 13th 2017. The vast majority of this time, the battery is either supplying high-power, low-energy services, or the battery is idle, and hence the data do not meet the requirements for parameter identification. Data from 36 days (roughly 10% of the sample year) meet the requirements and are used to update the model.

5.4.1 Model Learning

The initial parameters are steadily updated to more accurately forecast the battery's SoC and voltage. The EMS model's capacity parameter for each battery are shown in Fig. 5.4 displayed as a function of the number of days that have been processed. For the first ten days or so the learning algorithm corrects for the error in the initial parameter values. This correction also leads to a large increase in the modeling uncertainty. After the first ten days, the capacity only slowly changes, likely as a result of either battery degradation or changes in usage that exhibit different performance.

The initial open-circuit-voltage function is a straight line between a minimum voltage and a maximum voltage. As the model updates, the cubic function representation for open-circuit-voltage begins to reflect a plateau at partial SoC, and high slope regions at both high and low SoC. This trend is illustrated in Fig. 5.5, where the lines get progressively lighter as the model is updated.

These model changes are reflected in improved forecasting accuracy,

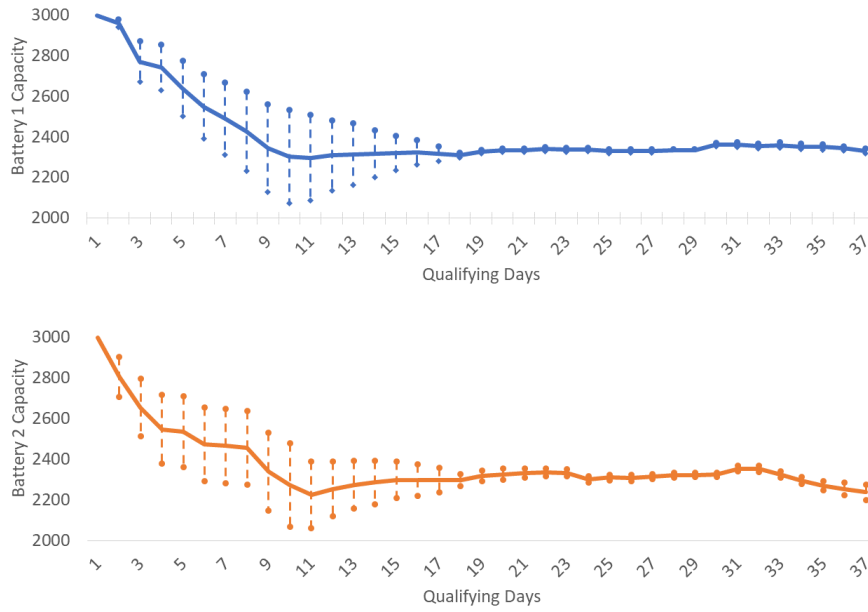


Figure 5.4: Updates to the capacity parameter for Battery 1 (top), Battery 2 (bottom). One standard deviation of the previous ten values is shown by upper and lower bounds.

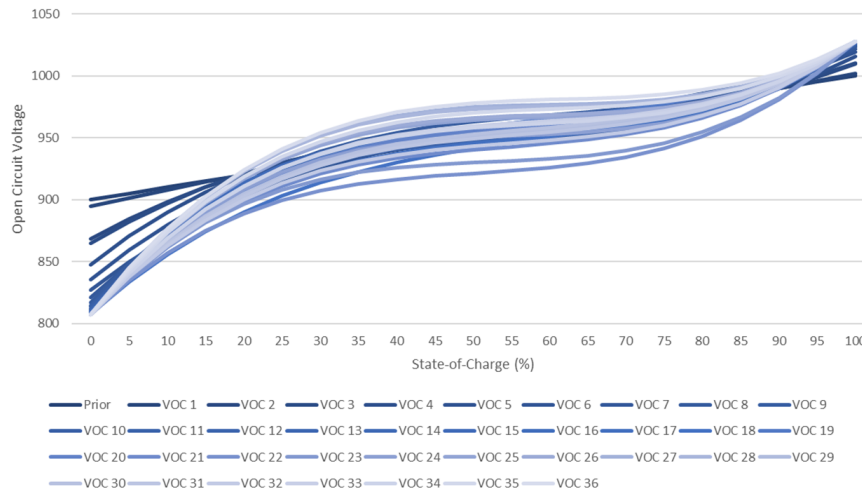


Figure 5.5: Updates to the battery model's open-circuit-voltage function

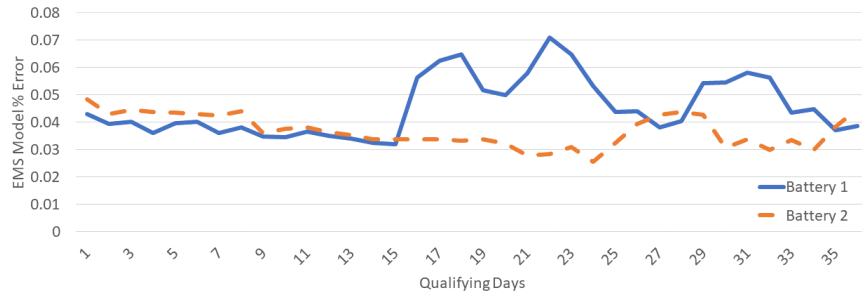


Figure 5.6: EMS model % Error on Baseline Test Data

and improved estimates of model uncertainty. A single day (July 1st, 2018), was used as a baseline day to test the accuracy of each model as the model changes. The % error that each model has when applied to the baseline day is shown in Fig. 5.6. An inconsistent but downward trend can be observed in the modeling error for each battery. The final model parameters, along with the uncertainty of each are listed in Table 5.2.

5.5 Summary

This chapter develops a process for using operational data to steadily improve the accuracy of an EMS model and calculate the modeling uncertainty for use in risk-averse control. The process starts with an initial parameter set, which can be based on manufacturer ratings or rough order of magnitude guesses. This parameter set is significantly smaller than alternative methods. It then takes operational data and filters out days that do not meet certain requirements for salience and quality. Qualifying data are then used to estimate candidate model parameters, whose accuracy is then tested on the most recent qualifying day not used for the estimate. This process improves EMS modeling accuracy, or at least keeps modeling error low, as qualifying data are supplied

Table 5.2: Charge Reservoir Model Final Parameters

Name	Battery 1	σ_1	Battery 2	σ_2	Units
Charge capacity	2330.9	11.550	2237.9	38.005	Ah
Coulombic efficiency	0.920	4.6e-2	0.972	7.0e-2	
Charge resistance	2.71e-2	1.42e-2	3.55e-2	1.55e-2	Ω
Discharge resistance	9.03e-2	6.46e-3	8.71e-2	8.75e-3	Ω
Dynamic element resistance	0.466	0.560	6.11e-2	1.82e-2	Ω
Dynamic element capacitance	18.50	0.648	19.69	0.627	F
Open-circuit-voltage parameter 0	703.2		743.1		
Open-circuit-voltage parameter 1	-1297.3		-1340.2		
Open-circuit-voltage parameter 2	814.3		817.3		
Open-circuit-voltage parameter 3	807.4		807.4		

over time and use. By applying this process, the EMS will always have an up-to-date and accurate model to work with in optimizing charge and discharge. The parameter uncertainty values estimated through this process enable the EMS to hedge its operational decisions against the uncertainty of battery performance. If incorporated into an EMS control system, the proposed process would improve system performance and make the controller more robust to modeling uncertainty.

Chapter 6

Risk-Averse Model Predictive Control Design for Battery Energy Storage Systems

¹ When batteries supply behind-the-meter services such as arbitrage or peak load management, an optimal controller can be designed to minimize the total electric bill. The state constraints of batteries that ensure safety and longevity, such as on voltage or state-of-charge, are represented in the model used to forecast the system's state dynamics. Control model inaccuracy can lead to an optimistic shortfall, where the achievable schedule will be costlier than the schedule derived using the model. To improve control performance and avoid optimistic shortfall, we develop a novel methodology for high performance, risk-averse battery energy storage controller design. Our method is based on two contributions. First, the application of a more accurate, but non-convex, battery system model is enabled by calculating upper and lower bounds on the globally optimal control solution. Second, the battery model

¹D. Rosewater, R. Baldick, and S. Santoso, "Risk-Averse model predictive control design for battery energy storage systems" *IEEE Trans. Smart Grid*, September 2019. DOI: 10.1109/TSG.2019.2946130

The dissertator was the principle investigator for this research including initial model characterization from experimental data, derivation of upper and lower optimization bounds, programming open and closed-loop control simulations for each model, derivation of the risk averse CRM modification, calculation of simulation results, and writing/editing the article itself. Ross Baldick provided invaluable technical guidance on convexity and bounding an optimization problem along with multiple rounds of technical review. Surya Santoso provided editorial guidance and multiple rounds of technical review.

is then modified to consistently underestimate capacity by a statistically selected margin, thereby hedging its control decisions against normal variations in battery system performance. The proposed model predictive controller, developed using this methodology, performs better and is more robust than the state-of-the-art approach, achieving lower bills for energy customers and being less susceptible to optimistic shortfall.

Contributions of this chapter were identified as follows: (*major*) the application of a more accurate, but non-convex, battery system model is enabled by calculating upper and lower bounds on the globally optimal control solution, and (*major*) the battery model is then modified to consistently underestimate capacity by a statistically selected margin, thereby hedging its control decisions against normal variations in battery system performance.

6.1 Introduction

Battery energy storage systems (BESS) are becoming an integral part of a resilient and efficient electrical system. Distributed energy resources (DER) such as BESS are able to support the grid through advanced control and functionality [177]. In addition to responding to local conditions of voltage and frequency, energy management systems can forecast future conditions of variables such as price and load to optimally schedule BESS operation. The time-of-use (ToU) and peak demand charge billing mechanisms are driving the adoption of BESS in commercial applications in many areas [12]. Both TOU and demand charge rate structures incentivize costumers to, in aggregate, reduce system peak demand, allowing a utility to defer or avoid costly capacity upgrades [178]. A primary concern in both applications is how to make control decisions that maximize the value of the BESS to the owner. Optimal

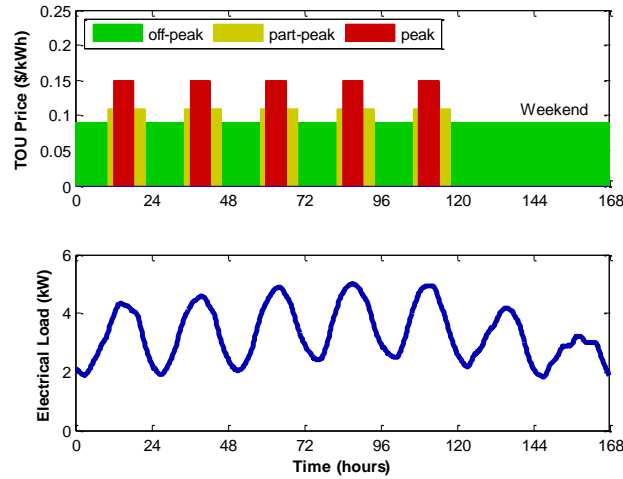


Figure 6.1: Time-of-use price schedule (top) [10], and electrical load (bottom) [4]

control of BESS is a challenging problem due to their complexity and the uncertainty of the underlying chemical processes. The objective of this chapter is to develop and demonstrate a methodology to design an advanced, energy management level controller for BESS. We accomplish this by first reducing model uncertainty, through model improvements, and then by shaping model uncertainty to impose a risk-averse bias on control decisions.

We introduce the following simple case study to provide a basis for an optimal control objective function. Note that this is very similar to the problem statement introduced in Chapter 2.2 except that it is over one week rather than just a day. Consider a hypothetical commercial electrical customer billed for power under both ToU and demand charges. This customer decides to purchase and install a battery to reduce their electrical bill. The energy contract charges 9¢/kWh during off-peak, 11¢/kWh during partial-peak hours, and 15¢/kWh during peak [10] according to the schedule shown in Fig. 6.1

Table 6.1: Summary of Case Study Assumptions

Ownership	Commercial Electrical Customer
Load Profile	From the EPRI test circuit ‘Ckt5’ loadshape summer, scaled to a 5 kW peak [4].
ToU Tariff	9¢/kWh off-peak, 11¢/kWh partial-peak hours (9:00 to 21:00 weekdays), 15¢/kWh peak (12:00 to 18:00 weekdays) [10]
Demand Tariff	$d = \$50/\text{kW}$ based on peak net load [31].
Billing	Weekly, 15 minute time steps.

(top). The utility then charges $\$50/\text{kW}$ service fee (d) according to the peak net load measured during the billing period. For simplicity we will assume a weekly billing period for this example, although it would be more typical to use a monthly or longer period to set the demand charge. This price is consistent with demand charges in specific localities in California and New York [31]. The customer’s week ahead load forecast is shown in Fig. 6.1 (bottom). These load data are adapted from the EPRI test circuit ‘Ckt5’ loadshape, July 20th through 26th, normalized to a 5 kW peak [4]. We will assume that the load and price are known a priori. Without the battery, total bill would be calculated according to (6.1.1).

$$f_{\text{bill}} = \Delta t \mathbf{c}^T \mathbf{l} + \max(\mathbf{l}) d \quad (6.1.1)$$

where f_{bill} is the total electric bill, \mathbf{l} is the n -length vector of load, \mathbf{c} is the n -length vector of ToU prices, d is the service fee in $\$/\text{kW}$ for peak net load measured during the billing period, and \bullet^T denotes a vector’s transpose. Unless otherwise stated, we use a time-step $\Delta t = 15$ minutes (0.25 hours), and $n = 672$ (1 week). With the addition of a BESS that can supply (–), or absorb

(+), power \mathbf{p} , the customer's cost can be modified to (6.1.2).

$$f_{\text{bill}} = \Delta t \mathbf{c}^T (\mathbf{l} + \mathbf{p}) + \max(\mathbf{l} + \mathbf{p}) d \quad (6.1.2)$$

where \mathbf{p} is the battery system power that element wise subtracts from \mathbf{l} when the battery system is discharging. The problem is thus formulated: design a control algorithm to optimally calculate a vector of battery system power \mathbf{p} that minimizes the customer's bill f_{bill} without exceeding the battery's limits, including those on charge rate and depth-of-discharge. Further, the quality of the solution will be judged based both on how much it reduces the customer's bill and how robust it is to uncertainty.

A common approach to controller design is called model predictive control (MPC). MPC is a real-time, state-feedback, optimal control approach that involves solving a finite-horizon online optimization problem at each time step that results in a sequence of future control actions as well as predictions of the future states [24, 179, 180]. In designing MPC, the choice of what model to use can be critical. The simplest BESS model assumes that changes in SoC are proportional to the energy charged or discharged from ac point of interconnection. This approach to optimal control represents the state-of-the-art and has been used for improving wind farm dispatch in Australian electricity markets [181], and achieving distribution feeder dispatchability [182]. Another common approach, based on the need for improved accuracy, is to use a BESS model that assumes that changes in SoC are proportional to the charge, in amp-hours, supplied or absorbed by the battery itself. While it has been used [55, 84, 183], this approach can be difficult because the feasible subspace it defines is fundamentally non-convex. Historically, the only way to apply the more accurate model to calculate optimal control schedules was to either

approximate the model using pseudospectral methods [55], or to use dynamic programming [84, 183]. Further, given the precision of this type of model, the performance of optimal controllers that rely on it can be sensitive to variations in battery performance.

This chapter makes two fundamental contributions to the state-of-the-art: 1) formulation of an optimal controller for a residential lithium-ion battery system, based on the more accurate charge reservoir model (Section 6.3) with upper and lower bounds to check the viability of solutions found through gradient based methods (Section 6.5), and 2) a method to modify the controller to be risk-averse to variations in battery performance (Section 6.6). In Section 6.7 we demonstrate the improved controller performance, due to using the more accurate model, and demonstrate how the risk-averse modification makes it more robust to model uncertainty. Together, these contributions make up an advanced methodology for designing BESS controllers that perform better and are more robust than those designed through traditional methods. Section 6.8 summarizes the chapter with a summary of the results and a discussion of the broad applicability of the proposed control design approach.

6.2 Energy Reservoir Model

Energy Reservoir Model (ERM), first introduced in Chapter 2, refers to a class of models that calculates SoC as a linear function of energy into and out of the BESS. The ERM is widely used in battery energy storage control problems [15, 43, 53, 181, 182] and has the advantage of being linear in charge and discharge power. This allows for convex, and therefore computationally efficient, formulations of the optimal control problem. The ERM formulation used here is shown in (6.2.1). Definitions for parameters are given in Table

Table 6.2: Energy Reservoir Model Parameters

Name	Symbol	Value
Energy Capacity*	Q_{cap}	5.944 kWh
Energy Efficiency*	η_e	61.7%
Maximum Power Discharge	p_{max}	7 kW
Maximum Power Charge	p_{min}	7 kW
Maximum SoC	\mathbf{s}_{max}	95%
Minimum SoC	\mathbf{s}_{min}	20%
Regularization Weight	Π_1	0.001 \$/kW ²

* derived from experimental analysis on a residential lithium-ion battery system

6.2.

$$\min_{\mathbf{x}_e \in \mathbb{R}^{3n+2}} \Delta t \mathbf{c}^T (\mathbf{l} + \mathbf{p}^+ + \mathbf{p}^-) + \tau d + \Pi_1 \|\mathbf{p}^+ + \mathbf{p}^-\|_2^2 \quad (6.2.1a)$$

$$\text{subject to: } Q_{\text{cap}} \mathbf{D} \boldsymbol{\varsigma} = \eta_e \mathbf{p}^+ + \mathbf{p}^-$$

$$\boldsymbol{\varsigma}_{[1]} = \varsigma_0 \quad (6.2.1b)$$

$$\boldsymbol{\varsigma}_{[1]} = \boldsymbol{\varsigma}_{[n]} \quad (6.2.1c)$$

$$\mathbf{0} \leq \mathbf{p}^+ \leq p_{\text{max}} \mathbf{1} \quad (6.2.1d)$$

$$p_{\text{min}} \mathbf{1} \leq \mathbf{p}^- \leq \mathbf{0} \quad (6.2.1e)$$

$$\boldsymbol{\varsigma}_{\text{min}} \mathbf{1} \leq \boldsymbol{\varsigma} \leq \boldsymbol{\varsigma}_{\text{max}} \mathbf{1} \quad (6.2.1f)$$

$$\mathbf{l} + \mathbf{p}^+ + \mathbf{p}^- \leq \tau \mathbf{1} \quad (6.2.1g)$$

where $\mathbf{x}_e = \{\mathbf{p}^+, \mathbf{p}^-, \boldsymbol{\varsigma}, \tau\} \in \mathbb{R}^{3n+2}$, $\mathbf{p}^+ \in \mathbb{R}_+^n$ is the ac electrical power provided to charge battery system, $\mathbf{p}^- \in \mathbb{R}_-^n$ is the ac electrical power discharged from the battery system, $\boldsymbol{\varsigma} \in \mathbb{R}^{n+1}$ is the battery SoC, $\tau \in \mathbb{R}$ is the peak demand

power and the differential matrix \mathbf{D} is shown in (6.2.2).

$$\mathbf{D} = \frac{1}{\Delta t} \begin{bmatrix} -1 & 1 & 0 & \cdot & \cdot & 0 \\ 0 & -1 & 1 & 0 & \cdot & \cdot \\ & & \cdot & \cdot & & \\ & & & \cdot & \cdot & \\ 0 & & & 0 & -1 & 1 \end{bmatrix}_{n \times (n+1)} \quad (6.2.2)$$

An ℓ_2 norm regularization is applied in (6.2.1a) and scaled by the constant Π_1 to even out peak battery power when it is not needed. The constraint (6.2.1b) ensures that control decisions are made based on the current estimated SoC (ς_0). The constraint (6.2.1c) represents the intuitive assumption that the BESS will continue to operate after the end of the current control horizon and that the next period will be similar to this one. While not necessary in closed-loop implementation, (6.2.1c) makes simulation results easier to interpret and compare. The application of these constraints is discussed in more detail in Chapter 2.

6.3 Charge Reservoir Model

Charge Reservoir Model (CRM), first introduced in Chapter 2, refers to a class of models that calculates SoC as a function of charge (current integrated over time) into and out of the battery itself. The CRM is also used in battery energy storage control problems and has the advantage of being more accurate over a longer time horizon or over larger range of SoC [55]. The disadvantage of the CRM is that the subspace of feasible solutions is fundamentally non-convex. Therefore, it is more computationally complex and difficult integrate into an on-board controller [84]. The CRM formulation used here is shown in (6.3.1). The parameters for this model are listed in Table 6.3.

$$\min_{\mathbf{x}_c \in \mathbb{R}^{8n+3}} \Delta t \mathbf{c}^T (\mathbf{l} + \mathbf{p}) + \tau d + \Pi_1 \|\mathbf{p}\|_2^2 + \Pi_2 \|\mathbf{v}_s\|_1 \quad (6.3.1a)$$

$$\text{subject to: } \phi_0 \mathbf{p}^2 + \phi_1 \mathbf{p} + \phi_2 \geq \mathbf{p}_{\text{dc}} \quad (6.3.1b)$$

$$\mathbf{p}_{\text{dc}} = (\mathbf{i}_{\text{bat}}^+ + \mathbf{i}_{\text{bat}}^-) \mathbf{v}_{\text{bat}} \quad (6.3.1c)$$

$$\mathbf{v}_{\text{bat}} = \mathbf{v}_{\text{oc}[1:n]} + R_0 (\mathbf{i}_{\text{bat}}^+ + \mathbf{i}_{\text{bat}}^-) + \mathbf{v}_s \quad (6.3.1d)$$

$$\mathbf{v}_{\text{oc}} = \alpha \boldsymbol{\varsigma}^3 + \beta \boldsymbol{\varsigma}^2 + \gamma \boldsymbol{\varsigma} + \delta \quad (6.3.1e)$$

$$C_{\text{cap}} \mathbf{D} \boldsymbol{\varsigma} = \eta_c \mathbf{i}_{\text{bat}}^+ + \mathbf{i}_{\text{bat}}^- \quad (6.3.1f)$$

$$\boldsymbol{\varsigma}_1 = \boldsymbol{\varsigma}_0 \quad (6.3.1g)$$

$$\boldsymbol{\varsigma}_1 = \boldsymbol{\varsigma}_{n+1} \quad (6.3.1h)$$

$$p_{\min}[\mathbf{1}] \leq \mathbf{p} \leq p_{\max}[\mathbf{1}] \quad (6.3.1i)$$

$$\varsigma_{\min}[\mathbf{1}] \leq \boldsymbol{\varsigma} \leq \varsigma_{\max}[\mathbf{1}] \quad (6.3.1j)$$

$$v_{\min}[\mathbf{1}] \leq \mathbf{v}_{\text{bat}} \leq v_{\max}[\mathbf{1}] \quad (6.3.1k)$$

$$[\mathbf{0}] \leq \mathbf{i}_{\text{bat}}^+ \leq i_{\max}[\mathbf{1}] \quad (6.3.1l)$$

$$i_{\min}[\mathbf{1}] \leq \mathbf{i}_{\text{bat}}^- \leq [\mathbf{0}] \quad (6.3.1m)$$

$$\mathbf{l} + \mathbf{p} \leq \tau [\mathbf{1}] \quad (6.3.1n)$$

where $\mathbf{x}_c = \{\mathbf{p}, \mathbf{p}_{\text{dc}}, \mathbf{i}_{\text{bat}}^+, \mathbf{i}_{\text{bat}}^-, \mathbf{v}_{\text{bat}}, \mathbf{v}_s, \mathbf{v}_{\text{oc}}, \boldsymbol{\varsigma}, \tau\} \in \mathbb{R}^{8n+3}$, $\mathbf{p}_{\text{dc}} \in \mathbb{R}^n$ is the dc electrical power provided to battery, $\mathbf{v}_{\text{bat}} \in \mathbb{R}^n$ is the battery terminal voltage, $\mathbf{v}_s \in \mathbb{R}_+^n$ is the slack voltage used in calculation of an upper bound, $\mathbf{v}_{\text{oc}} \in \mathbb{R}^{n+1}$ is the battery open-circuit voltage, and $\tau \in \mathbb{R}$ is the peak power demand. The CRM objective includes a ℓ_2 norm power regularization and an ℓ_1 norm slack voltage cost, weighted by the constant Π_2 . The weight Π_2 is chosen, using a simple trial and error sweep, to be the smallest value that is still large enough to drive the slack voltage to zero under normal operation. The CRM includes constraints on inverter conversion efficiency (6.3.1b), Ohm's law

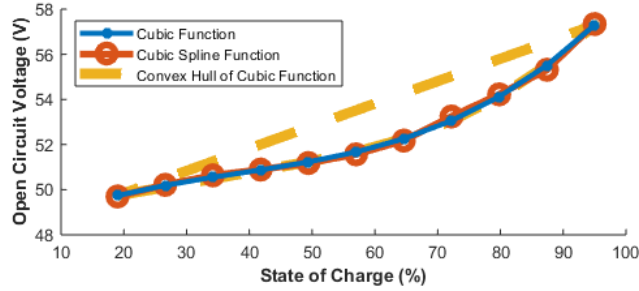


Figure 6.2: Open-circuit voltage constraint satisfying (6.3.1e)

relating dc power, voltage and current (6.3.1c), the battery equivalent circuit model (6.3.1d), and the open-circuit voltage curve (6.3.1e). Note that the inverter conversion efficiency (6.3.1b) is a convex inequality that collapses to equality as long as energy prices in the objective are positive. This model uses the big cell method discussed in [81]. These additional parameters and constraints allow the CRM to more accurately represent the physical dynamics of battery systems.

6.4 Extended CRM for Simulation

To perform a pseudo-empirical analysis of the optimal schedules calculated from each model we simulate how the battery system would respond to each control signal using an extended CRM that incorporates additional constraints and parameters to improve its accuracy. The simulation model uses slightly different functions and parameters, enabling an analysis of the effects of model and parameter uncertainty on controller performance. The modified constraints are shown in (6.4.1). The parameters for these modified constraints are shown in Table 6.4.

Table 6.3: Charge Reservoir Model Parameters

Name	Symbol	Mean	σ	
Charge Capacity*	C_{cap}	135.2 Ah	2.6 Ah	
Coulombic Efficiency*	η_c	94.6%	0.74%	
Inverter Efficiency Coefficient*	ϕ_0	-4.7865e-07		
Inverter Efficiency Coefficient*	ϕ_1	0.99107		
Inverter Efficiency Coefficient*	ϕ_2	-0.0721		
Battery Internal Resistance*	R_0	15.35 m Ω	0.34 m Ω	
Maximum Power Discharge	p_{max}	7 kW		
Maximum Power Charge	p_{min}	7 kW		
Maximum SoC	$\mathfrak{s}_{\text{max}}$	95%		
Minimum SoC	$\mathfrak{s}_{\text{min}}$	20%		
Maximum Battery Voltage	v_{max}	58.8 V		
Minimum Battery Voltage	v_{min}	46.2 V		
Maximum Current Discharge	p_{max}	150 A		
Maximum Current Charge	p_{min}	150 A		
Regularization Weight	Π_1	0.001 \$/kW ²		
Slack Voltage Weight	Π_2	0.035 \$/V		
Cubic Polynomial Fit*	α	β	γ	δ
$0.2 \leq \mathfrak{s} \leq 0.95$	22.884	-26.339	14.357	47.806

* derived from experimental analysis on a residential lithium-ion battery system

$$\mathbf{v}_{\text{bat}} = \mathbf{v}_{\text{oc}} + \mathbf{v}_1 + R_0(\mathbf{i}_{\text{bat}}^+ + \mathbf{i}_{\text{bat}}^-) \quad (6.4.1a)$$

$$\mathbf{D}\mathbf{v}_1 = \frac{1}{R_1 C_1} \mathbf{v}_1 + \frac{1}{C_1}(\mathbf{i}_{\text{bat}}^+ + \mathbf{i}_{\text{bat}}^-) \quad (6.4.1b)$$

$$\begin{aligned} \mathbf{v}_{\text{oc}} = & \alpha(\boldsymbol{\varsigma}) (\boldsymbol{\varsigma} - \zeta(\boldsymbol{\varsigma}))^3 \\ & - \beta(\boldsymbol{\varsigma}) (\boldsymbol{\varsigma} - \zeta(\boldsymbol{\varsigma}))^2 \\ & - \gamma(\boldsymbol{\varsigma}) (\boldsymbol{\varsigma} - \zeta(\boldsymbol{\varsigma})) - \delta(\boldsymbol{\varsigma}) \end{aligned} \quad (6.4.1c)$$

where $\mathbf{v}_1 \in \mathbb{R}^n$ is the dynamic voltage component of the battery's terminal voltage, $\zeta : [0, 1] \mapsto [0, 1]$ is a piecewise constant function whose value is equal to the start of each SoC range when passed values within the range. For example, $\zeta(0.22) = 0.19$, and $\zeta(0.32) = 0.263$. This is a common approach to implementing cubic-splines that keeps coefficient magnitudes relatively low. The extended CRM uses (6.3.1b), (6.3.1c), and (6.3.1f) through (6.3.1n) from base model. Constraint (6.3.1d) is modified to (6.4.1a) and the additional constraint (6.4.1b) is added to represent the dynamic response of battery voltage to changes in current. Note that the slack voltage is not needed this model as it is only used for simulation. Constraint (6.3.1e) is then modified to (6.4.1c) to more closely approximate the relationship between SoC and open-circuit voltage with a piecewise cubic-spline fit, as has been shown to be highly accurate [61].

The simulation timestep is 1 second, meaning that it is executed 900 times between controller time steps (with $\Delta t = 15$ minutes). The extended CRM is implemented in simulation using the Battery-Inverter fleet model discussed in [184]. The resulting schedules are distinguished by the tags 'calculated', which stands for the optimal schedules calculated using the ERM or CRM, and 'achieved', which stands for the results of simulating the calculated

Table 6.4: Additional Extended CRM Parameters

	Symbol	Value		
Dynamic Resistance*	R_1	0.491 Ω		
Dynamic Capacitance*	C_1	1.019 F		
Cubic Spline Fit*	α	β	γ	δ
$0.19 \leq \varsigma \leq 0.263$	-59.303	5.4337	6.6949	49.7
$0.263 \leq \varsigma \leq 0.340$	-59.303	-7.6235	6.5342	50.197
$0.340 \leq \varsigma \leq 0.416$	124.05	-21.32	4.306	50.628
$0.416 \leq \varsigma \leq 0.492$	8.2153	6.7098	3.2056	50.884
$0.492 \leq \varsigma \leq 0.568$	3.2897	8.5874	4.371	51.171
$0.568 \leq \varsigma \leq 0.643$	242.75	9.3355	5.7297	51.553
$0.643 \leq \varsigma \leq 0.720$	-381.66	64.069	11.247	52.14
$0.720 \leq \varsigma \leq 0.795$	94.732	-24.414	14.311	53.215
$0.795 \leq \varsigma \leq 0.869$	357.11	-3.0923	12.248	54.192
$0.869 \leq \varsigma \leq 0.95$	357.11	75.96	17.625	55.222

* derived from experimental analysis on a residential lithium-ion battery system

schedule using the extended CRM. The discrepancy between ‘calculated’ and ‘achieved’ schedules is a result of inaccurate parameters and unrepresented battery system characteristics in the ERM and CRM models.

6.5 Bounding the Global Minimum

The nonlinear CRM optimization problem shown in (6.3.1) is non-convex. Further, it can be shown that the Lagrangian of this problem is not pseudoconvex as defined in [185]. If it had either of these properties then we would know that any minimum found would be in the set of global minima but as it is, we cannot make this guarantee. Because of this some argue that gradient based methods such as Newton-Raphson are not viable for CRM op-

timization due to local minima in the solution space [183]; however, we find this not to be the case. Our contribution to the state-of-the-art is to bound the global minimum of this problem such that if we find a local minimum inside this range, we can be confident that it is, or is close to, the globally optimal solution. An upper bound to a minimization problem can be found by restricting the feasible set (adding additional constraints) while a lower bound can be calculated by expanding the feasible set (relaxing or removing constraints) [186].

To calculate a convex lower bound we relax the non-convex constraints to their convex hulls. First, the constraint (6.3.1b) is modified to include positive and negative dc power (6.5.1a). We then relax the ohm's power law constraint (6.3.1c) to a convex space bounded by eight affine surfaces as shown in Fig. 6.3 and represented in (6.5.1b) and (6.5.1c). To do this while maintaining feasibility we split the dc power into separate positive and negative decision variables. Finally, we relax the open-circuit-voltage constraint (6.3.1e) to the convex hull shown in Fig. 6.2 and represented in (6.5.1d). The resulting convex problem in (6.5.1) provides a lower bound on the global minimum of (6.3.1).

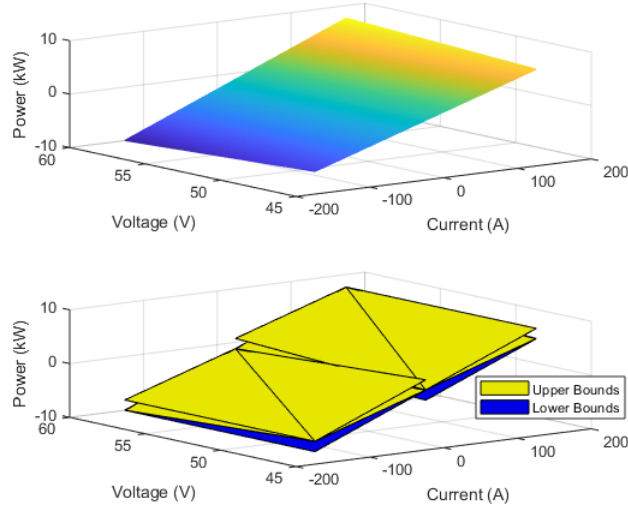


Figure 6.3: Convex Relaxation of Ohms Power Law (6.3.1c), split between positive and negative current

$$\begin{aligned}
 & \min_{\mathbf{x}_c \in \mathbb{R}^{8n+3}} \Delta t \mathbf{c}^T (\mathbf{1} + \mathbf{p}) + \tau d + \Pi_1 \|\mathbf{p}\|_2^2 + \Pi_2 \|\mathbf{v}_s\|_1 \\
 & \mathbf{p}_{\text{dc}}^+ \in \mathbb{R}_+^n \\
 & \mathbf{p}_{\text{dc}}^- \in \mathbb{R}_-^n
 \end{aligned}$$

subject to: $\dot{\cdot}$ (6.3.1d) and (6.3.1f) through (6.3.1n) unchanged

$$\text{relaxing (6.3.1b)} \quad \phi_0 \mathbf{p}^2 + \phi_1 \mathbf{p} + \phi_2 \geq \mathbf{p}_{\text{dc}}^+ + \mathbf{p}_{\text{dc}}^- \quad (6.5.1a)$$

$$\text{relaxing (6.3.1c)} \quad \mathbf{A}_1 [\mathbf{i}_{\text{bat}}^+, \mathbf{v}_{\text{bat}}, \mathbf{p}_{\text{dc}}^+]^T \leq \mathbf{b}_1 [\mathbf{1}]_{1 \times n} \quad (6.5.1b)$$

$$\mathbf{A}_2 [\mathbf{i}_{\text{bat}}^-, \mathbf{v}_{\text{bat}}, \mathbf{p}_{\text{dc}}^-]^T \leq \mathbf{b}_2 [\mathbf{1}]_{1 \times n} \quad (6.5.1c)$$

$$\text{relaxing (6.3.1e)} \quad \mathbf{A}_3 [\boldsymbol{\varsigma}, \mathbf{v}_{\text{oc}}]^T \leq \mathbf{b}_3 [\mathbf{1}]_{1 \times n} \quad (6.5.1d)$$

where \mathbf{p}_{dc}^+ and \mathbf{p}_{dc}^- are the charge and discharge dc powers respectively.

To calculate an upper bound we restrict battery terminal voltage to a constant ($\mathbf{v}_{\text{bat}} = v_{\text{ocmin}}$). The slack voltage allows the battery equivalent circuit

(6.5.2b) to become non-binding, thereby making the fixed voltage restriction feasible. To efficiently calculate the global minimum of the upper bound we use a piecewise linear approximation of the open circuit-voltage function, as shown in (6.5.2c) through (6.5.2j). This approximation makes the upper bound a mixed-integer nonlinear program (MINLP) with a convex objective and convex constraint functions, for which there exist effective exact solution algorithms [186]. Given that the approximation embodied in the piecewise linearization is fairly accurate, we expect that the resulting solution will be a useful upper bound to the original, non-convex problem.

$$\begin{aligned}
& \min && \Delta t \mathbf{c}^T (\mathbf{1} + \mathbf{p}) + \tau d + \Pi_1 \|\mathbf{p}\|_2^2 + \Pi_2 \|\mathbf{v}_s\|_1 \\
& \mathbf{x}_c \in \mathbb{R}^{8n+3} \\
& \boldsymbol{\nu}_{1-5} \in \mathbb{R}_+^{n+1} \\
& \boldsymbol{\varsigma}_{1-5} \in \mathbb{R}_+^{n+1} \\
& \mathbf{w}_{1-5} \in \{0, 1\}^{n+1}
\end{aligned}$$

subject to: \vdots (6.3.1b) and (6.3.1f) through (6.3.1n) unchanged

$$\text{restricting (6.3.1c) } \mathbf{p}_{\text{dc}} = (\mathbf{i}_{\text{bat}}^+ + \mathbf{i}_{\text{bat}}^-) v_{\text{ocmin}} \quad (6.5.2a)$$

$$\text{restricting (6.3.1d) } v_{\text{ocmin}}[\mathbf{1}] = \mathbf{v}_{\text{oc}[1:n]} + R_0(\mathbf{i}_{\text{bat}}^+ + \mathbf{i}_{\text{bat}}^-) + \mathbf{v}_s \quad (6.5.2b)$$

$$\text{approx. (6.3.1e) } \mathbf{v}_{\text{oc}} = v_{\text{ocmin}}[\mathbf{1}] + \boldsymbol{\nu}_1 + \boldsymbol{\nu}_2 + \boldsymbol{\nu}_3 + \boldsymbol{\nu}_4 + \boldsymbol{\nu}_5 \quad (6.5.2c)$$

$$\boldsymbol{\varsigma} = \boldsymbol{\varsigma}_{\text{min}}[\mathbf{1}] + \boldsymbol{\varsigma}_1 + \boldsymbol{\varsigma}_2 + \boldsymbol{\varsigma}_3 + \boldsymbol{\varsigma}_4 + \boldsymbol{\varsigma}_5 \quad (6.5.2d)$$

$$[\boldsymbol{\nu}_1, \boldsymbol{\nu}_2, \boldsymbol{\nu}_3, \boldsymbol{\nu}_4, \boldsymbol{\nu}_5]^T = \mathbf{A}_4[\boldsymbol{\varsigma}_1, \boldsymbol{\varsigma}_2, \boldsymbol{\varsigma}_3, \boldsymbol{\varsigma}_4, \boldsymbol{\varsigma}_5]^T \quad (6.5.2e)$$

$$\varsigma_{\text{seg}} \mathbf{w}_1 \leq \varsigma_1 \leq \varsigma_{\text{seg}} \quad (6.5.2f)$$

$$\varsigma_{\text{seg}} \mathbf{w}_2 \leq \varsigma_2 \leq \varsigma_{\text{seg}} \mathbf{w}_1 \quad (6.5.2g)$$

$$\varsigma_{\text{seg}} \mathbf{w}_3 \leq \varsigma_3 \leq \varsigma_{\text{seg}} \mathbf{w}_2 \quad (6.5.2h)$$

$$\varsigma_{\text{seg}} \mathbf{w}_4 \leq \varsigma_4 \leq \varsigma_{\text{seg}} \mathbf{w}_3 \quad (6.5.2i)$$

$$0 \leq \varsigma_5 \leq \varsigma_{\text{seg}} \mathbf{w}_4 \quad (6.5.2j)$$

where $\boldsymbol{\nu}_1, \boldsymbol{\nu}_2, \boldsymbol{\nu}_3, \boldsymbol{\nu}_4, \boldsymbol{\nu}_5 \in \mathbb{R}_+^n$ are the linear segment voltages, $\varsigma_1, \varsigma_2, \varsigma_3, \varsigma_4, \varsigma_5 \in \mathbb{R}_+^n$ are the linear segment states-of-charge, $\mathbf{w}_1, \mathbf{w}_2, \mathbf{w}_3, \mathbf{w}_4 \in \{0, 1\}^n$ are Boolean variables that ensure that the segments maintain correct ordering.

With these bounds and properties established, we can use an off-the-shelf primal-dual, interior-point method to solve the optimal control problem using the CRM. The freely downloadable modeling language Pyomo [74, 75] and nonlinear solver Ipopt [76] are used to implement this algorithm efficiently. The nonlinear solver Gurobi is used for calculation of the upper bound as it is able to efficiently work with integer variables [187].

6.6 Reducing Control Sensitivity to Uncertainty

Parameters such as capacity are functions of many physical mechanisms we do not consider in the model. To consider this uncertainty, we break capacity² into its mean value and a random component as shown in (6.6.1).

$$(C_{\text{cap}} + \tilde{C}_{\text{cap}})D\boldsymbol{\varsigma} = \eta_c \mathbf{i}_{\text{bat}}^+ + \mathbf{i}_{\text{bat}}^- \quad (6.6.1)$$

where $\tilde{C}_{\text{cap}} \sim \mathcal{N}(\mu = 0, \sigma = 2.6\text{Ah})$ is the random component of the battery's capacity, assumed to be a zero-mean, normal distribution.

²The uncertainty of coulombic efficiency and internal resistance parameters are also listed in Table 6.3. The effects of these uncertainties is negligible for the example application when compared to the capacity.

Table 6.5: Convex Relaxation and Approximation Parameters

Ohm's Power Law Relaxation

$$\mathbf{A}_1 = \begin{bmatrix} 0.0462 & 0.15 & -1.0 \\ 0.0588 & 0 & -1.0 \\ 0.0462 & 0 & -1.0 \\ 0.0588 & 0.15 & -1.0 \end{bmatrix}$$

$$\mathbf{b}_1 = \begin{bmatrix} 6.93 \\ 0 \\ 0 \\ 8.82 \end{bmatrix}$$

$$\mathbf{A}_2 = \begin{bmatrix} 0.0462 & 0 & -1.0 \\ 0.0588 & -0.15 & -1.0 \\ 0.0462 & -0.15 & -1.0 \\ 0.0588 & 0 & -1.0 \end{bmatrix}$$

$$\mathbf{b}_2 = \begin{bmatrix} 0 \\ -8.82 \\ -6.93 \\ 0 \end{bmatrix}$$

Open Circuit Voltage Relaxation

$$\mathbf{A}_3 = \begin{bmatrix} 4.900 & -1.0 \\ 5.796 & -1.0 \\ 7.741 & -1.0 \\ 10.479 & -1.0 \\ 14.009 & -1.0 \\ 18.333 & -1.0 \\ 23.450 & -1.0 \\ -9.941 & 1.0 \end{bmatrix}$$

$$\mathbf{b}_3 = \begin{bmatrix} -48.809 \\ -48.366 \\ -47.258 \\ -45.489 \\ -42.940 \\ -39.490 \\ -35.0178 \\ 47.851 \end{bmatrix}$$

**Open Circuit Voltage Piecewise
Linear Approximation**

$$\mathbf{A}_4 = [5.3350 \quad 4.4656 \quad 6.7686 \quad 12.2438 \quad 20.8913]$$

$$v_{ocmin} = 49.74 \text{ V}$$

$$\varsigma_{min} = 19\%$$

$$\varsigma_{seg} = 15.2\%$$

Price arbitrage has symmetric risk, meaning that overestimating capacity is just as bad as underestimating capacity. Peak demand charge management, in contrast, has asymmetric risk, in that the down-side of overestimating capacity is larger in magnitude than the down-side of underestimating capacity. Because of asymmetric risk, we expect a risk-neutral controller to have a skewed performance distribution as shown in Fig. 6.4. We modify the proposed controller to consider asymmetric risk. The value-at-risk constraint needed for this modification is shown in (6.6.2).

$$\hat{C}_{\text{cap}} = \min\{C_{\text{cap}} \in \mathbb{R} \mid \mathbb{P}(\tilde{C}_{\text{cap}} \leq C_{\text{cap}}) \geq 0.13\%\} \quad (6.6.2)$$

where \hat{C}_{cap} is the value-at-risk capacity, and \mathbb{P} is the probability function. Because of our assumption that the capacity has a normal distribution, calculating the value-at-risk is trivial in that we can use lookup tables to determine how many standard deviations from the mean will yield a risk of 0.13% (-3σ from the table supplied in [188]). By using $\hat{C}_{\text{cap}} = 135.2 \text{ Ah} - 3 \times 2.6 \text{ Ah} = 127.4 \text{ Ah}$, we design the controller to consistently underestimate the battery's capacity, thereby making its control decisions robust to fluctuations in capacity. Due to this modification, we expect that a risk-averse controller will have performance distribution with reduced downside risk, in exchange for slightly reduced average performance, as illustrated in Fig. 6.4.

As described above some services have asymmetric risk of overestimating or underestimating capacity. The degree of this asymmetry corresponds to the potential advantage of risk-averse control. For example: backup power for a critical load has an extreme imbalance in cost between not having sufficient energy and having more than enough energy. Because of this, the intuitive risk-averse control solution is to maintain full charge at all times.

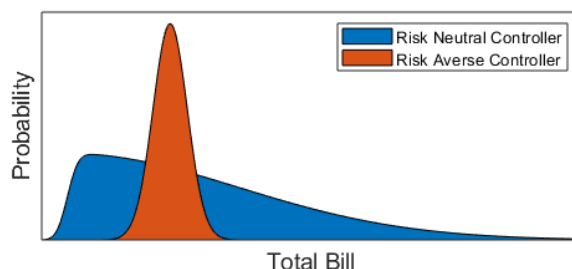


Figure 6.4: Notional examples of risk-neutral and risk-averse control bill savings probability density functions

Additionally, the accuracy and precision of the BESS model is important to consider as illustrated in Fig. 6.5. Model accuracy refers to how close the mean estimated capacity parameter is to the capacity expressed during the control horizon (in our case, the extended CRM used in simulation). Precision is a measure of how consistent the BESS capacity is in this application. If the model consistently underestimates or overestimates available energy, low accuracy with high precision, then the marginal benefit of risk-averse control will be negligible. If the model has high accuracy and precision then there is only a small margin for improvement. For controllers with low accuracy and precision, performance consistency comes at a large cost in average performance. It is the case where the BESS model has high accuracy, and relatively low precision where risk-averse control is most useful because it is able to hedge decisions for uncertainties in performance. Such controllers can achieve consistency with only a small sacrifice in average performance.

To assess the sensitivity of the proposed controller to off normal circumstances we use the optimistic shortfall. Optimistic shortfall is the difference between expected controller performance and achieved controller performance, which in our case is the total bill achieved minus the calculated optimal bill. In

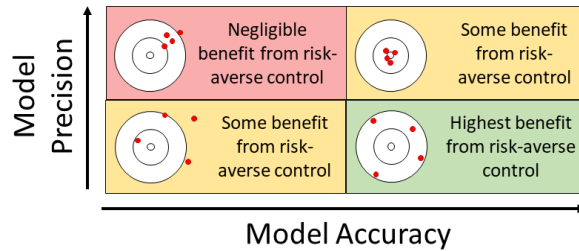


Figure 6.5: Relative benefits of risk-averse control based on model accuracy/precision, given an asymmetric risk application

Fig. 6.4, the risk-neutral controller would have significant optimistic shortfall in the ‘extreme case’ ($\tilde{C}_{\text{cap}} = -3\sigma$), whereas the risk-averse controller would have low optimistic shortfall throughout the normal range of battery capacity.

6.7 Results

This section explains the results of simulated control action calculated using the ERM, CRM, and Risk-Averse (RA) CRM as discussed above, applied to the extended CRM model of the BESS as a pseudo-empirical analysis of controller performance and sensitivity to parameter uncertainty. Open-loop control is assessed first to provide a baseline controller performance and a clear picture of the effect that uncertainty has on control. The closed-loop, model predictive controllers are then assessed for their ability to reduce the effects of uncertainty under normal operations and reduce optimistic shortfall. The effects of extreme case parameters are then analyzed to illustrate that risk-averse control design is needed to make the controller robust to the normal variations in system performance. Last, the performance of the proposed risk-averse controller is analyzed. A summary of the customer bill, % savings, and optimistic shortfall under each simulation scenario is shown in Table 6.6.

Table 6.6: Summary of Results from Simulated Control Scenarios

Controller Scenario	Scenario	Sim-Model*	Total Bill	% Savings	Optimistic Shortfall**
Baseline		–	\$310.88	–	
ERM OL	Cal	–	\$274.91	11.6%	–
ERM OL	Ach	mean	\$273.93	11.9%	-\$0.98
ERM CL	Ach	mean	\$273.56	12.0%	-\$1.35
ERM CL	Ach	extreme	\$273.69	12.0%	-\$1.22
–upper bound		–	\$272.72✓		
CRM OL	Cal	–	\$269.55	13.3%	–
–lower bound		–	\$228.89✓		
CRM OL	Ach	mean	\$274.98	11.5%	\$5.43
CRM CL	Ach	mean	\$269.55	13.3%	\$0.00
CRM CL	Ach	extreme	\$292.53	5.9%	\$22.98
–upper bound		–	\$274.21✓		
RA CRM OL	Cal	–	\$271.22	12.8%	–
–lower bound		–	\$235.35✓		
RA CRM OL	Ach	mean	\$271.17	12.8%	-\$0.05
RA CRM CL	Ach	mean	\$271.08	12.8%	-\$0.14
RA CRM CL	Ach	extreme	\$271.21	12.8%	-\$0.01

✓ denotes that the solution to the non-convex problem satisfies the bound

* The extended CRM is used to simulate the BESS being controlled. It's parameters are selected to represent average behavior 'mean', or 'extreme case' lower than normal available energy as described in Section 6.6

** Optimistic Shortfall compares the bill achieved by applying control action to the simulated BESS to the open-loop calculated bill from each controller
 Cal - calculated, Ach - achieved, OL - open-loop, CL - closed-loop, RA - risk-averse

6.7.1 Open-Loop Control

The optimal ‘calculated’ schedules, along with the ‘achieved’ schedules, for the customer using the ERM and CRM in open-loop are shown in Fig. 6.6. The resulting net load curves for their control schedules are shown in Fig. 6.7 and 6.8. While the ERM is clearly more computationally efficient than the CRM, optimal schedules can be calculated using either model in just a few seconds on a mid-range laptop (hardware used for this study: i7-7600U CPU at 2.8 GHz) meaning either approach could be used for on-board control.

For the customer introduced in the introduction to this chapter, the baseline cost of electrical service is \$311 (\$61 energy, \$250 peak demand). The schedule calculated using the ERM reduces this by 11.6% to \$275. The schedule calculated using the CRM reduces the cost of electrical service by 13.3% to \$270. These bill reductions come primarily from the BESS reducing the peak electrical load by 14.38% (ERM) and 16.0% (CRM) respectively. As this bill falls between the calculated upper and lower bounds on the global minimum, we are confident that the minimum calculated is, or is close to, the global. While a \$5 improvement in savings over the ERM does not sound significant in absolute terms, it is important to remember the scale of power systems. With approximately 5 million commercial customers in the U.S. currently eligible for tariffs with a demand charge rate of at least \$15/kW [31], a 14.7% improvement in cost savings, over the ERM, from a simple change in software would have a significant impact. Note that a IEEE 1547-2018 compliant inverter would be able support local grid voltage with volt-var [177], or the voltage smoothing method described in Chapter 8, while applying this control schedule.

While the CRM more accurately forecasts SoC, in this case, improved

accuracy makes the CRM more susceptible than the ERM to overestimating future SoC and hence not being able to supply sufficient energy during the critical peak. This phenomena is illustrated in Fig. 6.8 where the achieved net load, derived by simulating the extended CRM using the calculated power schedule, has a peak significantly higher than the calculated net load. The gap between calculated and achieved net load schedules comes from the BESS being unable to supply sufficient energy to shave the complete peak, needing to curtail its discharge prematurely. This gap creates a large optimistic shortfall, where the achieved bill is \$5.43 higher than the calculated bill. We demonstrate in the next section that this optimistic shortfall can be mostly eliminated with closed loop control.

6.7.2 Closed-Loop control

Closed-loop control recalculates the optimal schedule at each time step. The net loads achieved by both closed-loop ERM and CRM based controllers are shown in Fig. 6.9. When implemented on the ERM, closed-loop control generates a small negative optimistic shortfall (optimistic surplus). This is because, as it starts to shave the peak load at a level based on its underestimation of capacity, the SoC is updated and the controller has more energy to work with than expected. It then applies this excess energy to a discharge during the window of peak ToU price that is coincident with peak load. The CRM based model predictive controller reduces the optimistic shortfall from \$5.43 (open-loop, see Fig. 6.8) to \$0.00 (closed-loop). This is a result of the open-loop controller not supplying sufficient charge to reach ς_{\max} before the beginning of the peak. The closed-loop controller is able to adjust for the insufficient charge and have enough energy to shave the peak completely.

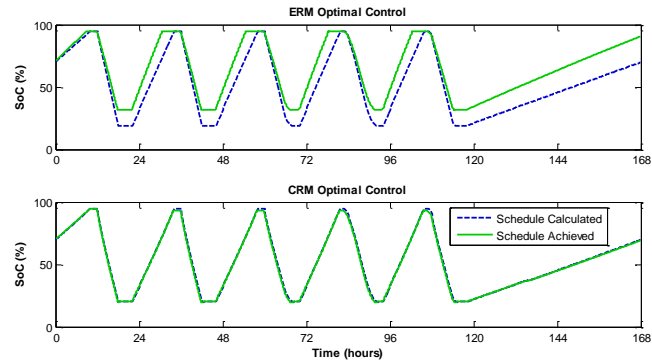


Figure 6.6: Optimal SoC schedules calculated and achieved in open-loop control from ERM (top), and CRM (bottom)

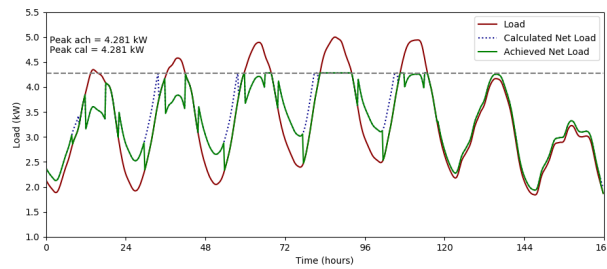


Figure 6.7: Optimal customer net-load results for the ERM in open-loop

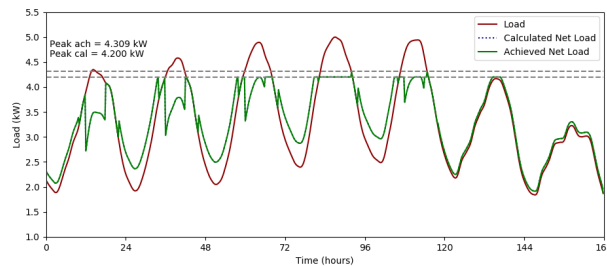


Figure 6.8: Optimal customer net-load results for the CRM in open-loop

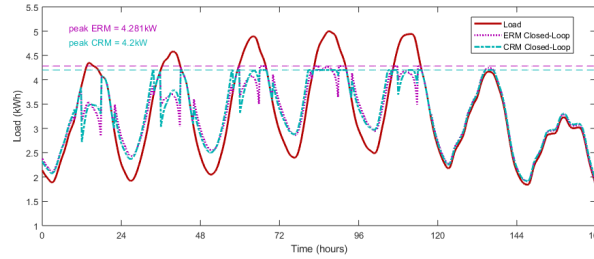


Figure 6.9: Closed-Loop Control Results for ERM and CRM

6.7.3 Risk-Averse Closed-Loop Control

The physical parameters of a BESS vary under normal operation and these variations can have a large impact on the optimistic shortfall of a controller. Fig. 6.10 shows the sensitivity of the total bill achieved by the CRM and RA CRM due to variations in capacity. When the battery’s capacity is at its mean value and above (μ , $+1\sigma$, $+2\sigma$, and $+3\sigma$), the risk-neutral CRM has a slight performance advantage. However, when the battery’s capacity is below expectations (-1σ , -2σ , and -3σ), the risk-neutral CRM’s performance drops off, producing an optimistic shortfall up to \$22.98 in the ‘extreme case’ at $\tilde{C}_{\text{cap}} = -3\sigma$, while the performance of the risk-averse controller does not decline. In terms of peak net load reduction, the risk-neutral controller is only 50% confident it will reduce the peak by 16.0%, but it has a roughly one in six chance it will reduce the peak less than 14%. In contrast, the risk-averse controller is 99.87% confident that it can reduce the peak by 15.4%. This achieves the goal of making the controller more robust to battery model uncertainty.

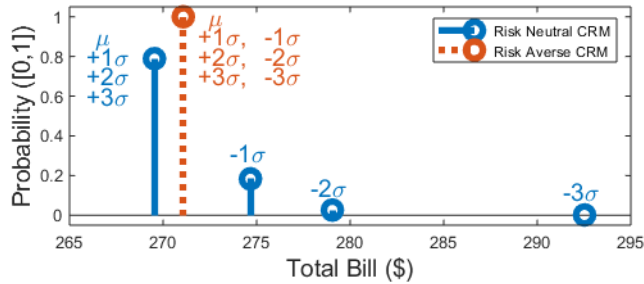


Figure 6.10: Control performance sensitivity of the risk-neutral and risk-averse CRM based model predictive controllers (compare to the ideal in Fig. 6.4). Probability refers to the likelihood that the capacity is less than the signified value. When total bills resulting from different capacity values are very close (within 25¢), their probabilities are added, and the total bill is averaged.

6.8 Summary

In this chapter we develop and demonstrate an advanced methodology for designing BESS controllers under ToU price arbitrage and peak demand charge management applications. A state-of-the-art ERM is used as the baseline for control performance comparison. The proposed CRM based model predictive controller outperforms the ERM based controller by achieving a lower total electric bill when pseudo-empirically applied in an example scenario. Because peak load management has asymmetric risk for overestimating available energy, we then shape the uncertainty of the CRM to consistently underestimate capacity. This risk-averse CRM yields better controller performance than the ERM and is more robust to variations in BESS performance than the CRM. This methodology for designing BESS controllers can be applied in a broad range of energy storage applications, wherever the risk profile of a scheduled service is asymmetric. Incremental improvements in controller performance can reduce the cost of deploying storage to make the grid more efficient and resilient.

Chapter 7

Optimal Field Voltage and Energy Storage Control for Stabilizing Synchronous Generators on Flexible AC Transmission Systems

¹ Power systems can become unstable under transient periods such as short-circuit faults, leading to equipment damage and large scale blackouts. Power system stabilizers (PSS) can be designed to improve the stability of generators by quickly regulating the exciter field voltage to damp the swings of generator rotor angle and speed. The stability achieved through exciter field voltage control can be further improved with a relatively small, fast responding energy storage system (ESS) connected at the terminals of the generator that enables electrical power damping. PSS are designed and studied using a single-machine infinite-bus (SMIB) model. In this chapter, we present a comprehensive optimal-control design for a flexible ac synchronous generator PSS using both exciter field voltage and ESS control including estimation of

¹D. Rosewater, Q. Nguyen and S. Santoso, “Optimal Field Voltage and Energy Storage Control for Stabilizing Synchronous Generators on Flexible AC Transmission Systems,” in *Proc 2018 IEEE/PES Transmission and Distribution Conference and Exposition (T&D)*, Denver, CO, 2018, pp. 1-9. doi: 10.1109/TDC.2018.8440436

The dissertator and Quan Nguyen were partners in performing this research, which was developed out of a final class project. The dissertator took lead on writing the initial draft of the report while Quan Nguyen developed most of the figures. Surya Santoso provided editorial guidance and multiple rounds of technical review.

unmeasurable states. The controller is designed to minimize disturbances in rotor frequency and angle, and thereby improve stability. The design process is based on a linear quadratic regulator of the SMIB model with a test system linearized about different operating frequencies in the range 10 Hz to 60 Hz. The optimal performance of the PSS is demonstrated along with the resulting stability improvement.

Contributions of this chapter were identified as follows: (*minor*) designed and demonstrated an advanced controller that is able to optimally stabilize a synchronous generator, over a range of frequencies, using both field voltage and a co-located energy storage system.

7.1 Introduction

Dynamic response in power systems can become unstable, leading to equipment damage and large scale blackouts. Power system stabilizers (PSS) improve the dynamic response of generators by modulating the exciter field voltage. The exciter field in a generator links the mechanical power of the rotor to the electrical power transmitted and used by the grid. A bus PSS takes measurements of the system states, including the rotor speed, rotor angle, and field voltage of the generator, and calculates a control signal for the reference field voltage that improves the stability of the generator. PSS implementation allows generators to operate at higher power output, over longer, weaker transmission lines, thereby improving the profitability of the capital investment.

Two strategies are employed in this chapter to further improve generator dynamic stability: low-frequency power transmission and energy storage power damping. Low-frequency high-voltage ac (LF-HVAc) transmission has

recently been proposed as an alternative solution to conventional 60-Hz HVac and the high-voltage direct-current (HVdc) approaches for bulk power transfer. LF-HVac transmission not only retains the ability of using existing ac devices, reliable protection schemes, and multi-terminal structure from the 60-Hz HVac but also provide better voltage regulation and system stability [189]. In addition, LF-HVac approximates the high power transfer capability of HVdc transmission if the operating frequency is sufficiently low [190]. Energy storage systems (ESS) can also be used to improve the performance of PSS and further stabilize the grid. An ESS co-located with a generator enables additional control over the power transferred to the grid and modulating its power can improve the dynamic response of the system [191].

This chapter investigates the intersection of both of these strategies, along with modern control for PSS, to evaluate the improvement of system stability when they are employed together. The closed-loop optimal design includes a linear quadratic regulator (LQR) [165] and a reduced order observer to account for the difficulty in measuring states such as the quadrature transient terminal voltage of the generator. The proposed analysis can be extended to multi-machine systems.

In the remainder of this chapter, Section II describes the structure of the system under consideration and its state space model. Section III elaborates on the design of the optimal closed-loop controller as well as the reduced-order observer for the PSS. The simulation results and discussion on system responses under various operating conditions are in Section IV. Section V completes the chapter with a conclusion.

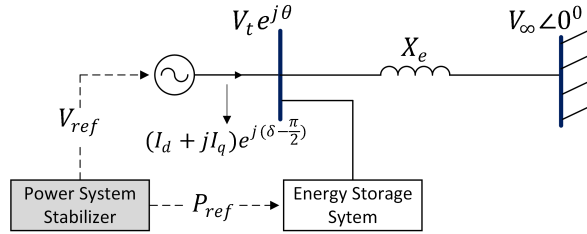


Figure 7.1: The model of a single electric machine connected to a infinite bus with PSS and ESS.

7.2 System Modeling

In [192] a PSS is designed using a simple model of a single machine oscillating with an infinite bus (SMIB). The PSS, with ESS enhancement, is designed and studied through a modified SMIB model in Fig. 7.1. This model uses an ideal bus, defined to have constant voltage V_{inf} at angle 0° , to represent the grid. Connected to this bus, by way of a transmission line, is a generator with scalar terminal voltage V_1 at angle θ . The internal voltage leads the voltage at the infinite bus by the angle δ . For simplicity of designing optimal controllers, generator parameters such as voltage and current are translated from the three-phase sinusoidal abc frame into the synchronously rotating frame with *direct* and *quadrature* components.

The following notation is used throughout this chapter:

$\Delta E'_q$	perturbed quadrature-axis transient voltage of the generator,
$\Delta \delta$	perturbed rotor angle,
$\Delta \omega$	normalized perturbed rotor angular velocity;
ΔE_{fd}	d -axis component of the perturbed field voltage in the excitation coil,
ΔP_{ess}	perturbed power supplied (+) or absorbed (-) by the ESS,
K_A, T_A	machine amplifier gain and time constant,
T_M	mechanical torque applied to the shaft,
T'_{do}	direct-axis open-circuit transient time constant of the generator,
V_{ref}	reference steady-state value of terminal voltage,
P_{ref}	reference steady-state value of ESS power,
H, D	shaft inertia and damping of the generator.

7.2.1 SMIB Model Equations

The model of SMIB system includes machine differential equations, stator equations, network equations, and ESS equations. In the machine model, the exciter coils generate the magnetic field that enables the spinning rotor to produce electrical voltage on the stator coils. These electromagnetic dynamics are represented in (7.2.1). The limits placed on E_{fd} represent safety restrictions on the field voltage and are strictly imposed. The stator equations (7.2.2) govern how energy in the rotor is transferred from and to the stator, while the network equations (7.2.3) represent the power transfer across the transmission line between the generator and the infinite bus. The first order response dynamics, energy function, and power limits of the ESS are shown in

(7.2.4). This adaptation of the ESS model from [193] ignores reactive power, auxiliary power, and the dynamic converter model. ESS energy limits are an output of simulation to be used as design requirements for a practical ESS, and charge/discharge power limits are held constant and is strictly imposed in simulation to explore the effect of ESS power saturation on the controller's performance.

Machine equations [192]:

$$\begin{aligned}
\dot{\delta} &= \Delta\omega_{pu}\omega_s, \\
\dot{\omega}_{pu} &= \frac{1}{2H} [T_M - (E'_q I_q + (X_d - X'_d) I_d I_q + D\Delta\omega_{pu})], \\
\dot{E}'_q &= \frac{1}{T_{do}} (-E'_q - (X_d - X'_d) I_d + E_{fd}), \\
E_{fd,min} &\leq E_{fd} \leq E_{fd,max}.
\end{aligned} \tag{7.2.1}$$

Stator equations [192]:

$$\begin{aligned}
X_q I_q - V_d &= 0, \\
E'_q - V_q - X'_q I_q &= 0.
\end{aligned} \tag{7.2.2}$$

Network equations [192]:

$$\begin{aligned}
R_e I_d - X_e I_q &= V_d - V_{inf} \sin\delta, \\
X_e I_d + R_e I_q &= V_q - V_{inf} \cos\delta.
\end{aligned} \tag{7.2.3}$$

Energy storage equations [193]:

$$\begin{aligned}
P_{ess} &= \frac{P_{ref}}{1 + sT_{ess}}, \\
\dot{E}_{ess} &= P_{ess}, \\
P_{ess,min} &\leq P_{ess} \leq P_{ess,max}.
\end{aligned} \tag{7.2.4}$$

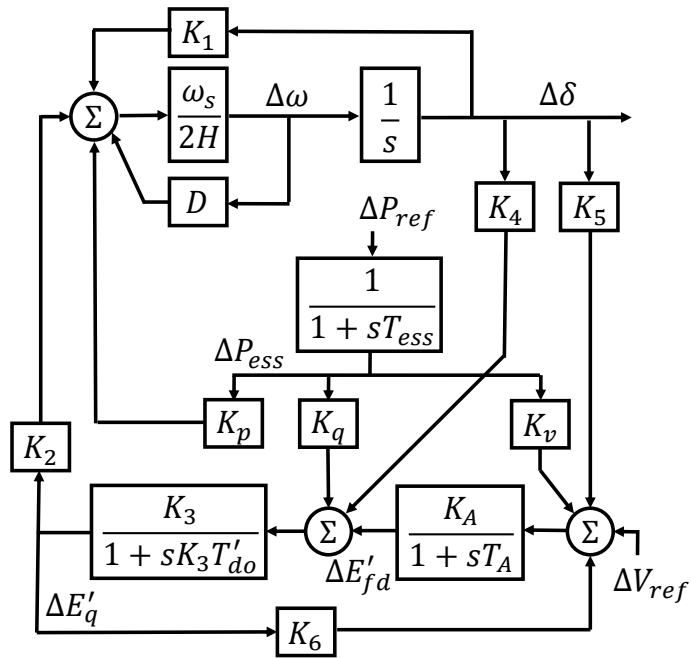


Figure 7.2: Block diagram representing the system shown in Fig 7.1.

7.2.2 State Space Model

Based on (7.2.1) - (7.2.4), the linearized state-space model of the SMIB is shown in (7.2.5) and (7.2.6), where K_1 - K_6 are given from [192] and new coefficients K_p , K_q , and K_v are given in [191]. The values of these coefficients depends on the reactances X_q , X_d , X'_d , and X_e as well as the shaft inertial constant H . While the reactances are each proportional to the operating frequency, H is proportional to the operating frequency squared [192]. The block diagram of the system is shown in Fig. 7.2, which is the combination of the classical PSS model and the integrated ESS model. In addition to the only control input ΔV_{ref} in the classical SMIB model, (7.2.5) has another control input ΔP_{ref} , which represents the control signal sent to the ESS. The saturation limits on the field voltage E_{fd} and ESS power P_{ess} are imposed. The state space output \mathbf{z} is a 4×1 vector that represents the four measurable states. As $\Delta E'_q$ is assumed to be unmeasurable in this design, the first column of the \mathbf{C} matrix is zeros.

$$\begin{aligned}
 \begin{bmatrix} \Delta \dot{E}'_q \\ \Delta \dot{\delta} \\ \Delta \dot{\omega} \\ \Delta \dot{E}_{fd} \\ \Delta \dot{P}_{ess} \end{bmatrix} &= \begin{bmatrix} -\frac{1}{K_3 T'_{do}} & -\frac{K_4}{T'_{do}} & 0 & \frac{1}{T'_{do}} & \frac{K_q}{T'_{do}} \\ 0 & 0 & \omega_s & 0 & 0 \\ -\frac{K_2}{2H} & -\frac{K_1}{2H} & -\frac{D\omega_s}{2H} & 0 & \frac{K_p}{2H} \\ -\frac{K_A K_6}{T_A} & -\frac{K_A K_5}{T_A} & 0 & -\frac{1}{T_A} & -\frac{K_A K_v}{T_A} \\ 0 & 0 & 0 & 0 & -\frac{1}{T_{ess}} \end{bmatrix} \\
 &\times \begin{bmatrix} \Delta E'_q \\ \Delta \delta \\ \Delta \omega \\ \Delta E_{fd} \\ \Delta P_{ess} \end{bmatrix} + \begin{bmatrix} 0 & 0 \\ 0 & 0 \\ 0 & 0 \\ \frac{K_A}{T_A} & 0 \\ 0 & \frac{1}{T_{ess}} \end{bmatrix} \begin{bmatrix} \Delta V_{ref} \\ \Delta P_{ref} \end{bmatrix}, \quad (7.2.5)
 \end{aligned}$$

$$\mathbf{z} = \mathbf{C}\mathbf{x} = \begin{bmatrix} 0 & 1 & 0 & 0 & 0 \\ 0 & 0 & 1 & 0 & 0 \\ 0 & 0 & 0 & 1 & 0 \\ 0 & 0 & 0 & 0 & 1 \end{bmatrix} \begin{bmatrix} \Delta E'_q \\ \Delta\delta \\ \Delta\omega \\ \Delta E_{fd} \\ \Delta P_{ess} \end{bmatrix}. \quad (7.2.6)$$

7.3 Optimal Controller Design

7.3.1 The LQR Optimal Controller

A closed-loop controller is designed to improve the stability of the SMIB systems by changing the eigenvalues of the open-loop system to desired values. This controller is designed to minimize a performance index, which is chosen based on the specific requirements of the system and its application. In this chapter, the performance index in (7.3.1) is defined to minimize the disturbances in rotor frequency $\Delta\omega$ and angle $\Delta\delta$ as well as the control inputs ΔV_{ref} and ΔP_{ref} :

$$L = \frac{1}{2} \int_0^{\infty} \left[(\Delta\delta)^2 + (\Delta\omega)^2 + r_1(\Delta V_{ref})^2 + r_2(\Delta P_{ref})^2 \right] dt \quad (7.3.1)$$

Positive definite weights r_1 and r_2 are applied to the input variables which enable adjustment of their relative and absolute utilization by the controller. The optimal control \mathbf{u}^* which minimizes (7.3.1) is determined as follows [165]:

$$\begin{aligned} \mathbf{u}^* &= -\mathbf{K}\mathbf{x}, \\ \mathbf{K} &= \mathbf{R}^{-1}\mathbf{B}^T\mathbf{S}^*, \end{aligned} \quad (7.3.2)$$

where:

$$\mathbf{R} = \begin{bmatrix} r_1 & 0 \\ 0 & r_2 \end{bmatrix}, \quad (7.3.3)$$

and \mathbf{S}^* is the steady-state solution of the matrix Ricatti equation, which is defined as follows [165]:

$$\dot{\mathbf{S}} = -\mathbf{S}\mathbf{A} - \mathbf{A}^T\mathbf{S} - \mathbf{Q} + \mathbf{S}\mathbf{B}\mathbf{R}^{-1}\mathbf{B}^T\mathbf{S} = \mathbf{0}. \quad (7.3.4)$$

With this optimal control, the closed-loop eigenvalues are calculated as follows:

$$|\lambda\mathbf{I} - (\mathbf{A} - \mathbf{B}\mathbf{K})| = 0. \quad (7.3.5)$$

7.3.2 Reduced Order Observer Design

In practice, measuring the quadrature transient terminal voltage of the generator is not trivial. Therefore, in this design, it is assumed that $\Delta E'_q$ is unmeasurable in that there is no sensor that is able to feed data to a controller. Therefore, $\Delta E'_q$ needs to be estimated based on the measurements of the other states along with the system state equations in (7.2.5) and (7.2.6). A reduced order observer used to estimate the value of $\Delta E'_q$ is designed as follows. Let the observer $\varphi = \Delta E'_q$ be a linear combination of system states that is unmeasurable and independent of the measurements \mathbf{z} :

$$\varphi = \mathbf{T}\mathbf{x} \Rightarrow \dot{\varphi} = \mathbf{T}\dot{\mathbf{x}} = \mathbf{T}\mathbf{A}\mathbf{x} + \mathbf{T}\mathbf{B}\mathbf{u} \quad (7.3.6)$$

where $\mathbf{T} = [t_1 \ t_2 \ t_3 \ t_4 \ t_5]$ is unknown and $[\mathbf{T} \ \mathbf{C}]^T$ is nonsingular. From (7.2.6) and (7.3.6), the system states can be determined as follows:

$$\mathbf{x} = \begin{bmatrix} \mathbf{T} \\ \mathbf{C} \end{bmatrix}^{-1} \begin{bmatrix} \varphi \\ \mathbf{z} \end{bmatrix} = [\mathbf{S}_1 \ \mathbf{S}_2] \begin{bmatrix} \varphi \\ \mathbf{z} \end{bmatrix} = \mathbf{S}_1\varphi + \mathbf{S}_2\mathbf{z}. \quad (7.3.7)$$

Substituting (7.3.7) into (7.3.6) yields:

$$\dot{\varphi} = \mathbf{T}\dot{\mathbf{x}} = \mathbf{T}\mathbf{A}\mathbf{S}_1\varphi + \mathbf{T}\mathbf{A}\mathbf{S}_2\mathbf{z} + \mathbf{T}\mathbf{B}\mathbf{u} \quad (7.3.8)$$

Let $\hat{\varphi}$ and $\hat{\mathbf{x}}$ are the estimated values of φ and the system states. From (7.3.7) and (7.3.8), their estimation errors $\tilde{\varphi}$ and $\tilde{\mathbf{x}}$ satisfy the following equations:

$$\dot{\tilde{\varphi}} = \dot{\varphi} - \dot{\hat{\varphi}} = \mathbf{TAS}_1(\varphi - \hat{\varphi}) = \mathbf{TAS}_1\tilde{\varphi}, \quad (7.3.9)$$

and:

$$\dot{\tilde{\mathbf{x}}} = \mathbf{S}_1\dot{\varphi} = \mathbf{S}_1\mathbf{TAS}_1\tilde{\varphi} = \mathbf{S}_1\mathbf{TA}\tilde{\mathbf{x}} = (\mathbf{I} - \mathbf{S}_1\mathbf{C})\mathbf{A}\tilde{\mathbf{x}} \quad (7.3.10)$$

The coefficient matrix $(\mathbf{I} - \mathbf{S}_1\mathbf{C})\mathbf{A}$ has the following non-zero eigenvalue:

$$\lambda_{obs} = \frac{1}{K_3 T'_{do}} - \frac{t_3 K_2}{t_1 2H} - \frac{t_4 K_A K_6}{t_1 T_A}. \quad (7.3.11)$$

In order to guarantee system stability when the observer is implemented, the eigenvalue in (7.3.11) is chosen to be much faster than the eigenvalues of the closed-loop system obtained in the previous section.

7.4 Simulation Results

This section shows the response of a test system, as shown in Fig. 7.1, without and with the designed optimal controllers described in Section III. The effect of the operating frequency on the response of the system under disturbances is also included. The remainder of this section addresses the effect of weighting factors in the performance index on the system response.

The parameters of the test system at 60 Hz are $T'_{do} = 9.6$ sec, $K_A = 400$, $D = 0$, $X_q = 2.1$ p.u, $X_d = 2.5$ p.u, $X'_d = 0.39$ p.u, $H = 3.2$, $T_A = 0.2$ sec, and $T_{ess} = 0.01667$ sec, $R_e = 0$, $X_e = 0.5$, $V_t = 1$ p.u, $\theta_t = 15^\circ$, $V_\infty = 1.05$ p.u, $\theta_\infty = 0^\circ$ [192]. These values are consistent with a high-speed water wheel or non-condensing turbine generator with a 100 MVA rating. The state limits are $E_{fd,min} = -0.5$ p.u, $E_{fd,max} = 0.5$ p.u, $P_{ess,min} = -0.1$ p.u, and $P_{ess,max} = 0.1$ p.u.

Table 7.1: Open-loop settling time performace

State	60 Hz	50 Hz	40 Hz	30 Hz	20 Hz	10 Hz
$\Delta\delta(sec.)$	63.3655	17.0457	15.8578	35.4401	∞	∞
$\Delta\omega(sec.)$	62.7212	17.2029	15.9886	35.5478	∞	∞

7.4.1 The Open-Loop System Response

At a frequency of 60 Hz the open-loop eigenvalues of the system without any closed-loop controllers are:

$$\lambda_1 = -60, \lambda_{2,3} = -2.588 \pm j8.502, \lambda_{4,5} = -0.087 \pm j7.114.$$

The eigenvalues of the open-loop system have negative real parts; therefore, the system is stable. However, λ_4 and λ_5 are close to zero, which means that the system might become unstable under large disturbances. λ_1 is the eigenvalue of the ESS controller. Table 7.1 shows the settling times for the open-loop system from 60 Hz to 10 Hz. Settling time is measured as the time it takes for the states to enter and remain in a 2% error band. Reducing the operating frequency from 60 Hz to 40 Hz results in shorter settling times. Settling time then increases at 30 Hz and becomes unstable below 20 Hz.

7.4.2 The Closed-Loop System Response

The rotor speed is assumed to have a initial disturbance of 0.12 Hz. The weighting factors of the input controls ΔV_{ref} and ΔP_{ref} in (7.3.1) are chosen to be $r_1 = 1$ and $r_2 = 0.01$, respectively. With the closed-loop optimal

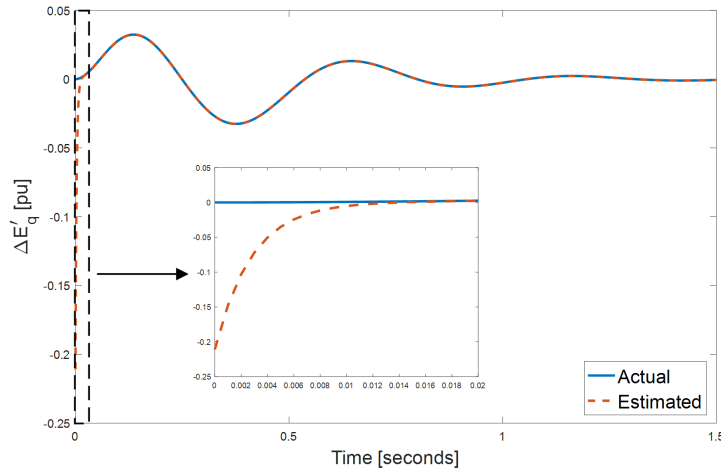


Figure 7.3: Observer performance.

control described in Section III.A, the eigenvalues of the 60 Hz system become:

$$\lambda_1 = -52.428, \lambda_2 = -28.245,$$

$$\lambda_3 = -13.920, \lambda_{4,5} = -4.974 \pm j10.537.$$

Since these eigenvalues are pushed further from the imaginary axis, the stability of the system is improved.

The reduced order observer described in Section III.B is determined by first choosing $t_2 = t_5 = 0$ and $t_3 = t_4 = 1$, and then solving for t_1 using (7.3.11). With the eigenvalue of the observer being $\lambda_{obs} = -300$, the performance of the observer when the operating frequency is 60 Hz is shown in Fig. 7.3. The initial error between the actual and estimated values of the quadrature transient terminal voltage of the generator becomes zero shortly after 0.1 seconds.

With the designed reduced order observer, the response of the states and the optimal input controls to the initial rotor speed disturbance of 0.12 Hz at different operating frequencies is shown in Fig. 7.4. The optimal control is

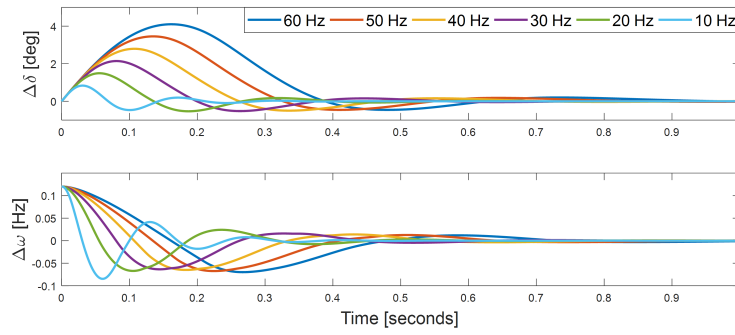


Figure 7.4: The response of states at each frequency of interest.

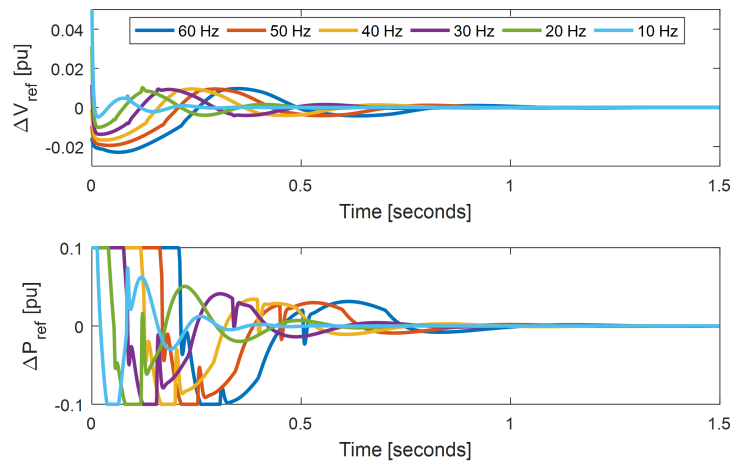


Figure 7.5: Optimal controls.

Table 7.2: Closed-loop settling time performance

State	60 Hz	50 Hz	40 Hz	30 Hz	20 Hz	10 Hz
$\Delta\delta(sec.)$	0.8755	0.7724	0.6608	0.6490	0.5130	0.3395
$\Delta\omega(sec.)$	0.9214	0.8188	0.7095	0.5875	0.5371	0.3581

shown in Fig. 7.5, where a lower input control is needed at a lower frequency. Table 7.2 shows the improved settling time response of the rotor speed and angles. Compared to the open-loop response, the closed-loop controller improves the settling time by more than a factor of 60 at 60 Hz. It is also able to stabilize the system at operating frequencies lower than 20 Hz while continuing to improve the settling time.

Fig. 7.6 shows the energy required from the ESS at different operating frequencies to suppress the oscillations in rotor speed. At 60 Hz, the ESS has a peak change in energy of 0.0119 p.u power seconds. This would mean that a 100 MVA generator at 60 Hz would require 1.19 MW-seconds (19.8 kWh) of energy supplied/absorbed from storage to achieve this performance. Lower frequencies require less energy reserves to supply the desired damping. The same generator operating at 10 Hz would only require 230 kW-seconds (3.83 kWh) of energy to achieve this performance.

7.4.3 The Effect of Weighting Factors in the Performance Index

This section shows the effects of adjusting the input weighting factors in the LQR performance index (7.3.1). Fig. 7.7 shows the response of rotor speed and angle when the weighting factor r_2 of ΔP_{ref} increases from 0.01 as in the previous studies to 0.5, and then to ∞ . $r_2 = \infty$ represents the case

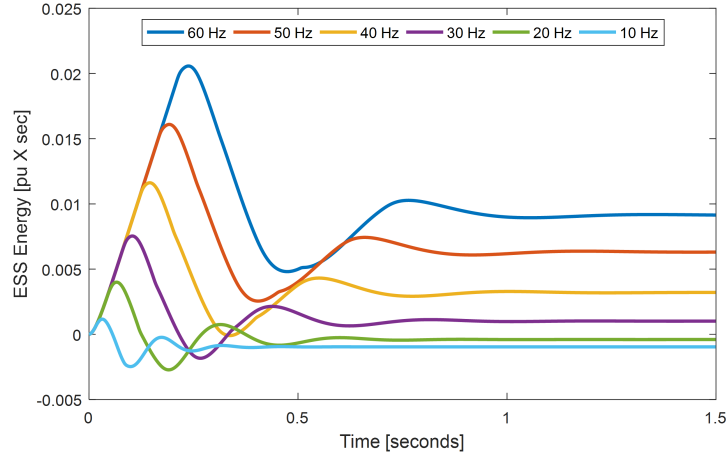


Figure 7.6: Energy storage response

Table 7.3: Settling time performance with reduced ESS control action

State	$r_2 = 0.01$	$r_2 = 0.5$	$r_2 = \infty$
$\Delta\delta(sec.)$	0.8755	1.9639	5.2233
$\Delta\omega(sec.)$	0.9214	1.8569	5.3269

where the ESS is not utilized as any non-zero input to ΔP_{ref} would drive the performance index to ∞ . The coefficients of the other components are kept constant, and the operating frequency is 60 Hz. Practically, this allows designers to adjust the requirements of the energy storage system to reach a stability performance target. Reducing r_2 results in a higher deployment the ESS, which improves the stability performance of the system. Table 7.3 shows the settling time as r_2 in (7.3.1). When compared to the case where energy storage is not used $r_2 = \infty$, settling time is more than cut in half when $r_2 = 0.5$ and halved again when $r_2 = 0.01$.

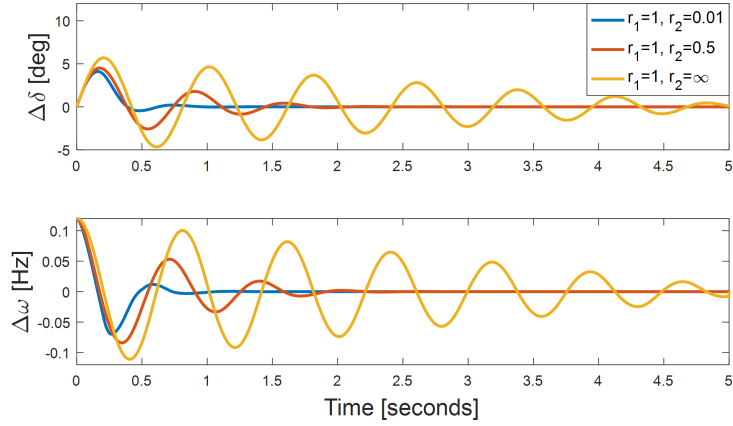


Figure 7.7: The resulting states when r_2 varies. ($r_2 = \infty$ represents no ESS control action)

7.5 Summary

An optimal closed-loop controller is designed for PSS to improve the stability of a generator using both the reference field voltage and ESS power as input controls. This controller minimizes the perturbations in rotor frequency and angle in response to disturbances. The designed reduced order observer is able to exactly estimate the unmeasurable state after 0.1 seconds. At 60 Hz and with the same initial rotor speed disturbance of 0.12 Hz, the open loop-system requires 63 seconds to settle, while the proposed controller reduces the settling time to 5.3 seconds without the use of ESS and 0.92 second with the ESS. At a lower operating frequency of 10 Hz, the open-loop system is unstable while the closed-loop system is stable and has a settling time of 0.34 seconds. With the proposed closed-loop controller the ESS requires less energy to be effective at low frequencies. To damp out the same disturbance, the system operating at 10 Hz only needs 3.83 kWh of energy, while 19.8 kWh is required when the operating frequency is 60 Hz.

Chapter 8

A Voltage Smoothing Algorithm using Energy Storage PQ Control in PV-integrated Power Grid

¹ Changes in solar irradiance cause variations in photovoltaic (PV) power generation and thus affect customer voltage. Load tap changers (LTC) in substations are used to mitigate voltage variations, but they are relatively slow and cannot regulate the voltage adequately. Furthermore, abrupt voltage changes induced by PVs could greatly cause mechanical wear and reduce their lifetime. This chapter develops a novel voltage smoothing control algorithm for distributed energy storage (ES) systems to reduce the impact of PV generation on voltage quality. Different from other works, the proposed control can improve the performance by having both active and reactive power control and monitoring voltage directly. The technique's performance is verified through simulation and modeling of the IEEE 4-bus test system. The proposed technique can effectively smooth the voltage and reduce the number of

¹P. Siratarnsophon, K. W. Lao, D. Rosewater and S. Santoso, "A Voltage Smoothing Algorithm using Energy Storage PQ Control in PV-integrated Power Grid," in *IEEE Transactions on Power Delivery*. doi: 10.1109/TPWRD.2019.2892611

The dissertator, P. Siratarnsophon, and K. W. Lao were partners in performing this research, which was developed out of a final class project. P. Siratarnsophon took lead on writing and editing the article. The dissertator contributed substantially to the controller algorithm development and provided technical review of the article. Surya Santoso provided editorial guidance and multiple rounds of technical review.

tap operations by approximately 50%.

Contributions of this chapter were identified as follows: (*minor*) designed and demonstrated an advanced controller to smooth grid voltage using energy storage in distribution systems with high penetration PV.

8.1 Introduction

Increasing photovoltaic (PV) integration and weather conditions could vary PV active power injection and causes voltage fluctuations [194]. Load tap changers (LTC) at transformer substations can mitigate voltage variations; however, LTC response is relatively slow and thus is not suitable for the ramp rate and frequency of fluctuations induced by PV. The volt-var control was proposed to regulate the voltage [195,196]. However, the control only used reactive power to maintain the voltage and may not be effective on systems with high PV penetration levels or with low reactance to resistance (X/R) ratio. An algorithm was proposed for controlling the active power injection from energy storage (ES) to counteract with PV inverter power output fluctuations [194, 197, 198]. However, these control algorithm uses solely active power and as a result only mitigates the voltage fluctuations induced by only the monitored PV. Voltage fluctuations caused by other PV systems are not considered.

Thus in this chapter, a novel control algorithm for ES power injection is proposed to achieve voltage smoothing and voltage regulation. It uses both active and reactive power to reduce (smooth out) changes in voltage over time. In the proposed algorithm, instead of monitoring PV inverter power, the PV bus voltage is monitored to mitigate voltage fluctuations caused by other PV panels in the grid directly. However the nonlinearity between active,

reactive power and voltage makes the approach challenging, and is overcome by adding a special iterative control loop. The proposed voltage smoothing control algorithm is described in Section II. Section III presents the system model modified from IEEE 4-bus test system and simulation verifications. Section IV concludes the chapter.

8.2 Voltage Smoothing Techniques by ES Power Injection Control

Two voltage smoothing strategies are presented below. The first is based on an existing active power ramp rate control, while the second is our proposed method of voltage control.

8.2.1 Technique I: Active power ramp rate control by monitoring PV inverter power output

The first technique, designated as “Technique I”, monitors PV inverter active power output to control active power ramp rate [197]. The control algorithm is shown in Fig. 8.1 In Technique I, the PV inverter active power output is monitored and recorded for computing average value. The difference between the current PV inverter active power output and its average value is used to determine the required active power injection to reduce active power and voltage fluctuations. In addition, in order to avoid over-usage of the ES and to lengthen ES lifecycle, a power set-point correction based on state of charge (SOC) is included so that the ES will be ready for future voltage smoothing operation. This correction factor is also used to adjust the trade-off between smoothing performance and battery longevity. There are two major deficiencies for this technique. First, fluctuations caused by other PV systems,

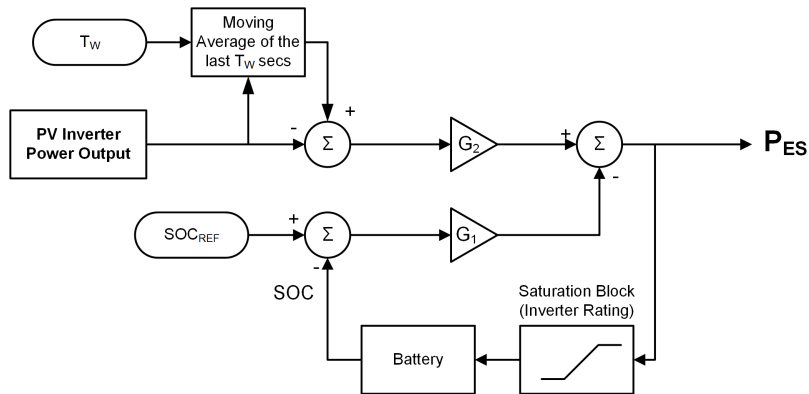


Figure 8.1: Control algorithm of voltage smoothing by limiting active power ramp rate in Technique I.

which don't have ES smoothing, cannot be mitigated. Second, the effect of other mitigation strategies, such as LTC action or reactive power control, cannot be considered and hence the battery could be needlessly overworked.

Shown in Fig. 8.2 (a) is a diagram illustrating the range of the power injection from the ES using Technique I. The ES power injection control point would vary along the horizontal axis of P_{ES} only since no reactive power control is concerned.

8.2.2 Technique II: Proposed algorithm of PQ power injection control by monitoring voltage

The second technique, designated as "Technique II", is the proposed active and reactive power injection control by monitoring local PV bus voltage which the inverter is connected to. It combines both technique I and volt-var control. Fig. 8.3 shows the proposed control algorithm. In order to overcome the drawbacks in Technique I, two major modifications are proposed. First, the voltage of local PV bus is monitored instead of PV inverter power

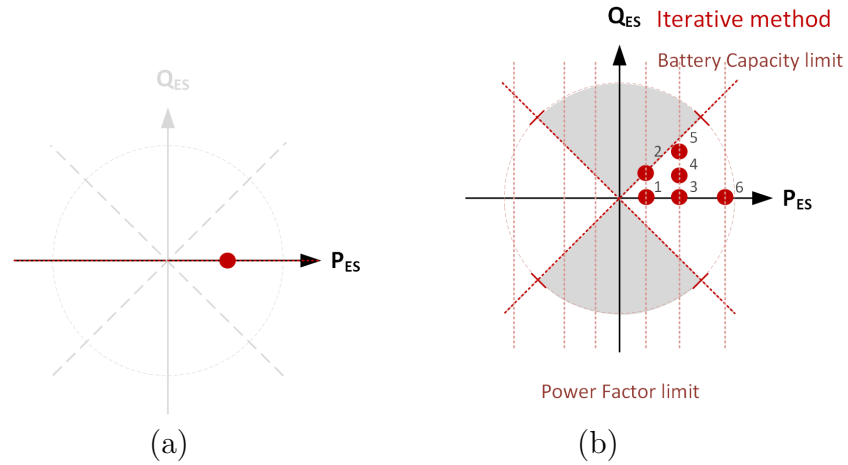


Figure 8.2: Power injection control point for ES in (a) Technique I; and (b) Technique II.

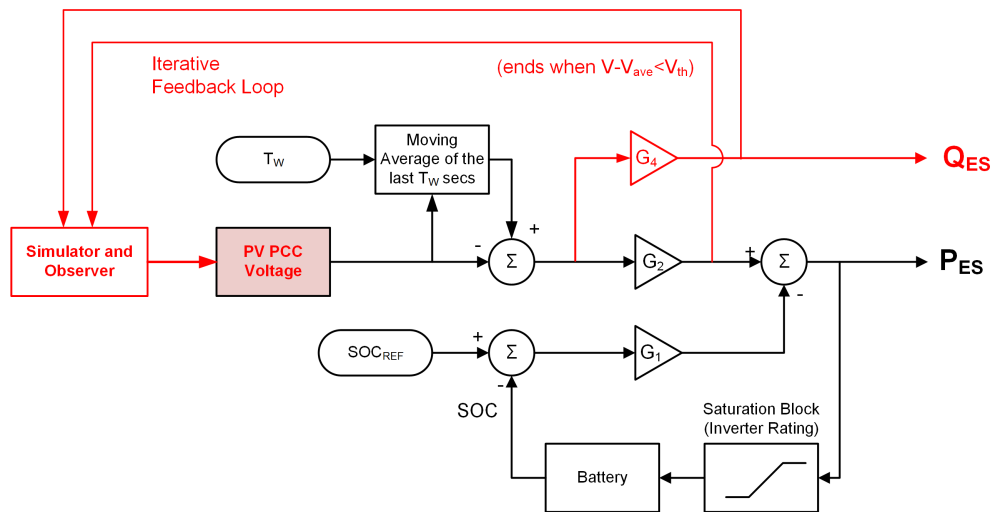


Figure 8.3: Proposed control algorithm of ES PQ power injection by monitoring local PV bus voltage in Technique II.

output to take into consideration voltage fluctuations caused by changes in load and the output of other PV generation without ES smoothing. Second, because the control is based on voltage measurements and not active power, instead of controlling ES active power alone, reactive power is also controlled to reduce the costly active power required from the battery and provide additional voltage support for the system. By doing so, effective voltage smoothing can be achieved to reduce the number of LTC operations.

1) P_{ES} Control: For the active power PES control loop, PV bus voltage and ES SOC are monitored. The value of control update ΔP_{ES} is computed from (1). Voltage fluctuations caused by other PV panels without ES smoothing will be reflected in the parameter V and be controlled. Different from Technique I, the relationship between active power P_{ES} and bus voltage V is nonlinear. Therefore, an iterative loop is introduced in the proposed technique to determine the optimal power control operation point of P_{ES} . A simulator/observer is used to simulate and observe the voltage resulting from different P_{ES}/Q_{ES} combinations, and is compared with the average value V_{ave} and the iterative loop will continue until the absolute difference is within a threshold value (V_{th}).

$$\Delta P_{ES} = -G_1(SOC_{REF} - SOC) + G_2(V_{ave} - V) \quad (8.2.1)$$

where SOC_{REF} refers to the desired SOC reference level, and V_{ave} is the average value of bus voltage calculated over a set time window.

2) Q_{ES} Control: For the reactive power Q_{ES} control loop, the PV bus voltage V is monitored. The expression for determining the updated ΔQ_{ES} is shown in (2). Similarly, the value of bus voltage V is compared with its

average value V_{ave} to compute Q_{ES} and the iterative loop continues until the absolute difference is within a threshold value V_{th} .

$$\Delta Q_{ES} = G_4(V_{ave} - V) \quad (8.2.2)$$

Fig. 8.2 (b) shows the power injection control point from ES in Technique II. Compared to Technique I, the control involves reactive power QES. In order to reserve ES active power for future usage, the controller will iteratively search for the optimal power injection which requires the least real power. The value of PES is first set to a certain value, and the value of QES is gradually increased until the system reaches the optimal operation point. In case if the operation point exceeds the power factor limit, the value of PES will be increased by a certain proportion, and the iteration procedure continues by increasing reactive power QES. The iteration will stop when it reaches the optimal operation point or the ES capacity limit.

8.3 System Model for Verifications

Verifications of the proposed voltage smoothing technique is done by using the modified IEEE 4-bus test system shown in Fig. 8.4 Two scenarios are investigated. In scenario 1, a PV system (with 50% penetration rate), and an ES system (with initial SOC of 60 %) is installed at phase A of the load bus (bus 4). In scenario 2, in order to simulate the case of voltage fluctuations caused by other PV systems, a PV system (with 25% penetration rate) is added at the transformer bus (bus 3). The unbalanced load for phase A, B and C of the load bus (bus 4) is set to 1275 kW, 1800 kW, and 2375 kW, with power factor of 0.85, 0.90 and 0.95 respectively.

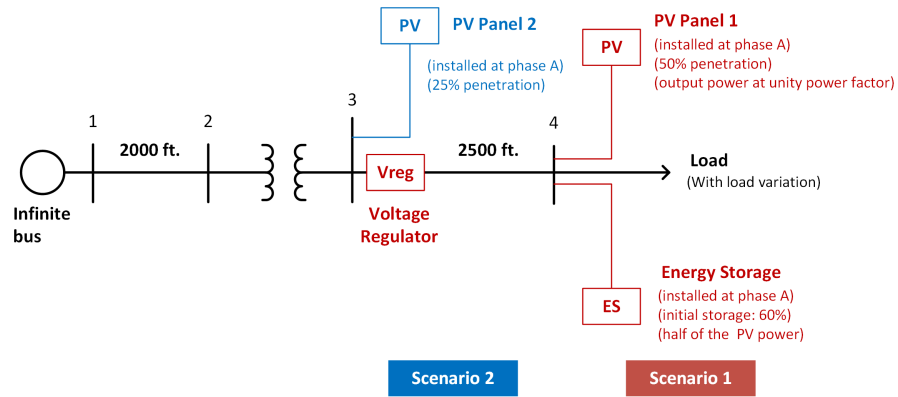


Figure 8.4: System model used for verification.

In both scenarios 1 and 2, the ES is set to have a power rating of 320 kW, and 640 kWh.

The line to neutral voltage of the load bus (bus 4) phase A and tap position at load tap changer (LTC) during daytime (8 a.m. to 8 p.m.) obtained through simulation is shown in Fig. 8.5 The condition without any voltage smoothing control is selected as the base case for the study. The load voltage profile is highly affected by PV power generation and the tap position is changed rapidly to regulate the voltage. A total of 201 tap changes are recorded in the simulated 24 hour period.

In Technique I, the value of $G1=1.0$ and $G2=1.0$. Compared to the base case, the number of tap changes at LTC is reduced to 27. For reference, the active and reactive power injection from ES and ES SOC status are shown in Fig. 8.6 Using Technique I control, overuse of active power causes rapid changes in the SOC and accelerated battery degradation.

In Technique II, the control accuracy is higher when the values of $G2$ and $G4$ are lower, but it also takes longer to search for the optimum point.

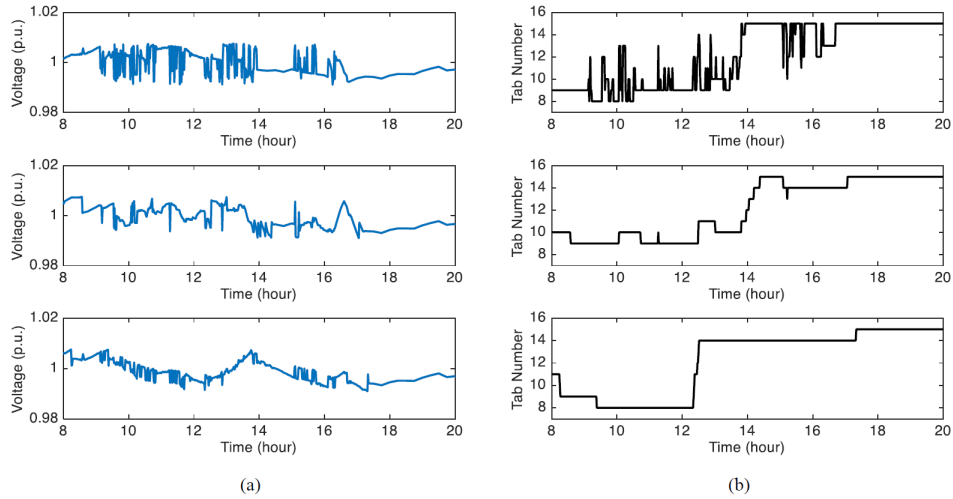


Figure 8.5: (a) Line to neutral voltage at the load bus (bus 4 phase A); (b) Tap number at load tap changer: (top) case without any voltage smoothing control; (middle) using Technique I; (bottom) using Technique II

In the simulation, $G1=1.0$, $G2=0.1$, and $G4=0.3$. Compared to Technique I, the voltage profile is more stationary, and the root mean square deviation (RMSD) is reduced by 57%, while the number of tap changes is reduced to 13. Fig. 8.6 shows the ES power injection and SOC status during verifications.

In scenario 2 these results are more pronounced. The voltage fluctuations caused by the addition of unregulated PV increases the number of tap-changes using Technique I to 35 while Technique II is unaffected. The verification results for both scenarios are summarized in Table. 8.1 With proposed Technique II, the number of tap changes and RMSD is greatly reduced by around 50% and 58% respectively, while reducing the active power required from the ES thereby prolonging the battery life.

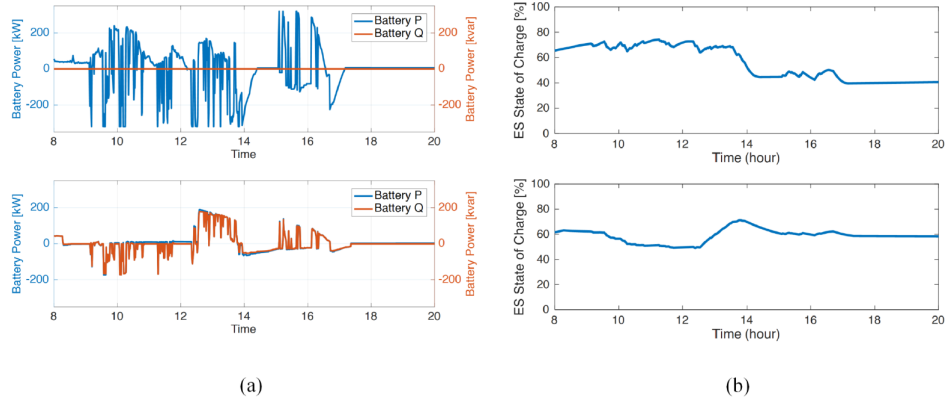


Figure 8.6: (a) Injection of active and reactive power from ES; (b) Battery SOC: (top) Technique I; (bottom) Technique II

Table 8.1: Summary of Verification Results

Scenario 1						
Control	Tap Changes	P_{max}	Q_{max}	SOC_{max}	SOC_{min}	$RMSD$
No Control	201	0	0	0	60	0.101 kV
Tech. I	27	320	0	320	39.58	0.068 kV
Tech. II	13	197	193	274	44.68	0.029 kV
Scenario 2						
Control	Tap Changes	P_{max}	Q_{max}	SOC_{max}	SOC_{min}	$RMSD$
No Control	245	0	0	0	60	0.121 kV
Tech. I	35	320	0	320	39.58	0.074 kV
Tech. II	13	231	219	319	43.69	0.031 kV

8.4 Summary

A control algorithm to mitigate the impact of PV on grid voltage and LTC action is presented. Different from others, the proposed control smooths voltage directly and uses both active and reactive power control loops to improve battery life and mitigate voltage fluctuations caused by other PV panels in the system. Verified through simulations on IEEE 4-bus test system, less battery energy is used and the number of LTC tap operations are reduced by around 50%, which is lower than the alternative control. The proposed control method is expected to be more effective in providing voltage regulation over wider range of X/R ratio compared to controlling active or reactive power alone.

Chapter 9

Optimal Control of a Battery Energy Storage System with a Charge-Temperature-Health Model

¹ Battery energy storage is being installed behind-the-meter to reduce electrical bills while improving power system efficiency and resiliency. This chapter demonstrates the development and application of an advanced optimal control method for battery energy storage systems to maximize these benefits. We combine methods for accurately modeling the state-of-charge, temperature, and state-of-health of lithium-ion battery cells into a model predictive controller to optimally schedule charge/discharge, air-conditioning, and forced air convection power to shift a electric customer's consumption and hence reduce their electric bill. While linear state-of-health models produce linear relationships between battery usage and degradation, a non-linear, stress-factor model accounts for the compounding improvements in lifetime that can be achieved by reducing several stress factors at once. Applying this controller to

¹D. Rosewater, A. Headley, F. Mier, and S. Santoso, "Optimal Control of a Battery Energy Storage System with a Charge-Temperature-Health Model" in *Proc. 2019 IEEE Power & Energy Society General Meeting*, August 2019

The dissertator was the principle investigator for this research including model development, simulation and performance analysis, and writing/editing the article itself. Alex Headley contributed to the control algorithm development. Frank Austin Mier experimentally calculated the thermal model parameters for an 18650 cell in cross flow. Surya Santoso provided editorial guidance and multiple rounds of technical review.

a simulated system shows significant benefits from cooling-in-the-loop control and that relatively small sacrifices in bill reduction performance can yield large increases in battery life. This trade-off function is highly dependent on the battery’s degradation mechanisms and what model is used to represent them.

Contributions of this chapter were identified as follows: (*minor*) designed and demonstrated an advanced control system to optimally reduce a customer’s electrical bill using a battery energy storage system, subject to a minimum operational life constraint.

9.1 Introduction

Time-of-use, demand charge, and other electrical tariff structures are established by utilities to reduce load factor within an area and defer expensive infrastructure upgrades. These tariffs incentivize customers to use energy during off-peak times and hence can mutually benefit both the utility and the customer. Behind-the-meter energy storage systems can reduce the electrical bill for customers within these areas by shifting load away from when it is expensive.

Designing controllers to schedule a battery energy storage system (BESS) for this and other applications has been a growing field of research [22]. In this chapter we develop a controller for a battery energy storage system (BESS) that optimally shifts a customer’s electrical useage and hence reduces their electric bill, while being constrained by a desired operational lifetime. This is a particularly difficult problem as accurate state-of-health (SoH) models depend on accurate temperature and state-of-charge (SoC) models. Previous work has used reduced order models that abstract many of the underlying degradation mechanisms [59, 64, 84]. Others use a detailed SoH model but as-

sume a constant temperature [131]. We utilize an empirical stress-factor based degradation model that accounts for time, SoC, temperature, and depth-of-discharge (DoD). To model temperature, we use a radial volumetric finite element model for a representative cell, coupled with a simplified model for air flow and temperature within the enclosure, to estimate the cell-core temperature driving degradation. To model SoC, we use a charge-based reservoir model which accounts for battery voltage and current.

The proposed controller includes a novel combination of models for SoC, Temperature, and SoH, each of which have been designed to balance accuracy and computational simplicity. These models incorporate factors that can cause degradation in complex ways and have previously not been considered together in controller design. The proposed controller can be utilized by BESS owner/operators to extend the operational lifetime of their assets and/or by BESS manufactures to reduce the risk in providing a warranty.

The remainder of this chapter, Section 9.2 formally establishes the controllers objectives and operational constraints, Section 9.3 develops the Charge-Temperature-Health BESS model used by the proposed controller, Section 9.4 then discusses the simulation results and the trade-off between controller performance and operational life, Section 9.5 summarizes the research and discusses the broader implications of the controller's design.

9.2 Problem Statement

We consider a hypothetical commercial electrical customer billed for both daily time-of-use (TOU) energy and monthly peak-demand charges. This customer decides to purchase and install a battery to reduce their electricity bill. The energy contract the customer has charges 9¢ / kWh during off-peak,

11¢ / kWh during partial-peak hours, and 15¢ during peak [10] according to the schedule in Fig.9.1 (top). The utility then charges \$50 / kW service fee according to the peak net load measured during the billing period [31]. The load data used for this problem, as shown in Fig. 9.1 (bottom), are adapted from the EPRI test circuit ‘Ckt5’ loadshape, normalized to a 1MW peak [4]. We will assume that the load and price are known a priori and that the control horizon shown is known to be the peak-load day in the billing period. Without the battery, the total bill is calculated according to (9.2.1). For this problem we assume that the net-load is always greater than zero. The total baseline electrical bill for this day is \$52,080 (\$50,000 demand, \$2,080 energy).

$$\mathbf{c}'\mathbf{l} + \$50 \max(\mathbf{l}) \quad (9.2.1)$$

where \mathbf{l} is the n length vector of load (kW), \mathbf{c} is the n length vector of TOU energy prices (\$/kWh), and \bullet' denotes a vector’s transpose. We use a time-step $\Delta t = 15$ minutes (0.25 hours), and $n = 96$ (1 day). With the addition of a BESS that can supply (-), or absorb (+), power \mathbf{p}_e , the customers cost can be modified to (9.2.2).

$$\mathbf{c}'(\mathbf{l} + \mathbf{p}_e + \mathbf{p}_{AC} + \mathbf{p}_{fan}) + \$50 \max(\mathbf{l} + \mathbf{p}_e + \mathbf{p}_{AC} + \mathbf{p}_{fan}) \quad (9.2.2)$$

where \mathbf{p}_e is the battery system power that element wise subtracts from \mathbf{l} when the battery system is discharging, \mathbf{p}_{AC} is the air-conditioning (AC) power, and \mathbf{p}_{fan} is the cooling fan power. The problem is thus formulated: design a controller to optimally calculate a vector of battery system power \mathbf{p}_e , AC power \mathbf{p}_{AC} , and fan power \mathbf{p}_{fan} that minimizes the customer’s cost without exceeding the battery’s limits. Among these limits, the controller must restrict operation such that the battery’s lifetime will meet or exceed a chosen operational life (5, 10, 15, or 20 years). Note that the solution to this narrow control problem can easily be adapted to fit many different tariff structures.

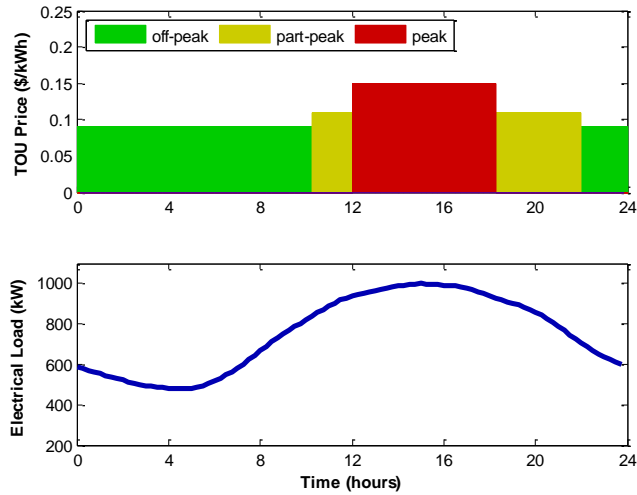


Figure 9.1: Time-of-use price schedule (top), and customer electrical load (bottom) [4]

9.3 BESS Model

This section outlines the set of differential equations and constraints that define a BESS model. This model is used for model-predictive-controller (MPC) to solve the control problem established in Section 9.2. The following

constraints define the feasible range of each decision variable.

$$p_{min} \leq p_e \leq p_{max} \quad (9.3.1a)$$

$$0 \leq p_{AC} \leq p_{AC-max} \quad (9.3.1b)$$

$$0 \leq p_{fan} \leq p_{fan-max} \quad (9.3.1c)$$

$$\varsigma_{min} \leq \varsigma \leq \varsigma_{max} \quad (9.3.1d)$$

$$v_{min} \leq v_{bat} \leq v_{max} \quad (9.3.1e)$$

$$i_{min} \leq i_{bat} \leq i_{max} \quad (9.3.1f)$$

$$T_{min} \leq T \leq T_{max} \quad (9.3.1g)$$

$$\dot{q}_{min} \leq \dot{q} \quad (9.3.1h)$$

where p_e is the BESS ac power (kW) (+ charge, - discharge), ς is the SoC (%), v_{bat} is the battery voltage (V), T is the battery's core temperature (K), and \dot{q} is the rate of degradation (% per hour). The limits p_{min} , p_{max} , v_{min} , v_{max} , i_{min} , i_{max} , T_{min} , T_{max} are box constraints on power, voltage, current, and temperature respectively. As the rate of change of SoH is always negative, \dot{q}_{min} the limit on the rate of degradation is also negative.

The relationships between decision variables are defined by differential equations. We build these relationships up in three general categories (SoC, Temperature, and SoH) each of which is covered in one of the following sections. It should be noted that BESS manufacturers may view these model parameters as proprietary while an owner/operator may view the load profile or tariff structure as similarly protected information. As the controller requires both, it may not be feasible in all circumstances for these non-technical reasons.

9.3.1 Charge Model

Charge reservoir model (CRM) is an umbrella term for the class of SoC models that define capacity in units of charge (Ah) [15]. The set of differential equations that make up the CRM used here is shown in (9.3.2). We have selected these permutations of the available models for open-circuit-voltage (VOC) and SoC to balance accuracy and simplicity.

$$p_{dc} = \phi_2 p_e^2 + \phi_1 p_e + \phi_0 \quad (9.3.2a)$$

$$p_{dc} = i_{bat} v_{bat} \quad (9.3.2b)$$

$$v_{bat} = v_{oc} + R i_{bat} \quad (9.3.2c)$$

$$v_{oc} = \alpha \zeta^3 + \beta \zeta^2 + \gamma \zeta + \delta \quad (9.3.2d)$$

$$C_{cap} \dot{\zeta} = \min(i_{bat}, 0) + \eta_c \max(i_{bat}, 0) \quad (9.3.2e)$$

where ϕ_2 , ϕ_1 , and ϕ_0 are the coefficients of a quadratic efficiency function for the inverter, p_{dc} is the dc power, i_{bat} is the dc current, R is the Thevenin source resistance of the battery equivalent circuit, v_{oc} is the battery open-circuit-voltage, α , β , γ , and δ are the coefficients for a cubic polynomial fit for open-circuit-voltage, C_{cap} is the charge capacity, η_c is the coulombic efficiency, and $\dot{\bullet}$ represents the derivative with respect to time.

9.3.2 Temperature Model

The temperature of the battery is a function of the rate of heat generated by the battery during operation and the rate of heat lost to its environment. Further, within a cell, temperature can differ significantly from the surface to the core. Fig. 9.2 shows the model used here to estimate internal

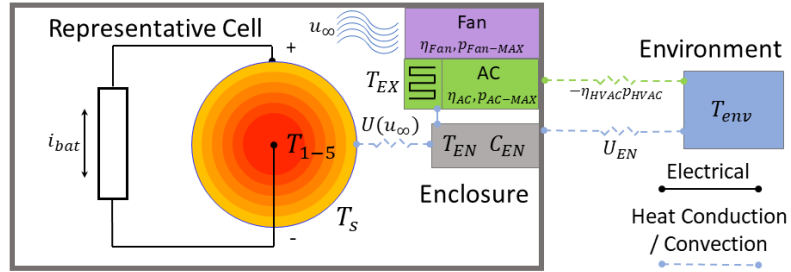


Figure 9.2: Representative-cell model with internal temperature

temperatures for use in the degradation models. The set of differential equations that make up the temperature model used here is shown in (9.3.3). In this model we include heat generated only from joule (resistive) heating as in [105]. Note that we use thermal transmittance (U) instead of its reciprocal value, thermal resistance, to simplify notation. Also, we choose five cell volumes, (9.3.3a)-(9.3.3e), each with heat generation and conduction, and a surface volume (9.3.3f), with heat conduction in and convection out, to resolve the internal temperature gradient. The number of internal volumes is to balance model accuracy with simplicity.

$$(C_i V_1) \dot{T}_1 = V_1 R(i_{bat})^2 + U_1(T_2 - T_1) \quad (9.3.3a)$$

$$(C_i V_2) \dot{T}_2 = V_2 R(i_{bat})^2 + U_1(T_1 - T_2) + U_2(T_3 - T_2) \quad (9.3.3b)$$

$$(C_i V_3) \dot{T}_3 = V_3 R(i_{bat})^2 + U_2(T_2 - T_3) + U_3(T_4 - T_3) \quad (9.3.3c)$$

$$(C_i V_4) \dot{T}_4 = V_4 R(i_{bat})^2 + U_3(T_3 - T_4) + U_4(T_5 - T_4) \quad (9.3.3d)$$

$$(C_i V_5) \dot{T}_5 = V_5 R(i_{bat})^2 + U_4(T_4 - T_5) + U_5(T_s - T_5) \quad (9.3.3e)$$

$$C_s \dot{T}_s = U_5(T_5 - T_s) + U_s(u_\infty) (T_{EN} - T_s) \quad (9.3.3f)$$

$$C_{EN} \dot{T}_{EN} = N U_s(u_\infty) (T_s - T_{EN}) + U_{env}(T_{env} - T_{EN}) \\ + U_{EX} (T_{EX} - T_{EN}) \quad (9.3.3g)$$

$$C_{EX} \dot{T}_{EX} = U_{EX} (T_{EN} - T_{EX}) - \eta_{AC} p_{AC} \quad (9.3.3h)$$

$$u_\infty = \eta_{fan} p_{fan} \quad (9.3.3i)$$

$$U_s(u_\infty) = a_f u_\infty^4 + b_f u_\infty^3 + c_f u_\infty^2 + d_f u_\infty + e_f \quad (9.3.3j)$$

where T_{1-5} are the temperatures of each internal battery element starting with the core through just below the surface (K), T_s is the battery surface temperature (K), T_{EN} is the air temperature in the enclosure (K), T_{env} is the environmental temperature (K), C_i is the battery's internal volume-fraction-specific heat capacity ($J K^{-1} \%^{-1}$), V_{1-5} are the volumetric fractions for each radial element, C_s is the battery's surface total heat capacity ($J K^{-1}$), U_{1-5} are the battery's thermal transmittances between each internal element ($W K^{-1}$), $U_s(u_\infty)$ is the polynomial fit for the thermal transmittance from the surface of the battery to the air in the enclosure which is a function of u_∞ the air velocity ($m s^{-1}$), η_{fan} is the fan's efficiency ($m s^{-1} kW^{-1}$), U_{EX} is the thermal transmittance from the AC heat exchanger to the air in the enclosure, η_{AC} is the AC unit's coefficient of performance, a_f , b_f , c_f , d_f , and e_f are the forth

order polynomial fit for the convective thermal transmittance. The function and parameter values for the thermal transmittance ($U_s(u_\infty)$) is a polynomial fit of a piecewise function of the Reynolds number, fluid density, dynamic viscosity, and several empirically derived parameters, all of which are found in [2].

9.3.3 Health Model

It is common to represent degradation based on an exponential decay function of calendar and cycle degradation [128], as shown in (9.3.4). This decay is driven by a degradation function (f_d) based on a combination of calendar life stress factors, and cycle life stress factors. The summation in (9.3.4b) represents a rainflow cycle counting algorithm which is widely used for accurate cycle-life modeling [129].

$$\varrho = e^{-f_d} \quad (9.3.4a)$$

$$f_d = S_t S_\zeta S_T + \sum_{i=1}^N w_i S_\delta S_\zeta S_T \quad (9.3.4b)$$

where ϱ is the SoH, f_d is the degradation function, S_t is the time stress factor, S_ζ is the SoC stress factor, S_T is the temperature stress factor, S_δ is the DoD stress factor, and w_i indicates a full or partial cycle.

While the rainflow cycle counting algorithm is highly accurate, it is also recursive and hence difficult to express in an optimization problem [131]. Because we know that the solution will have one cycle in the one-day control horizon, we can simplify the rainflow algorithm by removing the summation. This method has limited applicability as it would not be accurate for two days, or a day with a double peak. Hence, the set of differential equations that make up the degradation model used here is shown in (9.3.5).

$$\dot{q} = -\zeta k_t S_\zeta S_T e^{-f_d} \quad (9.3.5a)$$

$$f_d = S_t S_\zeta S_T + S_\delta S_\zeta S_T \quad (9.3.5b)$$

$$S_t = k_t t \quad (9.3.5c)$$

$$S_\zeta = e^{k_\zeta (s - s_{ref})} \quad (9.3.5d)$$

$$S_T = e^{k_T (T - T_{ref}) \frac{T_{ref}}{T}} \quad (9.3.5e)$$

$$S_\delta = a_{DoD} \delta^4 + b_{DoD} \delta^3 + c_{DoD} \delta^2 + d_{DoD} \delta + e_{DoD} \quad (9.3.5f)$$

where t is time, δ is DoD, and ζ is a scaling factor we use to modify the life of the simulated battery cells. The parameters k_t , k_ζ , k_T , a_{DoD} , b_{DoD} , c_{DoD} , d_{DoD} , and e_{DoD} enable their associated stress factors to be tuned to specific batteries. The limit on the degradation rate that specify a minimum lifetime is shown in (9.3.6).

$$\dot{q}_{min} = -\frac{\varrho}{L_{op} - L} \quad (9.3.6)$$

where L_{op} is the total operational life expectation (e.g. 15 years) and L is the current life (years that the BESS has been in service).

9.4 Results

We select model parameters to represent an 200kW/600kWh lithium-manganese-oxide type BESS. The 800Ah battery is constructed from four parallel strings, each with 14 56-V racks in series, each with 14 modules in series, where each module has 77 cells in parallel (as each cell is 2.6Ah). This battery is enclosed in a standard 12.2m (40') container. Table 9.2 shows the model parameters used here. The cell electrical and thermal parameters are derived

Table 9.1: Simulations Results

Operational Life	Mean SoC	Mean Core Temp.	Max Core Temp.	DoD	\$ Savings	% Savings
5 years	55.79%	31.08°C	45.00°C	75.00%	\$3756.32	7.77%
10 years	42.50%	25.88°C	42.27°C	73.13%	\$3559.55	7.34%
15 years	35.72%	22.76°C	32.57°C	59.47%	\$2890.92	5.88%
20 years	28.24%	20.74°C	24.23°C	38.98%	\$1979.55	3.95%

from experimental analysis on cells and a small scale system, while the degradation model parameters are taken from [128] (note that the DoD stress factor was refit as a polynomial). We choose a degradation rate scaling factor (ζ) of six to represent a low cycle life battery where the impact of the advanced controller is most clear. Limits on voltage, current, and temperature are from manufacturer specifications, and internal cell volumes and material thermal transmittance properties are retrieved from [199]. The convection heat transfer function is developed from [200]. This problem is formulated and solved with the freely downloadable modeling language ‘pyomo’ [74,75] and non-linear solver ‘ipopt’ [76].

Computation for each case takes roughly 15 seconds on a i7-7600U CPU at 2.80 GHz. The net-load, and corresponding BESS power (p_e) and SoC (ζ) trajectories for a range of selected operational life expectations are shown in Fig. 9.3. The net-load includes the air-conditioner and fan power which are optimized in conjunction with the charge/discharge power. As an illustrative example of how the air-conditioner and fan are able to cool the battery cells, Fig. 9.4 shows their power trajectories along with the temperature of the representative cell. By modeling the distribution of temperature within the battery, it is possible to plan AC/fan power outputs to limit thermal degra-

Table 9.2: Battery Energy Storage System Model Parameters I

Name	Symbol	Value
Total String Charge Capacity	C_{cap}	800 Ah
Coulombic Efficiency	η_c	94.6 %
Self-Discharge Current	i_{sd}	0.50 A
Battery Internal Resistance	R	55 m Ω
Maximum Power Charge	p_{max}	200 kW
Maximum Power Discharge	p_{min}	-200 kW
Maximum SoC	S_{max}	95 %
Minimum SoC	S_{min}	20 %
Maximum Cell Voltage	v_{max}	4.2 V
Minimum Cell Voltage	v_{min}	3.3 V
Maximum Current Charge	i_{max}	4.0 A
Maximum Current Discharge	i_{min}	-2.6 A
Number of Cells Total in BESS	N	60,368
Battery Internal Heat Capacity	C_i	67.08 J/ $^{\circ}\text{C}$
Battery Surface Heat Capacity	C_o	2.45 J/ $^{\circ}\text{C}$
Maximum Temperature	T_{max}	45 $^{\circ}\text{C}$
Minimum Temperature	T_{min}	20 $^{\circ}\text{C}$
Enclosure Thermal Transmittance	U_{env}	1 W/ $^{\circ}\text{C}$
Enclosure Heat Capacity	C_{EN}	63 kJ/ $^{\circ}\text{C}$
Max AC power	$p_{\text{AC-max}}$	30 kW
AC Coefficient of Performance	η_{AC}	4
Max Fan power	$p_{\text{fan-max}}$	5 kW
Fan Efficiency	η_{fan}	0.6 (m/s)/kW
Heat Exchanger Heat Capacity	C_{EX}	0.5 kJ/ $^{\circ}\text{C}$
Heat Exchanger Thermal Transmittance	U_{EX}	9.18 W/ $^{\circ}\text{C}$
Degradation Rate Scaling Factor	ζ	6
Thermal Degradation Constant	k_T	0.0693
Time Degradation Constant	k_t	1.49e-6
SoC Degradation Constant	k_{ζ}	1.04
Reference SoC	S_{ref}	50 %
Reference Temperature	T_{ref}	25 $^{\circ}\text{C}$

Note: these model parameters are meant to represent a hypothetical battery system and do not necessarily reflect any specific equipment.

Table 9.3: Battery Energy Storage System Model Parameters II

Inverter Efficiency	ϕ_0	ϕ_1	ϕ_2		
Coefficients	-2.0503 e-04	0.9953	-6.163		
Open-Circuit-Voltage	α	β	γ	δ	
$0.2 \leq \varsigma \leq 0.95$	320.377	-368.742	201.004	669.282	
Internal Cell Volumes	(core) Vol. 1	Vol. 2	Vol. 3	Vol. 4	Vol. 5
Volume Proportion	4%	12%	20%	28%	36%
Surface Thermal Transmittance	a_f	b_f	c_f	d_f	e_f
$U_s(u_\infty)$	-1.286 e-05	6.086 e-04	-1.048 e-02	1.050 e-01	9.426 e-02
Internal Thermal Transmittance	U_1	U_2	U_3	U_4	U_5
U_{1-5}	0.245	0.490	0.735	0.980	1.225
DoD Stress Factor	a_{DoD}	b_{DoD}	c_{DoD}	d_{DoD}	e_{DoD}
Polynomial	1.158	-1.366	0.664	0.107	0.012

Note: these model parameters are meant to represent a hypothetical battery system and do not necessarily reflect any specific equipment.

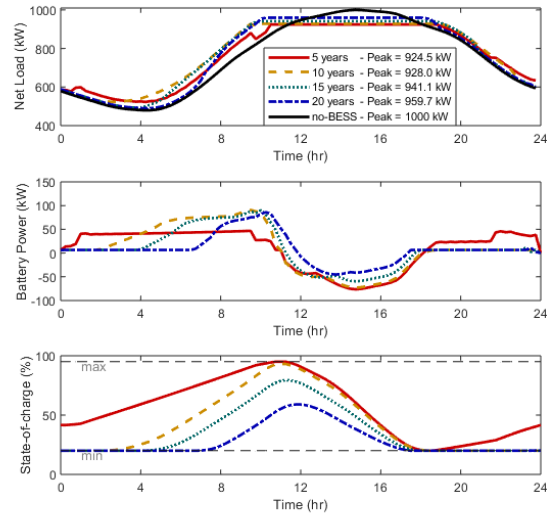


Figure 9.3: Optimal net-load (top), charge/discharge (middle), and SoC (bottom) schedules for different operational life expectations

dation based on the battery core temperature.

The reason that small changes in the schedule result in large changes in the operational life is because of the compounding effect of the stress factors. To show this, we will consider the transition from the schedule under a 5 year operational life to a 10 year operational life. This change yields a 12.91% reduction in SoC stress factor, a 29.47% reduction in temperature stress factor, and a 5.29% reduction in the DoD stress factor. These in turn reduce the degradation function (f_d) by 41.83% which compounds with the SoC and temperature stress factor to reduce the the degradation rate by half.

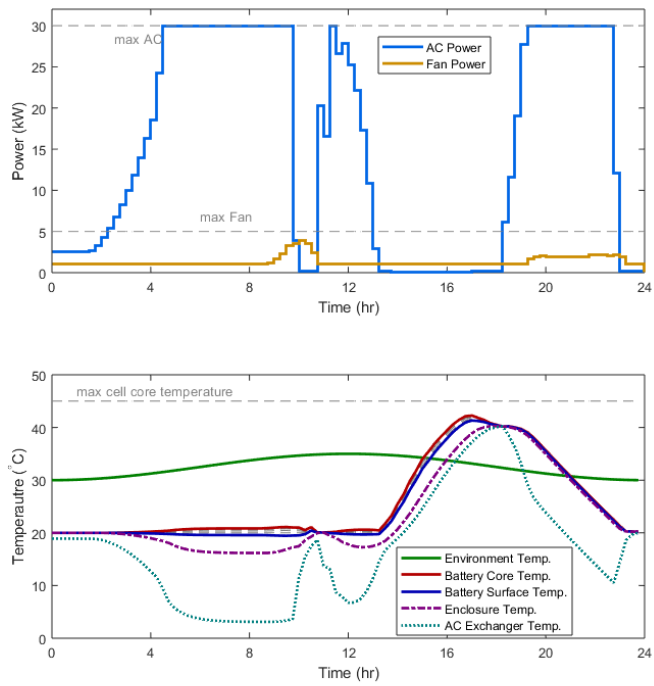


Figure 9.4: Example AC power, fan power (top), cell, enclosure, and heat-exchanger temperature (bottom) results for 10-year operational life expectation

9.5 Summary

This chapter demonstrates the development and application of an advanced BESS controller. This controller optimally schedules the power draw for charge/discharge, air-conditioning, and forced air circulation based on a combined electrical, thermal, and degradation model of a lithium-ion battery system. This controller is applied to an example BESS to maximally reduce the bill for a simulated electric customer under TOU energy and peak-demand charges, subject to a selected minimum operational life.

The developed controller can reduce the electric bill by 8%, if a 5-year operational life is selected, to 4%, for 20-years. While the model was constructed using reasonable parameters, these results may not represent the optimal life/performance trade-off for any specific BESS. However, we can conclude more generally that a large gain in life may be derived from a small sacrifice in performance. This is a result of the compounding effects of stress-factors on battery degradation. Further, we can conclude that coordinating the air-conditioning and circulation systems with charge and discharge can be advantageous to optimal control as these systems can play a significant role in reducing cell core temperature and hence prolonging life. This controller can be used by manufactures or owner/operators to improve the value and operational life of BESS.

Bibliography

- [1] D. K. Karthikeyan, G. Sikha, and R. E. White, “Thermodynamic model development for lithium intercalation electrodes,” *J. Power Sources*, vol. 185, pp. 1398–1407, 2008. [Online]. Available: <https://doi.org/10.1016/j.jpowsour.2008.07.077>
- [2] T. Bergman, A. Lavine, F. Incropera, D. Dewitt, and L. Ratts, *Fundamentals of Heat and Mass Transfer*. John Wiley & Sons, 2011.
- [3] V. Ramadesigan, P. W. C. Northrop, S. De, S. Santhanagopalan, R. D. Braatz, and V. R. Subramanian, “Modeling and simulation of lithium-ion batteries from a systems engineering perspective,” *J. Electrochem. Soc.*, vol. 159, no. 3, pp. R31–R45, 2012. [Online]. Available: <https://doi.org/10.1149/2.018203jes>
- [4] EPRI OpenDSS Test Circuits, “Ckt5 Loadshape,” Online, revision 2236. [Online]. Available: <http://svn.code.sf.net/p/electricdss/code/trunk/Distrib/EPRITestCircuits/ckt5/>
- [5] G. L. Plett, *Battery Management Systems: Volume 1, Battery Modeling*. Artech House, 2015.
- [6] T. Lambert, P. Gilman, and P. Lilienthal, “Micropower system modeling with HOMER,” in *Integration of Alternative Sources of Energy*. John Wiley & Sons, Inc., apr 2006, pp. 379–418. [Online]. Available: <https://doi.org/10.1002/0471755621.ch15>

- [7] J. F. Manwell and J. G. McGowan, "Lead acid battery storage model for hybrid energy system," *Solar Energy*, vol. 50, no. 5, pp. 399–405, May 1993. [Online]. Available: [https://doi.org/10.1016/0038-092X\(93\)90060-2](https://doi.org/10.1016/0038-092X(93)90060-2)
- [8] T. Kim and W. Qiao, "A hybrid battery model capable of capturing dynamic circuit characteristics and nonlinear capacity effects," *IEEE Trans. Energy Convers.*, vol. 26, no. 4, pp. 1172–1180, Dec. 2011. [Online]. Available: <https://doi.org/10.1109/TEC.2011.2167014>
- [9] V. Viswanathan, D. W. Daiwon Choi, S. T. Wu Xu, R. E. Williford, J.-G. Zhang, J. Liu, and Z. Yang, "Effect of entropy change of lithium intercalation in cathodes and anodes on Li-ion battery thermal management," *J. Power Sources*, 2010. [Online]. Available: <https://doi.org/10.1016/j.jpowsour.2009.11.103>
- [10] T. A. Nguyen and R. H. Byrne, "Maximizing the cost-savings for time-of-use and net-metering customers using behind-the-meter energy storage systems," in *North American Power Symposium (NAPS)*, Sep. 2017. [Online]. Available: <https://doi.org/10.1109/NAPS.2017.8107380>
- [11] M. Arbabzadeh, R. Sioshansi, J. X. Johnson, and G. A. Keoleian, "The role of energy storage in deep decarbonization of electricity production," *Nature Communications*, vol. 10, no. 3413, 2019. [Online]. Available: <https://doi.org/10.1038/s41467-019-11161-5>
- [12] A. A. Akhil, G. Huff, A. B. Currier, B. C. Kaun, D. M. Rastler, S. B. Chen, A. L. Cotter, D. T. Bradshaw, and W. D. Gauntlett, "DOE/EPRI 2013 Electricity Storage Handbook

in Collaboration with NRECA,” Sandia National Laboratories, techreport, Sep. 2013, SAND2013-5131. [Online]. Available: <http://www.sandia.gov/ess/publications/SAND2013-5131.pdf>

- [13] D. Rosewater, D. Copp, T. Nguyen, R. Byrne, and S. Santoso, “Battery energy storage models for optimal control,” *IEEE Access*, Dec. 2019.
- [14] D. Rosewater, B. Schenkman, and S. Santoso, “Adaptive modeling process for a battery energy management system,” in *2020 SPEEDAM, to be published.*, 2020.
- [15] D. Rosewater, S. Ferreira, D. Schoenwald, J. Hawkins, and S. Santoso, “Battery energy storage state-of-charge forecasting: Models, optimization, and accuracy,” *IEEE Transactions on Smart Grid*, 2018.
- [16] D. Conover, S. Ferreira, A. Crawford, D. Schoenwald, J. Fuller, D. Rosewater, S. Gourisetti, and V. Viswanathan, “Protocol for Uniformly Measuring and Expressing the Performance of Energy Storage Systems,” Sandia National Laboratories and Pacific Northwest National Laboratories, techreport, 2016, SAND2016-3078R. [Online]. Available: <http://www.sandia.gov/ess/publications/SAND2016-3078R.pdf>
- [17] D. Rosewater, P. Scott, and S. Santoso, “Application of a uniform testing protocol for energy storage systems,” in *IEEE Power Energy Society General Meeting*, July 2017, pp. 1–5. [Online]. Available: <https://doi.org/10.1109/PESGM.2017.8274603>
- [18] D. Rosewater, R. Baldick, and S. Santoso, “Risk-averse model predictive control design for battery energy storage systems,” *IEEE*

- Trans. Smart Grid*, 2019. [Online]. Available: <https://doi.org/10.1109/TSG.2019.2946130>
- [19] D. Rosewater, Q. Nguyen, and S. Santoso, “Optimal field voltage and energy storage control for stabilizing synchronous generators on flexible ac transmission systems,” in *IEEE/PES Transmission and Distribution Conference and Exposition*, April 2018, pp. 1–9. [Online]. Available: <https://doi.org/10.1109/TDC.2018.8440436>
- [20] P. Siratarnsophon, K. W. Lao, D. Rosewater, and S. Santoso, “A voltage smoothing algorithm using energy storage pq control in pv-integrated power grid,” *IEEE Trans. Power Del.*, 2019.
- [21] D. Rosewater, A. Headley, F. A. Mier, and S. Santoso, “Optimal control of a battery energy storage system with a charge-temperature-health model,” in *IEEE Power and Energy Society General Meeting*, Aug. 2019.
- [22] R. H. Byrne, T. A. Nguyen, D. A. Copp, B. R. Chalamala, and I. Gyuk, “Energy management and optimization methods for grid energy storage systems,” *IEEE Access*, vol. 6, pp. 13 231–13 260, Aug. 2018. [Online]. Available: <https://doi.org/10.1109/ACCESS.2017.2741578>
- [23] D. N. T. How, M. A. Hannan, M. S. Hossain Lipu, and P. J. Ker, “State of charge estimation for lithium-ion batteries using model-based and data-driven methods: A review,” *IEEE Access*, vol. 7, pp. 136 116–136 136, 2019. [Online]. Available: <https://doi.org/10.1109/ACCESS.2019.2942213>
- [24] B. Hredzak, V. G. Agelidis, and M. Jang, “A model predictive control system for a hybrid battery-ultracapacitor power source,” *IEEE Trans.*

- Power Electron.*, vol. 29, no. 3, pp. 1469–1479, March 2014. [Online]. Available: <https://doi.org/10.1109/TPEL.2013.2262003>
- [25] M. A. Xavier and M. S. Trimboli, “Lithium-ion battery cell-level control using constrained model predictive control and equivalent circuit models,” *J. Power Sources*, vol. 285, pp. 374 – 384, 2015. [Online]. Available: <https://doi.org/10.1016/j.jpowsour.2015.03.074>
- [26] J. Donadee and J. Wang, “AGC signal modeling for energy storage operations,” *IEEE Trans. Power Syst.*, vol. 29, no. 5, pp. 2567–2568, 2014. [Online]. Available: <https://doi.org/10.1109/tpwrs.2014.2301592>
- [27] E. Perez, H. Beltran, N. Aparicio, and P. Rodriguez, “Predictive power control for PV plants with energy storage,” *IEEE Trans. Sustain. Energy*, vol. 4, no. 2, pp. 482–490, April 2013. [Online]. Available: <https://doi.org/10.1109/TSTE.2012.2210255>
- [28] H. S. Ko and J. Jatskevich, “Power quality control of wind-hybrid power generation system using fuzzy-LQR controller,” *IEEE Trans. Energy Convers.*, vol. 22, no. 2, pp. 516–527, June 2007. [Online]. Available: <https://doi.org/10.1109/TEC.2005.858092>
- [29] R. Klein, N. A. Chaturvedi, J. Christensen, J. Ahmed, R. Findeisen, and A. Kojic, “Electrochemical model based observer design for a lithium-ion battery,” *IEEE Trans. Control Syst. Technol.*, vol. 21, no. 2, pp. 289–301, March 2013. [Online]. Available: <https://doi.org/10.1109/TCST.2011.2178604>
- [30] M. T. Lawder, B. Suthar, P. W. C. Northrop, S. De, C. M. Hoff, O. Leiternann, M. L. Crow, S. Santhanagopalan, and V. R.

- Subramanian, “Battery energy storage system (BESS) and battery management system (BMS) for grid-scale applications,” *Proceedings of the IEEE*, vol. 102, no. 6, pp. 1014–1030, June 2014. [Online]. Available: <https://doi.org/10.1109/JPROC.2014.2317451>
- [31] J. McLaren and S. Mullendore, “Identifying potential markets for behind-the-meter battery energy storage: A survey of U.S. demand charges,” National Renewable Energy Laboratory, Tech. Rep., Aug. 2017, nREL/BR-6A20-68963. [Online]. Available: <https://www.nrel.gov/docs/fy17osti/68963.pdf>
- [32] A. Y. S. Lam, K.-C. Leung, and V. O. K. Li, “Capacity estimation for vehicle-to-grid frequency regulation services with smart charging mechanism,” *IEEE Trans. Smart Grid*, vol. 7, no. 1, pp. 156–166, 2016. [Online]. Available: <https://doi.org/10.1109/tsg.2015.2436901>
- [33] Modeling and V. W. Group, “WECC battery storage dynamic modeling guideline,” Western Electricity Coordinating Council, Tech. Rep., 2016. [Online]. Available: https://www.wecc.org/Reliability/WECCBatteryStorageGuidelineupdates_Bo4-5-17SLT4-7-17XXSC.docx
- [34] H. Mohsenian-Rad, “Coordinated price-maker operation of large energy storage units in nodal energy markets,” *IEEE Trans. Power Syst.*, vol. 31, no. 1, pp. 786–797, 2016. [Online]. Available: <https://doi.org/10.1109/tpwrs.2015.2411556>
- [35] J. Donadee and M. Ilic, “Stochastic optimization of grid to vehicle frequency regulation capacity bids,” *IEEE Trans. Smart Grid*, vol. 5, no. 2, pp. 1061–1069, 2014. [Online]. Available: <https://doi.org/10.1109/tsg.2013.2290971>

- [36] T. Erseghe, A. Zanella, and C. G. Codemo, “Optimal and compact control policies for energy storage units with single and multiple batteries,” *IEEE Trans. Smart Grid*, vol. 5, no. 3, pp. 1308–1317, May 2014. [Online]. Available: <https://doi.org/10.1109/TSG.2014.2303824>
- [37] Y. Huang, S. Mao, and R. M. Nelms, “Adaptive electricity scheduling in microgrids,” *IEEE Trans. Smart Grid*, vol. 5, no. 1, pp. 270–281, Jan 2014. [Online]. Available: <https://doi.org/10.1109/TSG.2013.2282823>
- [38] C. Suazo-Martinez, E. Pereira-Bonvallet, R. Palma-Behnke, and X.-P. Zhang, “Impacts of energy storage on short term operation planning under centralized spot markets,” *IEEE Trans. Smart Grid*, vol. 5, no. 2, pp. 1110–1118, 2014. [Online]. Available: <https://doi.org/10.1109/tsg.2013.2281828>
- [39] L. H. Macedo, J. F. Franco, M. J. Rider, and R. Romero, “Optimal operation of distribution networks considering energy storage devices,” *IEEE Trans. Smart Grid*, vol. 6, no. 6, pp. 2825–2836, 2015. [Online]. Available: <https://doi.org/10.1109/tsg.2015.2419134>
- [40] R. H. Byrne, M. K. Donnelly, V. W. Loose, and D. J. Trudnowski, “Methodology to determine the technical performance and value proposition for grid-scale energy storage systems,” Sandia National Laboratories, techreport SAND2012-10639, 2012. [Online]. Available: <https://www.sandia.gov/ess-ssl/publications/SAND2012-10639.pdf>
- [41] Y. Wen, C. Guo, H. Pandzic, and D. S. Kirschen, “Enhanced security-constrained unit commitment with emerging utility-scale energy storage,” *IEEE Trans. Power Syst.*, vol. 31, no. 1, pp. 652–662, 2016. [Online]. Available: <https://doi.org/10.1109/tpwrs.2015.2407054>

- [42] J. Tant, F. Geth, D. Six, P. Tant, and J. Driesen, “Multiobjective battery storage to improve PV integration in residential distribution grids,” *IEEE Trans. Sustain. Energy*, vol. 4, no. 1, pp. 182–191, Jan 2013. [Online]. Available: <https://doi.org/10.1109/TSTE.2012.2211387>
- [43] T. Wang, H. Kamath, and S. Willard, “Control and optimization of grid-tied photovoltaic storage systems using model predictive control,” *IEEE Trans. Smart Grid*, vol. 5, no. 2, pp. 1010–1017, 2014. [Online]. Available: <https://doi.org/10.1109/TSG.2013.2292525>
- [44] N. Jayasekara, M. A. S. Masoum, and P. J. Wolfs, “Optimal operation of distributed energy storage systems to improve distribution network load and generation hosting capability,” *IEEE Trans. Sustain. Energy*, vol. 7, no. 1, pp. 250–261, Jan 2016. [Online]. Available: <https://doi.org/10.1109/TSTE.2015.2487360>
- [45] *OpenDSS STORAGE Element and STORAGECONTROLLER Element*, EPRI, Mar. 2011. [Online]. Available: <http://svn.code.sf.net/p/electricdss/code/trunk/Distrib/Doc/OpenDSS%20STORAGE%20Element.pdf>
- [46] P. P. Zeng, Z. Wu, X. Zhang, C. Liang, and Y. Zhang, “Model predictive control for energy storage systems in a network with high penetration of renewable energy and limited export capacity,” in *2014 Power Systems Computation Conference*, Aug 2014, pp. 1–7. [Online]. Available: <https://doi.org/10.1109/PSCC.2014.7038359>
- [47] P. Malysz, S. Sirouspour, and A. Emadi, “An optimal energy storage control strategy for grid-connected microgrids,” *IEEE Trans. Smart*

- Grid*, vol. 5, no. 4, pp. 1785–1796, July 2014. [Online]. Available: <https://doi.org/10.1109/TSG.2014.2302396>
- [48] Vank348, “GridLAB-D Wiki: Battery Model,” Online, 2018. [Online]. Available: <http://gridlab-d.shoutwiki.com/wiki/Battery>
- [49] X. Qiu, T. A. Nguyen, J. D. Guggenberger, M. L. Crow, and A. C. Elmore, “A field validated model of a vanadium redox flow battery for microgrids,” *IEEE Trans. Smart Grid*, vol. 5, no. 4, pp. 1592–1601, July 2014. [Online]. Available: <https://doi.org/10.1109/TSG.2014.2310212>
- [50] G. Zini, *Green electrical energy storage*. McGraw-Hill Education Ltd, 2016. [Online]. Available: http://www.ebook.de/de/product/26046671/gabriele_zini_green_electrical_energy_storage.html
- [51] T. A. Nguyen, D. A. Copp, R. H. Byrne, and B. R. Chalamala, “Market evaluation of energy storage systems incorporating technology-specific nonlinear models,” *IEEE Trans. Power Syst.*, 2019. [Online]. Available: <https://doi.org/10.1109/TPWRS.2019.2909764>
- [52] D. A. Copp, T. A. Nguyen, and R. H. Byrne, “Adaptive model predictive control for real-time dispatch of energy storage systems,” in *American Control Conference (ACC)*. IEEE, 2019, pp. 3611–3616. [Online]. Available: <https://ieeexplore.ieee.org/document/8814902>
- [53] S. Kim, J. Kim, K. Cho, and G. Byeon, “Optimal operation control for multiple besss of a large-scale customer under time-based pricing,” *IEEE Trans. Power Syst.*, vol. 33, no. 1, pp. 803–816, Jan 2018. [Online]. Available: <https://doi.org/10.1109/TPWRS.2017.2696571>

- [54] S. Grillo, M. Marinelli, S. Massucco, and F. Silvestro, "Optimal management strategy of a battery-based storage system to improve renewable energy integration in distribution networks," *IEEE Trans. Smart Grid*, vol. 3, no. 2, pp. 950–958, 2012. [Online]. Available: <https://doi.org/10.1109/tsg.2012.2189984>
- [55] S. Teleke, M. E. Baran, S. Bhattacharya, and A. Q. Huang, "Optimal control of battery energy storage for wind farm dispatching," *IEEE Trans. Energy Convers.*, vol. 25, no. 3, pp. 787–794, 2010. [Online]. Available: <https://doi.org/10.1109/tec.2010.2041550>
- [56] X. Feng, H. B. Gooi, and S. X. Chen, "Hybrid energy storage with multimode fuzzy power allocator for PV systems," *IEEE Trans. Sustain. Energy*, vol. 5, no. 2, pp. 389–397, 2014. [Online]. Available: <https://doi.org/10.1109/tste.2013.2290543>
- [57] L. Xiong, W. Peng, and L. Poh Chiang, "A hybrid AC/DC microgrid and its coordination control," *IEEE Trans. Smart Grid*, vol. 2, no. 2, pp. 278–286, 2011. [Online]. Available: <https://doi.org/10.1109/tsg.2011.2116162>
- [58] H. H. Abdeltawab and Y. A. R. I. Mohamed, "Market-oriented energy management of a hybrid wind-battery energy storage system via model predictive control with constraint optimizer," *IEEE Trans. Ind. Electron.*, vol. 62, no. 11, pp. 6658–6670, Nov 2015. [Online]. Available: <https://doi.org/10.1109/TIE.2015.2435694>
- [59] S. J. Moura, J. L. Stein, and H. K. Fathy, "Battery-health conscious power management in plug-in hybrid electric vehicles via electrochemical

- modeling and stochastic control,” *IEEE Trans. Control Syst. Technol.*, vol. 21, no. 3, pp. 679–694, May 2013. [Online]. Available: <https://doi.org/10.1109/TCST.2012.2189773>
- [60] Y. Liu, Z. Li, Z. Lin, K. Zhao, and Y. Zhu, “Multi-objective optimization of energy management strategy on hybrid energy storage system based on radau pseudospectral method,” *IEEE Access*, vol. 7, pp. 112 483–112 493, 2019. [Online]. Available: <https://doi.org/10.1109/ACCESS.2019.2935188>
- [61] M. Chen and G. Rincon-Mora, “Accurate electrical battery model capable of predicting runtime and I-V performance,” *IEEE Trans. Energy Convers.*, vol. 21, no. 2, pp. 504–511, jun 2006. [Online]. Available: <https://doi.org/10.1109/tec.2006.874229>
- [62] A. Rahmoun and H. Biechl, “Modelling of Li-ion batteries using equivalent circuit diagrams,” *Przegląd Elektrotechniczny*, vol. 88, no. 7, pp. 152–156, Jan. 2012. [Online]. Available: <http://www.red.pe.org.pl/articles/2012/7b/40.pdf>
- [63] M. Ceraolo, “New dynamical models of lead-acid batteries,” *IEEE Trans. Power Syst.*, vol. 15, no. 4, pp. 1184–1190, Nov 2000. [Online]. Available: <https://doi.org/10.1109/59.898088>
- [64] H. E. Perez, X. Hu, S. Dey, and S. J. Moura, “Optimal charging of Li-Ion batteries with coupled electro-thermal-aging dynamics,” *IEEE Trans. Veh. Technol.*, vol. 66, no. 9, pp. 7761–7770, Sept 2017. [Online]. Available: <https://doi.org/10.1109/TVT.2017.2676044>

- [65] A. M. Gee, F. V. P. Robinson, and R. W. Dunn, “Analysis of battery lifetime extension in a small-scale wind-energy system using supercapacitors,” *IEEE Trans. Energy Convers.*, vol. 28, no. 1, pp. 24–33, mar 2013. [Online]. Available: <https://doi.org/10.1109/tec.2012.2228195>
- [66] S. Santhanagopalan, Q. Guo, P. Ramadass, and R. E. White, “Review of models for predicting the cycling performance of lithium ion batteries,” *J. Power Sources*, vol. 156, no. 2, pp. 620 – 628, 2006. [Online]. Available: <https://doi.org/10.1016/j.jpowsour.2005.05.070>
- [67] S. Santhanagopalan, Q. Guo, and R. E. White, “Parameter estimation and model discrimination for a lithium-ion cell,” *J. Electrochem. Soc.*, vol. 154, no. 3, pp. A198–A206, 2007. [Online]. Available: <https://doi.org/10.1149/1.2422896>
- [68] M. Guo and R. White, “Thermal model for lithium ion battery pack with mixed parallel and series configuration,” *J. Electrochem. Soc.*, vol. 158, no. 10, pp. A1166–A1176, 2011. [Online]. Available: <https://doi.org/10.1149/1.3624836>
- [69] M. Torchio, L. Magni, R. D. Braatz, and D. M. Raimondo, “Design of piecewise affine and linear time-varying model predictive control strategies for advanced battery management systems,” *J. Electrochem. Soc.*, vol. 164, no. 4, pp. A949–A959, 2017. [Online]. Available: <https://doi.org/10.1149/2.0201706jes>
- [70] M. Torchio, N. A. Wolff, D. M. Raimondo, L. Magni, U. Kreuer, R. B. Gopaluni, J. A. Paulson, and R. D. Braatz, “Real-time model

- predictive control for the optimal charging of a lithium-ion battery,” in *American Control Conference (ACC)*, July 2015, pp. 4536–4541. [Online]. Available: <https://doi.org/10.1109/ACC.2015.7172043>
- [71] M. Bahramipanah, D. Torregrossa, R. Cherkaoui, and M. Paolone, “A decentralized adaptive model-based real-time control for active distribution networks using battery energy storage systems,” *IEEE Trans. Smart Grid*, vol. 9, no. 4, pp. 3406 – 3418, 2016. [Online]. Available: <https://doi.org/10.1109/tsg.2016.2631569>
- [72] R. Baldick, *Applied Optimization: Formulation and Algorithms for Engineering Systems*. Cambridge University Press, 2006.
- [73] S. Boyd and L. Vandenberghe, *Convex Optimization*, 1st ed. Cambridge University Press, 2004. [Online]. Available: <https://web.stanford.edu/~boyd/cvxbook/>
- [74] W. E. Hart, C. D. Laird, J.-P. Watson, D. L. Woodruff, G. A. Hackebeil, B. L. Nicholson, and J. D. Siirola, *Pyomo—optimization modeling in python*, 2nd ed. Springer Science & Business Media, 2017, vol. 67.
- [75] W. E. Hart, J. Watson, and D. L. Woodruff, “Pyomo: modeling and solving mathematical programs in python,” *Math. Prog. Comp.*, vol. 3, no. 3, pp. 219–260, Aug. 2011. [Online]. Available: <https://doi.org/10.1007/s12532-011-0026-8>
- [76] A. Wächter and L. T. Biegler, “On the implementation of an interior-point filter line-search algorithm for large-scale nonlinear programming,” *Math. Program.*, vol. 106, no. 1, pp. 25–57, Mar 2006. [Online]. Available: <https://doi.org/10.1007/s10107-004-0559-y>

- [77] D. Linden and T. Reddy, *Linden's Handbook of Batteries*. McGraw Hill, 2011.
- [78] A. R. Sparacino, G. F. Reed, R. J. Kerestes, B. M. Grainger, and Z. T. Smith, "Survey of battery energy storage systems and modeling techniques," in *IEEE Power and Energy Society General Meeting*, July 2012, pp. 1–8. [Online]. Available: <https://doi.org/10.1109/PESGM.2012.6345071>
- [79] D. Cadar, D. Petreus, I. Ciocan, and P. Dobra, "An improvement on empirical modelling of the batteries," in *32nd International Spring Seminar on Electronics Technology*, May 2009, pp. 1–6. [Online]. Available: <https://doi.org/10.1109/ISSE.2009.5207015>
- [80] G. Wang, M. Ciobotaru, and V. G. Agelidis, "Power management for improved dispatch of utility-scale PV plants," *IEEE Trans. Power Syst.*, vol. 31, no. 3, pp. 2297–2306, May 2016. [Online]. Available: <https://doi.org/10.1109/TPWRS.2015.2459065>
- [81] R. Xiong, J. Cao, Q. Yu, H. He, and F. Sun, "Critical review on the battery state of charge estimation methods for electric vehicles," *IEEE Access*, vol. 6, pp. 1832–1843, 2018. [Online]. Available: <https://doi.org/10.1109/ACCESS.2017.2780258>
- [82] Y.-H. Kim and H.-D. Ha, "Design of interface circuits with electrical battery models," *IEEE Trans. Ind. Electron.*, vol. 44, no. 1, pp. 81–86, Feb 1997. [Online]. Available: <https://doi.org/10.1109/41.557502>
- [83] A. Hentunen, T. Lehmuspelto, and J. Suomela, "Time-domain parameter extraction method for thvenin-equivalent circuit battery

- models,” *IEEE Trans. Energy Convers.*, vol. 29, no. 3, pp. 558–566, Sept 2014. [Online]. Available: <https://doi.org/10.1109/TEC.2014.2318205>
- [84] Y. Riffonneau, S. Bacha, F. Barruel, and S. Ploix, “Optimal power flow management for grid connected PV systems with batteries,” *IEEE Trans. Sustain. Energy*, vol. 2, no. 3, pp. 309–320, jul 2011. [Online]. Available: <https://doi.org/10.1109/tste.2011.2114901>
- [85] O. Tremblay and L. Dessaint, “Experimental validation of a battery dynamic model for EV applications,” *World Electric Vehicle Journal*, vol. 3, May 2009. [Online]. Available: <https://pdfs.semanticscholar.org/8f16/68ffef08c83a3a69f8f3c557d04cd9a5ffc2.pdf>
- [86] H. U. R. Habib, S. Wang, M. R. Elkadeem, and M. F. Elmorshedy, “Design optimization and model predictive control of a standalone hybrid renewable energy system: A case study on a small residential load in pakistan,” *IEEE Access*, vol. 7, pp. 117 369–117 390, 2019. [Online]. Available: <https://doi.org/10.1109/ACCESS.2019.2936789>
- [87] D. L. King, S. Gonzalez, G. M. Galbraith, and W. E. Boyson, “Performance model for grid-connected photovoltaic inverters,” Sandia National Laboratories, techreport, 2007, SAND2007-5036. [Online]. Available: <http://energy.sandia.gov/download/21044/>
- [88] W. Bower, C. Whitaker, W. Erdman, M. Behnke, and M. Fitzgerald, “Performance test protocol for evaluating inverters used in grid-connected photovoltaic systems,” Sandia National Laboratories, Tech. Rep., 2004. [Online]. Available: https://www.gosolarcalifornia.ca.gov/equipment/documents/2004-11-22_Test_Protocol.pdf

- [89] G. L. Plett, *Battery Management Systems: Volume 2, Equivalent-Circuit Methods*. Artech House, 2016.
- [90] L. McCurlie, M. Preindl, and A. Emadi, “Fast model predictive control for redistributive lithium-ion battery balancing,” *IEEE Trans. Ind. Electron.*, vol. 64, no. 2, pp. 1350–1357, Feb 2017. [Online]. Available: <https://doi.org/10.1109/TIE.2016.2611488>
- [91] J. Liu, G. Li, and H. K. Fathy, “An extended differential flatness approach for the health-conscious nonlinear model predictive control of lithium-ion batteries,” *IEEE Trans. Control Syst. Technol.*, vol. 25, no. 5, pp. 1882–1889, Sep. 2017. [Online]. Available: <https://doi.org/10.1109/TCST.2016.2624143>
- [92] X. Han, M. Ouyang, L. Lu, and J. Li, “Simplification of physics-based electrochemical model for lithium ion battery on electric vehicle. part I: Diffusion simplification and single particle model,” *J. Power Sources*, vol. 278, pp. 802 – 813, 2015. [Online]. Available: <https://doi.org/10.1016/j.jpowsour.2014.12.101>
- [93] M. Pathak, S. Kolluri, and V. R. Subramanian, “Generic model control for lithium-ion batteries,” *J. Electrochem. Soc.*, vol. 164, no. 6, pp. A973–A986, 2017. [Online]. Available: <https://doi.org/10.1149/2.1521704jes>
- [94] N. A. Chaturvedi, R. Klein, J. Christensen, J. Ahmed, and A. Kojic, “Modeling, estimation, and control challenges for lithium-ion batteries,” in *Proceedings of the 2010 American Control Conference*, June 2010, pp. 1997–2002. [Online]. Available: <https://doi.org/10.1109/ACC.2010.5531623>

- [95] G. Ning and B. N. Popov, “Cycle life modeling of lithium-ion batteries,” *J. Electrochem. Soc.*, vol. 151, no. 10, pp. A1584–A1591, 2004. [Online]. Available: <https://doi.org/10.1149/1.1787631>
- [96] W. M. Deen and K. E. Gubbins, *Analysis of Transport Phenomena*. Oxford University Press, 1998.
- [97] C. Y. Wang and W. B. Gu, “Micro-macroscopic coupled modeling of batteries and fuel cells: I. model development,” *J. Electrochem. Soc.*, vol. 145, no. 10, pp. 3407–3417, 1998. [Online]. Available: <https://doi.org/10.1149/1.1838820>
- [98] M. Guo, G. Sikha, and R. E. White, “Single-particle model for a lithium-ion cell: Thermal behavior,” *J. Electrochem. Soc.*, vol. 158, no. 2, pp. A122–A132, 2011. [Online]. Available: <https://doi.org/10.1149/1.3521314>
- [99] X. Han, M. Ouyang, L. Lu, and J. Li, “Simplification of physics-based electrochemical model for lithium ion battery on electric vehicle. part II: Pseudo-two-dimensional model simplification and state of charge estimation,” *J. Power Sources*, vol. 278, pp. 814 – 825, 2015. [Online]. Available: <https://doi.org/10.1016/j.jpowsour.2014.08.089>
- [100] A. Jokar, B. Rajabloo, M. Désilets, and M. Lacroix, “Review of simplified pseudo-two-dimensional models of lithium-ion batteries,” *J. Power Sources*, vol. 327, pp. 44 – 55, 2016. [Online]. Available: <https://doi.org/10.1016/j.jpowsour.2016.07.036>
- [101] T. F. Fuller, M. Doyle, and J. Newman, “Simulation and optimization of the dual lithium ion insertion cell,” *J. Electrochem. Soc.*, vol. 141, no. 1,

- pp. 1–10, 1994. [Online]. Available: <https://doi.org/10.1149/1.2054684>
- [102] *Specification of Li-ion Polymer Battery 3.7V 10000 mAh*, 2nd ed., AA Portable Power Group, 2004, q/WMDCJ06005-2004. [Online]. Available: <https://www.batteryspace.com/prod-specs/3.7V9059156.pdf>
- [103] Q. Wang, B. Jiang, B. Li, and Y. Yan, “A critical review of thermal management models and solutions of lithium-ion batteries for the development of pure electric vehicles,” *Renewable Sustainable Energy Rev.*, vol. 64, pp. 106 – 128, 2016. [Online]. Available: <https://doi.org/10.1016/j.rser.2016.05.033>
- [104] G.-H. Kim, K. Smith, K.-J. Lee, S. Santhanagopalan, and A. Pesaran, “Multi-domain modeling of lithium-ion batteries encompassing multi-physics in varied length scales,” *J. Electrochem. Soc.*, vol. 158, no. 8, pp. A955–A969, 2011. [Online]. Available: <https://doi.org/10.1149/1.3597614>
- [105] S. Barsali and M. Ceraolo, “Dynamical models of lead-acid batteries: implementation issues,” *IEEE Trans. Energy Convers.*, vol. 17, no. 1, pp. 16–23, Mar 2002. [Online]. Available: <https://doi.org/10.1109/60.986432>
- [106] T. I. Bo and T. A. Johansen, “Battery power smoothing control in a marine electric power plant using nonlinear model predictive control,” *IEEE Trans. Control Syst. Technol.*, vol. 25, no. 4, pp. 1449–1456, July 2017. [Online]. Available: <https://doi.org/10.1109/TCST.2016.2601301>
- [107] C. Masjosthusmann, U. Köhler, N. Decius, and U. Büker, “A vehicle energy management system for a battery electric vehicle,” in *IEEE*

- Vehicle Power and Propulsion Conference*, Oct 2012, pp. 339–344.
[Online]. Available: <https://doi.org/10.1109/VPPC.2012.6422676>
- [108] S. Mohan, J. B. Siegel, A. G. Stefanopoulou, and R. Vasudevan, “An energy-optimal warm-up strategy for Li-Ion batteries and its approximations,” *IEEE Trans. Control Syst. Technol.*, vol. 27, no. 3, pp. 1–16, Mar. 2018. [Online]. Available: <https://doi.org/10.1109/TCST.2017.2785833>
- [109] H. E. Perez, S. Dey, X. Hu, and S. J. Moura, “Optimal charging of Li-Ion batteries via a single particle model with electrolyte and thermal dynamics,” *J. Electrochem. Soc.*, vol. 164, no. 7, pp. A1679–A1687, 2017. [Online]. Available: <https://doi.org/10.1149/2.1301707jes>
- [110] P. H. L. Notten, W. S. Kruijt, and H. J. Bergveld, “Electronic network modeling of rechargeable batteries: II. the NiCd system,” *J. Electrochem. Soc.*, vol. 145, no. 11, Nov. 1998. [Online]. Available: <https://doi.org/10.1149/1.1838872>
- [111] H. E. Perez, X. Hu, and S. J. Moura, “Optimal charging of batteries via a single particle model with electrolyte and thermal dynamics,” in *American Control Conference (ACC)*, July 2016, pp. 4000–4005. [Online]. Available: <https://doi.org/10.1109/ACC.2016.7525538>
- [112] H. J. Bergveld, W. S. Kruijt, and P. H. L. Notten, *Battery Modeling*. Springer, 2005.
- [113] T. M. Bandhauer, S. Garimella, and T. F. Fuller, “A critical review of thermal issues in lithium-ion batteries,” *J. Electrochem. Soc.*,

- vol. 158, no. 3, pp. R1–R25, 2011. [Online]. Available: <https://doi.org/10.1149/1.3515880>
- [114] D. Berndt, “Valve-regulated lead-acid batteries,” *J. Power Sources*, pp. 29–46, 2001. [Online]. Available: [https://doi.org/10.1016/S0378-7753\(01\)00881-3](https://doi.org/10.1016/S0378-7753(01)00881-3)
- [115] N. F. Ponchaut, F. Colella, V. Somandepalli, and M. Stern, “Thermal management modeling for thermal runaway avoidance in lithium-ion batteries,” Exponent, Tech. Rep., 2014. [Online]. Available: <https://doi.org/10.4271/2014-01-0707>
- [116] *ENERGY STAR Program Requirements for Air Source Heat Pump (ASHP) and Central Air Conditioner Equipment - Eligibility Criteria*, 3rd ed., U.S. Environmental Protection Agency. [Online]. Available: https://www.energystar.gov/sites/default/files/specs/private/Room_Air_Conditioner_Program_Requirements_Version_3.pdf
- [117] M. B. Pinson and M. Z. Bazant, “Theory of SEI formation in rechargeable batteries: Capacity fade, accelerated aging and lifetime prediction,” *J. Electrochem. Soc.*, vol. 160, no. 2, pp. A243–A250, 2013. [Online]. Available: <https://doi.org/10.1149/2.044302jes>
- [118] P. Arora, M. Doyle, and R. E. White, “Mathematical modeling of the lithium deposition overcharge reaction in lithium-ion batteries using carbon-based negative electrodes,” *J. Electrochem. Soc.*, vol. 146, no. 10, pp. 3543–3553, 1999. [Online]. Available: <https://doi.org/10.1149/1.1392512>

- [119] B. Suthar, P. W. C. Northrop, R. D. Braatz, and V. R. Subramanian, “Optimal charging profiles with minimal intercalation-induced stresses for lithium-ion batteries using reformulated pseudo 2-dimensional models,” *J. Electrochem. Soc.*, vol. 161, no. 11, pp. F3144–F3155, 2014. [Online]. Available: <https://doi.org/10.1149/2.0211411jes>
- [120] Y.-T. Cheng and M. W. Verbrugge, “Evolution of stress within a spherical insertion electrode particle under potentiostatic and galvanostatic operation,” *J. Power Sources*, vol. 190, no. 2, pp. 453 – 460, 2009. [Online]. Available: <https://doi.org/10.1016/j.jpowsour.2009.01.021>
- [121] US CAR, “Battery test manual for electric vehicles,” Idaho National Laboratory, techreport, 2015, INL/EXT-15-34184. [Online]. Available: http://www.uscar.org/commands/files_download.php?files_id=405
- [122] Y. Wang, Z. Song, V. D. Angelis, and S. Srivastava, “Battery life-cycle optimization and runtime control for commercial buildings demand side management: A new york city case study,” *Energy*, vol. 165, pp. 782 – 791, Dec. 2018, part A. [Online]. Available: <https://doi.org/10.1016/j.energy.2018.09.117>
- [123] S. Ebbesen, P. Elbert, and L. Guzzella, “Battery state-of-health perceptive energy management for hybrid electric vehicles,” *IEEE Trans. Veh. Technol.*, vol. 61, no. 7, pp. 2893–2900, Sept 2012. [Online]. Available: <https://doi.org/10.1109/TVT.2012.2203836>
- [124] C. Vagg, S. Akehurst, C. J. Brace, and L. Ash, “Stochastic dynamic programming in the real-world control of hybrid electric vehicles,”

- IEEE Trans. Control Syst. Technol.*, vol. 24, no. 3, pp. 853–866, May 2016. [Online]. Available: <https://doi.org/10.1109/TCST.2015.2498141>
- [125] C. Vagg, C. J. Brace, S. Akehurst, and L. Ash, “Minimizing battery stress during hybrid electric vehicle control design: Real world considerations for model-based control development,” in *IEEE Vehicle Power and Propulsion Conference (VPPC)*, Oct 2013, pp. 1–6. [Online]. Available: <https://doi.org/10.1109/VPPC.2013.6671713>
- [126] E. Vinot, R. Trigui, and B. Jeanneret, “Optimal management of electric vehicles with a hybrid storage system,” in *IEEE Vehicle Power and Propulsion Conference*, Sept 2010, pp. 1–6. [Online]. Available: <https://doi.org/10.1109/VPPC.2010.5729126>
- [127] Y. Tian, A. Bera, J. Mitra, B. Chalamala, and R. H. Byrne, “Effect of operating strategies on the longevity of lithium-ion battery energy storage systems,” in *IEEE Industry Applications Society Annual Meeting (IAS)*, Sep. 2018, pp. 1–8. [Online]. Available: <https://doi.org/10.1109/IAS.2018.8544518>
- [128] B. Xu, A. Oudalov, A. Ulbig, G. Andersson, and D. Kirschen, “Modeling of lithium-ion battery degradation for cell life assessment,” *IEEE Trans. Smart Grid*, vol. 9, no. 2, pp. 1131 – 1140, 2016. [Online]. Available: <https://doi.org/10.1109/TSG.2016.2578950>
- [129] Y. Niu and S. Santoso, “Sizing and coordinating fast- and slow-response energy storage systems to mitigate hourly wind power variations,” *IEEE Trans. Smart Grid*, vol. 9, no. 2, pp. 1107 – 1117, 2016. [Online]. Available: <https://doi.org/10.1109/tsg.2016.2577549>

- [130] X. Ke, N. Lu, and C. Jin, “Control and size energy storage systems for managing energy imbalance of variable generation resources,” *IEEE Trans. Sustain. Energy*, vol. 6, no. 1, pp. 70–78, jan 2015. [Online]. Available: <https://doi.org/10.1109/tste.2014.2355829>
- [131] B. Xu, J. Zhao, T. Zheng, E. Litvinov, and D. S. Kirschen, “Factoring the cycle aging cost of batteries participating in electricity markets,” *IEEE Trans. Power Syst.*, vol. 33, no. 2, pp. 2248 – 2259, Mar. 2018. [Online]. Available: <https://doi.org/10.1109/TPWRS.2017.2733339>
- [132] Y. Shi, B. Xu, Y. Tan, D. Kirschen, and B. Zhang, “Optimal battery control under cycle aging mechanisms in pay for performance settings,” *IEEE Trans. Autom. Control*, vol. 64, no. 6, pp. 2324–2339, June 2019. [Online]. Available: <https://doi.org/10.1109/TAC.2018.2867507>
- [133] H. Bindner, T. Cronin, P. Lundsager, J. Manwell, U. Abdulwahid, and I. Baring-Gould, *Lifetime modelling of lead acid batteries*. Risø National Laboratory, 2005. [Online]. Available: https://orbit.dtu.dk/fedora/objects/orbit:88309/datastreams/file_7710966/content
- [134] J. M. Reniers, G. Mulder, S. Ober-Blöbaum, and D. A. Howey, “Improving optimal control of grid-connected lithium-ion batteries through more accurate battery and degradation modelling,” *J. Power Sources*, vol. 379, pp. 91 – 102, 2018. [Online]. Available: <https://doi.org/10.1016/j.jpowsour.2018.01.004>
- [135] J. Christensen and J. Newman, “Cyclable lithium and capacity loss in Li-Ion cells,” *J. Electrochem. Soc.*, vol. 152, no. 4, pp. A818–A829, 2005. [Online]. Available: <https://doi.org/10.1149/1.1870752>

- [136] M. Safari, M. Morcrette, A. Teyssot, and C. Delacourt, “Multimodal physics-based aging model for life prediction of Li-ion batteries,” *J. Electrochem. Soc.*, vol. 156, no. 3, pp. A145–A153, 2009. [Online]. Available: <https://doi.org/10.1149/1.3043429>
- [137] M. K. S. Verma, S. Basu, K. S. Hariharan, S. M. Kolake, T. Song, and J. Jeon, “A strain-diffusion coupled electrochemical model for lithium-ion battery,” *J. Electrochem. Soc.*, vol. 164, no. 13, pp. A3426–A3439, 2017. [Online]. Available: <https://doi.org/10.1149/2.0021714jes>
- [138] M. Safari, M. Morcrette, A. Teyssot, and C. Delacourt, “Life-prediction methods for lithium-ion batteries derived from a fatigue approach i. introduction: Capacity-loss prediction based on damage accumulation,” *J. Electrochem. Soc.*, vol. 157, no. 6, pp. A713–A720, 2010. [Online]. Available: <https://doi.org/10.1149/1.3374634>
- [139] J. Schmalstieg, S. Käbitz, M. Ecker, and D. U. Sauer, “A holistic aging model for Li(NiMnCo)O₂ based 18650 lithium-ion batteries,” *J. Power Sources*, vol. 257, pp. 325 – 334, 2014. [Online]. Available: <https://doi.org/10.1016/j.jpowsour.2014.02.012>
- [140] Y. Cui, C. Du, G. Yin, Y. Gao, L. Zhang, T. Guan, L. Yang, and F. Wang, “Multi-stress factor model for cycle lifetime prediction of lithium ion batteries with shallow-depth discharge,” *J. Power Sources*, vol. 279, pp. 123 – 132, 2015, 9th International Conference on Lead-Acid Batteries 2014. [Online]. Available: <https://doi.org/10.1016/j.jpowsour.2015.01.003>
- [141] J. Wang, J. Purewal, P. Liu, J. Hicks-Garner, S. Soukazian, E. Sherman, A. Sorenson, L. Vu, H. Tataria, and M. W. Verbrugge,

- “Degradation of lithium ion batteries employing graphite negatives and nickel-cobalt-manganese oxid + spinel manganese oxide positives: Part 1, aging mechanisms and life estimation,” *J. Power Sources*, vol. 269, pp. 937 – 948, 2014. [Online]. Available: <https://doi.org/10.1016/j.jpowsour.2014.07.030>
- [142] S. D. Downing and D. F. Socie, “Simple rainflow counting algorithms,” *Int. J. Fatigue*, vol. 4, no. 1, pp. 31–40, Jan. 1982. [Online]. Available: [https://doi.org/10.1016/0142-1123\(82\)90018-4](https://doi.org/10.1016/0142-1123(82)90018-4)
- [143] E. Thomas, I. Bloom, J. Christophersen, and V. Battaglia, “Statistical methodology for predicting the life of lithium-ion cells via accelerated degradation testing,” *J. Power Sources*, vol. 184, no. 1, pp. 312 – 317, 2008. [Online]. Available: <https://doi.org/10.1016/j.jpowsour.2008.06.017>
- [144] M. Ecker, J. B. Gerschler, J. Vogel, S. Kabitz, F. Hust, P. Dechent, and D. U. Sauer, “Development of a lifetime prediction model for lithium-ion batteries based on extended accelerated aging test data,” *J. Power Sources*, vol. 215, pp. 248 – 257, 2012. [Online]. Available: <https://doi.org/10.1016/j.jpowsour.2012.05.012>
- [145] K. Abdulla, J. de Hoog, V. Muenzel, F. Suits, K. Steer, A. Wirth, and S. Halgamuge, “Optimal operation of energy storage systems considering forecasts and battery degradation,” *IEEE Transactions on Smart Grid*, vol. 9, no. 3, pp. 2086–2096, May 2018. [Online]. Available: <https://doi.org/10.1109/TSG.2016.2606490>

- [146] M. R. Palacin and A. de Guibert, “Why do batteries fail?” *Science*, vol. 351, no. 6273, 1253292, pp. 1–7, Feb. 2016. [Online]. Available: <https://doi.org/10.1126/science.1253292>
- [147] Y. K. Lee, J. Park, and W. Lu, “A comprehensive experimental and modeling study on dissolution in Li-Ion batteries,” *J. Electrochem. Soc.*, vol. 166, no. 8, pp. A1340–A1354, 2019. [Online]. Available: <https://doi.org/10.1149/2.0111908jes>
- [148] T. Lu, Y. Luo, Y. Zhang, W. Luo, L. Yan, and J. Xie, “Degradation analysis of commercial lithium-ion battery in long-term storage,” *J. Electrochem. Soc.*, vol. 164, no. 4, pp. A775–A784, 2017. [Online]. Available: <https://doi.org/10.1149/2.1321704jes>
- [149] J. Wang, P. Liu, J. Hicks-Garner, E. Sherman, S. Soukiazian, M. Verbrugge, H. Tatara, J. Musser, and P. Finamore, “Cycle-life model for graphite-lifepo4 cells,” *J. Power Sources*, 2011. [Online]. Available: <https://doi.org/10.1016/j.jpowsour.2010.11.134>
- [150] P. Arorat, R. E. White, and M. Doyle, “Capacity fade mechanisms and side reactions in lithium-ion batteries,” *J. Electrochem. Soc.*, vol. 145, no. 10, pp. 3647–3667, 1998. [Online]. Available: <https://doi.org/10.1149/1.1838857>
- [151] T. Waldmann, B.-I. Hogg, and M. Wohlfahrt-Mehrens, “Li plating as unwanted side reaction in commercial Li-ion cells - a review,” *J. Power Sources*, vol. 384, pp. 107 – 124, 2018. [Online]. Available: <https://doi.org/10.1016/j.jpowsour.2018.02.063>

- [152] P. Ramadass, B. Haran, P. M. Gomadam, R. White, and B. N. Popov, “Development of first principles capacity fade model for Li-Ion cells,” *J. Electrochem. Soc.*, vol. 151, no. 2, pp. A196–A203, 2004. [Online]. Available: <https://doi.org/10.1149/1.1634273>
- [153] M. Hand, S. Baldwin, E. DeMeo, J. Reilly, T. Mai, D. Arent, G. Porro, M. Meshek, and D. Sandor, “Renewable Electricity Futures Study, Volume 2: Renewable Electricity Generation and Storage Technologies,” National Renewable Energy Laboratory, Tech. Rep., 2012, NREL/TP-6A20-52409. [Online]. Available: http://www.nrel.gov/analysis/re_futures/
- [154] Stationary Batteries Committee, “IEEE Recommended Practice for the Characterization and Evaluation of Emerging Energy Storage Technologies in Stationary Applications,” *IEEE Std 1679-2010*, Oct 2010.
- [155] Member Services, “Definitions and acronyms,” PJM, Tech. Rep., 2014. [Online]. Available: <http://www.pjm.com/~media/documents/manuals/m35.ashx>
- [156] D. Rosewater and S. Ferreira, “Development of a frequency regulation duty-cycle for standardized energy storage performance testing,” *Journal of Energy Storage*, vol. 7, pp. 286 – 294, 2016. [Online]. Available: <http://www.sciencedirect.com/science/article/pii/S2352152X16300536>
- [157] P. Scott and D. Rosewater, “Energy storage used for frequency regulation and grid firming,” in *Energy, Utility and Environment Conference (EUEC)*, February 2016.

- [158] N. S. Nise, *Control Systems Engineering 4th Edition*. John Wiley and Sons, 2004.
- [159] D. Rosewater, “Energy Storage Systems Analysis Laboratory at Sandia,” Website, accessed: 11-03-2016. [Online]. Available: www.sandia.gov/batterytesting
- [160] P. Scott and M. Simon, “Energy Research and Development Division, FINAL PROJECT REPORT, UTILITY SCALE ENERGY STORAGE, Grid-Saver Fast Energy Storage System,” Prepared for the California Energy Commission, Tech. Rep., 2015.
- [161] M. Hand, S. Baldwin, E. DeMeo, J. Reilly, T. Mai, D. Arent, G. Porro, M. Meshek, and D. Sandor, “Renewable electricity futures study, volume 2: Renewable electricity generation and storage technologies,” National Renewable Energy Laboratory, Tech. Rep., 2012. [Online]. Available: http://www.nrel.gov/analysis/re_futures/
- [162] M. U. Cuma and T. Koroglu, “A comprehensive review on estimation strategies used in hybrid and battery electric vehicles,” *Renewable Sustainable Energy Rev.*, vol. 42, p. 517–531, 2015. [Online]. Available: <https://doi.org/10.1016/j.rser.2014.10.047>
- [163] D. Zhou, A. Ravey, F. Gao, D. Paire, A. Miraoui, and K. Zhang, “Online estimation of state of charge of li-ion battery using an iterated extended kalman particle filter,” in *2015 IEEE Transportation Electrification Conference and Expo (ITEC)*. IEEE, jun 2015.
- [164] D. Zhou, K. Zhang, A. Ravey, F. Gao, and A. Miraoui, “Online estimation of lithium polymer batteries state-of-charge using particle filter-

- based data fusion with multimodels approach,” *IEEE Transactions on Industry Applications*, vol. 52, no. 3, pp. 2582–2595, may 2016.
- [165] F. L. Lewis, D. Vrabie, and V. L. Syrmos, *Optimal Control*, 3rd ed. Wiley, 2012. [Online]. Available: <http://www.uta.edu/utari/acs/FL%20books/Lewis%20optimal%20control%203rd%20edition%202012.pdf>
- [166] C. Hill and D. Chen, “Development of a real-time testing environment for battery energy storage systems in renewable energy applications,” in *2011 IEEE Power and Energy Society General Meeting*, July 2011, pp. 1–8. [Online]. Available: <https://doi.org/10.1109/PES.2011.6039733>
- [167] C. Hill, M. Such, D. Chen, J. Gonzalez, and W. Grady, “Battery energy storage for enabling integration of distributed solar power generation,” *IEEE Trans. Smart Grid*, vol. 3, no. 2, pp. 850–857, 2012. [Online]. Available: <https://doi.org/10.1109/tsg.2012.2190113>
- [168] D. Link, N. J. R. Ridley, M. Manahan, J. Henderson, and J. Pretzlaf, “Energy Storage Integration Council (ESIC) Energy Storage Test Manual 2016,” Electric Power Research Institute, Tech. Rep., 2016.
- [169] D. F. Mix and L. Ratts, *Random Signal Processing*. Prentice Hall, 1995.
- [170] D. Roberson, J. F. Ellison, D. Bhatnagar, and D. A. Schoenwald, “Performance assessment of the pnm prosperity electricity storage project,” Sandia National Laboratories, techreport, 2014, SAND2014-2883. [Online]. Available: <http://www.sandia.gov/ess/publications/SAND2014-2883.pdf>
- [171] A. Cooper, J. Furakawa, L. Lam, and M. Kellaway, “The ultrabattery - a new battery design for a new beginning in hybrid electric vehicle

- energy storage,” *J. Power Sources*, vol. 188, no. 2, pp. 642–649, 2009. [Online]. Available: <https://doi.org/10.1016/j.jpowsour.2008.11.119>
- [172] B. B. McKeon, J. Furukawa, and S. Fenstermacher, “Advanced lead-acid batteries and the development of grid-scale energy storage systems,” *Proc. IEEE*, vol. 102, no. 6, pp. 951–963, 2014. [Online]. Available: <https://doi.org/10.1109/JPROC.2014.2316823>
- [173] B. Kim, Y. Kim, C. Shin, and R. Baldick, “Adaptive energy management system with a bess through experimental-based cell modeling and adaptive model predictive control,” in *IEEE Innovative Smart Grid Technologies - Asia (ISGT Asia)*, 2018.
- [174] J. Wei, G. Dong, and Z. Chen, “On-board adaptive model for state of charge estimation of lithium-ion batteries based on kalman filter with proportional integral-based error adjustment,” *J. Power Sources*, vol. 365, pp. 308–319, 2017. [Online]. Available: <http://dx.doi.org/10.1016/j.jpowsour.2017.08.101>
- [175] Y. Wang, X. Lin, and M. Pedram, “Adaptive control for energy storage systems in households with photovoltaic modules,” *IEEE Trans. Smart Grid*, vol. 5, no. 2, pp. 992–1001, mar 2014. [Online]. Available: <https://doi.org/10.1109/tsg.2013.2292518>
- [176] S. Galbraith and T. Olinsky-Paul, “Resilient power project case study: Sterling municipal light department,” Clean Energy Group, techreport, Mar. 2018. [Online]. Available: <https://www.cleangroup.org/wp-content/uploads/Sterling-case-study.pdf>

- [177] IEEE Standards Coordinating Committee 21, “IEEE Standard for Interconnection and Interoperability of Distributed Energy Resources with Associated Electric Power Systems Interfaces,” *IEEE Std 1547-2018 (Revision of IEEE Std 1547-2003)*, pp. 1–138, April 2018.
- [178] F. Stern and J. Spencer, “Chapter 10: Peak demand and time-differentiated energy savings cross-cutting protocol,” NREL, techreport NREL/SR-7A40-68566, 2017.
- [179] E. F. Camacho and C. B. Alba, *Model predictive control*. Springer Science & Business Media, 2013.
- [180] D. Copp and J. Hespanha, “Simultaneous nonlinear model predictive control and state estimation,” *Automatica*, vol. 77, pp. 143–154, 2017. [Online]. Available: <https://doi.org/10.1016/j.automatica.2016.11.041>
- [181] A. Khatamianfar, M. Khalid, A. V. Savkin, and V. G. Agelidis, “Improving wind farm dispatch in the Australian electricity market with battery energy storage using model predictive control,” *IEEE Transactions on Sustainable Energy*, vol. 4, no. 3, pp. 745–755, July 2013.
- [182] F. Sossan, E. Namor, R. Cherkaoui, and M. Paolone, “Achieving the dispatchability of distribution feeders through prosumers data driven forecasting and model predictive control of electrochemical storage,” *IEEE Transactions on Sustainable Energy*, vol. 7, no. 4, pp. 1762–1777, Oct 2016.
- [183] Y. Levron, J. M. Guerrero, and Y. Beck, “Optimal power flow in microgrids with energy storage,” *IEEE Trans. Power Syst.*,

- vol. 28, no. 3, pp. 3226–3234, aug 2013. [Online]. Available: <https://doi.org/10.1109/tpwrs.2013.2245925>
- [184] D. Rosewater and S. Gonzalez, “Implementation of a grid connected battery-inverter fleet model,” Sandia National Laboratories, Tech. Rep. SAND18-11692, 2018.
- [185] H. D. Sherali, C. M. Shetty, and M. S. Bazaraa, *Nonlinear Programming Theory and Algorithms*, 3rd ed. John Wiley and Sons, 2006.
- [186] S. Burer and A. N. Letchford, “Non-convex mixed-integer nonlinear programming: a survey.” *Surveys in Oper. Res. and Mgmt. Sci.*, vol. 17, no. 2, pp. 97–106, 2012. [Online]. Available: http://www.optimization-online.org/DB_FILE/2012/02/3378.pdf
- [187] L. Gurobi Optimization, “Gurobi optimizer reference manual,” 2018. [Online]. Available: <http://www.gurobi.com>
- [188] Devore, Farnum, and C. Crockett, *Applied Statistics for Engineers and Scientists*, 2nd ed. Thomson Brooks/Cole, 2005.
- [189] T. Funaki and K. Matsuura, “Feasibility of the low frequency ac transmission,” in *Power Engineering Society Winter Meeting, 2000. IEEE*, vol. 4, 2000, pp. 2693–2698 vol.4.
- [190] T. Ngo, M. Lwin, and S. Santoso, “Steady-state analysis and performance of low frequency AC transmission lines,” *IEEE Trans. Power Syst.*, vol. 31, no. 5, pp. 3873–3880, Sep. 2015. [Online]. Available: <https://doi.org/10.1109/TPWRS.2015.250213>

- [191] C. Zhongwei et al, “Application of flywheel energy storage to damp power system oscillations,” *Przegląd Elektrotechniczny*, vol. 87, no. 3, pp. 333–337, 2011. [Online]. Available: <http://pe.org.pl/articles/2011/3/82.pdf>
- [192] P. Sauer and M. Pai, *Power system dynamics and stability*. Potsdam: Prentice Hall, 1998.
- [193] P. Pourbeik, “Wecc energy storage system model–phase ii,” WECC Renewable Energy Modeling Task Force, Tech. Rep., 2015.
- [194] M. J. E. Alam, K. M. Muttaqi, and D. Sutanto, “A novel approach for ramp-rate control of solar PV using energy storage to mitigate output fluctuations caused by cloud passing,” *IEEE Trans. Energy Convers.*, vol. 29, no. 2, pp. 507–518, June 2014. [Online]. Available: <https://doi.org/10.1109/TEC.2014.2304951>
- [195] C. Sabillon-Antunez, O. D. Melgar-Dominguez, J. F. Franco, M. Lavorato, and M. J. Rider, “Volt-var control and energy storage device operation to improve the electric vehicle charging coordination in unbalanced distribution networks,” *IEEE Trans. Sustain. Energy*, vol. 8, no. 4, p. 1560–1570, Oct. 2017.
- [196] A. Safayet, P. Fajri, and I. Husain, “Reactive power management for overvoltage prevention at high pv penetration in a low-voltage distribution system,” *IEEE Trans. Ind. Appl.*, vol. 53, no. 6, p. 5786–5794, Nov. 2017.
- [197] M. J. Reno, M. Lave, J. E. Quiroz, and R. J. Broderick, “PV ramp rate smoothing using energy storage to mitigate increased voltage reg-

- ulator tapping,” in *2016 IEEE 43rd Photovoltaic Specialists Conference (PVSC)*, Jun. 2016, p. 2015–2020.
- [198] A. Ellis, D. Schoenwald, J. Hawkins, S. Willard, and B. Arellano, “PV output smoothing with energy storage,” in *2012 38th IEEE Photovoltaic Specialists Conference*, June 2012, pp. 001 523–001 528. [Online]. Available: <https://doi.org/10.1109/PVSC.2012.6317885>
- [199] S. Drake, D. Wetz, J. Ostanek, S. Miller, J. Heinzl, and A. Jain, “Measurement of anisotropic thermophysical properties of cylindrical li-ion cells,” *Journal of Power Sources*, vol. 252, pp. 298 – 304, 2014. [Online]. Available: <http://www.sciencedirect.com/science/article/pii/S0378775313019502>
- [200] Y. Cengel and A. J. Ghajar, *Heat and Mass Transfer and Fundamentals and Applications*, 5th ed. McGraw Hill, 2014.

Vita

David Rosewater was born near Seattle, Washington in 1988, the son of Dr. Craig Rose and Sarah Rose. He received a Bachelor of Science degree and a Master of Science degree in Electrical Engineering from Montana Tech of the University of Montana in 2009 and 2011 respectively. During graduate school, David worked as an research intern at the Idaho National Laboratory developing advanced spectral impedance measurement techniques for hybrid vehicles batteries. In 2011 David was started at the Sandia National Laboratories in Albuquerque, New Mexico as a member of the technical staff. There his research was focused on collecting and publishing experimental performance data from large scale battery energy storage systems. He obtained a license as a professional engineer in the state of New Mexico in 2014. In 2016 David moved to Austin, Texas to attend classes in the PhD program in Electrical Engineering at UT Austin. He obtained candidacy, completed coursework, and moved back to New Mexico by 2018. David's current work is split between improving battery energy storage control systems, battery systems safety engineering, and battery systems standardization. He is married to Kit Rosewater and they are expecting their first child in May of 2020.

Permanent address: P.O. BOX 5800, MS 1108
Albuquerque, New Mexico 87185

This dissertation was typeset with \LaTeX^\dagger by the author.

[†] \LaTeX is a document preparation system developed by Leslie Lamport as a special version of Donald Knuth's \TeX Program.